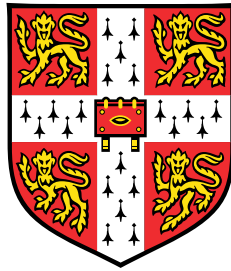


$B = 4N$ Nuclei in the Skyrme Model



Christopher King

Department of Applied Mathematics and Theoretical Physics
University of Cambridge

This dissertation is submitted for the degree of
Doctor of Philosophy

Gonville and Caius College

October 2018

$B = 4N$ Nuclei in the Skyrme Model

Christopher King

The Skyrme model enables us to approximate nuclei via topological solitons known as Skyrmions. The $B = 4$ Skyrmion is of particular importance as its symmetry and stability means that multiple $B = 4$ Skyrmions can combine with each other to form larger $B = 4N$ Skyrmions. In this thesis we investigate the properties of these $B = 4N$ Skyrmions and compare them with results found in the wider nuclear physics community.

We go beyond rigid body quantization and develop a formalism of using vibrational quantisation to generate the energy spectrum of the Oxygen-16 nucleus. The Oxygen-16 nucleus is treated as an arrangement of four $B = 4$ Skyrmions, whose dynamics enable us to create a 2-dimensional manifold of $B = 16$ configurations. We solve the Schrödinger equation on this manifold and discover new states previously not found in the $B = 16$ sector of the Skyrme model. We compare these states with those found experimentally and find that there is an excellent fit to the energy spectrum.

In order to apply vibrational quantization to a wider range of nuclei we create a novel approximation for Skyrmions and the interactions between them. By generating Skyrmions with Gaussian sources we find analytic expressions for the pion fields and interaction energies of Skyrmions, with particular focus on the $B = 1$ and $B = 4$ Skyrmions, and show how this could be applied to vibrational quantization and the clustering of $B = 4$ Skyrmions.

$B = 4N$ nuclei are the only nuclei with zero spin and isospin, which means that their electric charge density is proportional to their baryon density. This simplification makes these nuclei particularly susceptible to investigation via electron scattering. We develop a classical averaging method to calculate the Patterson function and the form factor for a $B = 4N$ nucleus and make comparisons with experimental data. We also discover a way of using the baryon density directly to approximate the locations of zeroes and stationary points of the form factor.

To Mum and Dad

Declaration

This dissertation is the result of my own work and includes nothing which is the outcome of work done in collaboration except as declared in the Preface and specified in the text.

It is not substantially the same as any that I have submitted, or, is being concurrently submitted for a degree or diploma or other qualification at the University of Cambridge or any other University or similar institution except as declared in the Preface and specified in the text. I further state that no substantial part of my dissertation has already been submitted, or, is being concurrently submitted for any such degree, diploma or other qualification at the University of Cambridge or any other University or similar institution except as declared in the Preface and specified in the text

Christopher King

October 2018

Acknowledgements

I would like to thank my supervisor Professor Nick Manton for his constant support and ideas, without which this thesis would not have been possible. His constant enthusiasm has always been inspiring, particularly when my own motivation has been lacking.

I would like to thank Chris Halcrow for being such an enjoyable person to collaborate with, I have never found my work as interesting as when we worked together. Weekly group discussions with Chris, Mareike and Rafael were one of the early highlights of my PhD and sharing ideas with Jonathan Rawlinson later on has also been a source of much interest.

Pav B has always provided excellent coffee breaks, lunches and occasional pub trips which have hugely added to my time here as a PhD Student. I would like to thank Carl, Charles, James, Jack, Manda, Ruadhaí, Toby and Will in particular, but also Andrew and Alec for making the office such a fun place to 'work' and Nathan and Sam for leaving the Euro 2016 blackboard up for so long.

I would like to thank my family for their belief in me and their encouragement, no matter what I choose to pursue. I thank my grandparents for their assistance during my school education which helped me get where I am today.

Finally, I would like to thank Alice for her love and support which has made the final year of my PhD far better than I could have ever imagined.

Table of contents

List of figures	xv
List of tables	xxi
1 Introduction	1
1.1 The Skyrme model	1
1.2 The $B = 1$ Skyrmion	3
1.3 The rational map approximation	5
1.4 Visualising Skyrmions	6
1.5 The $B = 4$ Skyrmion	7
1.5.1 Rotational energy	7
1.5.2 Finkelstein-Rubinstein constraints	8
1.5.3 $B = 4N$ nuclei	11
2 A dynamical alpha cluster model of Oxygen-16	15
2.1 Introduction	15
2.2 Rigid body quantization	17
2.3 The vibrational spaces of the tetrahedron	19
2.4 The vibrational manifold of the E vibration	21
2.4.1 The kinetic operator	23
2.4.2 Boundary conditions	26
2.4.3 The potential on \mathcal{M}_H	31
2.4.4 Solving the Schrödinger equation	32
2.4.5 Rovibrational states	33
2.4.6 Energies of the rovibrational states	40
2.5 Local vibrations of the tetrahedron	44
2.5.1 The A Vibration	44
2.5.2 The F Vibration	45

2.5.3	Combining vibrations	47
2.6	Isospin	50
2.7	Conclusions	53
3	Interactions between Skyrmions	55
3.1	Introduction	55
3.2	Yukawa interactions	56
3.2.1	Massive scalar field theory	56
3.2.2	Point multipole sources	58
3.2.3	The Gaussian monopole source	59
3.3	Gaussian multipole sources	60
3.3.1	The Herglotz generating function	60
3.3.2	Gaussian multipole pion fields	62
3.3.3	Further Gaussian multipole sources	63
3.3.4	Asymptotics of Gaussian multipole pion fields	65
3.3.5	Interaction energies between Gaussian multipole sources	66
3.4	Modeling Skyrmions	69
3.4.1	Calibration of coefficients	69
3.4.2	The $B = 1$ Skyrmion	71
3.4.3	The $B = 2$ Skyrmion	73
3.4.4	The $B = 3$ Skyrmion	74
3.4.5	The $B = 4$ Skyrmion	76
3.5	The interaction energy between Skyrmions	80
3.5.1	Two $B = 1$ Skyrmions	80
3.5.2	Two $B = 4$ Skyrmions	83
3.5.3	The $B = 32$ Skyrmion	87
3.5.4	The Skyrme crystal	88
3.5.5	The $B = 12$ Skyrmion	88
3.5.6	The E vibration of the $B = 16$ Skyrmion	89
3.5.7	The E vibration of the $B = 4$ Skyrmion	92
3.6	Conclusion	100
4	Electron scattering intensities and Patterson functions of Skyrmions	103
4.1	Introduction	103
4.2	Form factors and intensities	105
4.2.1	Scattering from a fixed Skyrmion	105
4.2.2	The quantum averaged intensity	107

4.2.3	The angular velocity of a Skyrmion	108
4.2.4	The classically averaged intensity	109
4.2.5	Comparison of the scattering intensities	111
4.3	Scattering intensities of $B = 4N$ Skyrmions	112
4.3.1	Calibration of Skyrme units	112
4.3.2	The $B = 4$ Skyrmion	113
4.3.3	The $B = 8$ Skyrmion	116
4.3.4	The $B = 12$ Skyrmion	119
4.3.5	The $B = 16$ Skyrmion	124
4.3.6	The $B = 32$ Skyrmion	126
4.3.7	The $B = 108$ Skyrmion	127
4.3.8	The Skyrme crystal	129
4.4	Approximating the zeros and stationary points of the form factor . . .	130
4.4.1	Zeros of the form factor	130
4.4.2	Stationary points of the form factor	131
4.4.3	Accuracy of approximations	132
4.5	Vibrational effects	132
4.5.1	Approximation for the charge densities of Oxygen-16	133
4.5.2	The scattering intensity of a single configuration of Oxygen-16 . . .	133
4.5.3	The scattering intensity of the ground state of Oxygen-16 . . .	134
4.6	Conclusions	135
5	Conclusions and outlook	137
	References	139
	Appendix A Spin states for each representation	143
	Appendix B Combining vibrations	147

List of figures

1.1	The profile functions for $\mu = 0$ and $\mu = 1$	4
1.2	The first four Skyrmions.	7
1.3	The effect of parity of the $B = 4$ Skyrmion.	11
1.4	The experimental spectrum for Helium-4. Positive parity states are denoted by circles and negative parity states are denoted by triangles. Isospin 0 states are coloured black and isospin 1 states are coloured red. There is also the 0^+ ground state which is not shown.	11
1.5	The binding energies for $B = 1 - 8$ in the Skyrme model and from experimental data. The $B = 5$ nucleus is excluded in both cases.	12
1.6	Arrangements of $B = 4$ Skyrmions for $B = 8, 12, 16$ and 32	13
1.7	Different low energy arrangements of $B = 4$ Skyrmions for the $B = 12$ Skyrmion.	13
2.1	The tetrahedral, flat square and bent square $B = 16$ configurations.	17
2.2	The A vibration and a basis for the E vibration.	20
2.3	A basis for the F vibration	20
2.4	The scattering line containing the tetrahedral, flat square and bent square configurations.	21
2.5	An approximation of \mathcal{M} . Regions of the same colour are related by D_2 symmetry and the black line corresponds to the scattering line from Figure 2.4.	22
2.6	The equivalence between \mathcal{M}_q and \mathcal{M}_H	25
2.7	The correspondence between the tetrahedral configuration and a coloured cube.	27
2.8	The effect of the (123) and (12) rotations on the coloured cube.	27
2.9	The effect of (13) and then parity on the point ζ_+ . The curve C is highlighted in red.	29
2.10	The vibrational wavefunctions $\psi_{T,0}^+$, $\psi_{T,1}^+$, $\psi_{T,2}^+$ and $\psi_{T,3}^+$	35

2.11	The vibrational wavefunctions $\psi_{T,0}^-$ and $\psi_{S,0}^+$	36
2.12	The vibrational wavefunctions $\psi_{S,0}^-, \psi_{S,1}^-, \psi_{S,2}^-$ and $\psi_{S,3}^-$	37
2.13	The vibrational wavefunctions $u_0^+ + v_0^+, u_1^+ + v_1^+$ and $u_2^+ + v_2^+$	38
2.14	The vibrational wavefunctions $u_0^+ - v_0^+, u_1^+ - v_1^+$ and $u_2^+ - v_2^+$	38
2.15	The vibrational wavefunctions $u_0^- + v_0^-, u_1^- + v_1^-$ and $u_2^- + v_2^-$	39
2.16	The vibrational wavefunctions $u_0^- - v_0^-, u_1^- - v_1^-$ and $u_2^- - v_2^-$	39
2.17	The states from our vibrational model and corresponding states in the experimental spectrum of Oxygen-16. The hollow black shapes denote experimental states, the blue shapes denote states in the sign or trivial representations and the green shapes denote states in the standard representation. Circles denote positive parity states and triangles denote negative parity states.	41
2.18	A C_3 symmetric vibration in the F vibrational space.	45
2.19	The states of the E vibration in our model along with the states from the A and F vibrations of the tetrahedron and states in the experimental spectrum of Oxygen-16 below 20 MeV. The hollow black shapes denote experimental states with isospin 0, the hollow orange shapes denote experimental states with unknown isospin, the blue shapes denote states in the trivial or sign representations, the green shapes denote states in the standard representation and the red shapes denote states in the F representation. Circles denote positive parity states and triangles denote negative parity states.	50
2.20	The isospin 1 states of the E vibration in our model along with the states from the A and F vibrations of the tetrahedron and states in the experimental spectrum of Oxygen-16 below 20 MeV. The hollow black shapes denote experimental states with isospin 1, the hollow orange shapes denote experimental states with unknown isospin, the blue shapes denote states in the trivial or sign representations, the green shapes denote states in the standard representation and the red shapes denote states in the F representation. Circles denote positive parity states and triangles denote negative parity states.	51
3.1	The $B = 1$ and $B = 2$ Skyrmions.	71
3.2	The relative error of the function $\sin g_A(r)$	72
3.3	The numerical and approximate π_1 field in the $x - z$ plane for the $B = 2$ Skyrmion.	74

3.4	The numerical and approximate π_3 field in the $x - z$ plane for the $B = 2$ Skyrmion.	74
3.5	The $B = 3$ and $B = 4$ Skyrmons.	75
3.6	The numerical and approximate π_3 field in the $x - y$ plane for the $B = 3$ Skyrmion.	75
3.7	The numerical and approximate π_3 field in the $z = 0.75$ plane for the $B = 3$ Skyrmion.	76
3.8	The numerical and approximate π_1 field in the $x - y$ plane for the $B = 4$ Skyrmion.	77
3.9	The numerical and approximate π_2 field in the $x - z$ plane for the $B = 4$ Skyrmion.	78
3.10	The numerical and approximate π_3 field in the $z = 0.75$ plane for the $B = 4$ Skyrmion.	78
3.11	The moment functions, $M_3^{-2}(r)$, with varying values of I_4 ($E_4 = 0, X_4 = 0$).	79
3.12	The difference between the numerical and approximate moment functions for different sets of parameters.	80
3.13	The attractive channel for two $B = 1$ Skyrmons.	81
3.14	The interaction energy for two $B = 1$ Skyrmons in the attractive channel.	82
3.15	The lowest energy arrangements of two $B = 4$ Skyrmons.	84
3.16	The untwisted and twisted $B = 8$ configurations.	84
3.17	The interaction energy as a function of angle of rotation θ for a separation of 4 and 3 Skyrme units.	85
3.18	The interaction energy as a function of separation for the untwisted channel.	85
3.19	The interaction energy as a function of separation for the twisted channel.	86
3.20	The arrangement of eight $B = 4$ cubes in a $B = 32$ Skyrmons.	87
3.21	The linear chain, bent chain and triangle configurations of the $B = 12$ Skyrmion	89
3.22	The scattering line from $\theta = 0$ to $\theta = \pi$	90
3.23	The energy, scale factor and orientations of the $B = 16$ Skyrmion as a function of θ	90
3.24	The $\theta = 0$, $\theta = \arccos \frac{1}{\sqrt{3}}$ (tetrahedral) and $\theta = \frac{\pi}{2}$ (flat square) arrangements of $B = 4$ Skyrmons.	91
3.25	The arrangement for four $B = 1$ Skyrmons at $\theta = \frac{\pi}{4}, \phi = \frac{\pi}{6}, \alpha = \beta = \gamma = 0$	93

3.26	Approximation of the vibrational manifold for four $B = 1$ Skyrmions. Regimes 1, 2, 3 and 4 are denoted by the purple, blue, red and green regions respectively. The line $\phi = \frac{\pi}{2}$ between $\theta = 0$ and $\frac{\pi}{2}$ is shown in black.	95
3.27	The energies of the bonds B_1 , B_2 and B_3 at $\theta = \frac{\pi}{18}$, $\phi = 0$ (regime 1) and $\theta = \frac{\pi}{8}$, $\phi = 0$ (regime 2).	95
3.28	The total interaction energy for $\theta = \frac{\pi}{18}$ (regime 1), $\theta = \frac{\pi}{8}$ (regime 2), $\theta = \frac{\pi}{3}$ (regime 3) and $\theta = \frac{\pi}{2}$ (regime 4).	96
3.29	The energies of the bonds B_1 , B_2 and B_3 at $\theta = \frac{\pi}{3}$ (regime 3) and $\theta = \frac{\pi}{2}$ (regime 4).	97
3.30	The vibrational manifold and potential for four interacting $B = 1$ Skyrmions. Red corresponds to low interaction energy, blue corresponds to high interaction energy.	99
4.1	Feynman diagram of the scattering process	106
4.2	Charge density and Patterson function isosurfaces for the $B = 4$ Skyrmion. 114	
4.3	Patterson function contours in the $x - y$ plane for the $B = 4$ Skyrmion. 115	
4.4	Comparison of $\sqrt{\mathcal{I}}$ (blue) and $ \mathcal{F} $ (red) for the $B = 4$ Skyrmion with the form factor from experimental scattering data (green) for the Helium-4 nucleus.	116
4.5	Charge density and Patterson function isosurfaces for the twisted $B = 8$ Skyrmion.	117
4.6	Patterson function contours in the $x - z$ and $x - y$ planes for the twisted $B = 8$ Skyrmion.	118
4.7	$\sqrt{\mathcal{I}}$ and $ \mathcal{F} $ for the twisted $B = 8$ Skyrmion	118
4.8	Charge density isosurfaces for the triangular and linear $B = 12$ Skyrmions. 119	
4.9	Patterson function isosurfaces for the triangular and linear $B = 12$ Skyrmions.	120
4.10	Patterson function contours in the $x - z$ and $x - y$ planes for the triangular $B = 12$ Skyrmion.	120
4.11	Patterson function contours in the $x - y$ and $x - z$ planes for the linear $B = 12$ Skyrmion.	121
4.12	$\sqrt{\mathcal{I}}$ and $ \mathcal{F} $ for the triangular and linear $B = 12$ Skyrmions.	121
4.13	Radial profile functions for the triangular and linear $B = 12$ Skyrmions: $\rho(r)r^2$ (green), $P(w)w^2$ (blue) and $j_0(qw)$ (red).	122
4.14	Comparison of $\sqrt{\mathcal{I}}$ and $ \mathcal{F} $ for the triangular $B = 12$ Skyrmion with the form factor from experimental scattering data for the Carbon-12 nucleus. 123	

4.15 Charge density and Patterson function isosurfaces for the $B = 16$ Skyrmion.	124
4.16 Patterson function contours in the $x - z$ and $x - y$ planes for the $B = 16$ Skyrmion.	125
4.17 Comparison of $\sqrt{\mathcal{I}}$ and $ \mathcal{F} $ of the $B = 16$ Skyrmion with the form factor from experimental scattering data for the Oxygen-16 nucleus.	125
4.18 Charge density and Patterson function isosurfaces for the $B = 32$ Skyrmion.	126
4.19 Patterson function contours in the $x - y$ plane for the $B = 32$ Skyrmion.	127
4.20 $\sqrt{\mathcal{I}}$ and $ \mathcal{F} $ for the $B = 32$ Skyrmion.	128
4.21 Charge density and Patterson function isosurfaces for the $B = 108$ Skyrmion.	128
4.22 Patterson function contours in the $x - y$ plane for the $B1082$ Skyrmion.	129
4.23 $\sqrt{\mathcal{I}}$ and $ \mathcal{F} $ for the $B = 128$ Skyrmion.	129
4.24 Patterson function contours in the $x - y$ plane for the Skyrme crystal. .	130
4.25 The quantum (left) and classically (right) averaged form factors for the tetrahedral configuration and the vibrational wavefunctions, $\psi_{T,0}^+$ and $\psi_{T,1}^+$.	135

List of tables

2.1	The allowed rigid body spin states for configurations in the $B = 16$ sector.	18
2.2	The effect of elements S_3 on \mathcal{M}_q and \mathcal{M}_H .	28
2.3	The low energy states and the four lowest energy spin 6 states from our vibrational model. The table headings are the spin-parity, the vibrational wavefunction(s), the vibrational energy, the zeroth order rotational energy, the first order correction to the rotational energy and the total energy of the state. We also provide an identification with a state in the experimental spectrum if this is possible.	42
2.4	The low energy states produced by combining vibrations. (AEF) describes the number of vibrational units there is in each channel. We have listed the spin-parity of the state, the representation that it falls under, its vibrational energy, its rotational energy and its total energy. We have provided an identification with an experimental state if such a pairing seems clear.	49
2.5	The isospin 1 states below 20 MeV. We have listed the spin-parity of the state, the representation that it falls under, its vibrational energy, its rotational energy, its isorotational energy and its total energy.	52
3.1	The locations and values of the minima of the total interaction energy with and without a cut-off.	99
4.1	Table of charge radii for nuclei with zero isospin. The entries for $B = 8$ and $B = 108$ are estimates.	113
4.2	Approximate and actual locations of first zero and first minimum of $\mathcal{F}(q^2)$.	132

-
- A.1 The isospin 0 states in the trivial, sign and standard representations up to spin 4. The i th component of the vector in the spin J row corresponds to the coefficient of the spin state, $|J, J + 1 - i\rangle$. The letter T or S next to the state denotes whether the state is in the trivial or sign representations and the sign next to the state denotes the intrinsic parity. States in the standard representation allow either parity. 143
- A.2 The isospin 0 states in the F representation up to spin 4. The i th component of the vector in the spin J row corresponds to the coefficient of the spin state, $|J, J + 1 - i\rangle$. The sign next to the vector denotes the intrinsic parity. 144
- A.3 The isospin 1 states in the trivial, sign and standard representations up to spin 2. The (i, j) th entry of the matrix in the spin J row corresponds to the coefficient of the spin and isospin state, $|J, J + 1 - i\rangle |1, 2 - j\rangle$. The letter T or S next to matrix denotes whether the state is in the trivial or sign representations and the sign next to the matrix denotes the intrinsic parity. States in the standard representation allow either parity. 144
- A.4 The isospin 1 states in the F representation up to spin 2. The (i, j) th entry of the matrix in the spin J row corresponds to the coefficient of the spin and isospin state, $|J, J + 1 - i\rangle |1, 2 - j\rangle$. The sign next to the matrix denotes the intrinsic parity. 145

Chapter 1

Introduction

1.1 The Skyrme model

The Skyrme model [1, 2] is an effective theory of QCD where we retain only the pionic degrees of freedom. While the Skyrme Lagrangian can be expressed explicitly in terms of a triplet of pion fields, $\boldsymbol{\pi} = (\pi_1, \pi_2, \pi_3)$, and an auxiliary field σ , it is most easily expressed in terms of an $SU(2)$ matrix,

$$U(t, \mathbf{x}) = \sigma(t, \mathbf{x}) + i\boldsymbol{\pi}(t, \mathbf{x}) \cdot \boldsymbol{\tau}, \quad (1.1)$$

where $\boldsymbol{\tau} = (\tau_1, \tau_2, \tau_3)$ are the Pauli matrices and the fields satisfy $\sigma^2 + \boldsymbol{\pi} \cdot \boldsymbol{\pi} = 1$ so that the matrix, U , has determinant 1.

We would like our Lagrangian to be Lorentz invariant but we should also incorporate the approximate chiral symmetry of QCD. Chiral symmetry is the symmetry concerning the up and down quarks which gives them equal mass. To model this theory we would require a chirally symmetric Skyrme Lagrangian. In terms of the Skyrme field, U , this means that the Lagrangian would be invariant under

$$U \rightarrow CUD \quad (1.2)$$

for any $SU(2)$ matrices C and D .

We also require our Lagrangian to have at most second order time derivatives; this is because there are difficulties with the stability of the classical solutions of this model if we allow higher order time derivatives. This condition combined with Lorentz and

chiral symmetry leads to the Lagrangian,

$$\mathcal{L}_0 = -\frac{F_\pi^2}{16}\text{Tr}(R_\mu R^\mu) + \frac{1}{32e^2}\text{Tr}([R_\mu, R_\nu][R^\mu, R^\nu]), \quad (1.3)$$

where $R_\mu = (\partial_\mu U)U^\dagger$ is the right current of the Skyrme field and F_π and e are parameters which can be calibrated via comparison to experimental data. This Lagrangian is easiest to work with if we use Skyrme units where the energy and length units are $F_\pi/4e$ and $2/eF_\pi$ respectively. In Skyrme units the Skyrme Lagrangian becomes

$$\mathcal{L}_0 = -\frac{1}{2}\text{Tr}(R_\mu R^\mu) + \frac{1}{16}\text{Tr}([R_\mu, R_\nu][R^\mu, R^\nu]). \quad (1.4)$$

The second order term includes the standard kinetic term for the pions and if we only had this term we would have a sigma model. The fourth order term is called the Skyrme term and it is this term which allows stable soliton solutions in the Skyrme model.

In reality the up and down quarks have slightly different masses and we break this chiral symmetry with the introduction of a mass term for the pions giving us the massive Skyrme Lagrangian,

$$\mathcal{L} = -\frac{1}{2}\text{Tr}(R_\mu R^\mu) + \frac{1}{16}\text{Tr}([R_\mu, R_\nu][R^\mu, R^\nu]) + \mu^2\text{Tr}(U - I_2). \quad (1.5)$$

The introduction of the pion mass term breaks the $SU(2) \times SU(2)$ chiral symmetry down to an $SU(2)$ isospin symmetry such that the Lagrangian is now only invariant under

$$U \rightarrow CUC^\dagger \quad (1.6)$$

for any $SU(2)$ matrix C . The effect of this transformation is to rotate the triplet of pion fields via $\boldsymbol{\pi} \rightarrow M\boldsymbol{\pi}$, where $M_{ij} = \frac{1}{2}\text{Tr}(\tau_i C \tau_j C^\dagger)$ is an $SO(3)$ matrix. Therefore we call this transformation an isorotation.

If we now consider the static energy of the Skyrme field,

$$E = \int -\frac{1}{2}\text{Tr}(R_i R_j) - \frac{1}{16}\text{Tr}([R_i, R_j][R_i, R_j]) - \mu^2\text{Tr}(U - I_2) d^3x, \quad (1.7)$$

we see that the introduction of the pion mass term means that any finite energy solution must tend to the vacuum, $U = I_2$, as $|\mathbf{x}| \rightarrow \infty$. Note that a choice of a vacuum is enough to break chiral symmetry to isospin symmetry and therefore this condition is enforced by hand to break the chiral symmetry for the massless Skyrme model.

The choice of a vacuum also means that we compactify physical space, $\mathbb{R}^3 \cup \{\infty\} \cong S^3$, and, given that the target space $SU(2)$ has group manifold S^3 , this means that all finite energy configurations correspond to maps from S^3 to S^3 . Such maps can be labelled by the degree of the map,

$$B = -\frac{1}{24\pi^2} \int \epsilon_{ijk} \text{Tr} (R_i R_j R_k) d^3x, \quad (1.8)$$

which is a topological invariant. This provides a topological charge which we identify with the baryon number of the configuration.

The presence of a topological charge is not enough to allow stable topological solitons because we must also overcome Derrick's theorem [3]. If we look at the static energy we see that it splits into three parts, $E = E_2 + E_4 + E_0$, corresponding to terms which are quadratic and quartic in spatial derivatives and the mass term which has no spatial derivatives. Therefore under the rescaling $\mathbf{x} \rightarrow \lambda\mathbf{x}$, the energy becomes

$$E(\mu) = \frac{1}{\lambda} E_2 + \lambda E_4 + \frac{1}{\lambda^3} E_0. \quad (1.9)$$

Notice that the quadratic and quartic terms scale in opposite ways which means that we obtain a minimum for a finite non-zero value of λ . This means that the soliton has a preferred scale and will not expand or contract indefinitely in order to lower its energy. This shows that we require a term which is at least fourth order in spatial derivatives along with the kinetic term in order to allow stable solitons. The Skyrme term is the unique fourth order expression which is Lorentz invariant and has at most two time derivatives.

By looking at the strain tensor of the Skyrme field one can show that there is a Bogomolny bound on the static energy of a configuration,

$$E \geq 12\pi^2 B, \quad (1.10)$$

but that this bound can not be saturated.

1.2 The $B = 1$ Skyrmion

Skyrmions correspond to the local minimizers of the energy functional (1.7) and these are not known analytically for any baryon number. However the $B = 1$ global minimizer

has spherical symmetry and its Skyrme field can be expressed as,

$$U(\mathbf{x}) = \exp\{if(r)\hat{\mathbf{x}} \cdot \boldsymbol{\tau}\}, \quad (1.11)$$

with σ and $\boldsymbol{\pi}$ fields,

$$\sigma = \cos f(r), \quad \boldsymbol{\pi} = \sin f(r) \hat{\mathbf{x}}, \quad (1.12)$$

where $f(r)$ is the radial profile function subject to the constraints $f(0) = \pi$ and $f(\infty) = 0$ so that $U \rightarrow I_2$ as $\mathbf{x} \rightarrow \infty$. This is called a hedgehog solution because the pion fields point radially outwards away from the origin at all points in space. However, in order to find $f(r)$ we must substitute the expression in (1.11) into (1.7) which gives the following expression for the energy of the configuration,

$$E = 4\pi \int_0^\infty \left(r^2 f'^2 + 2(f'^2 + 1) \sin^2 f + \frac{\sin^4 f}{r^2} + 2\mu^2 r^2 (1 - \cos f) \right) dr \quad (1.13)$$

The energy minimizer for (1.13) can not be expressed analytically but can be found easily numerically via a shooting method. The profile functions for $\mu = 0$ and $\mu = 1$ are shown in Figure 1.1.

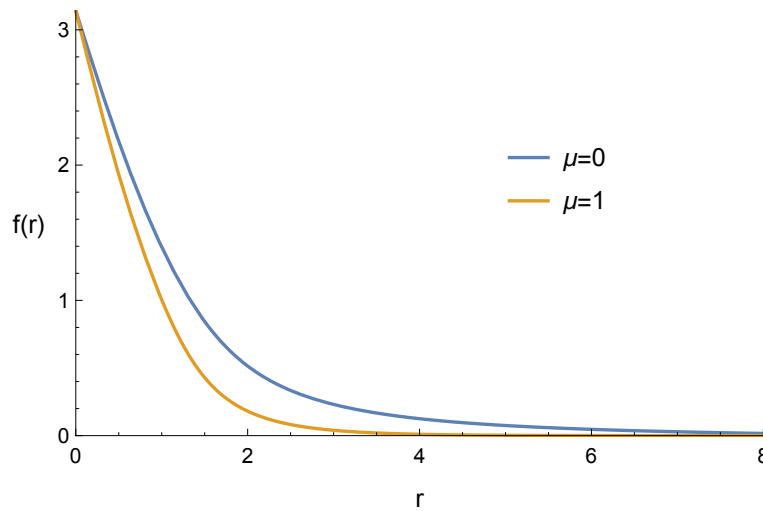


Fig. 1.1 The profile functions for $\mu = 0$ and $\mu = 1$.

Of particular interest are the asymptotics of f and, if we linearise the Euler-Lagrange equation that we obtain from (1.13), one can show that

$$f \sim \frac{A}{r} e^{-\mu r} \quad (1.14)$$

for large r . This means that pion fields are of the form,

$$\boldsymbol{\pi} \sim \frac{A\hat{\mathbf{x}}}{r} e^{-\mu r}, \quad (1.15)$$

and therefore at large distances $B = 1$ Skyrmions are well approximated by a triplet of Yukawa dipoles.

For the case of $\mu = 0$ these asymptotics become slightly different with,

$$f \sim \frac{A_0}{r^2} \quad (1.16)$$

for large r . This means that pion fields are of the form,

$$\boldsymbol{\pi} \sim \frac{A_0\hat{\mathbf{x}}}{r^2}, \quad (1.17)$$

and therefore at large distances $B = 1$ Skyrmions for $\mu = 0$ are well approximated by a triplet of Coulomb dipoles.

1.3 The rational map approximation

Skyrmions for higher values of B are not of the hedgehog form, but we can use an analogue to approximate them. For the domain, \mathbb{R}^3 , we change coordinates such that $\mathbf{x} = r\mathbf{n}_z$ with

$$\mathbf{n}_z = \frac{1}{1 + |z|^2} \left(z + \bar{z}, i(\bar{z} - z), 1 - |z|^2 \right), \quad (1.18)$$

so that z is the standard Riemann sphere coordinate and $r = |\mathbf{x}|$. For the target space, S^3 , we express the Skyrme field as

$$U(\mathbf{x}) = \exp\{if(r)\hat{\mathbf{n}}_{R(z)} \cdot \boldsymbol{\tau}\} \quad (1.19)$$

with

$$\mathbf{n}_R(z) = \frac{1}{1 + |R|^2} \left(R + \bar{R}, i(\bar{R} - R), 1 - |R|^2 \right), \quad (1.20)$$

where again R is a Riemann sphere coordinate. The Skyrme field is now encoded by the maps $R : S^2 \rightarrow S^2$ and $f : \mathbb{R}^+ \rightarrow \mathbb{R}$ so we have effectively separated the radial and angular degrees of freedom. The correspondence between rational maps and monopoles and the similarities between monopoles and Skyrmions suggests that using rational maps for R may lead to a good approximation to Skyrmions [4]. A rational map from

S^2 to S^2 takes the form,

$$R(z) = \frac{p(z)}{q(z)} \quad (1.21)$$

where p and q are polynomials in z that do not have a common root. It can be shown if f satisfies the boundary conditions $f(0) = \pi$ and $f(\infty) = 0$, then the corresponding Skyrmion has baryon number $B = \max(\deg(p), \deg(q))$, where \deg denotes the degree of the polynomial in z . Note that the $B = 1$ hedgehog solution corresponds to the rational map $R(z) = z$.

We now want to find the minimal energy rational map R and corresponding profile function f for each baryon number and to do this we substitute (1.19) into the expression for the static energy (1.7), giving

$$E = 4\pi \int_0^\infty \left(r^2 f'^2 + 2B(f'^2 + 1) \sin^2 f + \mathcal{I} \frac{\sin^4 f}{r^2} + 2m^2 r^2 (1 - \cos f) \right) dr \quad (1.22)$$

where

$$\mathcal{I} = \frac{1}{4\pi} \int \left(\frac{1 + |z|^2}{1 + |R|^2} \left| \frac{dR}{dz} \right| \right)^4 \frac{2idzd\bar{z}}{(1 + |z|^2)^2}. \quad (1.23)$$

In order to minimize the energy in (1.22) we must find the rational map, $R(z)$, that minimizes \mathcal{I} and then substitute this value of \mathcal{I} into (1.22) and find the radial profile function, $f(r)$, that minimizes the energy. The rational maps giving the lowest value of \mathcal{I} for $B = 1 - 4$ are,

$$R_1(z) = z, \quad R_2(z) = z^2, \quad R_3(z) = \frac{\sqrt{3}iz^2 - 1}{z^3 - \sqrt{3}iz}, \quad R_4(z) = \frac{z^4 + 2\sqrt{3}iz^2 + 1}{z^4 - 2\sqrt{3}iz^2 + 1}, \quad (1.24)$$

which have spherical, toroidal, tetrahedral and cubic symmetry respectively. These rational maps provide a good approximation for the shape and energies of these Skyrmions and can be used as a starting point from which to relax solutions numerically.

1.4 Visualising Skyrmions

There are a couple of important aspects of a Skyrmion that we would like to capture when we visualise it. The first is baryon density, this gives us an idea of where the nuclear matter actually lies in the Skyrmion and is useful for determining the symmetries that a Skyrmion has. Therefore when we visualise a Skyrmion we plot a surface of constant baryon density but we would also like to incorporate the direction of the pion fields, $\boldsymbol{\pi} = (\pi_1, \pi_2, \pi_3)$. We can do this by colouring the surface of constant

baryon density using the Runge colour sphere according to the colour scheme in [5]. We colour the Skyrmion white when $\pi_3 = 1$, black when $\pi_3 = -1$ and red, green and blue when $\pi_1 + i\pi_2$ equals 1 , $e^{\frac{2i\pi}{3}}$ and $e^{-\frac{2i\pi}{3}}$ respectively. We plot the first four Skyrmions with this visualisation scheme in Figure 1.6 with the $B = 1$ Skyrmion on the left increasing B up to the $B = 4$ Skyrmion on the right.

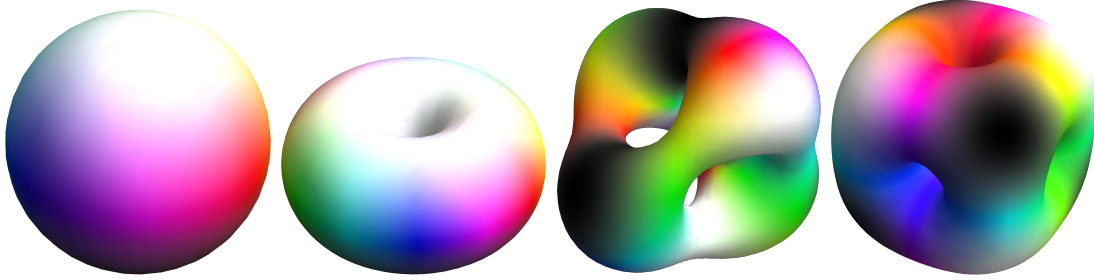


Fig. 1.2 The first four Skyrmions.

This colouring makes it easier to explain exactly what we mean by a symmetry of a Skyrmion. A symmetry is a pairing of a rotation and an isorotation that leaves the Skyrmion invariant. Thus, for a symmetry, the rotation of the Skyrmion must be equivalent to recolouring it via reorienting the Runge colour sphere. We will see that these symmetries provide constraints on the spin and isospin states that are permitted upon quantization the Skyrmions.

1.5 The $B = 4$ Skyrmion

In this section will consider some more aspects of the Skyrme model and in particular how they apply to the $B = 4$ Skyrmion.

1.5.1 Rotational energy

Consider the effect of a rotation and isorotation on a static Skyrme configuration:

$$U(\mathbf{x}) \rightarrow CU(M(D)\mathbf{x})C^\dagger, \quad (1.25)$$

where C and D are the $SU(2)$ matrices encoding the isorotation and rotation respectively and $M(D)_{ij} = \frac{1}{2}\text{Tr}(\tau_i D \tau_j D^\dagger)$. We perform semi-classical quantization by giving C and D time dependence [6],

$$U(\mathbf{x}, t) = C(t)U_0(M(D(t))\mathbf{x})C(t)^\dagger. \quad (1.26)$$

We substitute this expression into the Skyrme Lagrangian to determine the kinetic energy,

$$T = \frac{1}{2}a_i U_{ij} a_j - a_i W_{ij} b_j + \frac{1}{2}b_i V_{ij} b_j, \quad (1.27)$$

where $a_i = -i\text{Tr}(\tau_i C^\dagger \dot{C})$ and $b_i = i\text{Tr}(\tau_i \dot{D} D^\dagger)$ are the angular velocities in isospace and physical space respectively. The inertia tensors U_{ij} , W_{ij} and V_{ij} are defined as follows,

$$U_{ij} = - \int \text{Tr} \left(T_i T_j + \frac{1}{4} [R_k, T_i] [R_k, T_j] \right) d^3 \mathbf{x}, \quad (1.28)$$

$$W_{ij} = \int \epsilon_{jlm} x_l \text{Tr} \left(T_i R_m + \frac{1}{4} [R_k, T_i] [R_k, R_m] \right) d^3 \mathbf{x}, \quad (1.29)$$

$$V_{ij} = - \int \epsilon_{ilm} \epsilon_{jnp} x_l x_n \text{Tr} \left(R_m R_p + \frac{1}{4} [R_k, R_m] [R_k, R_p] \right) d^3 \mathbf{x}, \quad (1.30)$$

where $T_i = \frac{i}{2} [\tau_i, U_0] U_0^{-1}$ and R_i is the right current of the Skyrme field, U_0 . The total kinetic energy can also be expressed as,

$$T = \frac{1}{2} (\mathbf{K}, \mathbf{L}) \cdot \Lambda^{-1} \cdot (\mathbf{K}, \mathbf{L})^T \quad (1.31)$$

where $K_i = U_{ij} a_j - W_{ij} b_j$ and $L_i = -W_{ji} a_j + V_{ij} b_j$ are the body-fixed isospin and spin angular momenta and

$$\Lambda = \begin{pmatrix} U & -W \\ -W^T & V \end{pmatrix}.$$

The high degree of symmetry that the $B = 4$ Skyrmion has means that most of the elements of the inertia tensors are zero. The only non-zero elements are, $U_{11} = U_{22} = 142.84$ and $U_{33} = 169.41$ and $V_{11} = V_{22} = V_{33} = 663.16$ [7]. Substituting these into the expression for the kinetic energy (1.31) gives,

$$T = \frac{1}{2V_{11}} \mathbf{J}^2 + \frac{1}{2U_{11}} \mathbf{I}^2 + \frac{1}{2} \left(\frac{1}{U_{33}} - \frac{1}{U_{11}} \right) K_3^2 \quad (1.32)$$

where \mathbf{J} and \mathbf{I} are the space fixed spin and isospin angular momenta with $\mathbf{J}^2 = \mathbf{L}^2$ and $\mathbf{I}^2 = \mathbf{K}^2$.

1.5.2 Finkelstein-Rubinstein constraints

Having found the rotational energy of a given spin state we must now consider which spin states the $B = 4$ Skyrmion allows. The symmetries of the $B = 4$ Skyrmion

put constraints on the allowed spin states and the reasons behind this are down to Finkelstein and Rubinstein [8].

The configuration space for Skyrmions of a given baryon number, Q_B , is connected but has a non-trivial fundamental group, \mathbb{Z}_2 . In order to have a coherent theory we must define wavefunctions on the covering space, \tilde{Q}_B , which is a double cover of Q_B . If we have two distinct points p_1, p_2 in \tilde{Q}_B corresponding to the same point in Q_B , then fermionic quantisation dictates that the wavefunction defined on \tilde{Q}_B , ψ , must satisfy:

$$\psi(p_1) = -\psi(p_2) \quad (1.33)$$

Symmetries of the Skyrmion correspond to loops in Q_B and whether these symmetries should come with an associated flip of sign for the wavefunction can be determined via a variety of approaches [9].

Finkelstein-Rubinstein quantisation leads to the important result that a 2π rotation flips the wavefunction of a Skyrmion if and only if B is odd [10]. This means that Skyrmions with odd baryon number correspond to fermions and in particular the $B = 1$ Skyrmion, corresponding to a proton or neutron, is fermionic. It can also be shown that the interchange of two identical Skyrmions flips the wavefunctions if and only if their individual baryon numbers are odd. The combination of Finkelstein-Rubinstein constraints with the semi-classical treatment of rotational energy is called rigid body quantization.

The cubic symmetry group of the $B = 4$ can be generated by a C_3 and a C_4 symmetry both of which have no corresponding sign flip for the wavefunction. Therefore spin states, $|\Theta\rangle$, must obey the following constraints,

$$e^{\frac{2i\pi}{3\sqrt{3}}(\hat{L}_1 + \hat{L}_2 + \hat{L}_3)} e^{\frac{2i\pi}{3}\hat{K}_3} |\Theta\rangle = |\Theta\rangle, \quad (1.34)$$

$$e^{\frac{i\pi}{2}\hat{L}_3} e^{i\pi\hat{K}_1} |\Theta\rangle = |\Theta\rangle. \quad (1.35)$$

where \hat{L}_i and \hat{K}_i are the body fixed spin and isospin angular momentum operators respectively.

Cubic symmetry is very constraining and there are not many states which satisfy both (1.34) and (1.35). Using the notation $|J, L_3\rangle |I, K_3\rangle$ where J and I denote the total spin and isospin of the state respectively, then the ground state is $|0, 0\rangle |0, 0\rangle$.

The next isospin 0 state that is allowed is,

$$\left(|4, 4\rangle + \sqrt{\frac{14}{5}} |4, 0\rangle + |4, -4\rangle \right) |0, 0\rangle, \quad (1.36)$$

which is at 39.4 MeV for the values of the moments of inertia above. There are no states observed for Helium-4 with spin 4, however, all the known states have energy less than 30 MeV and therefore there is no contradiction with the Skyrme model. Spin 1, 2 and 3 states with zero isospin are not permitted by the cubic symmetry.

There is a lower energy state with isospin 1 and spin 2,

$$\left(|2, 2\rangle + \sqrt{2}i |2, 0\rangle + |2, -2\rangle \right) |1, 1\rangle - \left(|2, 2\rangle - \sqrt{2}i |2, 0\rangle + |2, -2\rangle \right) |1, -1\rangle, \quad (1.37)$$

which is at 28.7 MeV. There is a corresponding 2^- state with isospin 1 in the experimental spectrum found at 23.3 MeV which is a reasonable agreement with the Skyrme model.

Along with the C_3 and C_4 rotational symmetries above, the $B = 4$ Skyrmion also has a reflection symmetry. This means that we can determine the effect of the parity operator, $\hat{\mathcal{P}}$, on the $B = 4$ Skyrmion and resulting spin states. For a Skyrme field, $U(\mathbf{x})$, the parity operator acts as follows [7],

$$U(\mathbf{x}) \rightarrow U^\dagger(-\mathbf{x}), \quad (1.38)$$

or in terms of the pion fields,

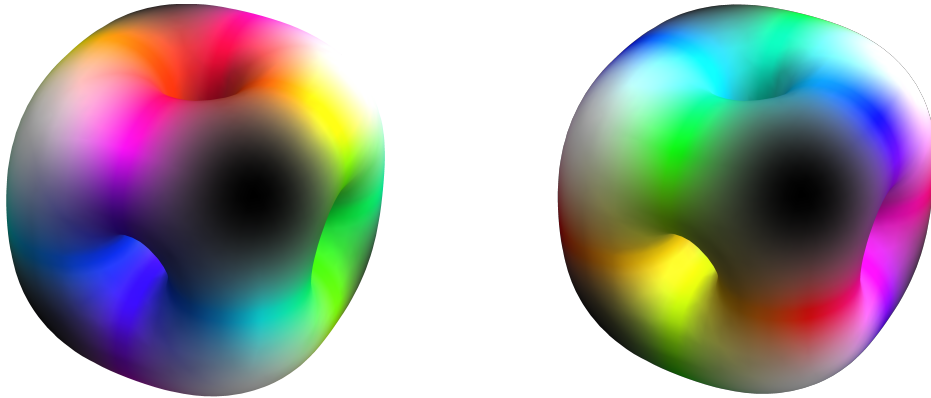
$$\boldsymbol{\pi}(\mathbf{x}) \rightarrow -\boldsymbol{\pi}(-\mathbf{x}). \quad (1.39)$$

The effect of parity on the $B = 4$ Skyrmion can be seen in Figure 1.3, which makes it clear that parity is equivalent to an isorotation of π about $(0, 0, 1)$. Therefore

$$\hat{\mathcal{P}} = e^{i\pi\hat{L}_3} \quad (1.40)$$

and this operator can be used to find the parity of the spin states above. We find that the spin 0 and spin 4 states with isospin 0 have positive parity and the spin 2, isospin 1 state has negative parity.

In Figure 1.4 we show the experimental spectrum for Helium-4 below 30 MeV (excluding the ground state). There are 16 states below 30 MeV, of which two are explained by the rigid body quantization of the $B = 4$ Skyrmion. The small number of spin states allowed by the $B = 4$ Skyrmion is due to its cubic symmetry which is very restrictive and one way to introduce more states is to consider vibrational excitations of the $B = 4$ Skyrmion [11, 12]. In [13] these vibrations are treated as harmonic and are quantized; this was able to reproduce some of the missing spin-parities seen in the experimental spectrum but the energies were an order of magnitude too large. A more

Fig. 1.3 The effect of parity of the $B = 4$ Skyrmion.

in-depth analysis may be able to lower these energies as would using different values of F_π and e .

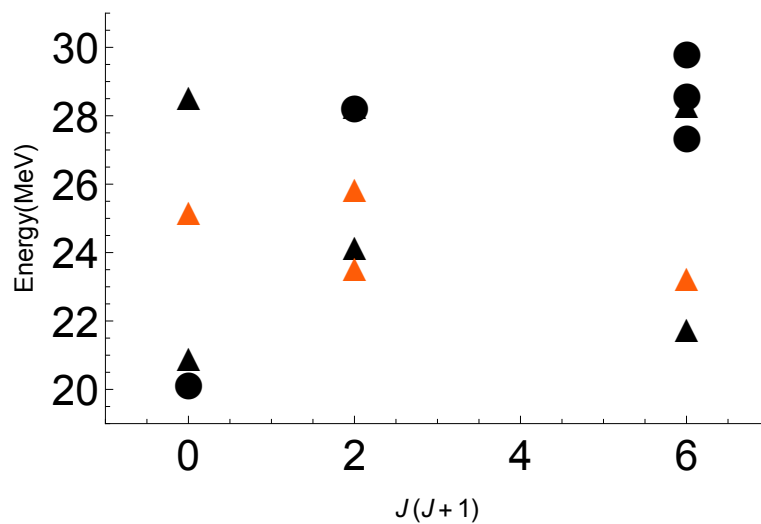


Fig. 1.4 The experimental spectrum for Helium-4. Positive parity states are denoted by circles and negative parity states are denoted by triangles. Isospin 0 states are coloured black and isospin 1 states are coloured red. There is also the 0^+ ground state which is not shown.

1.5.3 $B = 4N$ nuclei

The chapters of this thesis often involve $B = 4N$ Skyrmions as well as the $B = 4$ Skyrmion itself. The $B = 4$ Skyrmion is very strongly bound in comparison to its neighbours and this is seen in both the Skyrme model and experimental data as shown

in Figure 1.5; this means that it can be used as a building block for larger Skyrmions [14]. This is analogous to alpha cluster models in nuclear physics [15, 16].

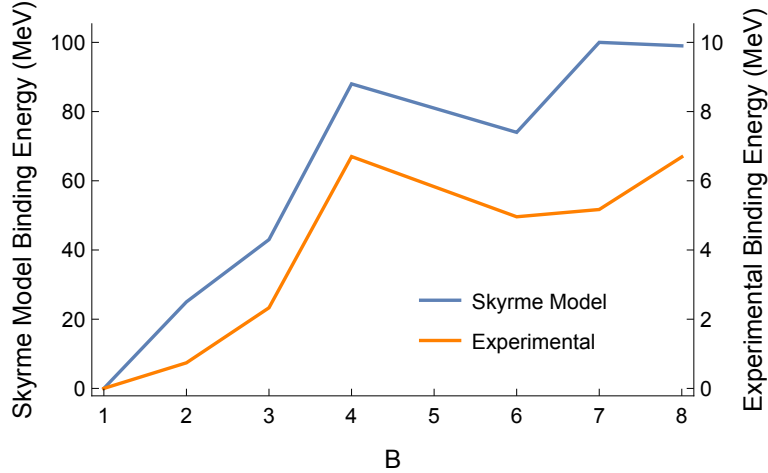


Fig. 1.5 The binding energies for $B = 1 - 8$ in the Skyrme model and from experimental data. The $B = 5$ nucleus is excluded in both cases.

The interactions between constituent $B = 4$ Skyrmions are relatively weak in a $B = 4N$ Skyrmion and as a result they can often be easily identified as shown in Figure 1.6. Another consequence of the weak interaction is that there are usually a few different arrangements of $B = 4$ Skyrmions which have roughly the same energy as shown in Figure 1.7. The presence of multiple low energy configurations for a given baryon number means that states in the same energy spectrum can be associated with different configurations. This becomes particularly crucial if the configurations have different symmetry groups because then they will also have different allowed spin states. This quantization can either be performed via a rigid body quantization as in [17, 18] for Carbon-12 and Oxygen-16 respectively or better still via a vibrational quantization which connects the different configurations as in [19] for Carbon-12. We provide an in-depth analysis of the vibrational quantization of Oxygen-16 in chapter 2 of this thesis.

One positive aspect of the spectrum of Helium-4 is that the lowest energy excitation is around 20 MeV because of the strong binding of the alpha particle. This means that for the states below 20 MeV in the experimental spectra of $B = 4N$ nuclei the constituent alpha particles must each be in its ground state and that these states are explained by the rotations, isorotations and vibrations of the collection of alpha particles. Therefore the Skyrme model does not need to have an accurate model of the alpha particle in order to explain the low-lying states of $B = 4N$ nuclei.

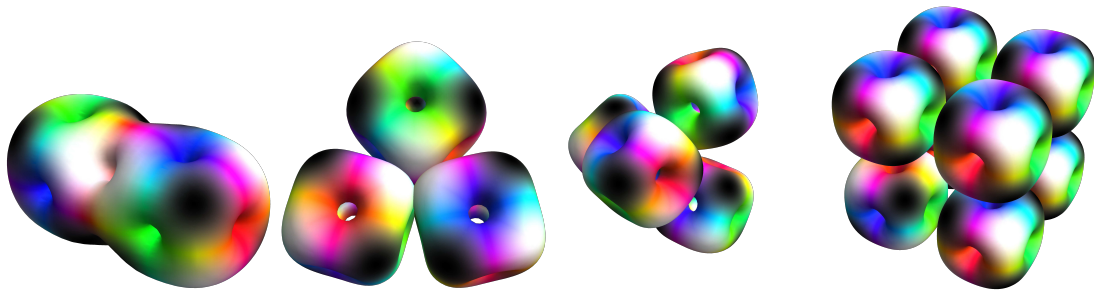


Fig. 1.6 Arrangements of $B = 4$ Skyrmions for $B = 8, 12, 16$ and 32 .

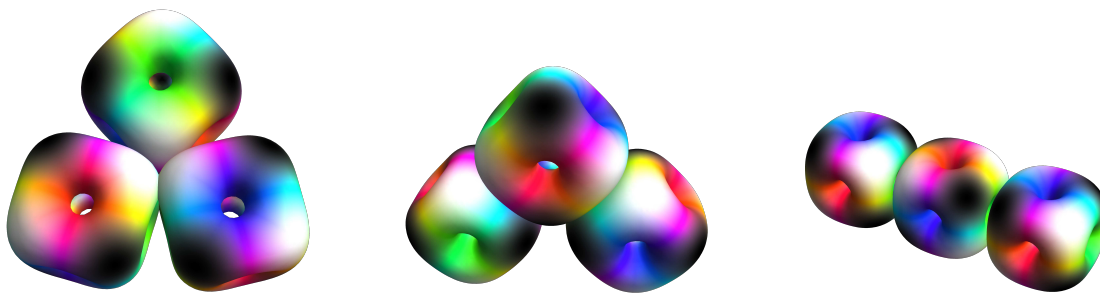


Fig. 1.7 Different low energy arrangements of $B = 4$ Skyrmions for the $B = 12$ Skyrmion.

Chapter 2

A dynamical alpha cluster model of Oxygen–16

This chapter is based on a joint paper with C.J. Halcrow and N.S. Manton [20].

2.1 Introduction

The energy spectrum of Oxygen–16 has presented a problem to nuclear physicists for decades. The ground state has spin-parity 0^+ , as would be expected for a nucleus with an equal and even number of protons and neutrons. The ground state is the base of a rotational band containing a 3^- state at 6.13 MeV and a 4^+ state at 10.36 MeV. The absence of a spin 2 state in this rotational band implies that the ground state nucleus has some enhanced symmetry. The first excited state is also 0^+ at 6.05 MeV and the lowest lying spin 2 state is 2^+ at 6.92 MeV. It is difficult to explain just these five states and the interpretation of them varies from model to model.

Much of the early work on the energy spectrum of Oxygen–16 [21, 22] uses alpha cluster models, in particular a tetrahedral arrangement of four alpha particles. The tetrahedron is the most symmetric arrangement of the four particles and is therefore an appealing candidate for the configuration with the lowest energy. Tetrahedral symmetry is also consistent with the observed 0^+ , 3^- , 4^+ ground state band and forbids any spin 2 states.

In terms of explaining the other low energy states in the spectrum there are a few different alpha cluster approaches that have been employed. One approach is to consider the perturbations of the tetrahedral arrangement [22]. One of these perturbations is the breathing mode, the symmetric stretching and squashing of the tetrahedron whilst retaining tetrahedral symmetry; in many models the breathing mode is thought to be

responsible for the first excited 0^+ state. Other, less symmetric, perturbations are able to explain spin 2 states, but this local approach has some difficulties with parity. The tetrahedron is not invariant under parity and is not linked with its dual configuration, the configuration obtained via the action of parity, via a small perturbation. This means that for a local vibrational wavefunction there is an even and an odd parity version globally which have exactly the same energy. This leads to pairs of states, which have the same spin but opposite parities, having the same energy, which is not observed in the experimental spectrum. In our model we propose the existence of a low energy path between the dual tetrahedra which alleviates this problem. Such alpha cluster models have also been shown to be a limit of the algebraic cluster model in [23, 24].

An alternative is to consider the rotational excitations of additional arrangements of alpha particles, such as the flat square, bent square and chain configurations as seen in [25]. These arrangements, along with the tetrahedron, were observed to be local minima of the configuration energy for a range of different models. In particular, rigid body quantization of these configurations has been looked at in the Skyrme model in [18]. Such approaches are able to reproduce some of the low lying states in the experimental spectrum but often struggle with matching the energies. We believe that this is because the tetrahedra, flat square and bent square arrangements are too close to each other in configuration space to be quantized separately.

The Oxygen–16 nucleus has also been considered in ab initio and shell models. In [26] they consider nucleons interacting via an effective theory and find that the ground state is correlated with a tetrahedral arrangement of alpha particles. The first excited 0^+ state is correlated with a flat square arrangement of alpha particles, with the lowest energy 2^+ corresponding to rotational excitation of the square. Interestingly this ab initio approach still suggests that the nucleons form alpha particles which then cluster together to form the Oxygen–16 nucleus and therefore there is significant overlap with alpha cluster models.

The ground state of Oxygen–16 is spherically symmetric in the shell model, but it is shown that this is equivalent to a tetrahedral arrangement of alpha particles for a harmonic approximation in [27]. There appears to be some difficulty in explaining the first excited 0^+ state with a four-particle-four hole interpretation being suggested in [28], but it is difficult to imagine this having sufficiently low energy [29].

The two different approaches in alpha clustering have been effective in explaining parts of the experimental spectrum but both have significant shortcomings. In our model we attempt to take the best parts of each approach by using the Skyrme model to

construct a vibrational manifold containing the tetrahedral, flat square and bent square configurations. This allows some states to be correlated with small perturbations of the tetrahedron, others to be correlated with the flat square or bent square configurations and some to be viewed as a mix of the two. Of particular importance is whether we can shed any light on the nature of the first excited 0^+ state, which in some models is viewed as correlated with a flat square configuration and in others is explained via the breather mode of the tetrahedral configuration.

2.2 Rigid body quantization

There are a number of different low energy configurations in the $B = 16$ sector of the Skyrme model, but each of these can be viewed as an arrangement of four $B = 4$ Skyrmions. Of particular importance are the tetrahedral, flat square and bent square configurations which are displayed in Figure 2.1. The presence of multiple low energy configurations means that all of these configurations must be taken into account in order to replicate the experimental energy spectrum of Oxygen–16. The simplest way to do this is via rigid body quantization, where we consider the states obtained by quantizing the rotational degrees of freedom of each individual configuration.

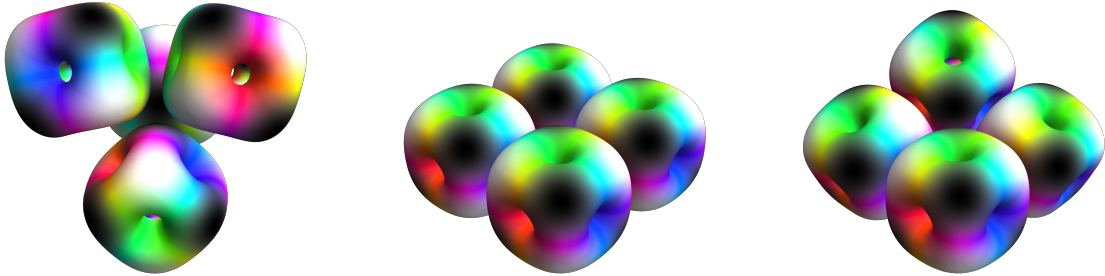


Fig. 2.1 The tetrahedral, flat square and bent square $B = 16$ configurations.

The T symmetry of the tetrahedral configuration gives the Finkelstein-Rubinstein constraints,

$$e^{\frac{2i\pi}{3\sqrt{3}}(\hat{L}_1 + \hat{L}_2 + \hat{L}_3)} e^{\frac{2i\pi}{3}\hat{K}_3} |\Psi\rangle = |\Psi\rangle \quad (2.1)$$

$$e^{i\pi\hat{L}_1} |\Psi\rangle = |\Psi\rangle, \quad (2.2)$$

where $|\Psi\rangle$ denotes a spin state. The D_4 symmetry of the flat square configuration lying in the $x - y$ plane gives the constraints,

$$e^{\frac{i\pi}{2}\hat{L}_3} e^{\frac{i\pi}{2}(\hat{K}_1 - \sqrt{3}\hat{K}_2)} |\Psi\rangle = |\Psi\rangle \quad (2.3)$$

J	Tetrahedron	Flat Square	Bent Square
0	$ 0, 0\rangle$	$ 0, 0\rangle$	$ 0, 0\rangle$
1	None	None	None
2	None	$ 2, 0\rangle$	$ 2, 0\rangle$ $ 2, 2\rangle + 2, -2\rangle$
3	$ 3, 2\rangle - 3, -2\rangle$	None	$ 3, 2\rangle - 3, -2\rangle$
4	$\sqrt{5} 4, 4\rangle + \sqrt{14} 4, 0\rangle + \sqrt{5} 4, -4\rangle$	$ 4, 0\rangle$ $ 4, 4\rangle + 4, -4\rangle$	$ 4, 0\rangle$ $ 4, 2\rangle + 4, -2\rangle$ $ 4, 4\rangle + 4, -4\rangle$
5	None	$ 5, 4\rangle - 5, -4\rangle$	$ 5, 2\rangle - 5, -2\rangle$ $ 5, 4\rangle - 5, -4\rangle$
6	$\sqrt{7} 6, 4\rangle - \sqrt{2} 6, 0\rangle + \sqrt{7} 6, -4\rangle$ $\sqrt{5} 6, 6\rangle - \sqrt{11} 6, 2\rangle - \sqrt{11} 6, -2\rangle + \sqrt{5} 6, -6\rangle$	$ 6, 0\rangle$ $ 6, 4\rangle + 6, -4\rangle$	$ 6, 0\rangle$ $ 6, 2\rangle + 6, -2\rangle$ $ 6, 4\rangle + 6, -4\rangle$ $ 6, 6\rangle + 6, -6\rangle$

Table 2.1 The allowed rigid body spin states for configurations in the $B = 16$ sector.

$$e^{i\pi\hat{L}_1} |\Psi\rangle = |\Psi\rangle, \quad (2.4)$$

and the D_2 symmetry of the bent square gives the constraints,

$$e^{i\pi\hat{L}_3} |\Psi\rangle = |\Psi\rangle \quad (2.5)$$

$$e^{i\pi\hat{L}_1} |\Psi\rangle = |\Psi\rangle. \quad (2.6)$$

Note that all three configurations have at least D_2 symmetry, therefore any state allowed by the tetrahedral or flat square configurations is also allowed by the bent square configuration. In table 2.1 we show the allowed spin states, up to spin 6, for each configuration.

However, there are a couple of reasons why we believe that rigid body quantization of these configurations is not sufficient to replicate the experimental energy spectrum of Oxygen-16.

First, whilst there is only one tetrahedral and one flat square configuration for a choice of the z axis, there is a whole family of configurations which could be classed as bent squares, that is configurations with D_2 symmetry. In particular the tetrahedral and flat square configurations are members of this family and therefore we should

quantize over this family of configurations rather than choosing just one of them to perform rigid body quantization upon.

Second, as seen in table 2.1, none of these configurations allow a spin 1 state, but there are spin 1 states present in the experimental spectrum of Oxygen–16. Therefore we must consider more configurations than those found in Figure 2.1 in order to replicate the entire spectrum.

2.3 The vibrational spaces of the tetrahedron

Now that we know that rigid body quantization can not explain many of the states in the experimental spectrum of Oxygen–16 we must decide how to incorporate some vibrational degrees of freedom and then how to quantize these. We consider each $B = 16$ configuration to be made up of four $B = 4$ Skyrmions, to simplify matters significantly we treat these as point particles. This is equivalent to the assumption that given the positions of the four $B = 4$ Skyrmions, these Skyrmions are in orientations so as to minimize the configuration energy. We have twelve degrees of freedom corresponding to the positions of the four $B = 4$ Skyrmions and another three corresponding to global isorotations of the whole configuration, meaning that we have a 15-dimensional space.

This is a prohibitively large dimension to quantize globally and therefore we would like to express this as a product of lower dimensional vibrational spaces. We know that 9 degrees of freedom come from zero energy modes: the translations, global rotations and isorotations of the configuration. The remaining six dimensional space is complicated in general but can be simplified if the configuration has symmetries, because then the vibrations must fall into representations of the symmetry group of the configuration [13]. Therefore we focus on the configuration with the most symmetry, the tetrahedron which has symmetry group T and representations A , E and F . The remaining six degrees of freedom can be classified by one these representations and split into the A , E and F vibrational spaces which have dimensions 1, 2 and 3 respectively. We will now show explicitly how these three vibrations act on the positions of the four $B = 4$ Skyrmions.

The A vibration consists of the symmetric stretching and squashing of the tetrahedron, retaining the tetrahedral symmetry as seen in the leftmost image of Figure 2.2. This is often called a breather mode.

The E vibration is most easily imagined if you imagine the tetrahedron embedded in a cube, with each edge of the tetrahedron corresponding to a face diagonal of the cube. The E vibration corresponds to the squashing or stretching of this cube applied to

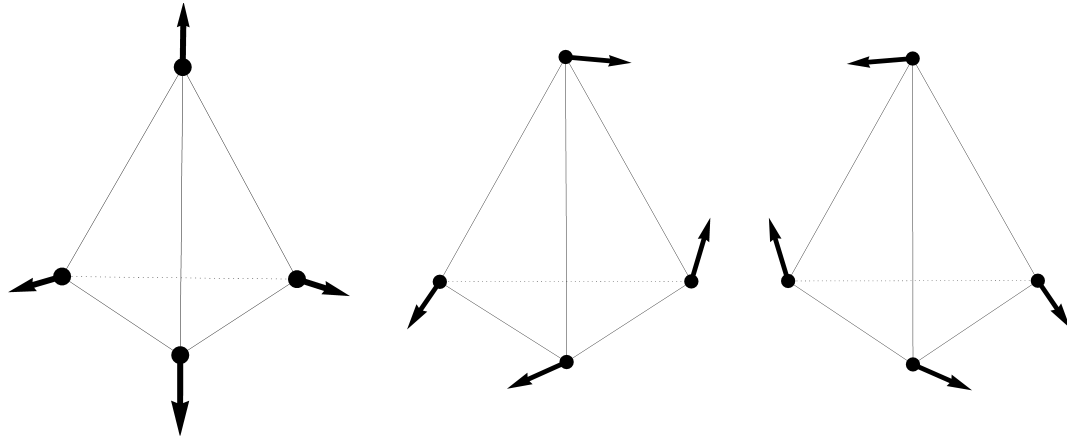


Fig. 2.2 The A vibration and a basis for the E vibration.

pairs of opposing faces. This can be applied in three possible ways, but stretching in all three ways equally and simultaneously would correspond to a tetrahedrally symmetric stretching which would be the A vibration. Therefore, after we quotient this one dimensional space out, the E vibration is only two dimensional and it can be generated by the vibrations shown in the central and rightmost image of Figure 2.2.

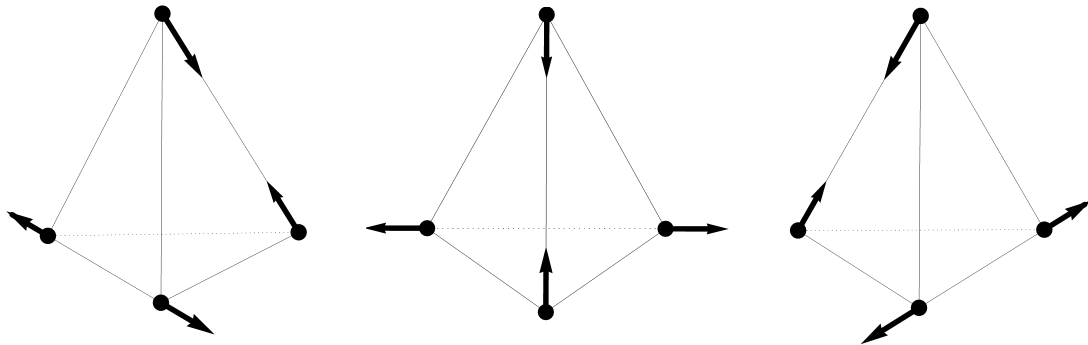


Fig. 2.3 A basis for the F vibration

The F vibration is generated by vibrations where a pair of particles gets closer together and the other pair gets further apart as seen in Figure 2.3. Given that there are three possible pairings of particles, this means that the F vibration is three dimensional. It also includes a vibration where one alpha particle separates from the remaining three.

In this chapter most of our focus will be upon the E vibration. This is because the E vibration is the vibration which retains D_2 symmetry, therefore, if we consider large vibrations away from the tetrahedron, we can incorporate the flat and bent square configurations from section 2.2 into the E vibration. This means that the E vibration

contains most of the low energy configurations known in the $B = 16$ sector of the Skyrme model and by quantising it we should be able to explain a lot of the low lying states of Oxygen–16. The focus of this chapter is how to extend this local vibrational analysis to a global vibrational manifold and then how to quantize this.

2.4 The vibrational manifold of the E vibration

We know that the vibrational manifold, \mathcal{M} , of the E vibration should contain the configurations with D_2 symmetry, but we would like to know where the tetrahedral, flat square and bent square configurations lie on this manifold. Using the Skyrme model for dynamics we find a scattering line which includes all three of these configurations.

We start with two well separated $B = 8$ Skyrmions, with orientations differing by $\frac{\pi}{2}$ as seen in Figure 2.4, and boost them towards each other. As they approach each other, the interactions between the $B = 8$ Skyrmions causes them to deform and then break to form a tetrahedron of $B = 4$ Skyrmions. This in turn flattens out going through the bent square configurations to form the flat square. The scattering continues, going through the dual tetrahedron, before again forming two $B = 8$ Skyrmions which separate. Note that all configurations in the first half of this line have their dual configuration, which is rotated by $\frac{\pi}{2}$ with respect to the original configuration, in the second half of the line.

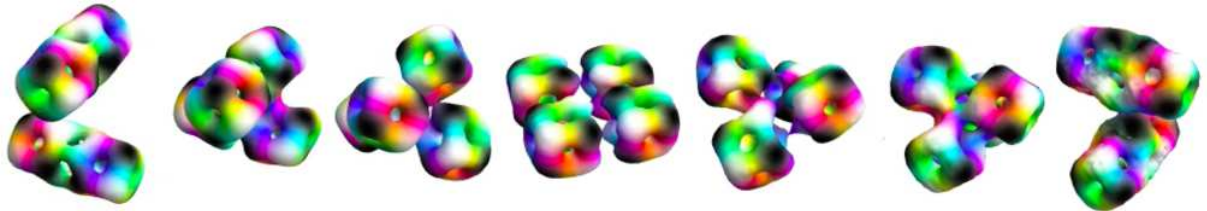


Fig. 2.4 The scattering line containing the tetrahedral, flat square and bent square configurations.

To see how this scattering line fits into our vibrational manifold, \mathcal{M} , we consider how many scattering lines of this nature pass through the tetrahedral configuration. As we saw in section 2.3, the E vibration is generated by modes corresponding to the stretching of the tetrahedron applied to opposing edges. The scattering line in Figure 2.4 is the extension of this stretching and therefore we have three scattering lines passing through one tetrahedron corresponding to its three pairs of opposing edges.

The vibrational manifold is defined such that the four $B = 4$ Skyrmions that make up a configuration lie on \mathcal{M} . If one of the $B = 4$ Skyrmions is located at $\mathbf{x} = (x, y, z)$ then the others must be at $(x, -y, -z)$, $(-x, y, -z)$ and $(-x, -y, z)$ because each configuration has D_2 symmetry. This gives us three degrees of freedom, but one of these corresponds to the overall scale, $r = |\mathbf{x}|$, of the configuration. This degree of freedom therefore corresponds to the breather mode of the configuration and can be quotiented out leaving us with a two dimensional space of configurations. This means that \mathcal{M} contains one configuration for each unit vector, $\hat{\mathbf{x}}$, with a corresponding scale, r , which minimizes the energy of the configuration.

The configurations at different unit vectors will have different preferred scales and therefore \mathcal{M} will not be a sphere. In particular we know that our manifold should have six directions where r tends to ∞ , corresponding to the three different ways that a tetrahedron can break into pairs of well separated $B = 8$ Skyrmions. Therefore we expect \mathcal{M} to resemble the manifold in Figure 2.5 with tetrahedral configurations corresponding to the points where three coloured regions meet and flat square configurations to the points where four coloured regions meet.

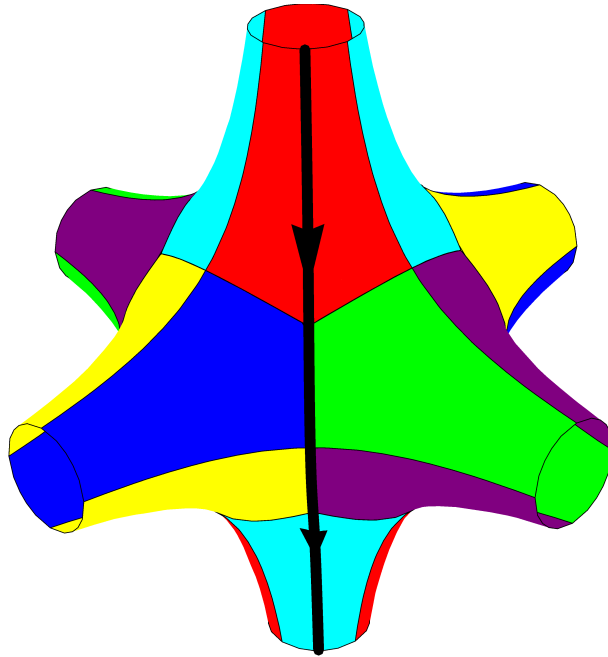


Fig. 2.5 An approximation of \mathcal{M} . Regions of the same colour are related by D_2 symmetry and the black line corresponds to the scattering line from Figure 2.4.

Presently we have some redundancy in our description of \mathcal{M} because a configuration corresponds to four points on \mathcal{M} , the locations of the four constituent $B = 4$ Skyrmions. Therefore the points (x, y, z) , $(x, -y, -z)$, $(-x, y, -z)$ and $(-x, -y, z)$ on \mathcal{M} all corre-

spond to the same configuration because they are related by D_2 transformations. It makes sense to quotient out this D_2 redundancy and focus on a quarter of \mathcal{M} with edges identified so that every point corresponds to a different configuration. We denote this manifold \mathcal{M}_q .

Given that we are trying to replicate the experimental spectrum of Oxygen-16, we will still want to quantize the rotational and isorotational degrees of freedom of configurations to find spin and isospin states. Therefore the total space that we wish to quantize is $\mathcal{M}_q \times SO(3)_J \times SO(3)_I$. We must then solve the Schrödinger equation,

$$-\frac{\hbar^2}{2}\Delta\Psi + V(\mathbf{x})\Psi = E\Psi, \quad (2.7)$$

where Δ is the kinetic operator on $\mathcal{M}_q \times SO(3)_J \times SO(3)_I$ and $V(\mathbf{x})$ is the static energy of the configuration at \mathbf{x} . Note that the potential only depends on the co-ordinates of \mathcal{M}_q because rotation and isorotation do not affect the static energy of a configuration. We must now decide upon a kinetic operator and a potential in order to solve equation (2.7).

2.4.1 The kinetic operator

Rather than using the Euclidean Laplacian for our kinetic operator we must use the extension of the Laplacian to a general manifold. This extension depends on the metric and is called the Laplace-Beltrami operator. The Laplace-Beltrami operator applied to a scalar function is,

$$\Delta f = \frac{1}{\sqrt{|g|}}\partial_i \left(\sqrt{|g|}g^{ij}\partial_j f \right), \quad (2.8)$$

where g is the determinant of the metric and g^{ij} is the inverse metric. Thus it is clear that we need to choose a metric on $\mathcal{M}_q \times SO(3)_J \times SO(3)_I$. The metric is determined by the kinetic energy,

$$T = \frac{1}{2}(\dot{\mathbf{x}}, \mathbf{b}, \mathbf{a}) \cdot g \cdot (\dot{\mathbf{x}}, \mathbf{b}, \mathbf{a})^T, \quad (2.9)$$

where \mathbf{x} is the co-ordinate on \mathcal{M}_q , \mathbf{b} is the angular velocity in physical space, and \mathbf{a} is the angular velocity in isospace.

The kinetic energy must respect the D_2 symmetry of our configurations which means there can be no terms linear in $\dot{\mathbf{x}}$ in equation (2.9) because these would change sign under one of the D_2 transformations. For example $\dot{x} \rightarrow -\dot{x}$ under $(x, y, z) \rightarrow (-x, y, -z)$. The lack of linear terms in $\dot{\mathbf{x}}$ corresponds to a lack of cross-terms in g between the vibrational and rotational/isorotational parts. The constituent $B = 4$ Skyrmions do

not have spin-isospin cross terms in their metrics and therefore neither does our metric on $\mathcal{M}_q \times SO(3)_J \times SO(3)_I$. As a result the g is block diagonal with respect to \mathcal{M}_q , $SO(3)_J$ and $SO(3)_I$. This means that the kinetic operator splits,

$$\Delta = \Delta_q + \nabla^2,$$

where ∇^2 is the standard Laplacian for a rigid rotor in rotational and isorotational space and Δ_q is the kinetic operator on \mathcal{M}_q .

At this point we approximate \mathcal{M}_q by the six-punctured sphere with constant negative curvature. Most importantly this is to capture the fact that r tends to ∞ in the six directions shown in Figure 2.5, but it also incorporates the fact that the scale r , is minimal at the tetrahedral configurations and has a saddle point at the flat square configurations.

Quantum mechanics on n -punctured spheres is facilitated by the fact that they are conformally equivalent to subsets of the upper half plane with the hyperbolic metric for $n \geq 3$. Generically these maps and subsets are not known explicitly, but for highly symmetric cases such as ours they can be determined. First we map from \mathcal{M}_q to the Riemann sphere by mapping each point \mathbf{x} to the corresponding unit vector $\hat{\mathbf{x}}$. Then, defining the complex coordinate $\zeta = \eta + i\epsilon$ for the upper half plane and the unit vector $\hat{\mathbf{x}} = (\hat{x}, \hat{y}, \hat{z})$ on the Riemann sphere, the map is

$$(\hat{x}, \hat{y}, \hat{z}) = \frac{1}{1 + |H(\zeta)|^2} \left(2\text{Re}[H(\zeta)], 2\text{Im}[H(\zeta)], 1 - |H(\zeta)|^2 \right) \quad (2.10)$$

where

$$H(\zeta) = \left(\frac{\Theta(0, 3, \zeta)}{\Theta(1, 3, \zeta)} \right) \quad (2.11)$$

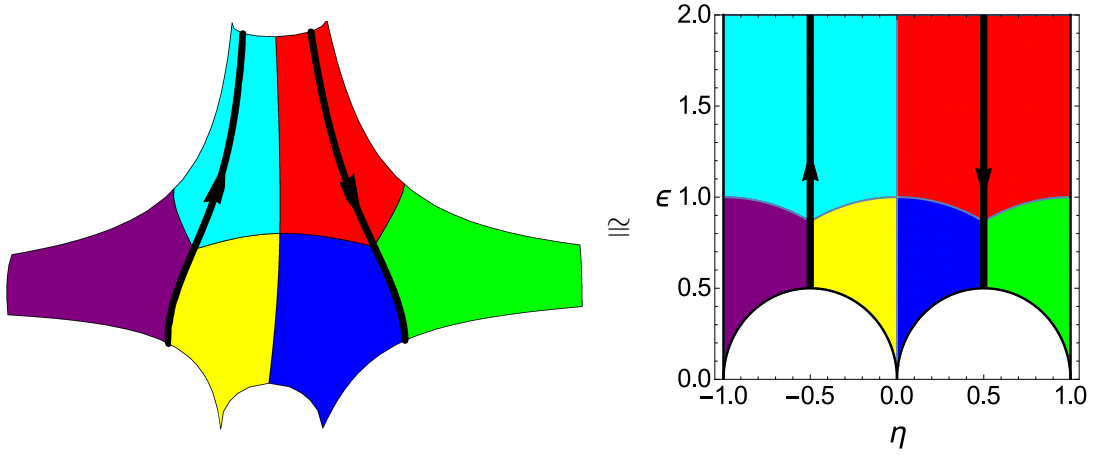
and

$$\Theta(a, n, \zeta) = \exp \left(2\pi i \left(\frac{1}{8} a^2 \zeta + \frac{1}{8} \right) \right) \tilde{\theta}_n \left(\pi \left(\frac{1}{4} + a \frac{\zeta}{2} \right), e^{i\pi\zeta} \right), \quad (2.12)$$

where $\tilde{\theta}_n$ are the Jacobi theta functions [30]. The subset of the upper half plane that covers \mathcal{M}_q is denoted \mathcal{M}_H and the equivalence is shown in Figure 2.6.

The benefit of mapping into the upper half plane is that here the metric with constant negative curvature is known and has a simple form, so the kinetic operator on \mathcal{M}_H is

$$-\Delta_q = -\epsilon^2 \left(\frac{\partial^2}{\partial \eta^2} + \frac{\partial^2}{\partial \epsilon^2} \right). \quad (2.13)$$

Fig. 2.6 The equivalence between \mathcal{M}_q and \mathcal{M}_H .

Returning to the Schrödinger equation from (2.7) we now have,

$$-\frac{\hbar^2}{2}\epsilon^2\left(\frac{\partial^2}{\partial\eta^2} + \frac{\partial^2}{\partial\epsilon^2}\right)\Psi - \frac{\hbar^2}{2}\nabla^2\Psi + V(\eta, \epsilon)\Psi = E\Psi. \quad (2.14)$$

Given the separation of the kinetic operator into vibrational and rotational parts it makes sense to try a separable solution. Therefore the total wavefunction can be expressed as

$$\Psi = \sum_{L_3, K_3} \psi_{L_3, K_3}(\zeta) |J, L_3\rangle |I, K_3\rangle, \quad (2.15)$$

where L_i and K_i are the body-fixed spin and isospin eigenvalues and J and I are the total space-fixed spin and isospin with $\hat{J}^2 = \hat{L}^2$ and $\hat{I}^2 = \hat{K}^2$. For a general configuration the rotational kinetic operator takes the form,

$$-\frac{\hbar^2}{2}\nabla^2 = \frac{\hbar^2}{2}\left(\frac{\hat{L}_1^2}{V_{11}} + \frac{\hat{L}_2^2}{V_{22}} + \frac{\hat{L}_3^2}{V_{33}} + \frac{\hat{K}_1^2}{U_{11}} + \frac{\hat{K}_2^2}{U_{22}} + \frac{\hat{K}_3^2}{U_{33}}\right) \quad (2.16)$$

where V_{ij} and U_{ij} are the moments of inertia and isoinertia which depend on the configuration and therefore depend on η and ϵ . D_2 symmetry ensures that we can chose a frame globally in which all configurations have diagonal moments of inertia and isoinertia. In order to use a separable solution we must split this kinetic operator into two parts,

$$-\frac{\hbar^2}{2}\nabla^2 = \frac{\hbar^2}{2V_{tet}}\hat{J}^2 + \frac{\hbar^2}{2U_{tet}}\hat{I}^2 + \frac{\hbar^2}{2}\sum_i \frac{V_{tet} - V_{ii}}{V_{tet}V_{ii}}\hat{L}_i^2 + \frac{\hbar^2}{2}\sum_i \frac{U_{tet} - U_{ii}}{U_{tet}U_{ii}}\hat{K}_i^2. \quad (2.17)$$

where V_{tet} and U_{tet} are such that the moments of inertia and isoinertia at the tetrahedron are $V_{tet} \delta_{ij}$ and $U_{tet} \delta_{ij}$. The first two terms of equation (2.17) give us the leading order contribution to the rotational energy, $E_{J,I}$ which does not depend on the coordinate ζ . The second two terms give us the next order contribution, $E_{rot}^{(1)}(\zeta)$, which does depend on ζ but is zero at the tetrahedron. We assume that the majority of the rotational energy comes from $E_{J,I}$, and so we neglect $E_{rot}^{(1)}$ for now and calculate this contribution later using perturbation theory.

When we plug the ansatz (2.15) into equation (2.14) we get the following equation for the vibrational wavefunction ψ to leading order,

$$-\frac{\hbar^2}{2}\epsilon^2 \left(\frac{\partial^2}{\partial \eta^2} + \frac{\partial^2}{\partial \epsilon^2} \right) \psi + V(\eta, \epsilon)\psi = \lambda\psi \quad (2.18)$$

where $\lambda = E - E_{J,I}$ is the vibrational energy of the wavefunction.

2.4.2 Boundary conditions

In order to solve equation (2.18) we require boundary conditions, and these can be obtained via the symmetries that we have on the vibrational manifolds \mathcal{M}_q and \mathcal{M}_H . In order to find the symmetry group of \mathcal{M}_q , it is easiest to first consider the manifold \mathcal{M} , the six-punctured sphere. The six punctures correspond to vertices of an octahedron and therefore \mathcal{M} has octahedral symmetry, O . When we quotient by the global D_2 symmetry to reduce to \mathcal{M}_q we are left with S_3 symmetry. We now choose an element from each of the cosets in O/D_2 to represent each element of this residual S_3 symmetry and these are shown in Table 2.2. This S_3 group of rotations can be viewed as the permutation group of the x, y and z axes of the 6-punctured sphere which we will label 1, 2 and 3 respectively.

The corresponding isorotations can be found by imagining the tetrahedral configuration embedded in a cube, with the edges of the tetrahedron corresponding to the faces of the cube. We colour a face according to the pion field colouring of the edge of the tetrahedral configuration as in Figure 2.7. This cube should be invariant under any rotation-isorotation pair of transformations in O and, by considering figures 2.7 and 2.8, we can see that $(1\ 2\ 3)$ requires an isorotation of $\frac{2\pi}{3}$ about $(0, 0, 1)$ and $(1\ 2)$ requires an isorotation of π about $(-\frac{1}{2}, \frac{\sqrt{3}}{2}, 0)$ to invert the corresponding rotations.

These transformations can also be viewed as acting on the position of an alpha particle on \mathcal{M}_q , which can be realised as a Möbius map acting on \mathcal{M}_H . In table 2.2 we provide details of both the rotation-isorotation pairs and the corresponding Möbius map of \mathcal{M}_H for all five non-trivial elements of S_3 .

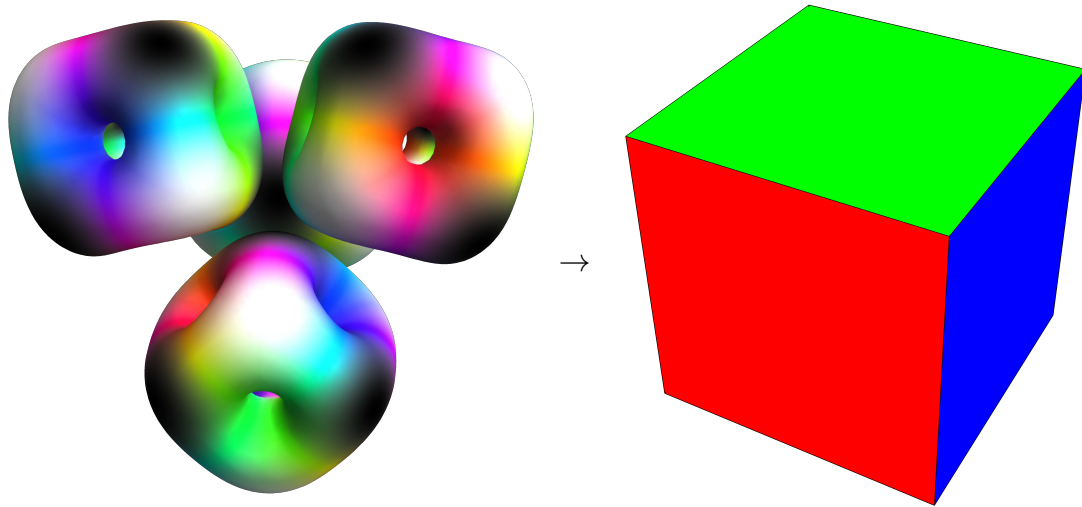


Fig. 2.7 The correspondence between the tetrahedral configuration and a coloured cube.

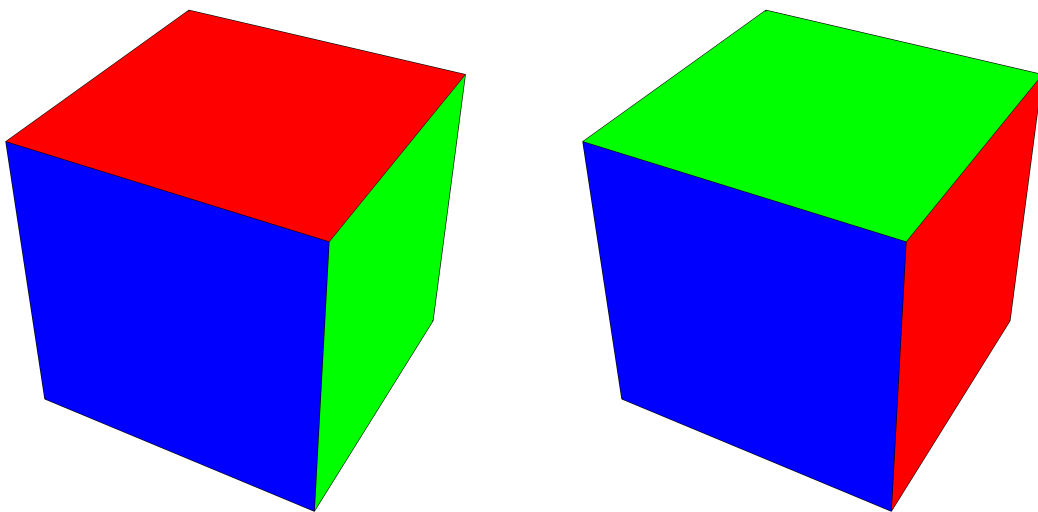


Fig. 2.8 The effect of the $(1\ 2\ 3)$ and $(1\ 2)$ rotations on the coloured cube.

We must also take account of parity, and in order to determine how this acts on a configuration and our vibrational manifold it is easiest to consider the transformation in two steps. The first step is to treat each configuration as a collection of four point particles and the effect of parity on this collection is to take each particle from its position \mathbf{x} to the position $-\mathbf{x}$, corresponding to the transformation $\zeta \rightarrow -\bar{\zeta}$ or more conveniently $\eta \rightarrow -\eta$ on \mathcal{M}_H . This tells us that the parity acts on the vibrational

Element of S_3	Rotation-Isorotation Pair	Möbius Map
(1 2 3)	$\frac{2\pi}{3}$ about (1, 1, 1) $\frac{2\pi}{3}$ about (0, 0, 1)	$\zeta \rightarrow \frac{1}{1-\zeta}$
(1 3 2)	$\frac{4\pi}{3}$ about (1, 1, 1) $\frac{4\pi}{3}$ about (0, 0, 1)	$\zeta \rightarrow \frac{\zeta-1}{\zeta}$
(1 2)	π about (1, -1, 0) π about (-1, $\sqrt{3}$, 0)	$\zeta \rightarrow \zeta - 1$
(1 3)	π about (-1, 0, 1) π about (1, 0, 0)	$\zeta \rightarrow -\frac{1}{\zeta}$
(2 3)	π about (0, 1, -1) π about (-1, $-\sqrt{3}$, 0)	$\zeta \rightarrow -\frac{\zeta}{1-\zeta}$

Table 2.2 The effect of elements S_3 on \mathcal{M}_q and \mathcal{M}_H .

wavefunction according to,

$$\hat{\mathcal{P}}\psi(\zeta) = \psi(-\bar{\zeta}) = P\psi(\zeta) \quad (2.19)$$

where $\hat{\mathcal{P}}$ is the vibrational part of the parity operator and P is the parity eigenvalue of the vibrational wavefunction. The second step is to consider the effect of parity on a single $B = 4$ Skyrmion and here we know that parity is equivalent to an isorotation of π about (0, 0, 1). The total effect of parity on a configuration is the combination of these two actions.

Rigid body quantization also provides a method of calculating parity for configurations with a reflection symmetry. If a configuration has reflection symmetry then parity can be expressed as a rotation operator for that configuration. This means that the spin states have an intrinsic parity at such configurations, in particular any spin 0 state must have positive parity because it will be invariant under any rotation. We will see that using the vibrational manifold to calculate parity allows us more freedom than rigid body quantization but we must remain consistent with it for all configurations with a reflection symmetry. Note that all of the configurations on the scattering lines like the one in Figure 2.4 have a reflection symmetry and thus states an intrinsic parity along such scattering lines.

The vibrational wavefunction must fall into one of the irreducible representations of S_3 of which there are three: the trivial, the sign and the standard representations.

This representation, combined with the parity of the wavefunction, will determine the boundary conditions on \mathcal{M}_H that the vibrational wavefunction must satisfy.

Vibrational wavefunctions in the trivial representation, ψ_T , are invariant under any element of S_3 and this can be used to determine the boundary conditions for the wavefunction. First we apply the element (13) to a point ζ_+ to take us to the point ζ_0 ,

$$\zeta_+ \rightarrow -\frac{1}{\zeta_+} = \zeta_0, \quad (2.20)$$

then we apply parity to ζ_0 to take us to the point ζ_-

$$\zeta_0 \rightarrow -\bar{\zeta}_0 = \zeta_-. \quad (2.21)$$

The result is that ζ_+ and ζ_- lie on opposite sides of the boundary C as shown in Figure 2.9. Then we have the following for ψ_T ,

$$\psi_T(\zeta_+) \stackrel{(13)}{=} \psi_T(\zeta_0) \stackrel{\hat{P}}{=} P\psi_T(\zeta_-). \quad (2.22)$$

We then consider the limit as ζ_+ and ζ_- tends towards the same point ζ on the

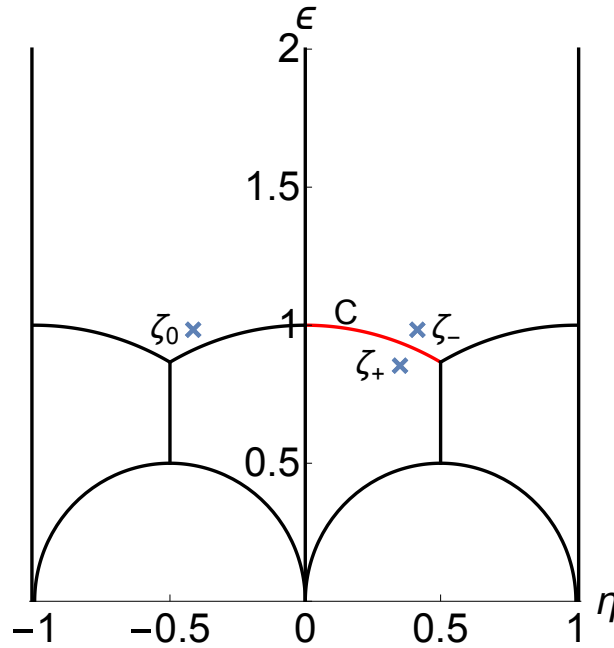


Fig. 2.9 The effect of (13) and then parity on the point ζ_+ . The curve C is highlighted in red.

boundary C and this gives us a boundary condition depending on whether $P = \pm 1$,

$$\partial_{\perp} \psi_T(\zeta) = 0 \text{ for } P = 1 \quad (2.23)$$

$$\psi_T(\zeta) = 0 \text{ for } P = -1, \quad (2.24)$$

for all ζ lying on the boundary C , where ∂_{\perp} denotes the derivative in the direction perpendicular to C .

Vibrational wavefunctions in the sign representation, ψ_S , are invariant under 3-cycles but flip sign under the transpositions of S_3 . This provides a slight variation of equation (2.22),

$$\psi_S(\zeta_+) \stackrel{(13)}{=} -\psi_S(\zeta_0) \stackrel{\hat{P}}{=} -P\psi_S(\zeta_-), \quad (2.25)$$

this change of sign essentially swaps the boundary conditions from the trivial case, so we have the boundary conditions,

$$\psi_S(\zeta) = 0 \text{ for } P = 1 \quad (2.26)$$

$$\partial_{\perp} \psi_S(\zeta) = 0 \text{ for } P = -1 \quad (2.27)$$

for vibrational wavefunctions in the sign representation.

The third irreducible representation of S_3 is the standard irrep, which is two dimensional. However it is most easily viewed as acting on a triplet of vibrational wavefunctions u , v and w subject to the constraint, $u + v + w = 0$. The action of S_3 is to permute these three wavefunctions in the obvious way; for example (13) has the effect,

$$u \rightarrow w, v \rightarrow v, w \rightarrow u. \quad (2.28)$$

We then focus on the combinations $u \pm w$ in order to find convenient boundary conditions,

$$(u + w)(\zeta_+) \stackrel{(13)}{=} (w + u)(\zeta_0) \stackrel{\hat{P}}{=} P(u + w)(\zeta_-), \quad (2.29)$$

and

$$(u - w)(\zeta_+) \stackrel{(13)}{=} (w - u)(\zeta_0) \stackrel{\hat{P}}{=} -P(u - w)(\zeta_-). \quad (2.30)$$

This provides two boundary conditions on C for the two wavefunctions u and w as follows,

$$u(\zeta) = -w(\zeta) \text{ and } \partial_{\perp} u(\zeta) = \partial_{\perp} w(\zeta) \text{ for } P = 1 \quad (2.31)$$

$$u(\zeta) = w(\zeta) \text{ and } \partial_{\perp} u(\zeta) = -\partial_{\perp} w(\zeta) \text{ for } P = -1. \quad (2.32)$$

These conditions are sufficient to determine u and w and thus $v = -(u + w)$ as well. This gives us boundary conditions along the curve C and we can use the Möbius maps from table 2.2 and parity to generate conditions for all of the boundaries between the coloured regions of \mathcal{M}_H shown in Figure 2.6. In particular positive parity wavefunctions have vanishing derivative across the lines $\eta = -1, 0$ and 1 and the negative parity wavefunctions vanishing along these lines.

2.4.3 The potential on \mathcal{M}_H

We must now determine the potential to insert into the Schrödinger equation in (2.18). We know that it must have be S_3 symmetric because configurations which are related by a rotation and/or an isorotation have the same energy. Therefore we need only determine the potential in one of the coloured regions of \mathcal{M}_H in Figure 2.6 and then use this symmetry to determine the potential elsewhere; we shall use the red region of \mathcal{M}_H for convenience.

Ideally we would use the Skyrme model to find the static energy of each configuration in our vibrational manifold. However, it is not known how to generate most of the configurations of \mathcal{M} , only the ones which are particularly symmetric such as the tetrahedral, flat square and bent square configurations. In chapter 3 we will consider how we could use an approximation scheme to generate a potential on \mathcal{M}_H . Additionally, there are many modifications to the Skyrme model which would alter the energies of the configurations and therefore the potential. However, the symmetries of the configurations and scattering lines found via the Skyrme model would be unlikely to changes much under modest modification. Therefore what we have said about the representations and boundary conditions of vibrational wavefunctions would still hold.

Alpha cluster models usually point to the tetrahedron as being the lowest energy arrangement of alpha particles and we would expect the energy of the two well-separated $B = 8$ Skyrmions to be the highest energy configuration. Our choice of potential incorporates these details with the additional benefit that we can solve the Schrödinger equation explicitly for our choice. In the red region of \mathcal{M}_H our potential takes the form,

$$V(\eta, \epsilon) = \epsilon^2 \left(\frac{1}{2} \omega^2 \left(\eta - \frac{1}{2} \right)^2 + \nu^2 \right), \quad (2.33)$$

where ω and ν are free parameters which can be chosen to produce a closer fit to the experimental energy spectrum. We find that $\omega^2 = 6$ and $\nu^2 = 128$ are able to provide a excellent fit to the experimental spectrum. One problem with this potential is that it diverges asymptotically as $\epsilon \rightarrow \infty$, whereas it should tend to the two times the

configuration energy of the twisted $B = 8$ Skyrmion. However, our main aim is to approximate the low energy states of Oxygen-16 which will be concentrated around the lower energy configurations and so this divergence should only have a small effect on these states.

2.4.4 Solving the Schrödinger equation

Using the potential in (2.33), the Schrödinger equation (2.18) becomes

$$-\frac{\hbar^2}{2}\epsilon^2\left(\frac{\partial^2}{\partial\eta^2} + \frac{\partial^2}{\partial\epsilon^2}\right)\psi + \epsilon^2\left(\frac{1}{2}\omega^2\left(\eta - \frac{1}{2}\right)^2 + \nu^2\right)\psi = \lambda\psi \quad (2.34)$$

in the red region of \mathcal{M}_H . If we consider the following separation of variables ansatz,

$$\psi(\eta, \epsilon) = \sum_n X_n(\eta)Y_n(\epsilon)\sqrt{\epsilon}, \quad (2.35)$$

then the equation for $X_n(\eta)$ becomes

$$-\frac{\hbar^2}{2}X_n'' + \frac{1}{2}\omega^2\left(\eta - \frac{1}{2}\right)^2 X_n = e_n X_n, \quad (2.36)$$

where we have incorporated the ν^2 term in the potential into the eigenvalue e_n .

We have the boundary conditions $X_n(0) = X_n(1) = 0$ for odd parity wavefunctions and $X_n'(0) = X_n'(1) = 0$ for even parity wavefunctions which discretise the allowed values of e_n . This system has analytic solutions which can be expressed in terms of confluent hypergeometric functions, ${}_1F_1(a; b; z)$. In particular for $\omega = 0$, they can be expressed in terms of trigonometric functions. The equation for Y_n then becomes,

$$\tilde{\epsilon}^2 Y_n''(\tilde{\epsilon}) + \tilde{\epsilon} Y_n'(\tilde{\epsilon}) - (\tilde{\epsilon}^2 - \Lambda^2) Y_n(\tilde{\epsilon}) = 0 \quad (2.37)$$

where $\tilde{\epsilon} = \frac{\sqrt{2e_n}}{\hbar}\epsilon$ and $\Lambda = \frac{2\lambda}{\hbar^2} - \frac{1}{4}$. We see that (2.37) is the modified Bessel equation, which has known solutions $K_{i\Lambda}(\tilde{\epsilon})$ and $I_{i\Lambda}(\tilde{\epsilon})$ but we discard the latter because it diverges as $\tilde{\epsilon}$ tends to ∞ .

Combining the solutions, X_n and Y_n , we get the following series for the vibrational wavefunction (with shifted origin),

$$\psi\left(\eta + \frac{1}{2}\right) = \sum_n a_{2n} {}_1F_1\left(\frac{1}{4} - \frac{e_{2n}}{\hbar\omega}; \frac{1}{2}; \frac{\omega\eta^2}{\hbar}\right) e^{-\frac{\omega\eta^2}{2\hbar}} K_{i\Lambda}\left(\frac{\sqrt{2e_{2n}}}{\hbar}\epsilon\right) \sqrt{\epsilon}$$

$$+ \sum_n a_{2n+1} \eta_1 F_1 \left(\frac{3}{4} - \frac{e_{2n+1}}{\hbar\omega}; \frac{3}{2}; \frac{\omega\eta^2}{\hbar} \right) e^{-\frac{\omega\eta^2}{2\hbar}} K_{i\Lambda} \left(\frac{\sqrt{2e_{2n+1}}}{\hbar} \epsilon \right) \sqrt{\epsilon}. \quad (2.38)$$

The first sum in (2.38) contains even parity solutions and the second sum contains odd parity solutions.

In order to place restrictions on the a_n and Λ we must enforce the boundary conditions from section 2.4.2. First we must truncate the series in (2.38), which is reasonable because the modified Bessel functions, $K_{i\Lambda} \left(\frac{\sqrt{2e_{2n}}}{\hbar} \epsilon \right)$, decay faster as n increases. Supposing that we allow only the first N terms in (2.38) and (??), then we fix Λ and apply the boundary conditions at N points on the boundary C , which will uniquely determine the coefficients a_n . We then apply boundary conditions at a different set of N points on the boundary and calculate the coefficients a_n using these points. We usually find that $N \approx 5$ is sufficient to find accurate solutions. If the two sets of coefficients agree then we have a solution and Λ is a permitted eigenvalue, if they disagree then there is no solution satisfying the boundary conditions across the whole of C and so we discard this value of Λ . In this way we can generate all of the solutions of the Schrödinger equation (2.34) and obtain the energy spectrum for Oxygen-16.

2.4.5 Rovibrational states

Now that we have found vibrational wavefunctions for each of the representations we must combine them with spin states to form rovibrational states. The idea is that if we apply an element of S_3 or parity to the rovibrational state, then it shouldn't matter how it is applied, whether as a rotation-isorotation pair or on \mathcal{M}_H directly. This means that the spin state has to be in the same representation as the vibrational wavefunction that it is paired with. It is worth remembering that since all configurations on \mathcal{M} have D_2 symmetry, all spin states must at least satisfy D_2 symmetry. There are then extra restrictions depending on the representation of the corresponding vibrational wavefunction.

The representation that a spin state or set of spin states falls under is determined by how it transforms under the elements (1 2 3) and (1 2) of S_3 . As seen in table 2.2, the element (1 2 3) corresponds to the rotation-isorotation operator,

$$\hat{C}_3 = e^{\frac{2i\pi}{3\sqrt{3}}(\hat{K}_1 + \hat{K}_2 + \hat{K}_3)} e^{\frac{2i\pi}{3}\hat{L}_3}, \quad (2.39)$$

and the element (1 2) is represented by

$$\hat{C}_2 = e^{\frac{i\pi}{\sqrt{2}}(\hat{K}_1 - \hat{K}_3)} e^{\frac{i\pi}{2}(-\hat{L}_1 + \sqrt{3}\hat{K}_2)}. \quad (2.40)$$

A spin state in the trivial representation must be invariant under all elements of S_3 and therefore we have the constraints,

$$\hat{C}_3 |\Theta\rangle = |\Theta\rangle \quad \text{and} \quad \hat{C}_2 |\Theta\rangle = |\Theta\rangle. \quad (2.41)$$

A spin state in the sign representation must be invariant under 3-cycles but flip sign under the transpositions of S_3 and therefore we have the constraints,

$$\hat{C}_3 |\Theta\rangle = |\Theta\rangle \quad \text{and} \quad \hat{C}_2 |\Theta\rangle = -|\Theta\rangle. \quad (2.42)$$

Spin states in the standard representation are most easily constructed using a triplet of spin states: $|U\rangle$, $|V\rangle$ and $|W\rangle$, which pair with our triplet of vibrational wavefunctions in the following way,

$$|\Psi\rangle = u|U\rangle + v|V\rangle + w|W\rangle. \quad (2.43)$$

It is important to note that since we are working with a basis of spin states, S_3 must act passively on the spin states such that,

$$\hat{C}_3 |U\rangle = |W\rangle, \quad \hat{C}_3 |V\rangle = |U\rangle, \quad \hat{C}_3 |W\rangle = |V\rangle, \quad (2.44)$$

$$\hat{C}_2 |U\rangle = |V\rangle, \quad \hat{C}_2 |V\rangle = |U\rangle, \quad \hat{C}_2 |W\rangle = |W\rangle. \quad (2.45)$$

As with the vibrational wavefunctions, the triplet of spin states must also sum to zero,

$$|U\rangle + |V\rangle + |W\rangle = 0, \quad (2.46)$$

to take us from the natural representation to the standard irrep.

We will now look at which spins are permitted for each representation and how this relates to the experimental energy spectrum of Oxygen-16. A summary of the spin states in the trivial, sign and standard representations is also provided in table A.1 in Appendix A.

Trivial Representation

The spin state $|0, 0\rangle$ is invariant under any rotation and therefore necessarily lies in the trivial irrep and so our 0^+ ground state is the combination

$$\psi_{T,0}^+ |0, 0\rangle. \quad (2.47)$$

This is the combination of the vibrational wavefunction with the least energy and the spin state with no rotational energy. However there are other rovibrational state that use the vibrational wavefunction, $\psi_{T,0}^+$, such as

$$\psi_{T,0}^+ \left(\sqrt{5} |4, 4\rangle + \sqrt{14} |4, 0\rangle + \sqrt{5} |4, -4\rangle \right), \quad (2.48)$$

$$\psi_{T,0}^+ \left(\sqrt{7} |6, 4\rangle - \sqrt{2} |6, 0\rangle + \sqrt{7} |6, -4\rangle \right). \quad (2.49)$$

These three states are responsible for the positive parity states in the ground state 0^+ , 3^- , 4^+ , 6^+ rotational band found in the experimental spectrum. As seen in Figure 2.10, the vibrational wavefunction, $\psi_{T,0}^+$, is focussed around the tetrahedral configurations at $\left(\pm\frac{1}{2}, \frac{\sqrt{3}}{2}\right)$ and this agrees with the rigid body analyses where this rotational band is due to quantization of the tetrahedron. We will see that rigid body quantization is frequently just a simplification of our vibrational model and as such the interpretation of states is often similar. The spin states above can be paired with any of the vibrational wavefunctions in Figure 2.10 to create a rovibrational state.

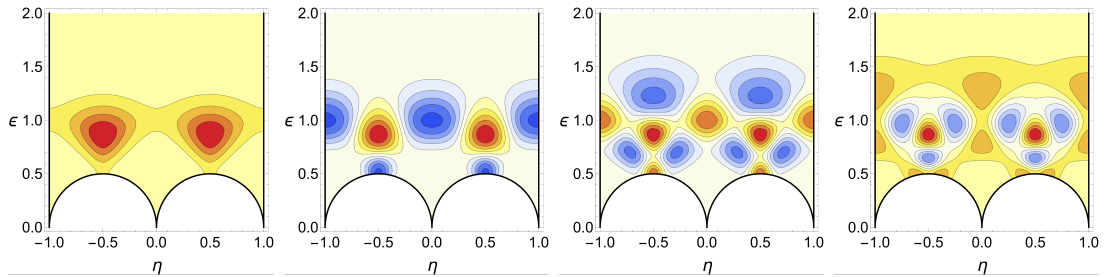


Fig. 2.10 The vibrational wavefunctions $\psi_{T,0}^+$, $\psi_{T,1}^+$, $\psi_{T,2}^+$ and $\psi_{T,3}^+$.

Another rovibrational state of particular importance is,

$$\psi_{T,1}^+ |0, 0\rangle, \quad (2.50)$$

which is responsible for the first excited 0^+ state found at 6.05 MeV in the experimental energy spectrum. We can see from the vibrational wavefunction in Figure 2.10 that this state is correlated with the tetrahedral and flat square configurations in equal

measure. This is in contrast to many rigid body analyses where it is solely explained by the flat square configuration [18] or the breather mode of the tetrahedron [22, 23]. This shows the importance of considering vibrational degrees of freedom; even the first excited state in our model can not be well approximated by the rotational excitations of a single configuration. Like the ground state this excited 0^+ is also the base of a rotational band containing 0^+ , 4^+ and 6^+ states.

The states above all feature in the rigid body quantization of Oxygen–16 configurations even if the interpretation of them may differ. However, we also find states in our vibrational model of Oxygen–16 which rigid body quantization does not allow. The state

$$\psi_{T,0}^- |0, 0\rangle, \quad (2.51)$$

corresponds to a 0^- state, where the vibrational wavefunction, $\psi_{T,0}^-$, is shown in the left image of Figure 2.11. It vanishes along all of the scattering lines which means that is highly constrained and therefore has high energy. It is precisely because it vanishes at all of the low energy configurations that it does not feature in a rigid body analysis of Oxygen–16. It is the base of a rotational band containing 0^- , 4^- and 6^- states.

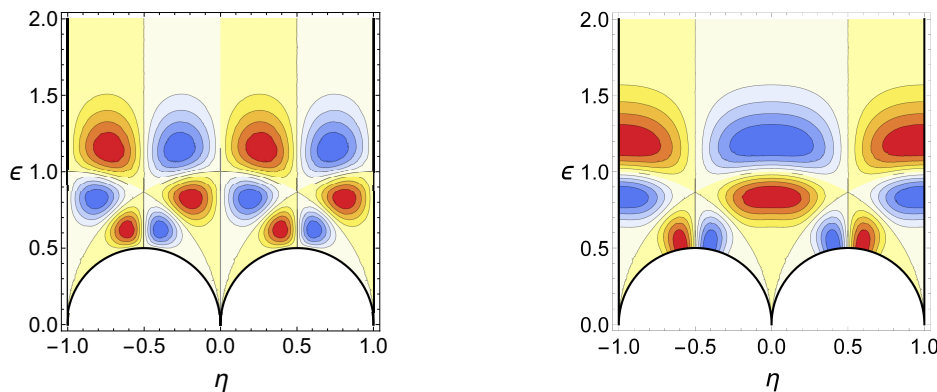


Fig. 2.11 The vibrational wavefunctions $\psi_{T,0}^-$ and $\psi_{S,0}^+$.

Sign Representation

The lowest spin where we see states in the sign representation is spin 3, with the 3^- state,

$$\psi_{S,0}^- (|3, 2\rangle - |3, -2\rangle). \quad (2.52)$$

As seen in Figure 2.12, this vibrational wavefunction, $\psi_{S,0}^-$ is focussed around the tetrahedral configurations like the lowest energy trivial rep wavefunction, $\psi_{T,0}^+$, and these wavefunctions look very similar in left hand side of \mathcal{M}_H . The $\psi_{S,0}^-$ is slightly

more constrained because it has odd parity but this only has a small effect on the energy of the state. This 3^- state, and a corresponding 6^- state, lie slightly above the ground state 0^+ , 4^+ , 6^+ rotational band of states in the trivial representation and so we reproduce the 0^+ , 3^- , 4^+ , 6^\pm band seen in the experimental energy spectrum. Thus we see that positive parity states in the trivial rep and negative parity states in the sign rep states are exactly those found via rigid body quantization of the tetrahedron.

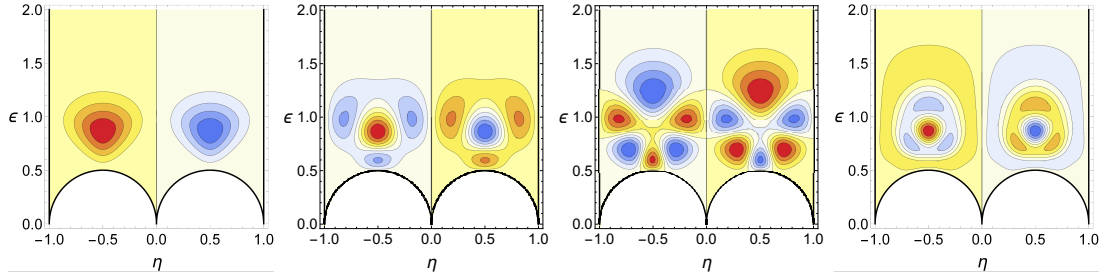


Fig. 2.12 The vibrational wavefunctions $\psi_{S,0}^-$, $\psi_{S,1}^-$, $\psi_{S,2}^-$ and $\psi_{S,3}^-$.

However, our vibrational approach again allows us states not permitted in rigid body quantization because we can also have positive parity states in the sign rep. The state 3^+

$$\psi_{S,0}^+ (|3, 2\rangle - |3, -2\rangle), \quad (2.53)$$

has the lowest energy of such states where $\psi_{S,0}^+$ is shown in the right image of Figure 2.11. Again this is severely restricted because it vanishes along all scattering lines and therefore has rather high energy. It has slightly lower energy than the trivial rep wavefunction, $\psi_{T,-}^0$, because it has even parity; therefore we expect the 3^+ and corresponding 6^+ state to lie slightly below the 0^- , 4^- , 6^- rotational band.

Standard Representation

The lowest spin where we see states in the standard representation is spin 2, with the lowest energy state corresponding to a 2^+ state,

$$(u_0^+ - v_0^+) (|2, 2\rangle + |2, -2\rangle) - \sqrt{6}(u_0^+ + v_0^+) |2, 0\rangle \quad (2.54)$$

As seen in Figure 2.14, the combination $u_0^+ - v_0^+$ vanishes at the points $(\pm\frac{1}{2}, \frac{1}{2})$ which correspond to the flat square configuration lying in the $x - y$ plane. As a result the rovibrational state in (2.54) is proportional to $|2, 0\rangle$ here which is the only spin state allowed at this flat square in a rigid body analysis. We also see in figures 2.13 and 2.14 that both of the vibrational wavefunctions, $u_0^+ \pm v_0^+$, have greatest magnitude at some

of the flat square configurations (with the flat squares lying in the $y-z$ and $z-x$ planes corresponding to the points $(\pm 1, 1)$ and $(0, 1)$ respectively) and therefore we are in agreement with models stating that the flat square configuration is responsible for this state. There are higher spin states with the same vibrational wavefunctions such as the spin 4 state,

$$2(u_0^+ - v_0^+) (|4, 2\rangle + |4, -2\rangle) - (u_0^+ + v_0^+) (\sqrt{7}|4, 4\rangle - \sqrt{10}|4, 0\rangle + \sqrt{7}|4, -4\rangle), \quad (2.55)$$

and spin 5 and 6 states. These states form a 2^+ , 4^+ , 5^+ , 6^+ rotational band; even though we are no longer quantizing the rotational degrees of freedom of a single configuration we still obtain rotational bands from our vibrational wavefunction. The spin states in (2.54) can be paired with any of the wavefunctions in figures 2.13 and 2.14 to form a positive parity state.

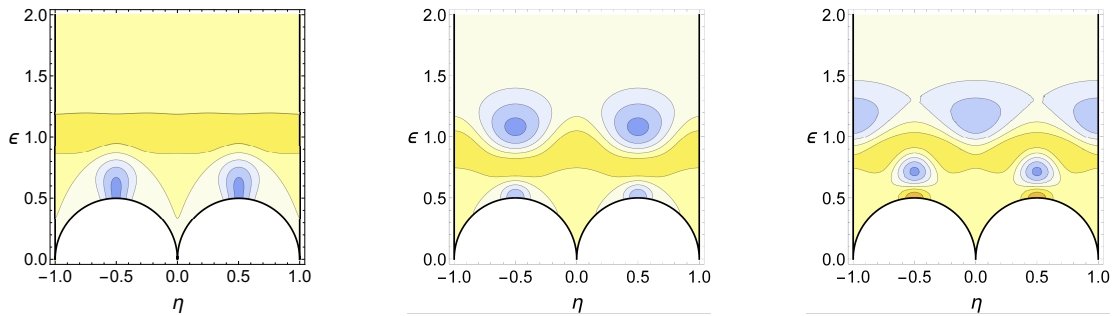


Fig. 2.13 The vibrational wavefunctions $u_0^+ + v_0^+$, $u_1^+ + v_1^+$ and $u_2^+ + v_2^+$.

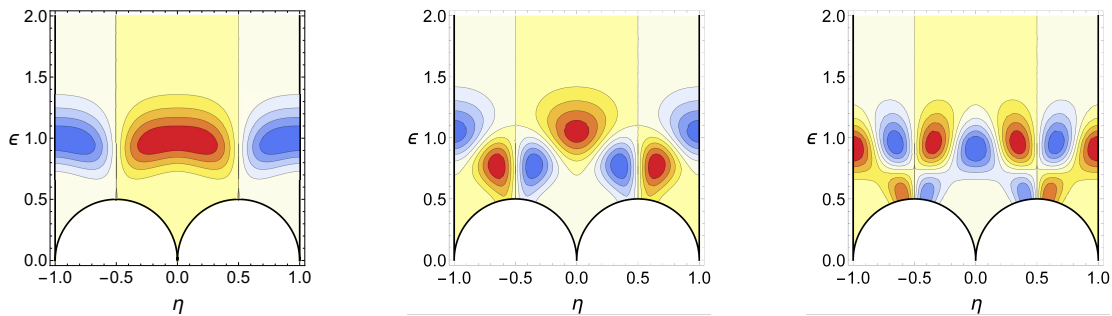


Fig. 2.14 The vibrational wavefunctions $u_0^+ - v_0^+$, $u_1^+ - v_1^+$ and $u_2^+ - v_2^+$.

If we look closer at the spin 4 state in (2.55) we find that it is proportional to $\sqrt{7}|4, 4\rangle - \sqrt{10}|4, 0\rangle + \sqrt{7}|4, -4\rangle$ at the flat square lying in the $x-y$ plane. This is orthogonal to the spin 4 state in the trivial representation found in (2.48). In a rigid body analysis of the flat square any combination of the spin states $|4, 0\rangle$ and $|4, 4\rangle + |4, -4\rangle$ would be permitted, whereas in our vibrational approach the spin state

must be in either the trivial or standard representation and a combination of these two states is not allowed.

There is a slightly higher energy spin 2^- rovibrational state corresponding to the negative parity vibrational wavefunctions,

$$(u_0^- - v_0^-) (|2, 2\rangle + |2, -2\rangle) - \sqrt{6}(u_0^- + v_0^-) |2, 0\rangle \quad (2.56)$$

This state has higher energy than the 2^+ state because its vibrational wavefunctions are more constrained because they vanish along the line $\eta = 0$. Notice that both combinations of vibrational wavefunctions, $u_0^- \pm v_0^-$, (figures 2.15 and 2.16) vanish at all of the flat square configurations. This is analogous to the fact that rigid body quantization of the flat square configuration does not allow negative parity states. This 2^- state is the base of a $2^-, 4^-, 5^-, 6^-$ rotational band analogously to the positive parity 2^+ state. The spin states in (2.56) can be paired with any of the vibrational wavefunctions in figures 2.15 and 2.16 to form a negative parity state.

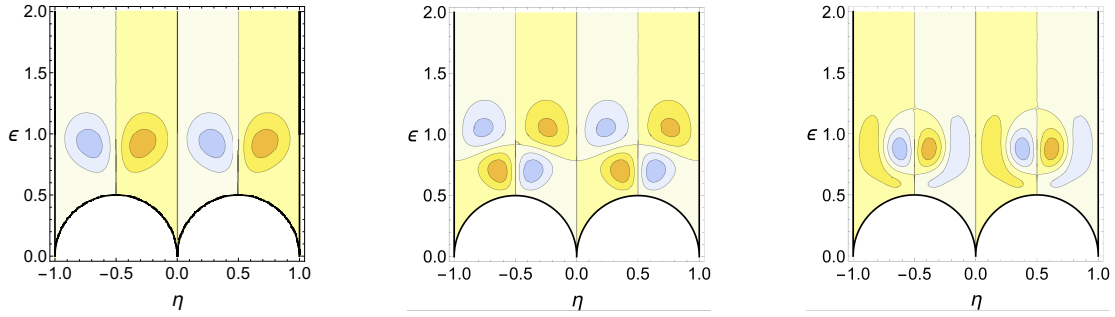


Fig. 2.15 The vibrational wavefunctions $u_0^- + v_0^-$, $u_1^- + v_1^-$ and $u_2^- + v_2^-$.

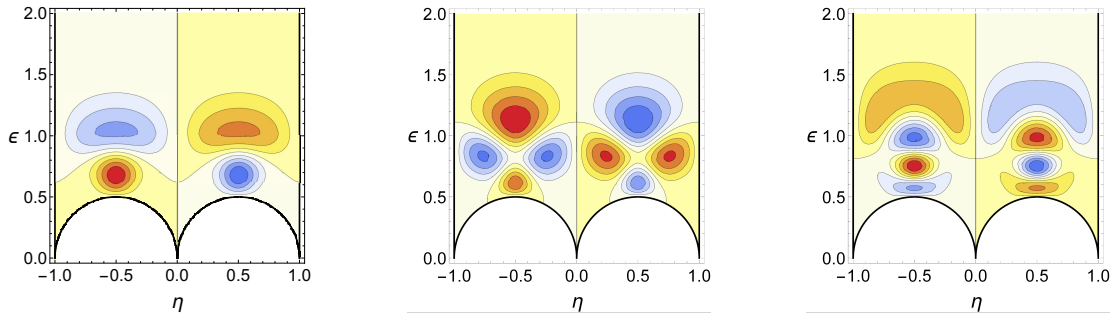


Fig. 2.16 The vibrational wavefunctions $u_0^- - v_0^-$, $u_1^- - v_1^-$ and $u_2^- - v_2^-$.

All of the spin states which lie in the trivial, sign and standard representations up to spin 6 are listed in A.1 in Appendix A.

2.4.6 Energies of the rovibrational states

In order to find the energies of our rovibrational states we have to reintroduce the first order correction to the rotational energy of $|\Psi\rangle$ for the configuration at ζ from equation (2.17),

$$E_{rot}^1(\zeta) = \frac{\hbar^2}{2} \sum_i \frac{V_{tet} - V_{ii}(\zeta)}{V_{tet} V_{ii}(\zeta)} \langle \Psi | \hat{K}_i^2 | \Psi \rangle + \frac{\hbar^2}{2} \sum_i \frac{U_{tet} - U_{ii}(\zeta)}{U_{tet} U_{ii}(\zeta)} \langle \Psi | \hat{L}_i^2 | \Psi \rangle. \quad (2.57)$$

We then integrate (2.57) over the domain \mathcal{M}_H to give the first order correction to the rotational energy, E_{rot}^1 . Therefore in order to calculate E_{rot}^1 we require an ansatz for the inertia tensors, V_{ij} and U_{ij} .

The simplest approximation would be to treat each configuration as an arrangement of four point particles and this means that we have to approximate the surface \mathcal{M} . The map (2.12) takes us from \mathcal{M}_H to the Riemann sphere, giving us a coordinate $\hat{\mathbf{x}}(\zeta)$. The asymptotic configurations consisting of two well-separated $B = 8$ Skyrmions tells us that $V_{11}(\zeta)$ and $V_{22}(\zeta)$ should tend to infinity as $\hat{z}(\zeta)$ tends to 1. As we go along the scattering line in Figure 2.4 it can be shown that V_{33} is essentially constant. We should also take account of the fact that the constituent $B = 4$ Skyrmions are not point particles but rather extended objects and this has the effect of adding a constant to each of the three diagonal entries of inertia tensor. Putting all of these ideas together we arrive at the following ansatz for the inertia tensor in the red region of Figure 2.6,

$$V_{11}(\zeta) = \left(a \frac{\hat{y}(\zeta)^2 + \hat{z}(\zeta)^2}{1 - \hat{z}^2(\zeta)} + b \right), \quad (2.58)$$

$$V_{22}(\zeta) = \left(a \frac{\hat{z}(\zeta)^2 + \hat{x}(\zeta)^2}{1 - \hat{z}^2(\zeta)} + b \right), \quad (2.59)$$

$$V_{33}(\zeta) = \left(a \frac{\hat{x}(\zeta)^2 + \hat{y}(\zeta)^2}{1 - \hat{z}^2(\zeta)} + b \right). \quad (2.60)$$

We then calibrate so that moments of inertia match those from the Skyrme model for the tetrahedral and flat square configurations [18] giving $a = 6586$ and $b = 2562$. In order to find the moments of inertia in the other coloured regions of \mathcal{M}_H one must act on the denominators of (2.58), (2.59) and (2.60) with elements of S_3 .

We can then use these moments of inertia to calculate the first order correction to the rotational energy, E_{rot}^1 , and therefore the total energy of each rovibrational state. In Figure 2.17 we plot the low lying states from our vibrational model and the states they correspond to in the experimental spectrum. In table 2.3 we list the low lying states with their vibrational wavefunctions, the vibrational energy, E_{vib} , the zeroth

order rotational energy, $E_{J,I}$ and the first order correction to the rotational energy, E_{rot}^1 . For the lowest lying states it is also possible to match our rovibrational states to states in the experimental spectrum and we show the experimental energy of the experimental state if there is such a match. The experimental values are taken from [31]. As the energy of the states increases, the experimental energy spectrum becomes more densely packed with states and this pairing off of calculated and experimental states is rarely possible. We use the first excited 0^+ state and the lowest energy 4^+ state to calibrate the vibrational and rotational energy units respectively. There are some discrepancies with the table in [32] due to a slightly different calibration.

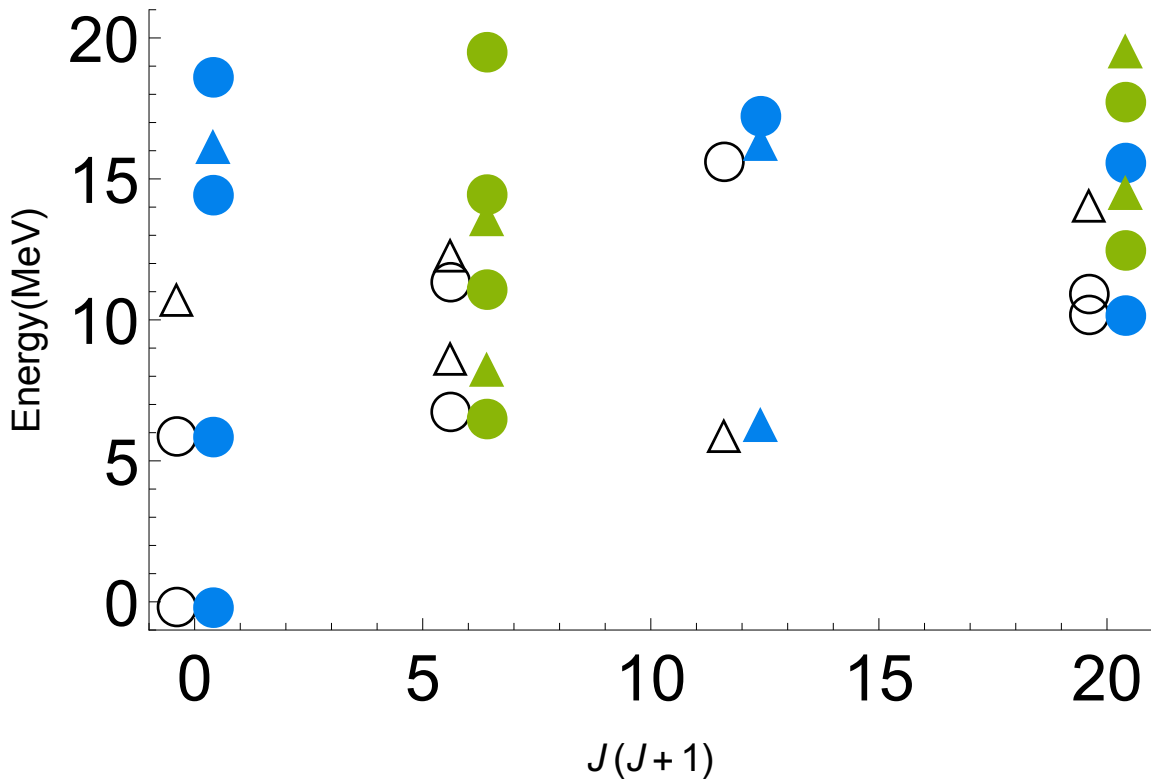


Fig. 2.17 The states from our vibrational model and corresponding states in the experimental spectrum of Oxygen-16. The hollow black shapes denote experimental states, the blue shapes denote states in the sign or trivial representations and the green shapes denote states in the standard representation. Circles denote positive parity states and triangles denote negative parity states.

The lowest energy 0^+ and 4^+ states and the lowest energy 3^- state have different vibrational wavefunctions and there is freedom in our model for them to not form a rotational band. They form an approximate band because both vibrational wavefunctions are focussed around the tetrahedron and its dual. This is evidence that the path between the dual tetrahedra is sufficiently high energy that a local vibrational analysis

J^P	Wavefunction(s)	E_{vib}	$E_{J,I}$	E_{rot}^1	E	E_{Exp}
0 ⁺	$\psi_{T,0}^+$	0	0	0	0	0
0 ⁺	$\psi_{T,1}^+$	6.05	0	0	6.05	6.05
3 ⁻	$\psi_{S,0}^-$	0.24	7.52	-1.24	6.52	6.13
2 ⁺	u_0^+, v_0^+	3.51	3.76	-0.57	6.69	6.92
2 ⁻	u_0^-, v_0^-	5.33	3.76	-0.61	8.48	8.87
4 ⁺	$\psi_{T,0}^+$	0	12.53	-2.17	10.36	10.36
2 ⁺	u_1^+, v_1^+	8.73	3.76	-1.21	11.28	11.52
4 ⁺	u_0^+, v_0^+	3.51	12.53	-3.37	12.67	11.10
2 ⁻	u_1^-, v_1^-	11.09	3.76	-1.03	13.82	12.53
0 ⁺	$\psi_{T,2}^+$	14.63	0	0	14.63	—
2 ⁺	u_2^+, v_2^+	12.15	3.76	-1.26	14.65	—
4 ⁻	u_0^-, v_0^-	5.33	12.53	-3.11	14.75	14.30
4 ⁺	$\psi_{T,1}^+$	6.05	12.53	-2.81	15.77	—
0 ⁻	$\psi_{T,0}^-$	16.38	0	0	16.38	10.96
3 ⁻	$\psi_{S,1}^-$	10.64	7.52	-1.67	16.49	—
5 ⁺	u_0^+, v_0^+	3.45	18.80	-5.37	16.94	—
3 ⁺	$\psi_{S,0}^+$	12.61	7.52	-2.70	17.43	15.79
4 ⁺	u_1^+, v_1^+	8.73	12.53	-3.33	17.93	—
0 ⁺	$\psi_{T,3}^+$	18.81	0	0	18.81	—
5 ⁻	u_0^-, v_0^-	5.33	18.80	-4.90	19.23	—
4 ⁻	u_1^-, v_1^-	11.09	12.53	-3.85	19.77	—
6 ⁺	$\psi_{T,0}^+$	0	26.32	-4.57	21.75	21.05
6 ⁻	$\psi_{S,0}^-$	0.18	26.32	-4.33	22.23	—
6 ⁺	u_0^+, v_0^+	3.45	26.32	-4.33	25.50	—
6 ⁻	u_0^-, v_0^-	5.27	26.32	-4.48	27.17	—

Table 2.3 The low energy states and the four lowest energy spin 6 states from our vibrational model. The table headings are the spin-parity, the vibrational wavefunction(s), the vibrational energy, the zeroth order rotational energy, the first order correction to the rotational energy and the total energy of the state. We also provide an identification with a state in the experimental spectrum if this is possible.

of the tetrahedron is valid for low energy vibrations. The higher the energy of the vibrational wavefunctions, the less valid a local analysis becomes and the larger the energy difference between wavefunctions with opposite parities.

The first excited 0^+ state has a novel interpretation as a mix of the tetrahedral and flat square configurations. This interpretation is consistent with the idea that different models view this state as being correlated with the tetrahedral or the flat square configurations, but ours is the first model to view it as a combination of the two.

The energies of the lowest 2^+ and 2^- states, at 6.69 MeV and 8.48 MeV respectively, in our model is in good agreement with the experimental spectrum as is the gap between them, 1.79 MeV, compared with 1.96 MeV in the experimental spectrum. In many local vibrational analyses of the tetrahedron these states have the same energy and thus the matching of this gap with experimental data is a test of the global structure of our vibrational manifold and potential. In [24] it is proposed that this splitting can be explained via higher order terms in the rotational Hamiltonian. However, given that the energy splitting is of the order of the total rotational energy of these states, this seems unlikely. It should also be noted that the first excited state 0^+ does not form a rotational band with the lowest lying 2^+ and 2^- states in our model because they lie in different representations, which is in contrast with rigid body quantization approaches.

The corresponding spin 4 states, those with the same vibrational wavefunctions as the spin 2 states above, have energies 12.67 MeV and 14.75 MeV and are matched with the states at 11.10 MeV and 14.30 MeV in the experimental spectrum. The 4^+ from our model has rather too high energy and we believe that the rotational energy of the state may be responsible for this. This state lies in the standard representation and thus its vibrational wavefunction vanishes at the tetrahedron. Therefore our method of calculating the rotational energy loses some validity, because the zeroth order approximation of the rotational energy uses the moments of inertia of the tetrahedron. Calculating the rotational energy as a perturbation away from the flat square may lead to a more promising result. The 4^- state is in good agreement with the experimental spectrum.

Our model has some difficulties for states with higher vibrational energies and we find that we often overestimate the energies of the higher energy states in the spectrum. One reason for this is that the more vibrational energy a state has the more correlated it is with the asymptotic configurations of \mathcal{M}_H ; our potential diverges asymptotically thereby giving these states more energy than they would have for a potential that flattens out asymptotically. However, due to the scarcity of 0^- states in

the experimental spectrum, we identify our state at 16.38 MeV with the one at 10.96 MeV in the experimental spectrum. Whilst this gap is rather large it is worth bearing in mind that many models are not able to incorporate any 0^- states at all and so the very existence of this state in our model is a plus. We also identify the 3^+ state at 17.43 MeV in our model with the one at 15.79 MeV in the experimental spectrum.

Our model also overestimates the energies of states with a lot of rotational energy, such as the spin 5 and spin 6 states. The only states with spin 5 from our model are in the standard representation, with our lowest state having spin-parity 5^+ and an energy of 16.94 MeV compared with the lowest energy 5^+ state at 14.40 MeV in the experimental spectrum. We would expect some centrifugal stretching of the configurations upon rotation, which scales like $L^2(L+1)^2$ and therefore becomes more relevant for high spins. Such stretching increases the moments of inertia and therefore decreases the rotational energies of these states. This would also have an effect on the 4^+ state at 12.67 in our model.

2.5 Local vibrations of the tetrahedron

Our model can not explain all of the states in the experimental energy spectrum of Oxygen–16, in particular it does not admit any spin 1 states because they are incompatible with D_2 symmetry. In order to find some of the missing states in the experimental spectrum of Oxygen–16, we need to consider more than just the E vibration of the tetrahedron. With this in mind we will consider local and harmonic vibrations of the tetrahedron in order to find the states obtained by quantizing the A and F vibrations from section 2.3.

2.5.1 The A Vibration

The A vibration corresponds to the symmetric stretching and squashing of the tetrahedral configuration, as shown in Figure 2.2, which means that it permits the same spin states as the positive parity trivial representation and negative parity sign representation found in our vibrational model. Therefore the trivial and sign representations are equivalent to the A representation close to the tetrahedron. We find a 0^+ , 3^- , 4^+ , 6^+ rotational band, with the vibrational energies of the states found by matching the energy with the 0^+ state found at 12.05 MeV in the experimental spectrum because this is the lowest lying 0^+ state not accounted for in our model. This gives a harmonic

frequency ω_A such that $\hbar\omega_A = 12.05$ MeV and as shown in [32] this frequency can be also used to accurately approximate the breather mode energy from Carbon–12.

2.5.2 The F Vibration

As seen in section 2.3, the F vibration is a three dimensional space. However, it is most easily described via a set of four vibrations which sum to zero. Each one of these vibrations corresponds to one alpha particle pulling away from the other three with the whole configuration retaining C_3 symmetry as seen in Figure 2.18.

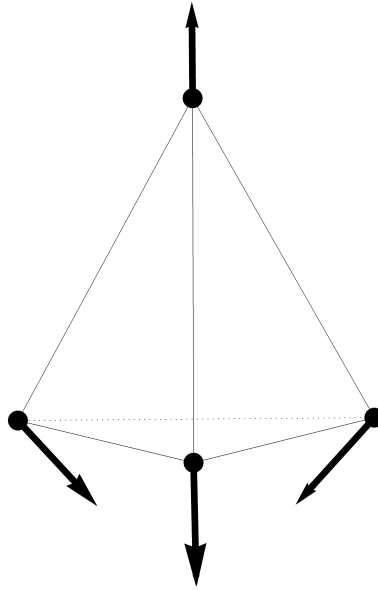


Fig. 2.18 A C_3 symmetric vibration in the F vibrational space.

Each of the four C_3 symmetric vibrations of the F vibrational space can be labelled by the particle that moves away from the others, which corresponds to a vertex of the tetrahedron. The tetrahedral symmetry group, T , can then be imagined as the orientation preserving permutations of its four vertices and so is isomorphic to A_4 , the alternating group of the 4 vertices. A_4 is generated by the elements $C_3 = (1\ 2\ 3)$ and $D_{2Z} = (1\ 2)(3\ 4)$.

The most natural way to consider vibrational wavefunctions in the F representation is via a quartet: a , b , c and d (with $a+b+c+d=0$), which A_4 acts on via permutation, such that

$$C_3(a) = a, C_3(b) = c, C_3(c) = d, C_3(d) = b \quad (2.61)$$

and

$$D_{2Z}(a) = b, D_{2Z}(b) = a, D_{2Z}(c) = d, D_{2Z}(d) = c. \quad (2.62)$$

The generators of A_4 can also be explicitly expressed in terms of rotation-isorotation pairs:

$$\hat{C}_3 = e^{\frac{2i\pi}{3\sqrt{3}}(\hat{L}_1 + \hat{L}_2 + \hat{L}_3)} e^{\frac{2i\pi}{3}\hat{K}_3}, \quad (2.63)$$

$$\hat{D}_{2Z} = e^{i\pi\hat{L}_3}. \quad (2.64)$$

We then construct the rovibrational state,

$$a|A\rangle + b|B\rangle + c|C\rangle + d|D\rangle, \quad (2.65)$$

with lies in the F representation so long as the spin states transform passively according to,

$$\hat{C}_3|A\rangle = |A\rangle, \hat{C}_3|B\rangle = |D\rangle, \hat{C}_3|C\rangle = |B\rangle, \hat{C}_3|D\rangle = |C\rangle, \quad (2.66)$$

$$\hat{D}_{2Z}|A\rangle = |B\rangle, \hat{D}_{2Z}|B\rangle = |A\rangle, \hat{D}_{2Z}|C\rangle = |D\rangle, \hat{D}_{2Z}|D\rangle = |C\rangle, \quad (2.67)$$

and

$$|A\rangle + |B\rangle + |C\rangle + |D\rangle = 0. \quad (2.68)$$

We make the approximation that the F vibration is harmonic and therefore each rovibrational state has vibrational energy that is a multiple of $\hbar\omega_F$ and we calculate the rotational energy of the state using the moment of inertia of the tetrahedral configuration.

The lowest energy state is the spin 1 state,

$$-(X - iY)|1, 1\rangle + \sqrt{2}Z|1, 0\rangle + (X + iY)|1, -1\rangle \quad (2.69)$$

where $X = a + c - b - d$, $Y = a + d - b - c$ and $Z = a + b - c - d$.

In order to calculate the parity of this state it helps to consider what the configuration looks like if we only excite the vibrational mode, a . However, this means that $b = c = d = -\frac{1}{3}a$ because the four modes must sum to zero. Now the state in (2.69) becomes proportional to

$$(-1 + i)|1, 1\rangle + \sqrt{2}|1, 0\rangle + (1 + i)|1, -1\rangle. \quad (2.70)$$

Such an excitation corresponds to the particle in the $(1, 1, 1)$ direction pulling away from the other three particles and such a configuration has a reflection symmetry.

Therefore we can express the parity operator in terms of rotations and isorotations,

$$\hat{\mathcal{P}} = e^{\frac{i\pi}{\sqrt{2}}(\hat{L}_1 - \hat{L}_2)} e^{\frac{i\pi}{2}(\sqrt{3}\hat{L}_1 + \hat{L}_2)}. \quad (2.71)$$

If we apply $\hat{\mathcal{P}}$ to the state in (2.70) we see that it flips sign, therefore we have a 1^- state. We then identify this with the lowest lying 1^- in the experimental spectrum at 7.12 MeV and use this determine to the vibrational frequency, $\hbar\omega_F = 5.84$ MeV. This 1^- state is the base of rotational band consisting of the states $1^-, 2^+, 3^\pm, 4^\pm, 5^\pm, 6^\pm$. Additional spin states that fall under the F representation are listed in A.2 in Appendix A.

2.5.3 Combining vibrations

So far we have only considered vibrations which are excited in either the A , E or F channels. However, it is also possible to excite more than one channel at the tetrahedron simultaneously and thereby combine different types of vibrations.

The combination of a state in the A representation with a state in any other representation gives a state in this other representation, this is because the A vibration is tetrahedrally symmetric. The combination of a state in the E representation with another state in the E representation gives states in the A or E representations. The combination of a state in the E representation with a state in the F representation only gives states in the F representation. The combination of a state in the F representation with another state in the F representation gives states in the A , E and F representations. Details of how these combinations work explicitly for our rovibrational states are given in Appendix B.

Notice that the combination of two states in the E representation can give states in the A representation. The E representation is equivalent to the standard representation and this explains how we can get states in the trivial and sign representations from our vibrational model. This also means that states in the trivial and sign representations in our vibrational model should have approximately two times the vibrational energy of the lowest energy states in the standard representation. As seen in table 2.3, the first excited 0^+ state has 6.05 MeV of vibrational energy and the lowest 2^+ state has 3.51 MeV of vibrational energy giving a ratio of 1.72. This ratio is not exactly two because we consider a global vibrational analysis rather than a local harmonic analysis.

We must also consider more closely how states in the E representation couple with states in the F representation because we have a global model of the E vibration. An example of this is the lowest energy 1^- state which has one unit of F vibration and no

units of A or E vibration. However, there is still the question of whether this state should be paired with the vibrational wavefunction in the trivial representation, $\psi_{T,0}^+$, or the sign representation, $\psi_{S,0}^-$, because both of these wavefunctions have no units of E vibration in a local analysis of the tetrahedron.

Recalling that all of our S_3 transformations in section 2.4 left the point $(1, 1, 1)$ fixed, it makes sense to look at the 1^- state when $b = c = d = -\frac{1}{3}a$ because in this excitation one of the alpha particles moves along the $(1, 1, 1)$ direction. For this excitation the rovibrational state is of the form,

$$|\Psi\rangle = \psi_? \left((-1 + i) |1, 1\rangle + \sqrt{2} |1, 0\rangle + (1 + i) |1, -1\rangle \right), \quad (2.72)$$

as shown in (2.70) where $\psi_?$ is the unknown vibrational wavefunction from the E vibration in either the trivial or sign representation. We can then apply our \hat{C}_2 and \hat{C}_3 operators to this spin state to find that

$$\hat{C}_2 |\Psi\rangle = -|\Psi\rangle \quad \text{and} \quad \hat{C}_3 |\Psi\rangle = |\Psi\rangle. \quad (2.73)$$

This should be equivalent to performing these actions on the vibrational wavefunction, $\psi_?$, directly and therefore we know that $\psi_?$ must be in the sign representation and therefore is the wavefunction $\psi_{S,0}^-$. Conversely we find that the 2^+ state which has one unit of F vibration and no units of A or E vibration should be paired with the vibrational wavefunction $\psi_{T,0}^+$, which is why the lowest energy 1^- and 2^+ states in table 2.4 have slightly different vibrational energies.

The states below 20 MeV that can be obtained via combining A , E and F vibrations are listed in table 2.4 along with the representations that they fall under, their vibrational, rotational and total energies and identifications with experimental states if known.

In Figure 2.19 we plot all of the states that we have found using both our vibrational model and the local vibrations of the tetrahedron. We see that by including in the F vibration we are able to explain the spin 1 states in the experimental spectrum which were not permitted by our vibrational model. The F vibration also increases the number of spin 2 and spin 3 states that we find which gives a stronger agreement with the experimental spectrum as well. There is a rather surprising gap in the energies of the spin 2 states between 15 and 17 MeV for our model which is not observed in the experimental spectrum. However, this is because we have used a crude approximation for the rotational energy of the spin 2 states in the F representation. A more accurate approximation of the rotational energy would make this gap disappear. We have a

$(A E F)$	J^P	Rep.	E_{vib}	E_{rot}	E	E_{Exp}
(001)	1 ⁻	F	6.08	1.04	7.12	7.12
(001)	2 ⁺	F	5.84	3.11	8.95	9.84
(011)	1 ⁻	F	9.35	1.04	10.39	9.59
(002)	0 ⁺	A	11.69	0	11.39	11.26
(100)	0 ⁺	A	12.05	0	12.05	12.05
(001)	3 ⁺	F	5.84	6.21	12.06	11.08
(011)	1 ⁺	F	11.17	1.04	12.21	13.66
(001)	3 ⁻	F	6.08	6.21	12.30	11.60
(011)	2 ⁺	F	9.35	3.11	12.46	—
(021)	1 ⁻	F	11.89	1.04	12.93	12.44
(002)	1 ⁻	F	11.93	1.04	12.96	13.01
(011)	2 ⁻	F	11.17	3.11	14.28	—
(002)	2 ⁺	E	11.69	3.11	14.79	—
(002)	2 ⁺	F	11.69	3.11	14.79	—
(021)	2 ⁺	F	11.89	3.11	15.00	—
(002)	2 ⁻	E	11.93	3.11	15.04	—
(011)	3 [±]	F	9.35	6.21	15.57	—
(021)	1 ⁻	F	14.57	1.04	15.61	—
(001)	4 ⁺	F	5.84	10.36	16.20	—
(001)	4 ⁻	F	6.08	10.36	16.44	—
(011)	3 [∓]	F	11.17	6.21	17.38	—
(021)	1 ⁺	F	16.48	1.04	17.52	—
(021)	2 ⁺	F	14.57	3.11	17.68	—
(002)	3 ⁺	F	11.69	6.21	17.90	—
(021)	1 ⁺	F	16.93	1.04	17.97	—
(002)	3 ⁻	F	11.93	6.21	18.14	—
(002)	3 ⁻	A	11.93	6.21	18.14	—
(100)	3 ⁻	A	12.05	6.21	18.26	—
(110)	2 ⁺	E	15.56	3.11	18.74	—
(101)	1 ⁻	F	18.13	1.04	19.17	—
(021)	2 ⁻	F	16.48	3.11	19.59	—
(011)	4 [±]	F	9.35	10.36	19.71	—

Table 2.4 The low energy states produced by combining vibrations. $(A E F)$ describes the number of vibrational units there is in each channel. We have listed the spin-parity of the state, the representation that it falls under, its vibrational energy, its rotational energy and its total energy. We have provided an identification with an experimental state if such a pairing seems clear.

very good agreement with the number of spin 4 states below 20 MeV and their energies are quite close to those found in the experimental spectrum.

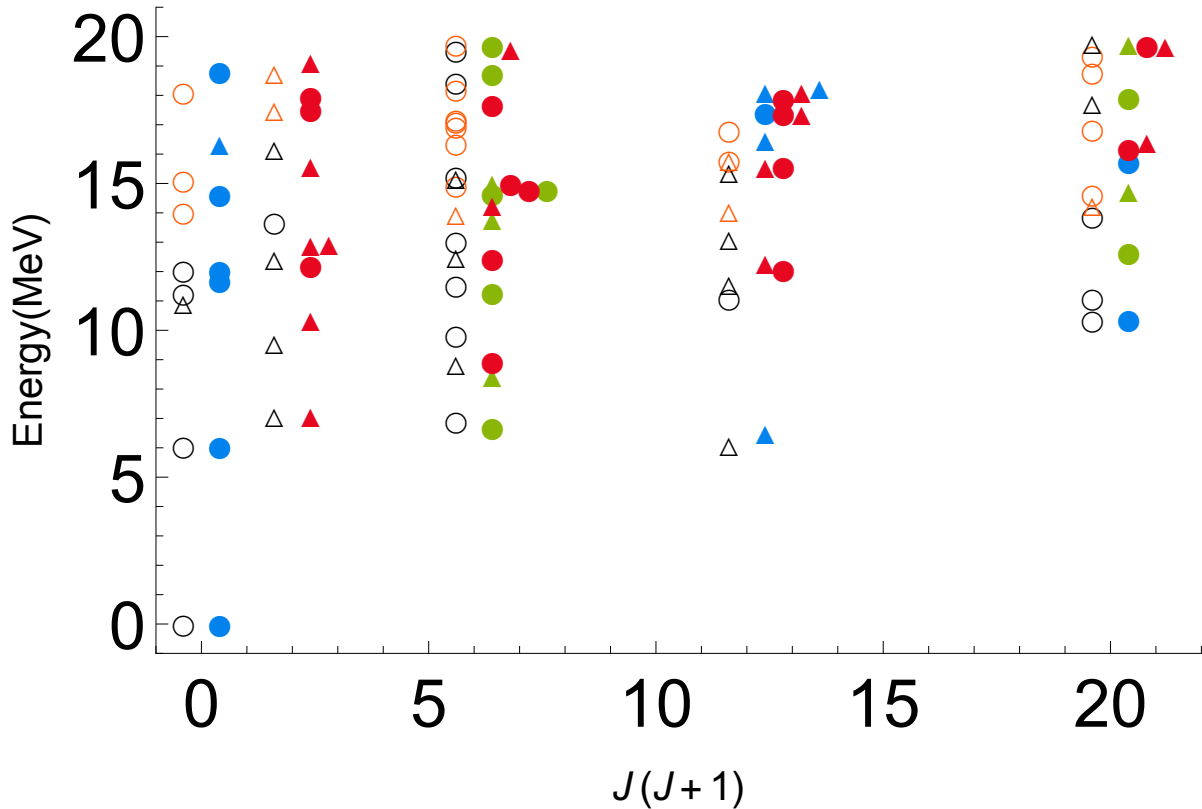


Fig. 2.19 The states of the E vibration in our model along with the states from the A and F vibrations of the tetrahedron and states in the experimental spectrum of Oxygen-16 below 20 MeV. The hollow black shapes denote experimental states with isospin 0, the hollow orange shapes denote experimental states with unknown isospin, the blue shapes denote states in the trivial or sign representations, the green shapes denote states in the standard representation and the red shapes denote states in the F representation. Circles denote positive parity states and triangles denote negative parity states.

2.6 Isospin

So far we have only considered states with isospin 0, but, since every rotational operator that we have used comes with a paired isorotational operator, we can easily expand our method to non-zero isospin. The vibrational wavefunctions are the same as for the isospin 0 states and the spin and isospin states that couple with them are given in tables A.3 and A.4 of Appendix A.

In order to calculate the energies of the states in our model we need an ansatz for the moments of isoinertia; fortunately these are much easier to calculate than the moments of inertia because the isoinertia tensor is approximately four times that of the $B = 4$ Skyrmion for any $B = 16$ configuration [18]. Therefore, using the values for a $B = 4$ Skyrmion found in [7], we take our moments of isoinertia to be $U_{11} = U_{22} = 571$ and $U_{33} = 678$ for all of our configurations, with all other elements equal to zero. The lowest energy states from our model are plotted in Figure 2.20 against the states from the experimental spectrum and listed in table 2.5.

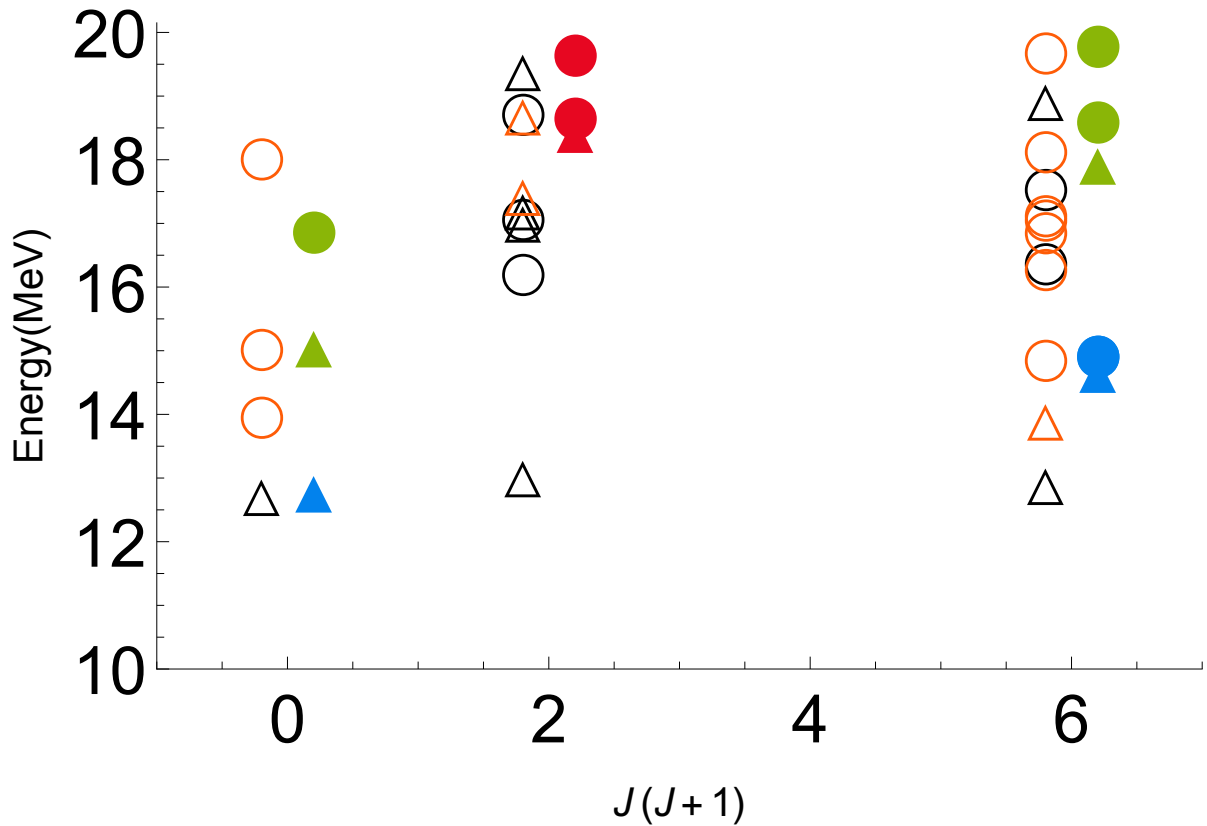


Fig. 2.20 The isospin 1 states of the E vibration in our model along with the states from the A and F vibrations of the tetrahedron and states in the experimental spectrum of Oxygen–16 below 20 MeV. The hollow black shapes denote experimental states with isospin 1, the hollow orange shapes denote experimental states with unknown isospin, the blue shapes denote states in the trivial or sign representations, the green shapes denote states in the standard representation and the red shapes denote states in the F representation. Circles denote positive parity states and triangles denote negative parity states.

The lowest energy isospin 1 state has spin parity 0^- and is in the sign representation. This agrees with the spin parity of the lowest energy isospin 1 state at 12.85 MeV

J^P	Rep.	E_{vib}	E_{rot}	E_{isorot}	E
0^-	A	0.24	0	12.61	12.85
2^-	A	0	3.11	11.62	14.73
2^+	A	0.24	3.14	11.62	15.00
0^-	E	3.51	0	11.62	15.13
0^+	E	5.33	0	11.62	16.95
2^-	E	3.51	2.87	11.62	18.00
1^-	F	5.84	1.04	11.62	18.50
1^+	F	6.08	1.04	11.62	18.74
1^+	F	6.08	1.04	12.61	19.73
2^+	E	3.51	2.56	12.61	18.68
2^+	E	5.33	2.92	11.62	19.87

Table 2.5 The isospin 1 states below 20 MeV. We have listed the spin-parity of the state, the representation that it falls under, its vibrational energy, its rotational energy, its isorotational energy and its total energy.

in the experimental spectrum and so we use this state to calibrate the isorotational energy unit.

The lowest lying 1^- , 2^- and 3^- states are well explained by a shell model approach [33] but we have no interpretation for them in our model. The next lowest isospin 1 state is in the trivial representation and has spin-parity 2^- which agrees with the fifth lowest energy state in the experimental spectrum. However, we find that the energy of the state is a little high in our model and this is true for all of the states that we find. Despite the fact that we are able to produce states with the correct spin-parity in our model, these differences in energies could indicate a problem with the Skyrme model.

This problem is even more serious for isospin 2 states; the lowest energy isospin 2 state in our model has spin-parity 0^+ and is at 37.82 MeV whereas the lowest energy isospin 2 state in the experimental spectrum has spin-parity 0^+ and is at 22.72 MeV. Whilst it is promising that we are able to match the spin-parity, the colossal difference in energies indicates that something is severely wrong with our method. In the Skyrme model isorotational energy scales like $I(I + 1)$ whereas the experimental spectrum would indicate that the isospin energy scaling linearly with isospin would be more appropriate for these isospin 2 states. This would mean that isospin energy is more akin to vibrational energy than rotational energy for some states, indicating that there may be a fundamental misunderstanding of isospin in the Skyrme model.

One possibility for rectification of this problem is that Skyrmions deform at high values of isospin [34]. The isospin moments of inertia for a $B = 16$ Skyrmions would still be bounded by sixteen times the isospin moments of inertia for a $B = 1$ Skyrmion, giving $U_{ij} = u \delta_{ij}$ where $u \leq 760$. However, this is still not large enough to account for gap between energies of the isospin 2 states in our model and the experimental spectrum.

2.7 Conclusions

Previous alpha cluster analyses of the Oxygen-16 have focussed on a tetrahedral arrangement of four alpha particles and the local vibrations of this tetrahedron. We have used the Skyrme model to create a vibrational manifold for the E vibration of the tetrahedron which incorporates the bent square and flat square arrangements of alpha particles as well. This global approach provides a fresh perspective on the first excited 0^+ state as a mixture of the tetrahedral and flat square configurations and is able to explain the gap between the lowest energy spin 2 states, which has proved challenging for other alpha cluster approaches. We have seen that a global treatment of the E vibration has a significant effect on the resulting energy spectrum, in particular providing us with challenging states such as the 0^- and 3^+ states seen in the experimental spectrum. It would be interesting to apply this idea of globalization to the F vibration as well. Combining the A , E and F vibrations is simple at the tetrahedron but if the vibrations were treated globally we would have to consider cross-terms in the metric which are not well understood at present.

We have found that there are some problems with the higher energy states in our model. States with high vibrational energy often have too much energy due to our potential losing validity for asymptotic configurations. States with high rotational energy also have too much energy because we do not incorporate the centrifugal deformation of configurations at higher spins. The vibrational energy problem could be resolved via a different choice of potential, this would likely lead to the loss of analytic solutions and require more extensive numerical work but seems a possible avenue for future work. The rotational energy problem could be resolved by looking at the effect of rotation on Skyrmions and the degree to which they deform. This project has also indicated some problems with isospin, in that the Skyrme model seems to overestimate the energy of higher isospin states. It would be worth considering how vibrations and isospin interact with each other and in particular whether isospin can

be generated without the quantizing of isorotational degrees of freedom via a rigid rotor interpretation.

Chapter 3

Interactions between Skyrmions

3.1 Introduction

A growing area of interest in the Skyrme model is vibrational quantization, which is the idea that when we want to quantize a Skyrmion we must consider configurations other than the configuration with the lowest energy (the energy minimizer). This is as opposed to rigid body quantization where we only quantize the zero energy modes of the energy minimizer (rotations and isorotations) [7].

The spin states allowed by a configuration depend on the amount of symmetry that it has; more symmetry leads to more restrictions on a spin state and as a result fewer spin states are permitted [9]. As a result, when we only consider rigid body quantization the Skyrme model frequently predicts less spin states than are present in the experimental energy spectrum. In vibrational quantization we take into account some additional low energy configurations which often have less symmetry than the energy minimizer [35, 11]. This reduction in symmetry leads to more allowed spin states and so a fuller spectrum in agreement with experimental findings.

In order to perform vibrational quantization we need to know the energy of the configurations far away from the energy minimizer in configuration space; such configurations frequently become composite and can be viewed as a collection of smaller Skyrmions. The energy of these configurations could be found via numerical simulation [36] but it would be very time consuming to find the energy of several different configurations and completely intractable if the dimension of the configuration space is large. An alternative, for these composite configurations, is to find the total energy of the constituent Skyrmions and subtract from this the total interaction energy between these constituents.

A related area is $B = 4N$ cluster nuclei; in the Skyrme model these are presented as arrangements consisting of N $B = 4$ Skyrmions [14]. The idea here is that the $B = 4$ Skyrmion (corresponding to the Helium nucleus or alpha particle) is a particularly stable configuration with high binding energy and so it is a good candidate for a ‘building block’ with which to construct larger nuclei. Once we know the number of $B = 4$ blocks that are present we need to find which arrangement of them has the lowest energy; given that the total energy of the constituent $B = 4$ Skyrmions is fixed this will depend entirely on the interaction energy between the pairs of $B = 4$ Skyrmions.

Both of these problems require the evaluation of interaction energies between Skyrmions for a range of separations and orientations. Again this could be done numerically, but for a pair of Skyrmions the space of possible separations and relative orientations is six dimensional (or even higher if we allow isorotations as well) so it is not feasible to find the energy for every possible situation numerically. Another approach is to treat Skyrmions as interacting point multipoles [37]; this has the benefit of producing an analytic expression for the interaction energy and so can be applied easily to all separations and orientations. However since the Skyrmions are treated as point particles the approximation loses accuracy as the Skyrmions approach each other.

In this chapter, we consider Skyrmions as sourced by extended Gaussian multipoles; this retains the analytic formulae from the point multipole approach whilst retaining some accuracy as the Skyrmions approach each other. We develop formulae for the pion fields and interaction energies of Skyrmions before applying these to some important examples of Skyrmions and their interactions.

3.2 Yukawa interactions

In this section we consider how a first approximation to interaction energy can be achieved via point multipole sources and then show how we can improve upon this approximation by extending this to Gaussian multipole sources.

3.2.1 Massive scalar field theory

In [38] it is shown that to linear order the interactions between Skyrmions are described by massive scalar field theory. In a massive scalar theory with scalar field, π , source, ρ

and mass, μ , the static energy is given by,

$$E = \int \left(\frac{1}{2} \nabla \pi \cdot \nabla \pi + \frac{1}{2} \mu^2 \pi^2 + \rho \pi \right) d^3 x, \quad (3.1)$$

resulting in the field equation

$$(\nabla^2 - \mu^2) \pi = \rho. \quad (3.2)$$

The field, π , corresponds to a pion field of the Skyrme model and μ corresponds to the pion mass; however, ρ does not have a direct counterpart and should be viewed as a source which generates the pion field, π . However, the duality between massive scalar theory and the Skyrme model only applies to interactions between Skyrmions so we can not use (3.1) to calculate the energy of a Skyrme model.

We define the interaction energy between two sources $\rho^{(1)}$ and $\rho^{(2)}$ (which generate pion fields $\pi^{(1)}$ and $\pi^{(2)}$ respectively) as

$$E_{int} = E(\rho^{(1)} + \rho^{(2)}, \pi^{(1)} + \pi^{(2)}) - E(\rho^{(1)}, \pi^{(1)}) - E(\rho^{(2)}, \pi^{(2)}). \quad (3.3)$$

This is related to the binding energy of the system; the difference between the energy of the system and the energy of its constituent parts.

Plugging the expression for the energy found in (3.1) into (3.3) and using the field equation (3.2) to simplify, we find a simple expression for the interaction energy,

$$E_{int} = \int d^3 x \rho^{(1)} \pi^{(2)}. \quad (3.4)$$

In our approximation the sources, ρ , will be the fundamental fields, despite not appearing in the Skyrme model directly, and so we would like to have expressions for π and E_{int} that only depend on these sources. Using the Green's function of (3.2), we find,

$$\pi(\mathbf{x}) = - \int d^3 \mathbf{y} \rho(\mathbf{y}) \frac{e^{-\mu|\mathbf{x}-\mathbf{y}|}}{4\pi|\mathbf{x}-\mathbf{y}|} = - \int d^3 \mathbf{y} \rho(\mathbf{x} + \mathbf{y}) \frac{e^{-\mu|\mathbf{y}|}}{4\pi|\mathbf{y}|}, \quad (3.5)$$

and a corresponding interaction energy,

$$E_{int} = - \int d^3 \mathbf{x} d^3 \mathbf{y} \rho_1(\mathbf{x}) \rho_2(\mathbf{x} + \mathbf{y}) \frac{e^{-\mu|\mathbf{y}|}}{4\pi|\mathbf{y}|}. \quad (3.6)$$

Note that (3.6) shows us that these sources interact via a Yukawa interaction. Additionally given that each Skyrme model has a triplet of pion fields the total interaction energy will involve three pairs of sources.

3.2.2 Point multipole sources

We now have integral expressions for the pion field generated by a source and the interaction energy between two sources. The problem is that, as stated in section 3.1, it is important to have an analytic expression for the interaction energy between Skyrmions, in order to apply it to range of different separations and orientations. This means that we need to generate our Skyrmions with sources for which the integrals in (3.5) and (3.6) can be performed explicitly.

In [38] it is shown that a point multipole source of the form,

$$\rho(\mathbf{x}) = (-1)^l Q_{i_1 \dots i_l} \partial_{i_1} \dots \partial_{i_l} \delta(\mathbf{x}), \quad (3.7)$$

generates a pion field of the form,

$$\pi(\mathbf{x}) = (-1)^{l+1} Q_{i_1 \dots i_l} \partial_{i_1} \dots \partial_{i_l} \left(\frac{e^{-\mu|\mathbf{x}|}}{4\pi|\mathbf{x}|} \right), \quad (3.8)$$

and that interaction between two sources of the form,

$$\rho^{(1)}(\mathbf{x}) = (-1)^l Q_{i_1 \dots i_l}^{(1)} \partial_{i_1} \dots \partial_{i_l} \delta(\mathbf{x}) \text{ and } \rho^{(2)}(\mathbf{x}) = (-1)^m Q_{j_1 \dots j_m}^{(2)} \partial_{j_1} \dots \partial_{j_m} \delta(\mathbf{x} - \mathbf{X}), \quad (3.9)$$

gives an interaction energy of

$$E_{int} = - Q_{i_1 \dots i_l}^{(1)} Q_{j_1 \dots j_m}^{(2)} \partial_{i_1} \dots \partial_{i_l} \partial_{j_1} \dots \partial_{j_m} \left(\frac{e^{-\mu|\mathbf{X}|}}{4\pi|\mathbf{X}|} \right). \quad (3.10)$$

Both the formulae for the pion field and the interaction energy are in a very convenient form, only requiring the evaluation of derivatives of $\frac{e^{-\mu|\mathbf{x}|}}{4\pi|\mathbf{x}|}$. The $Q_{i_1 \dots i_l}$'s are the multipole moments of the Skyrmion and, as shown in (3.10), these determine how two well-separated Skyrmions interact with each other. The multipole moments of a Skyrmion tell us about its symmetry group and this in turn determines the spin states that it permits; therefore it is of vital importance that our approximation scheme can also account for these multipole moments.

The approximation outlined here, using point sources, captures the leading order behaviour of the Skyrmion's pion field perfectly and as a consequence provides an accurate approximation of the interaction energy of Skyrmions at large separations. However, as the Skyrmions approach each other the accuracy of the interaction energy decreases significantly, because the effect of using a point source rather than an extended source is significant. We would like to find a form for the sources which retains the

convenient form for the expressions found in equations (3.8) and (3.10), whilst still remaining accurate as the interacting Skyrmions get closer to one another.

3.2.3 The Gaussian monopole source

A natural candidate for an extended source is a Gaussian and so we consider a source of the form,

$$\rho(G; \mathbf{x}) = e^{-\frac{G}{2}r^2}, \quad (3.11)$$

where $r = |\mathbf{x}|$. We then use (3.5) to calculate the pion field which is generated by this source,

$$\pi(G; \mathbf{x}) = - \int d^3\mathbf{y} e^{-\frac{G}{2}(\mathbf{x}+\mathbf{y})^2} \frac{e^{-\mu|\mathbf{y}|}}{4\pi|\mathbf{y}|} \quad (3.12)$$

$$= -\frac{1}{2}e^{-\frac{G}{2}r^2} \int_0^\infty \int_{-1}^1 dy d(\cos\theta) y e^{-\frac{G}{2}y^2} e^{-Gry \cos\theta} e^{-\mu y} \quad (3.13)$$

$$= \frac{1}{2Gr} e^{-\frac{G}{2}r^2} \int_0^\infty dy e^{-\frac{G}{2}y^2} (e^{-Gry} - e^{Gry}) e^{-\mu y} \quad (3.14)$$

$$= \frac{1}{2Gr} \int_0^\infty dy \left(e^{-\frac{G}{2}(y+r+\frac{\mu}{G})^2} e^{\mu r} e^{\frac{\mu^2}{2G}} - e^{-\frac{G}{2}(y-r+\frac{\mu}{G})^2} e^{-\mu r} e^{\frac{\mu^2}{2G}} \right) \quad (3.15)$$

$$= \frac{e^{\frac{\mu^2}{2G}}}{2Gr} \left(e^{\mu r} \int_{\frac{\mu}{G}+r}^\infty e^{-\frac{G}{2}y^2} dy - e^{-\mu r} \int_{\frac{\mu}{G}-r}^\infty e^{-\frac{G}{2}y^2} dy \right) \quad (3.16)$$

$$= \frac{\pi^{\frac{1}{2}} e^{\frac{\mu^2}{2G}}}{(2G)^{\frac{3}{2}} r} \left(\operatorname{erfc} \left(\frac{\mu + Gr}{\sqrt{2G}} \right) e^{\mu r} - \operatorname{erfc} \left(\frac{\mu - Gr}{\sqrt{2G}} \right) e^{-\mu r} \right) \quad (3.17)$$

$$\equiv f(G; r). \quad (3.18)$$

where the second equality involves going to spherical polars and performing the azimuthal integral. The expression in (3.17) is defined as the function $f(G; r)$ because this function will appear in many expressions later in this chapter. We see that the pion field generated by the Gaussian monopole source can be expressed in terms of convenient functions as in the case of a point source. Note that we have suppressed the μ dependence of the function $f(G; r)$. This is because we only consider $\mu = 1$ in this chapter and do not treat it as a variable; however, this dependence could be easily reinstated if one wanted to consider other pion masses.

Consider what happens to $f(G; r)$ as we take the limit of $G \rightarrow \infty$:

$$f(\infty; r) = \lim_{G \rightarrow \infty} \frac{\pi^{\frac{1}{2}} e^{\frac{\mu^2}{2G}}}{(2G)^{\frac{3}{2}} r} \left(\operatorname{erfc} \left(\frac{\mu + Gr}{\sqrt{2G}} \right) e^{\mu r} - \operatorname{erfc} \left(\frac{\mu - Gr}{\sqrt{2G}} \right) e^{-\mu r} \right) = - \left(\frac{2\pi}{G} \right)^{\frac{3}{2}} \frac{e^{-\mu r}}{4\pi r}. \quad (3.19)$$

As we take $G \rightarrow \infty$ the Gaussian monopole source becomes point-like and so we recover the pion field for a point monopole of the form in (3.8) (adjusting for the fact that the total charge of the source in (3.11) is $(\frac{2\pi}{G})^{\frac{3}{2}}$); thus we see that the point monopole source is just a limit of the Gaussian monopole source. We will consider this idea further when we have considered a larger class of Gaussian sources.

3.3 Gaussian multipole sources

So far we have shown that the pion field generated by a Gaussian monopole source has a convenient form; however, as mentioned in subsection 3.2.2 we also need to account for the multipole moments and symmetries of the Skyrmions that we are trying to approximate. This can be achieved by adding angular dependence to our sources via the use of solid harmonics,

$$\rho^{l,m}(G; \mathbf{x}) = \mathcal{Y}_l^m(\theta, \phi) e^{-\frac{G}{2}r^2}, \quad (3.20)$$

where $\mathcal{Y}_l^m = r^l Y_l^m$ are the solid harmonics and Y_l^m are the usual spherical harmonics. However, now we have to perform the following integral,

$$\pi^{l,m}(G; \mathbf{x}) = - \int d^3\mathbf{y} \mathcal{Y}_l^m(\mathbf{x} + \mathbf{y}) e^{-\frac{G}{2}(\mathbf{x}+\mathbf{y})^2} \frac{e^{-\mu|\mathbf{y}|}}{4\pi|\mathbf{y}|}, \quad (3.21)$$

in order to generate the pion field generated by this source. We see that the solid harmonic in (3.21) has a shifted origin and that there is angular dependence in the solid harmonic and the exponent of the Gaussian; these factors make the integral in (3.21) rather challenging. We now introduce a generating function for the solid harmonics which alleviates both of these problems and enables us to perform this integral more easily.

3.3.1 The Herglotz generating function

The Herglotz generating function uses an exponential to package the solid harmonics into a form which is easier to work with than the solid harmonics themselves. To see the idea behind the Herglotz generating function we consider the application of the Laplacian to the dot product $\mathbf{a} \cdot \mathbf{x}$,

$$\nabla^2((\mathbf{a} \cdot \mathbf{x})^l) = l(l-1)(\mathbf{a} \cdot \mathbf{a})(\mathbf{a} \cdot \mathbf{x})^{l-2}, \quad (3.22)$$

and notice that if $\mathbf{a} \cdot \mathbf{a} = 0$ then $\nabla^2((\mathbf{a} \cdot \mathbf{x})^l) = 0$. But if $(\mathbf{a} \cdot \mathbf{x})^l$ is killed by the Laplacian and is degree l in r then it must be a linear combination of the solid harmonics $\mathcal{Y}_l^m(\theta, \phi)$. We then choose a parametrization of \mathbf{a} that will provide us with convenient coefficients for this linear combination. Choosing

$$\mathbf{a} = \left(-\frac{\lambda}{2} + \frac{1}{2\lambda}, -i \left(\frac{\lambda}{2} + \frac{1}{2\lambda} \right), 1 \right), \quad (3.23)$$

leads to get the following expression for $(\mathbf{a} \cdot \mathbf{x})^l$,

$$(\mathbf{a} \cdot \mathbf{x})^l = l! \sum_{m=-l}^l \sqrt{\frac{4\pi}{2l+1}} \frac{\lambda^m}{\sqrt{(l+m)!(l-m)!}} \mathcal{Y}_l^m(\theta, \phi). \quad (3.24)$$

The Herglotz generating function then combines all of these $(\mathbf{a} \cdot \mathbf{x})^l$ into one exponential,

$$e^{v\mathbf{a} \cdot \mathbf{x}} = \sum_{l=0}^{\infty} \sum_{m=-l}^l \sqrt{\frac{4\pi}{2l+1}} \frac{v^l \lambda^m}{\sqrt{(l+m)!(l-m)!}} \mathcal{Y}_l^m(\theta, \phi), \quad (3.25)$$

and as a result we can now find any solid harmonic by considering the coefficients of v and λ in the Taylor expansion of $e^{v\mathbf{a} \cdot \mathbf{x}}$.

This means that we can package our multipole Gaussian source into a more convenient format,

$$\rho^{l,m}(G; \mathbf{x}) = \mathcal{Y}_l^m(\theta, \phi) e^{-\frac{G}{2}r^2} = \sqrt{\frac{2l+1}{4\pi}} \sqrt{(l+m)!(l-m)!} \left[e^{v\mathbf{a} \cdot \mathbf{x}} e^{-\frac{G}{2}r^2} \right]_{v^l \lambda^m}, \quad (3.26)$$

where $[\dots]_{v^l \lambda^m}$ denotes the coefficient of $v^l \lambda^m$ of the expression inside the square brackets. Now instead of using a source of the form in (3.20), we can work with a ‘generating’ source,

$$\rho_{gen}(G; \mathbf{x}) = e^{v\mathbf{a} \cdot \mathbf{x}} e^{-\frac{G}{2}r^2} = e^{-\frac{G}{2}(\mathbf{x} - \frac{v\mathbf{a}}{G})^2} e^{\frac{v^2 \mathbf{a} \cdot \mathbf{a}}{2G}} = e^{-\frac{G}{2}(\mathbf{x} - \frac{v\mathbf{a}}{G})^2}, \quad (3.27)$$

where the last equality follows from the fact that $\mathbf{a} \cdot \mathbf{a} = 0$. We now see the benefits of using the Herglotz generating function; the ‘generating’ source is simply a Gaussian with a shifted origin and so the integral (3.17) can be performed easily to give,

$$\pi_{gen}(G; \mathbf{x}) = f \left(G; \left| \mathbf{x} - \frac{v\mathbf{a}}{G} \right| \right), \quad (3.28)$$

where the shift of origin in $\rho_{gen}(G; \mathbf{x})$ just results in the same shift of origin for $\pi_{gen}(G; \mathbf{x})$.

3.3.2 Gaussian multipole pion fields

We have managed to package our multipole Gaussian sources into the generating source in (3.27) and then found the pion field generated by this source. However we would like to calculate the pion field which is generated by our multipole Gaussian source in (3.20) and so we need to unpackage the pion field in (3.28). We know from (3.26) that,

$$\rho^{l,m}(G; \mathbf{x}) = \sqrt{\frac{2l+1}{4\pi}} \sqrt{(l+m)!(l-m)!} [\rho_{gen}(\mathbf{x})]_{v^l \lambda^m}, \quad (3.29)$$

and so it follows that,

$$\pi^{l,m}(G; \mathbf{x}) = \sqrt{\frac{2l+1}{4\pi}} \sqrt{(l+m)!(l-m)!} [\pi_{gen}(\mathbf{x})]_{v^l \lambda^m}, \quad (3.30)$$

where $\pi^{l,m}(G; \mathbf{x})$ is the pion field generated by $\rho^{l,m}(G; \mathbf{x})$. Therefore we need to find the $v^l \lambda^m$ coefficient of $\pi_{gen}(G; \mathbf{x})$; to this end we consider the Taylor expansion of $f(G; |\mathbf{x} - \frac{v\mathbf{a}}{G}|)$ about \mathbf{x} . We find that the v^l coefficient of $\pi_{gen}(G; \mathbf{x})$ is

$$\left(\frac{-1}{G}\right)^l \frac{a_{i_1} \dots a_{i_l}}{l!} \frac{\partial^l f(G; r)}{\partial x_{i_1} \dots \partial x_{i_l}}. \quad (3.31)$$

When we apply the derivatives to $f(G; r)$ successively we obtain,

$$\begin{aligned} \frac{\partial^l f(G; r)}{\partial x_{i_1} \dots \partial x_{i_l}} &= \frac{\partial^{(l-1)}}{\partial x_{i_2} \dots \partial x_{i_l}} \left(x_{i_1} \left(\frac{1}{r} \frac{\partial}{\partial r} \right) f(G; r) \right) \\ &= \frac{\partial^{(l-2)}}{\partial x_{i_3} \dots \partial x_{i_l}} \left(x_{i_1} x_{i_2} \left(\frac{1}{r} \frac{\partial}{\partial r} \right)^2 f(G; r) + \delta_{i_1, i_2} \left(\frac{1}{r} \frac{\partial}{\partial r} \right) f(G; r) \right) \\ &\quad \vdots \\ &= x_{i_1} \dots x_{i_l} \left(\frac{1}{r} \frac{\partial}{\partial r} \right)^l f(G; r). \end{aligned} \quad (3.32)$$

In the second equality we see that we have two distinct terms; however, the δ_{i_1, i_2} term would result in an $\mathbf{a} \cdot \mathbf{a}$ term in (3.31) which is 0 and so this term can be neglected. Similarly any subsequent derivative acts only on the $f(G; r)$ part of the expression to avoid the creation of a Kronecker delta and so iteratively the final equality holds.

Plugging the expression in (3.32) back into (3.31) we get,

$$\left(\frac{-1}{G}\right)^l \frac{a_{i_1} \dots a_{i_l}}{l!} \frac{\partial^l f(G; r)}{\partial x_{i_1} \dots \partial x_{i_l}} = \left(\frac{-1}{G}\right)^l \frac{(\mathbf{a} \cdot \mathbf{x})^l}{l!} \left(\frac{1}{r} \frac{\partial}{\partial r}\right)^l f(G; r). \quad (3.33)$$

Then using (3.21), we can extract the λ^m term from (3.33) to find that

$$\pi^{l,m}(\mathbf{x}) = \mathcal{Y}_l^m(\theta, \phi) \left(\frac{-1}{G}\right)^l \left(\frac{1}{r} \frac{\partial}{\partial r}\right)^l f(G; r). \quad (3.34)$$

Here it is important to note that the solid harmonics decouple from each other, with the radial dependence of $\pi^{l,m}(G; \mathbf{x})$ depending only on l (and not m). This is crucial because if we have a source of the form,

$$\rho(\mathbf{x}) = \sum_{m=-l}^l a_m \rho^{l,m}(G; \mathbf{x}) = \left(\sum_{m=-l}^l a_m \mathcal{Y}_l^m(\theta, \phi) \right) e^{-\frac{G}{2}r^2}, \quad (3.35)$$

then the generated pion field is

$$\pi(\mathbf{x}) = \sum_{m=-l}^l a_m \pi^{l,m}(G; \mathbf{x}) = \left(\sum_{m=-l}^l a_m \mathcal{Y}_l^m(\theta, \phi) \right) \left(\frac{-1}{G}\right)^l \left(\frac{1}{r} \frac{\partial}{\partial r}\right)^l f(G; r). \quad (3.36)$$

This means that if the source has a symmetry (as exhibited by a linear combination of solid harmonics) then the generated pion field will have this same symmetry and vice versa. When we consider a Skyrmion we look at its pion fields rather than the sources which generate them; the result above means that we can look at the symmetry found in the pion fields, calculate which combination of solid harmonics it represents and then know which combination of solid harmonics the generating source has. This makes it easier to determine which source generates the pion field.

3.3.3 Further Gaussian multipole sources

Currently we have exactly one Gaussian source for each multipole moment, but we would like to have more freedom when it comes to approximating Skyrmons and their interaction energies. Although the angular dependence of a source is fixed by the multipole moment, the radial dependence is not and it is here that we have room to introduce more sources. We require our sources to be regular at the origin which means that the degree in r must be at least the order of the spherical harmonic; however, this still allows us with sources of the form, $p(r^2)\mathcal{Y}_l^m(\theta, \phi)e^{-\frac{G}{2}r^2}$, where p is a polynomial in

r^2 . We choose the following basis for these polynomials,

$$\rho^{n,l,m}(G; \mathbf{x}) = \text{Rad}_n(G; r) \mathcal{Y}_l^m(\theta, \phi) e^{-\frac{G}{2}r^2}, \quad (3.37)$$

where $\text{Rad}_n(G; r) = (\nabla^{2n} e^{-\frac{G}{2}r^2}) e^{\frac{G}{2}r^2}$. $\text{Rad}_n(G; r)$ is a polynomial of degree n in r^2 and can be viewed as an analogue to the Hermite polynomials, with a slight difference because $\nabla^2 \neq \frac{\partial^2}{\partial r^2}$. Note that $\text{Rad}_0(G; r) = 1$ and therefore $\rho^{l,m}(G; \mathbf{x}) = \rho^{l,m,0}(G; \mathbf{x})$.

We now consider the generating source,

$$\rho_{gen}^n(G; \mathbf{x}) \equiv \text{Rad}_n(G; r) e^{-\frac{G}{2}(\mathbf{x} - \frac{v\mathbf{a}}{G})^2} = \left[\nabla_X^{2n} \left(e^{-\frac{G}{2}(\mathbf{x} + \mathbf{X})^2} e^{v\mathbf{a} \cdot \mathbf{x}} e^{-\frac{v^2 \mathbf{a} \cdot \mathbf{a}}{2G}} \right) \right]_{\mathbf{X}=\mathbf{0}} \quad (3.38)$$

$$= \left[\nabla_X^{2n} \left(e^{-v\mathbf{a} \cdot \mathbf{X}} e^{-\frac{G}{2}(\mathbf{x} + \mathbf{X} - \frac{v\mathbf{a}}{G})^2} \right) \right]_{\mathbf{X}=\mathbf{0}}, \quad (3.39)$$

where the first equality comes from expanding the bracket in the Gaussian and noticing that $\left[\nabla_X^{2n} e^{-\frac{G}{2}(\mathbf{x} + \mathbf{X})^2} \right]_{\mathbf{X}=\mathbf{0}} = \left[\nabla^{2n} e^{-\frac{G}{2}(\mathbf{x} + \mathbf{X})^2} \right]_{\mathbf{X}=\mathbf{0}} = \nabla^{2n} e^{-\frac{G}{2}r^2} = \text{Rad}_n(G; r) e^{-\frac{G}{2}r^2}$. The pion field that is generated by this source is,

$$\pi_{gen}^n(G; \mathbf{x}) = \left[\nabla_X^{2n} \left(e^{-v\mathbf{a} \cdot \mathbf{X}} f \left(G; \left| \mathbf{x} + \mathbf{X} - \frac{v\mathbf{a}}{G} \right| \right) \right) \right]_{\mathbf{X}=\mathbf{0}} \quad (3.40)$$

$$= \left[\left(v^2 (\mathbf{a} \cdot \mathbf{a}) - 2va_i \frac{\partial}{\partial X_i} + \nabla_X^2 \right)^n f \left(G; \left| \mathbf{x} + \mathbf{X} - \frac{v\mathbf{a}}{G} \right| \right) \right]_{\mathbf{X}=\mathbf{0}} \quad (3.41)$$

$$= \left(-2va_i \frac{\partial}{\partial x_i} + \nabla^2 \right)^n f \left(G; \left| \mathbf{x} - \frac{v\mathbf{a}}{G} \right| \right), \quad (3.42)$$

where the first equality follows from (3.34), the second equality follows from the Leibnitz rule and the third equality follows from $\mathbf{a} \cdot \mathbf{a} = 0$. Focusing on the powers of v that come from the bracketed term in (3.42), we find that the coefficient of v^p is

$$(-2)^p \binom{n}{p} a_{i_1} \dots a_{i_p} \frac{\partial^p}{\partial x_{i_1} \dots \partial x_{i_p}} \nabla^{2(n-p)} f \left(G; \left| \mathbf{x} - \frac{v\mathbf{a}}{G} \right| \right). \quad (3.43)$$

We now focus on the coefficient of the v^l term of the entire expression in (3.42) and require the remaining powers of v to come from the Taylor expansion of $f \left(G; \left| \mathbf{x} - \frac{v\mathbf{a}}{G} \right| \right)$, resulting in

$$\frac{(-1)^l (2)^p}{G^{l-p}} \binom{n}{p} a_{i_1} \dots a_{i_p} \frac{a_{i_{p+1}} \dots a_{i_l}}{(l-p)!} \frac{\partial^p}{\partial x_{i_1} \dots \partial x_{i_p}} \frac{\partial^{l-p}}{\partial x_{i_{p+1}} \dots \partial x_{i_l}} \nabla^{2(n-p)} f(G; r). \quad (3.44)$$

This expression is similar to equation (3.31) with some additional prefactors. We then sum over all possible p to get all possible contributions to the v^l term, and then focus

on the λ^m term to find that

$$\pi^{l,m,n}(G; \mathbf{x}) = \sum_{p=0}^{\min(l,n)} (-1)^l \frac{\mathcal{Y}_l^m(\theta, \phi)}{G^l} \left(\frac{1}{r} \frac{\partial}{\partial r} \right)^l \left((2G)^p p! \binom{n}{p} \binom{l}{p} \nabla^{2(n-p)} \right) f(G; r). \quad (3.45)$$

where $\pi^{l,m,n}(G; \mathbf{x})$ denotes the pion field that is generated by the source $\rho^{l,m,n}(G; \mathbf{x})$. Again the radial dependence decouples from the angular dependence which means that symmetry is carried over from the source to the generated pion field.

3.3.4 Asymptotics of Gaussian multipole pion fields

The asymptotics of the generated pion fields give the leading order contribution to the interaction energy so it is worthwhile considering how the asymptotics of $\pi^{l,m,n}(G; \mathbf{x})$ depend on l, m and n . First we consider the asymptotics of the function $f(G; r)$ as r tends to infinity,

$$f_\infty(G; r) = \lim_{r \rightarrow \infty} f(G; r) \sim \frac{e^{-\mu r}}{r}. \quad (3.46)$$

As we can see from equation (3.45), $\pi^{l,m,n}(G; \mathbf{x})$ involves two types of derivatives acting on $f(G; r)$: $\frac{1}{r} \frac{\partial}{\partial r}$ and ∇^2 . We now investigate the effect that each of these derivatives has on $f_\infty(G; r)$. For the derivative $\frac{1}{r} \frac{\partial}{\partial r}$,

$$\frac{1}{r} \frac{\partial}{\partial r} (f_\infty(G; r)) \sim \frac{1}{r} \frac{\partial}{\partial r} \left(\frac{e^{-\mu r}}{r} \right) \sim -\frac{\mu e^{-\mu r}}{r^2} - \frac{e^{-\mu r}}{r^3} \sim \frac{e^{-\mu r}}{r^2}. \quad (3.47)$$

We see that $\frac{1}{r} \frac{\partial}{\partial r}$ has the effect of reducing the power of r by one and this works iteratively such that $\left(\frac{1}{r} \frac{\partial}{\partial r} \right)^l$ reduces the power of r by l . For the derivatives ∇^2 ,

$$\nabla^2 (f_\infty(G; r)) \sim \frac{1}{r^2} \frac{\partial}{\partial r} \left(r^2 \frac{\partial}{\partial r} \left(\frac{e^{-\mu r}}{r} \right) \right) \sim \frac{\mu^2 e^{-\mu r}}{r} - \frac{2\mu e^{-\mu r}}{r^2} \sim \frac{e^{-\mu r}}{r}. \quad (3.48)$$

We see that ∇^2 has no effect on $f_\infty(G; r)$ and thus neither does ∇^{2p} for any value of p .

$\pi^{l,m,n}(G; \mathbf{x})$ has l derivatives of the form $\frac{1}{r} \frac{\partial}{\partial r}$, l powers of r coming from the solid harmonics and a varying number of derivatives of the form ∇^2 . The combination of the two results above show that,

$$\pi^{l,m,n}(G; \mathbf{x}) \sim \frac{e^{-\mu r}}{r}, \quad (3.49)$$

as r tends to infinity. This means that the asymptotics of the pion field is independent of n, l and m which shows the importance of considering a large range of sources rather than just those with small values of l and n .

Notice, how this changes if we consider a Coulomb rather than Yukawa interaction (setting μ equal to zero). Now equation (3.47) shows that the leading order terms vanish and that the orders of r in the asymptotics of the pion field would decrease as the order of the multipole increases. Equation (3.48) shows that $\nabla^2 (f_\infty(G; r)) = 0$ and that therefore $\pi^{l,m,n}(G; \mathbf{x})$ is asymptotically zero for n not equal to 0 (this is equivalent to the fact that Coulomb multipoles are traceless). In combination this shows the importance of considering ‘higher order terms’ for a Yukawa interaction as opposed to focusing on the leading order terms for a Coulomb interaction.

3.3.5 Interaction energies between Gaussian multipole sources

We have shown that for a given Gaussian multipole source we can obtain an analytic expression for its generated pion field. However, the main focus of this chapter is the approximation of interaction energies to aid vibrational quantization and the evaluation of energies of cluster nuclei. Fortunately the process for calculating the interaction energy between Gaussian sources is rather similar to the one used to generate pion fields.

Recall that the interaction energy between two sources separated by \mathbf{R} has the integral expression,

$$E_{int}(\mathbf{R}) = - \int d^3\mathbf{x} d^3\mathbf{y} \rho_1(\mathbf{x}) \rho_2(\mathbf{x} - \mathbf{R} + \mathbf{y}) \frac{e^{-\mu|\mathbf{y}|}}{4\pi|\mathbf{y}|}. \quad (3.50)$$

We now consider two generating sources of the form,

$$\rho_{1,gen}(G; \mathbf{x}) = e^{-\frac{G}{2}(\mathbf{x} - \frac{v\mathbf{a}}{G})^2} \text{ and } \rho_{2,gen}(H; \mathbf{x}) = e^{-\frac{H}{2}(\mathbf{x} - \frac{v\mathbf{A}}{H})^2}, \quad (3.51)$$

where

$$\mathbf{a} = \left(-\frac{\lambda}{2} + \frac{1}{2\lambda}, -i \left(\frac{\lambda}{2} + \frac{1}{2\lambda} \right), 1 \right) \text{ and } \mathbf{A} = \left(-\frac{\Lambda}{2} + \frac{1}{2\Lambda}, -i \left(\frac{\Lambda}{2} + \frac{1}{2\Lambda} \right), 1 \right) \quad (3.52)$$

such that $\mathbf{a} \cdot \mathbf{a} = \mathbf{A} \cdot \mathbf{A} = 0$. Note that

$$\mathbf{a} \cdot \mathbf{A} = 1 - \frac{\lambda}{2\Lambda} - \frac{\Lambda}{2\lambda}, \quad (3.53)$$

which is generically non-zero.

We will only work through the derivation for sources with $n = 0$ for the sake of brevity; however, the derivation is easily generalized to $n \neq 0$ and we state the result for all n at the end. Again we perform the integral using generating sources, which package the solid harmonics into a convenient form, and then extract the result for solid harmonics afterwards. Plugging the sources $\rho_{1,gen}(G; \mathbf{x})$ and $\rho_{2,gen}(H; \mathbf{x})$ into (3.50) to calculate a generating interaction energy, we find

$$E_{gen}(\mathbf{R}) = - \int d^3\mathbf{x} d^3\mathbf{y} e^{-\frac{G}{2}(\mathbf{x} - \frac{v\mathbf{a}}{G})^2} e^{-\frac{H}{2}(\mathbf{x} - \mathbf{R} + \mathbf{y} - \frac{V\mathbf{A}}{H})^2} \frac{e^{-\mu|\mathbf{y}|}}{4\pi|\mathbf{y}|} \quad (3.54)$$

$$= - \int d^3\mathbf{y} \left(\frac{\pi}{G+H} \right)^{\frac{3}{2}} e^{-\frac{GH}{G+H}(\mathbf{y} - \mathbf{R} - \frac{v\mathbf{a}}{G} + \frac{V\mathbf{A}}{H})^2} \frac{e^{-\mu|\mathbf{y}|}}{4\pi|\mathbf{y}|} \quad (3.55)$$

$$= \left(\frac{\pi}{G+H} \right)^{\frac{3}{2}} f \left(\frac{GH}{G+H}; \left| \mathbf{R} - \frac{v\mathbf{a}}{G} + \frac{V\mathbf{A}}{H} \right| \right). \quad (3.56)$$

The first equality comes from integrating the product of the two Gaussians, which creates another Gaussian. The subsequent integral is of the form that we have been dealing with for the pion fields and so we use (3.17) for the final equality.

In direct analogy with the pion field derivation, in order to calculate the interaction energy between sources $\rho^{l,m,0}(G; \mathbf{x})$ and $\rho^{L,M,0}(H; \mathbf{x} - \mathbf{R})$, as defined in (3.20), we must focus on the coefficient of $v^l V^L$ in $E_{gen}(\mathbf{R})$,

$$\frac{(-1)^l}{G^l H^L l! L!} a_{i_1} \dots a_{i_l} A_{j_1} \dots A_{j_L} \frac{\partial^l}{\partial R_{i_1} \dots \partial R_{i_l}} \frac{\partial^L}{\partial R_{j_1} \dots \partial R_{j_L}} f \left(\frac{GH}{G+H}; R \right). \quad (3.57)$$

To calculate the pion field generated by a Gaussian multipole source we relied upon the fact that $\mathbf{a} \cdot \mathbf{a} = 0$, which is again a crucial aspect of our derivation of the interaction energy; however, we have an added complication because, although $\mathbf{a} \cdot \mathbf{a} = 0$ and $\mathbf{A} \cdot \mathbf{A} = 0$, $\mathbf{a} \cdot \mathbf{A}$ is non-zero.

Let us suppose that $l \geq L$ and apply all of the R_i derivatives first; these derivatives are all dotted with \mathbf{a} and so must all act radially to avoid the creation of Kronecker deltas (as for the pion field derivation in equation (3.32)),

$$\frac{(-1)^l}{G^l H^L l! L!} a_{i_1} \dots a_{i_l} A_{j_1} \dots A_{j_L} \frac{\partial^L}{\partial R_{j_1} \dots \partial R_{j_L}} \left(R_{i_1} \dots R_{i_l} \left(\frac{1}{R} \frac{\partial}{\partial R} \right)^l f \right). \quad (3.58)$$

The R_j derivatives can either act on one of the R_i 's (creating a δ_{ij}) or act on f radially (we will suppress the argument of f from now on for brevity). Note that a

Kronecker delta with one i index and one j index is permitted because this creates an $\mathbf{a} \cdot \mathbf{A}$ term in equation (3.58) which is non-zero. Let us consider the terms where $k \frac{\partial}{\partial R_j}$ derivatives act on k different R_i 's, giving

$$\frac{(-1)^l}{G^l H^L k! (l-k)! k! (L-k)!} (\mathbf{a} \cdot \mathbf{R})^{l-k} (\mathbf{A} \cdot \mathbf{R})^{L-k} (\mathbf{a} \cdot \mathbf{A})^k \left(\frac{1}{R} \frac{\partial}{\partial R} \right)^{l+L-k} f. \quad (3.59)$$

We now substitute in the explicit expressions for the dot products, using a combination of (3.24) and (3.53), to obtain,

$$\sum_{m,M} \frac{4\pi (-1)^l C_{lmLMk}}{G^l H^L k! k!} \left(1 - \frac{\lambda}{2\Lambda} - \frac{\Lambda}{2\lambda} \right)^k \lambda^m \Lambda^M \mathcal{Y}_{l-k}^m \mathcal{Y}_{L-k}^M \left(\frac{1}{R} \frac{\partial}{\partial R} \right)^{l+L-k} f \quad (3.60)$$

where

$$C_{lmLMk} = \sqrt{\frac{(2(l-k)+1)(l-k+m)!(l-k-m)!}{(2(L-k)+1)(L-k+M)!(L-k-M)!}} \quad (3.61)$$

and the sums over m and M are between $\pm(l-k)$ and $\pm(L-k)$ respectively. Note that the arguments of all solid harmonics in this derivation are θ and ϕ such that the separation vector $\mathbf{R} = (R, \theta, \phi)$ in spherical polars. If we now expand the bracket in (3.60), we get the expression,

$$\sum_{m,M,i,j} \frac{4\pi (-1)^l C_{lmLMk}}{G^l H^L k!} \frac{(-1)^{i+j} \lambda^{m+i-j} \Lambda^{M-i+j}}{2^{i+j} (k-i-j)! i! j!} \mathcal{Y}_{l-k}^m \mathcal{Y}_{L-k}^M \left(\frac{1}{R} \frac{\partial}{\partial R} \right)^{l+L-k} f, \quad (3.62)$$

where i goes between 0 and k and j goes between 0 and $k-i$. We then read off the coefficient of $\lambda^m \Lambda^M$ in (3.62) to find the interaction energy between the sources $\rho^{l,m,0}(G; \mathbf{x})$ and $\rho^{L,M,0}(H; \mathbf{x} - \mathbf{R})$,

$$\sum_{k=0}^{\min(l,L)} \sum_{i,j} \left(\frac{\pi}{G+H} \right)^{\frac{3}{2}} \frac{(-1)^{l+i+j}}{G^l H^L k! (k-i-j)! i! j!} \frac{C_{lmLMk}}{C_{lmLM0}} \mathcal{Y}_{l-k}^{m-i+j} \mathcal{Y}_{L-k}^{M+i-j} \left(\frac{1}{R} \frac{\partial}{\partial R} \right)^{l+L-k} f. \quad (3.63)$$

If we now wish to calculate the interaction energy between the two sources, $\rho^{l,m,n}(G; \mathbf{x})$ and $\rho^{L,m,n}(H; \mathbf{x} - \mathbf{R})$, as defined in equation (3.37), then it can be shown that we simply perform the replacement,

$$f \rightarrow \sum_{p=0}^{\min(l,n)} \sum_{P=0}^{\min(L,N)} \left((2G)^p (2H)^P p! P! \binom{n}{p} \binom{N}{P} \binom{l}{p} \binom{L}{P} (\nabla^2)^{n+N-p-P} \right) f, \quad (3.64)$$

in equation (3.63).

Although equation (3.63) looks rather complicated, it does provide an analytic expression for the interaction energy between any two multipole Gaussian sources enabling us to quickly generate the interaction energy for the whole range of separations and orientations of the Skyrmions.

3.4 Modeling Skyrmions

In this section we look at the process for the modelling the pion fields of Skyrmions and apply this to the first four Skyrmions.

3.4.1 Calibration of coefficients

We use our Gaussian multipole sources as a basis for the source of a particular Skyrmion, such that,

$$\rho(\mathbf{x}) = \sum_{l,m,n} a_{l,m,n} \rho^{l,m,n}(G_{l,m,n}; \mathbf{x}), \quad (3.65)$$

where $\rho(\mathbf{x})$ is the source which generates a pion field, $\pi(\mathbf{x})$, of the Skyrmion. Note that the $G_{l,m,n}$ which features in the sources $\rho^{l,m,n}(G_{l,m,n}; \mathbf{x})$ may vary for different values of l, m and n . The process of modeling a Skyrmion now comes down to choosing the coefficients, $a_{l,m,n}$, in this expansion and to do this we need to decide which characteristics of the Skyrmion we would like to capture in our approximation.

One important aspect is the symmetry of the Skyrmion because if we want to quantize the Skyrmion then its symmetries decide which spin states it allows. Another important aspect is the multipole moment; these decide how the pion field behaves at large r and determine the leading order contribution to the interaction energy at large separations. These two aspects are strongly interlinked; the multipole moments of a Skyrmion determine its symmetries at large r . Therefore if we capture the multipole behavior of the Skyrmion we get its symmetries as well for free. Skyrmions interact via a Yukawa interaction at large separations so we start by considering the multipole expansion of the Yukawa potential [39],

$$-\frac{e^{-\mu|\mathbf{x}-\mathbf{y}|}}{4\pi|\mathbf{x}-\mathbf{y}|} = -\mu \sum_{l=0}^{\infty} \sum_{m=-l}^l i_l(\mu R) k_l(\mu r) Y_l^m(\theta, \phi) Y_l^{-m}(\alpha, \beta), \quad (3.66)$$

where $\mathbf{x} = (r, \theta, \phi)$, $\mathbf{y} = (R, \alpha, \beta)$ and $R > r$. $i_l(r)$ and $k_l(r)$ are the modified spherical Bessel functions of the first and second kind respectively and can be expressed in terms of hyperbolic trigonometric functions. Recall that the pion field, $\pi(\mathbf{x})$, for a source,

$\rho(\mathbf{x})$, is determined by

$$\pi(\mathbf{x}) = - \int d^3\mathbf{y} \rho(\mathbf{y}) \frac{e^{-\mu|\mathbf{x}-\mathbf{y}|}}{4\pi|\mathbf{x}-\mathbf{y}|}. \quad (3.67)$$

Combining (3.66) and (3.67) we see that,

$$\pi(\mathbf{x}) = \sum_{l=0}^{\infty} \sum_{m=-l}^l M_l^m k_l(\mu r) Y_l^m(\theta, \phi), \quad (3.68)$$

where we have the multipole moment,

$$M_l^m = -\mu \int \rho(\mathbf{y}) i_l(\mu R) Y_l^{-m}(\alpha, \beta) d^3\mathbf{y}. \quad (3.69)$$

Recalling that our basis sources are of the form,

$$\rho^{l,m,n}(G; \mathbf{x}) = \text{Rad}_n(G; r) \mathcal{Y}_l^m(\theta, \phi) e^{-\frac{G}{2}r^2}, \quad (3.70)$$

orthogonality of the spherical harmonics implies that the multipole moment M_l^m only receives contributions from the sources, $\rho^{l,m,n}(G; \mathbf{x})$, where n is allowed to vary. For highly symmetric Skyrmions many of the multipole moments, M_l^m , are zero which means that the corresponding coefficients, $a_{l,m,n}$, are all zero as well. The most obvious way to calculate the moments which are not zero would be to use (3.69) directly; however this integral involves the source whereas for a Skyrmion it is the pion fields which are fundamental. This means that instead we invert (3.68) to calculate the multipole moments for a Skyrmion, giving the formula,

$$M_l^m(r) = \frac{\int \pi(\mathbf{x}) Y_l^{-m}(\theta, \phi) \sin \theta d\theta d\phi}{k_l(\mu r)}. \quad (3.71)$$

This gives us a multipole moment which depends on r , the radius of the spherical shell that we are integrating over); we then take r to infinity to get the multipole moment M_l^m .

Taking the limit of $M_l^m(r)$ as $r \rightarrow \infty$ ensures that our approximation matches the Skyrmion asymptotically and guarantees that the interaction energy will be correct to leading order for well separated Skyrmions. However we still have some freedom in our approximation; calibrating to the multipole moment M_l^m just gives us a constraint which the coefficients, $a_{l,m,n}$, must satisfy (which we usually enforce by expressing $a_{l,m,0}$ in terms of the other $a_{l,m,n}$ coefficients). We can use (3.71) to calculate $M_l^m(r)$ for both the actual Skyrmion and for our approximation of the Skyrmion and then compare these two functions for all r . In practice we choose the coefficients, $a_{l,m,n}$, to minimize

the absolute difference between the approximate and actual function, $M_l^m(r)$, across the whole range of r ; further details of this process will be provided in subsection 3.4.5 where we model the $B = 4$ Skyrmion. Of particular importance is how we decide to truncate the series in (3.65), that is, how we decide how many non-zero $a_{l,m,n}$ we will include for each value of l and m .

We will now detail our approximations for the pion fields of the first four Skyrmions, starting with the $B = 1$ Skyrmion.

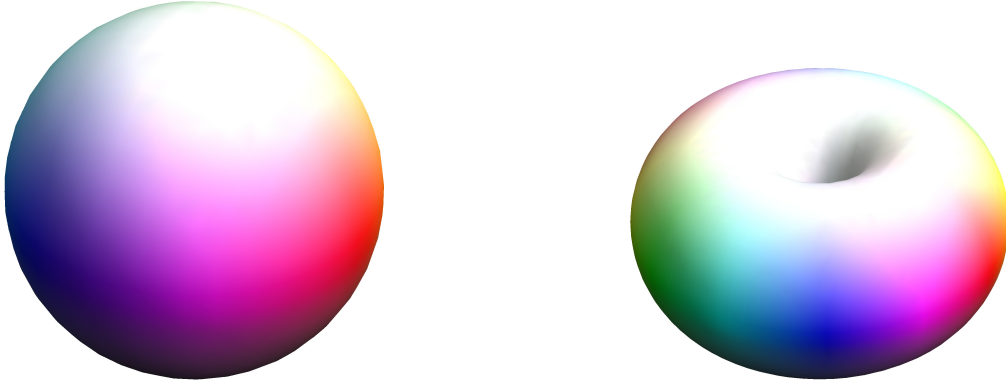


Fig. 3.1 The $B = 1$ and $B = 2$ Skyrmions.

3.4.2 The $B = 1$ Skyrmion

The $B = 1$ Skyrmion is a hedgehog solution, meaning that the vector of pion fields (and corresponding sources) always points radially outwards. It is very well approximated by a set of dipole moments and the spherical symmetry means that any two pion fields can be found in terms of the third. As a result the sources of the $B = 1$ Skyrmion can be very closely approximated using just two parameters, A_1 and G_1 . We use the sources

$$\rho_1(\mathbf{x}) = \frac{A_1}{\sqrt{2}} \left(\rho^{1,-1,0}(G_1; \mathbf{x}) - \rho^{1,1,0}(G_1; \mathbf{x}) \right) = \frac{A_1}{2} \sqrt{\frac{3}{\pi}} x e^{-\frac{G_1}{2} r^2}, \quad (3.72)$$

$$\rho_2(\mathbf{x}) = \frac{iA_1}{\sqrt{2}} \left(\rho^{1,1,0}(G_1; \mathbf{x}) + \rho^{1,-1,0}(G_1; \mathbf{x}) \right) = \frac{A_1}{2} \sqrt{\frac{3}{\pi}} y e^{-\frac{G_1}{2} r^2}, \quad (3.73)$$

$$\rho_3(\mathbf{x}) = A_1 \rho^{1,0,0}(G_1; \mathbf{x}) = \frac{A_1}{2} \sqrt{\frac{3}{\pi}} z e^{-\frac{G_1}{2} r^2}, \quad (3.74)$$

where $\rho_i(\mathbf{x})$ denotes the source which generates the pion field $\pi_i(\mathbf{x})$.

Using the calibration scheme in subsection 3.4.1, we find that $G_1 = 3.72$, ($A_1 = -68.2$), where A_1 has been put in brackets because it is determined by G_1 and the dipole moment of the $B = 1$ Skyrmion.

The spherical symmetry of the $B = 1$ Skyrmion means that we can write its pion fields in the following way,

$$\boldsymbol{\pi}(\mathbf{x}) = (\pi_1(\mathbf{x}), \pi_2(\mathbf{x}), \pi_3(\mathbf{x})) = \sin g(r) \hat{\mathbf{x}} \quad (3.75)$$

where $g(r)$ is called the radial profile function. Using (3.34), we obtain the following approximation for the pion fields for the $B = 1$ Skyrmion:

$$\boldsymbol{\pi}(\mathbf{x}) = \frac{A_1}{2G_1} \sqrt{\frac{3}{\pi}} \frac{\partial f(G_1; r)}{\partial r} \hat{\mathbf{x}} = \sin g_A(r) \hat{\mathbf{x}}, \quad (3.76)$$

where $g_A(r)$ is the radial profile function obtained via our approximation. In order to assess the accuracy of our approximation of the $B = 1$ Skyrmion we need only compare the radial profile functions (or their sines). To this end, in Figure 3.2 we plot $\frac{\sin g_A(r) - \sin g(r)}{\sin g(r)}$ (where $\sin g(r)$ is taken from the numerical solution of a $B = 1$ Skyrmion) against r to find the relative error of our approximation.

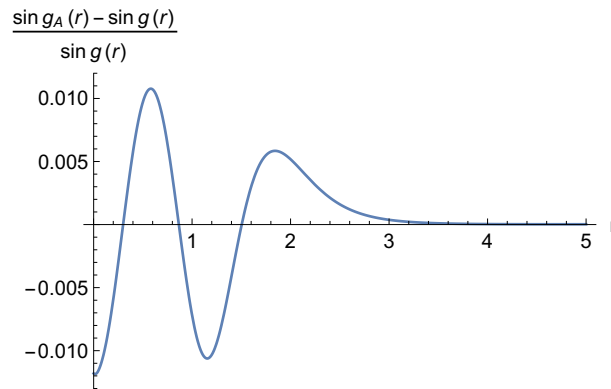


Fig. 3.2 The relative error of the function $\sin g_A(r)$

The relative error is always less than 1.2% and so, whilst the purpose of this chapter is to discuss the interaction energy between Skyrmions, we have managed to find a very close approximation to the pion field of $B = 1$ Skyrmion. Although this fit could be further improved by including more non-zero coefficients we believe that the simplicity gained from using the smallest possible number of parameters outweighs any slight improvement in accuracy.

Explicitly the formula for the sine of the radial profile function for our approximation of the $B = 1$ Skyrmion is,

$$\sin g_A(r) = \frac{\sqrt{3}A_1}{8G_1^{\frac{5}{2}}r^2} \left(\begin{array}{c} -\frac{2\sqrt{2G_1}}{\sqrt{\pi}}re^{-\frac{G_1}{2}r^2} + e^{-\mu r}e^{\frac{\mu^2}{2G_1}}(\mu r + 1)\operatorname{erfc}\left(\frac{\mu - G_1 r}{\sqrt{2G_1}}\right) \\ + e^{\mu r}e^{\frac{\mu^2}{2G_1}}(\mu r - 1)\operatorname{erfc}\left(\frac{\mu + G_1 r}{\sqrt{2G_1}}\right) \end{array} \right).$$

3.4.3 The $B = 2$ Skyrmion

The $B = 2$ Skyrmion is toroidal and this axial symmetry means that the $\rho_1(\mathbf{x})$ and $\rho_2(\mathbf{x})$ sources are rotations of one another and both can be well described by quadrupole moments. The distinct $\rho_3(\mathbf{x})$ source corresponds to the axial direction and has a dipole and octupole contribution. The sources are as follows

$$\rho_1(\mathbf{x}) = \frac{A_2}{\sqrt{2}}(\rho^{2,-2,0}(G_2; \mathbf{x}) + \rho^{2,2,0}(G_2; \mathbf{x})) = \sqrt{\frac{15}{\pi}} \frac{A_2}{4}(x^2 - y^2)e^{-\frac{G_2}{2}r^2}, \quad (3.77)$$

$$\rho_2(\mathbf{x}) = \frac{iA_2}{\sqrt{2}}(\rho^{2,-2,0}(G_2; \mathbf{x}) - \rho^{2,2,0}(G_2; \mathbf{x})) = -\sqrt{\frac{15}{\pi}} \frac{A_2}{2}xye^{-\frac{G_2}{2}r^2}, \quad (3.78)$$

$$\begin{aligned} \rho_3(\mathbf{x}) &= B_2\rho^{3,0,1}(H_2; \mathbf{x}) + C_2\rho^{3,0,0}(H_2; \mathbf{x}) + D_2\rho^{1,0,1}(I_2; \mathbf{x}) + E_2\rho^{1,0,0}(I_2; \mathbf{x}) \\ &= \frac{1}{4}\sqrt{\frac{7}{\pi}}(H_2B_2r^2 + (C_2 - 3B_2))z(5z^2 - 3r^2)e^{-\frac{H_2}{2}r^2} \\ &\quad + \frac{1}{2}\sqrt{\frac{3}{\pi}}(I_2D_2r^2 + (E_2 - 3D_2))ze^{-\frac{I_2}{2}r^2}, \end{aligned} \quad (3.79)$$

where $G_2 = 3.01$, $I_2 = 3.28$, $H_2 = 3.65$, $B_2 = 3.76$, $D_2 = -14.0$ ($A_2 = -85.9$, $C_2 = 33.1$, $E_2 = -72.3$).

The pion fields generated by these sources have more interesting angular dependence than the $B = 1$ case and so we now consider contour plots in order to check the accuracy of our approximation. For all of the contour plots in this section, the left plot is the numerical Skyrmion's pion field and the right plot is our approximation of the pion field. Contours are taken between -0.9 and 0.9 at intervals of 0.2 unless stated otherwise.

The axial symmetry of the $B = 2$ Skyrmion means we need only show contour plots in the $x - z$ plane because the rest of the pion fields of the Skyrmion can be extrapolated from this. We plot π_1 in Figure 3.3 and π_3 in Figure 3.4 and find a good agreement between the numerical and approximate fields in both cases

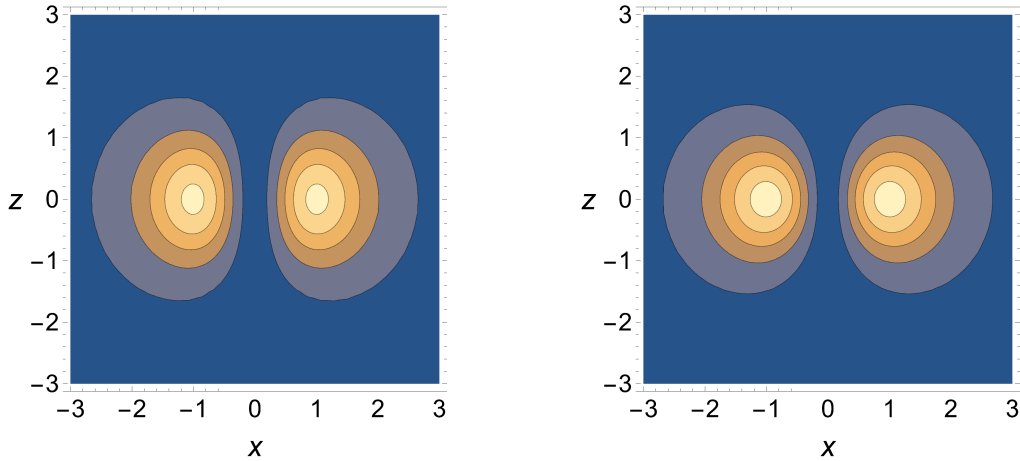


Fig. 3.3 The numerical and approximate π_1 field in the $x - z$ plane for the $B = 2$ Skyrmion.

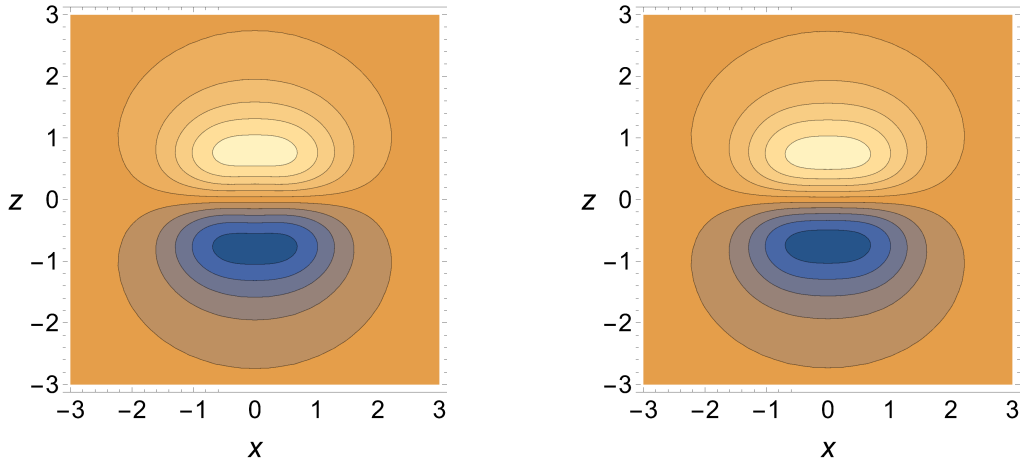


Fig. 3.4 The numerical and approximate π_3 field in the $x - z$ plane for the $B = 2$ Skyrmion.

3.4.4 The $B = 3$ Skyrmion

If the $B = 3$ Skyrmion is rotated and isorotated into the configuration shown in Figure 3.5, then all three of the pion fields are the same up to rotation; the trade off is that now each pion field involves a dipole, quadrupole and octupole moment. The source $\rho_3(\mathbf{x})$ can be expressed as,

$$\begin{aligned} \rho_3(\mathbf{x}) = & A_3 \rho^{3,0,1}(G_3; \mathbf{x}) + B_3 \rho^{3,0,0}(G_3; \mathbf{x}) + \frac{iC_3}{\sqrt{2}} \left(\rho^{2,2,0}(H_3; \mathbf{x}) - \rho^{2,-2,0}(H_3; \mathbf{x}) \right) \\ & + D_3 \rho^{1,0,1}(I_3; \mathbf{x}) + E_3 \rho^{1,0,0}(I_3; \mathbf{x}) \end{aligned}$$

$$\begin{aligned}
&= \frac{1}{4} \sqrt{\frac{7}{\pi}} (G_{33} A_3 r^2 + (B_3 - 3A_3)) z (5z^2 - 3r^2) e^{-\frac{G_3}{2} r^2} - \sqrt{\frac{15}{\pi}} \frac{C_3}{2} x y e^{-\frac{H_3}{2} r^2} \\
&+ \frac{1}{2} \sqrt{\frac{3}{\pi}} (G_{31} D_3 r^2 + (E_3 - 3D_3)) z e^{-\frac{I_3}{2} r^2}.
\end{aligned} \tag{3.80}$$

where $I_3 = 2.81$, $H_3 = 2.48$, $G_3 = 2.58$, $D_3 = 6.83$, $A_3 = -1.44$, ($E_3 = 21.0$, $C_3 = -58.4$, $B_3 = 38.7$). $\rho_1(\mathbf{x})$ and $\rho_2(\mathbf{x})$ can be found by replacing (x, y, z) with (y, z, x) and (z, x, y) respectively.

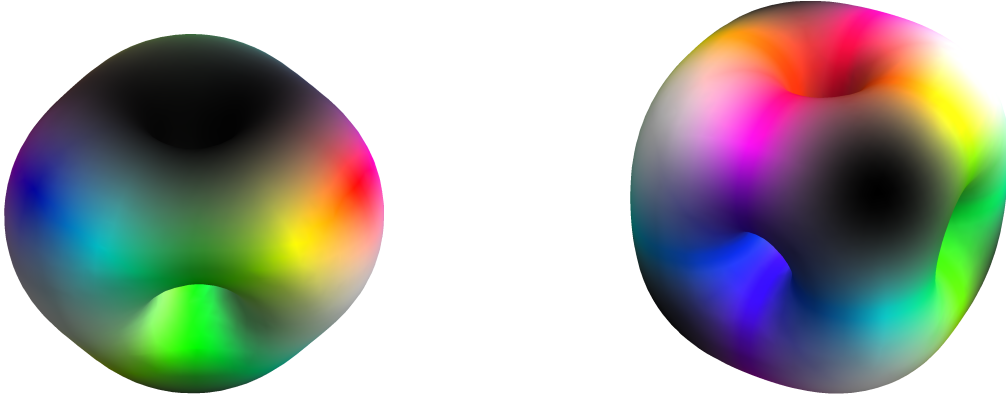


Fig. 3.5 The $B = 3$ and $B = 4$ Skyrmions.

We plot contours of the π_3 field in the $x - y$ (Figure 3.6) and $z = 0.75$ (Figure 3.7) planes and find that there is good agreement between the numerical and approximate fields. Given the symmetries of the $B = 3$ Skyrmion this is sufficient to show that there is good agreement for the all pion fields of the whole Skyrmion.

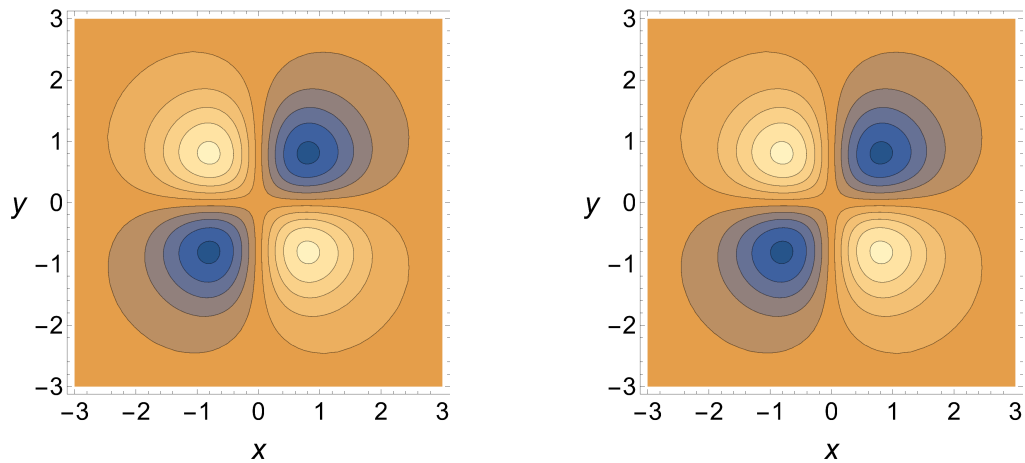


Fig. 3.6 The numerical and approximate π_3 field in the $x - y$ plane for the $B = 3$ Skyrmion.

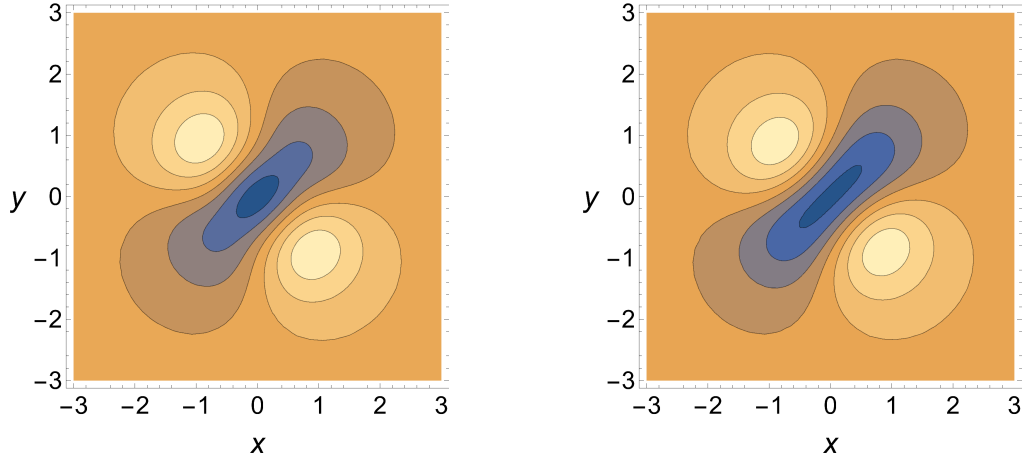


Fig. 3.7 The numerical and approximate π_3 field in the $z = 0.75$ plane for the $B = 3$ Skyrmion.

3.4.5 The $B = 4$ Skyrmion

The $B = 4$ Skyrmion corresponds to a Helium-4 nucleus or alpha particle; its high binding energy means that it is frequently observed as a building block for larger nuclei (particularly $B = 4N$ Skyrmions). If we can approximate the $B = 4$ Skyrmion and the interaction energy between two of them accurately then we will be able to get insight into these larger nuclei.

One of the reasons that the $B = 4$ Skyrmion has comparatively low energy is because of its cubic symmetry which we need to capture in our approximation. The cubic symmetry means that $\rho_1(\mathbf{x})$ and $\rho_2(\mathbf{x})$ are related and have quadrupole and hexadecapole moments, whereas $\rho_3(\mathbf{x})$ has an octupole moment. We use the sources

$$\begin{aligned}
\rho_1(\mathbf{x}) &= \frac{A_4}{4} \left(\sqrt{14}\rho^{4,4,1}(G_4; \mathbf{x}) - 2\sqrt{5}\rho^{4,0,1}(G_4; \mathbf{x}) + \sqrt{14}\rho^{4,-4,1}(G_4; \mathbf{x}) \right) \\
&+ \frac{B_4}{4} \left(\sqrt{14}\rho^{4,4,0}(G_4; \mathbf{x}) - 2\sqrt{5}\rho^{4,0,0}(G_4; \mathbf{x}) + \sqrt{14}\rho^{4,-4,0}(G_4; \mathbf{x}) \right) \\
&+ \sqrt{3}C_4\rho^{2,0,1}(H_4; \mathbf{x}) + \sqrt{3}D_4\rho^{2,0,0}(H_4; \mathbf{x}) \\
&= \frac{3}{8}\sqrt{\frac{5}{\pi}}(G_4A_4r^2 + (B_4 - 3A_4))(x^4 + y^4 - 2z^4 + 6x^2z^2 + 6y^2z^2 - 12x^2y^2)e^{-\frac{G_4}{2}r^2} \\
&+ \frac{1}{4}\sqrt{\frac{15}{\pi}}(H_4C_4r^2 + (D_4 - 3C_4))(2z^2 - x^2 - y^2)e^{-\frac{H_4}{2}r^2}, \tag{3.81}
\end{aligned}$$

$$\rho_2(\mathbf{x}) = \frac{A_4}{\sqrt{2}} \left(\rho^{4,2,1}(G_4; \mathbf{x}) + \rho^{4,-2,1}(G_4; \mathbf{x}) \right) + \frac{B_4}{\sqrt{2}} \left(\rho^{4,2,0}(G_4; \mathbf{x}) + \rho^{4,-2,0}(G_4; \mathbf{x}) \right)$$

$$\begin{aligned}
& + \frac{C_4}{\sqrt{2}} \left(\rho^{2,2,1}(H_4; \mathbf{x}) + \rho^{2,-2,1}(H_4; \mathbf{x}) \right) + \frac{D_4}{\sqrt{2}} \left(\rho^{2,2,0}(H_4; \mathbf{x}) + \rho^{2,-2,0}(H_4; \mathbf{x}) \right) \\
& = \frac{3}{8} \sqrt{\frac{5}{\pi}} (G_4 A_4 r^2 + (B_4 - 3A_4)(x^2 - y^2)(6z^2 - x^2 - y^2)) e^{-\frac{G_4}{2} r^2} \\
& + \frac{1}{4} \sqrt{\frac{15}{\pi}} (H_4 C_4 r^2 + (D_4 - 3C_4)(x^2 - y^2)) e^{-\frac{H_4}{2} r^2}, \tag{3.82}
\end{aligned}$$

$$\begin{aligned}
\rho_3(\mathbf{x}) & = -\frac{iE_4}{\sqrt{2}} (\rho^{3,2,1}(I_4; \mathbf{x}) - \rho^{3,-2,1}(I_4; \mathbf{x})) - \frac{iF_4}{\sqrt{2}} (\rho^{3,2,0}(I_4; \mathbf{x}) - \rho^{3,-2,0}(I_4; \mathbf{x})) \\
& = \frac{1}{2} \sqrt{\frac{105}{\pi}} (I_4 E_4 r^2 + (F_4 - 3E_4)xyz) e^{-\frac{I_4}{2} r^2}, \tag{3.83}
\end{aligned}$$

where $H_4 = 2.75$, $G_4 = 3.03$, $I_4 = 2.88$, $C_4 = -11.3$, $A_4 = -1.30$, $E_4 = -10.6$ ($D_4 = -36.0$, $B_4 = -17.9$, $F_4 = 85.7$).

In Figures 3.8 and 3.9 we look at contours in the $x - y$ plane for the π_1 and π_2 fields respectively. We look at contours for the π_3 field in the $z = 0.75$ plane because this is around where some of the corners of the $B = 4$ Skyrmion lie and where the π_3 field has greatest magnitude. These contours are plotted in Figure 3.10. We see from all three contour plots that there is good agreement between the numerical and approximate pion fields.

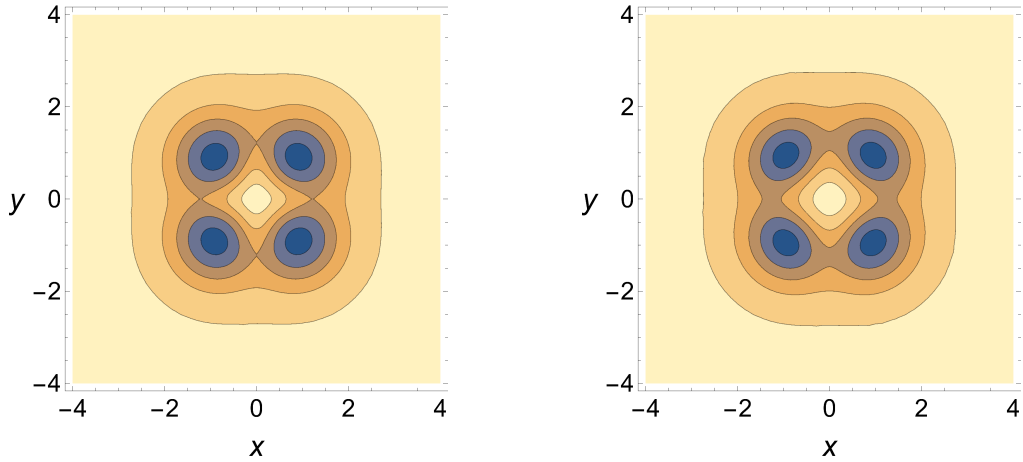


Fig. 3.8 The numerical and approximate π_1 field in the $x - y$ plane for the $B = 4$ Skyrmion.

We will now take a closer look at how calibration works for the example of the ρ_3 source of the $B = 4$ Skyrmion for which the multipole moments are $M_3^{-2} = M_3^2 = 1.38i$,

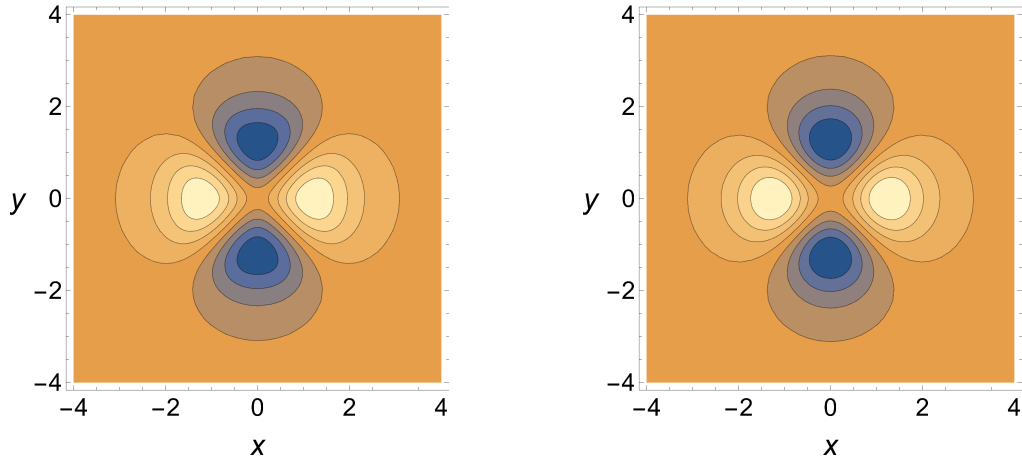


Fig. 3.9 The numerical and approximate π_2 field in the $x - z$ plane for the $B = 4$ Skyrmion.

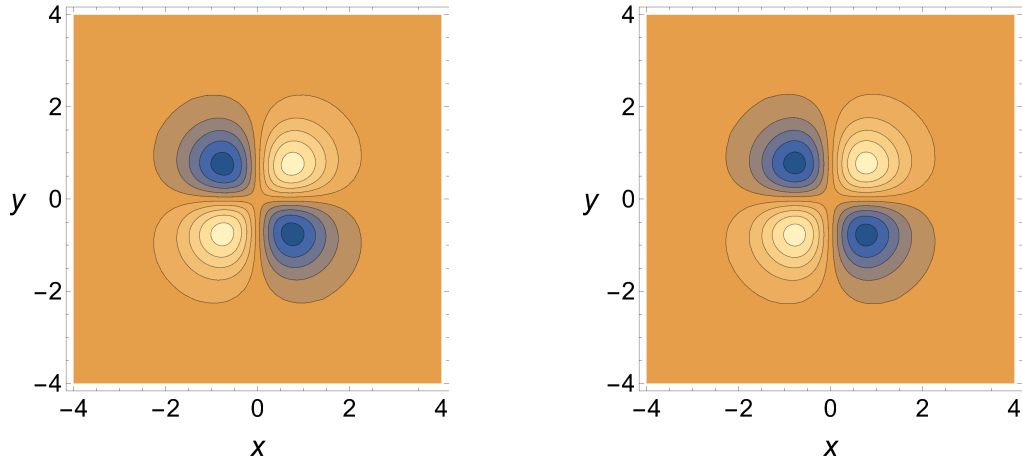


Fig. 3.10 The numerical and approximate π_3 field in the $z = 0.75$ plane for the $B = 4$ Skyrmion.

otherwise 0. If we allow more coefficients than in (3.83) then:

$$\begin{aligned}
 \rho_3(\mathbf{x}) &= X_4(\rho_{3,-2,2}(\mathbf{x}; I_4) - \rho_{3,2,2}(\mathbf{x}; I_4)) + E_4(\rho_{3,-2,1}(\mathbf{x}; I_4) - \rho_{3,2,1}(\mathbf{x}; I_4)) \\
 &\quad + F_4(\rho_{3,-2,0}(\mathbf{x}; I_4) - \rho_{3,2,0}(\mathbf{x}; I_4)) \\
 &= \frac{1}{2} \sqrt{\frac{105}{\pi}} (I_4^2 X_4 r^4 + I_4 (E_4 - 10X_4) r^2 + (F_4 - 3E_4 + 15X_4) x y z e^{-\frac{I_4}{2} r^2}) \quad (3.84)
 \end{aligned}$$

We put this source into (3.69) to find that

$$M_3^{-2} = \frac{\sqrt{\pi}\mu^4 i}{2|I_4|^{\frac{9}{2}}} e^{\frac{\mu^2}{2I_4}} \left(F_4 + E_4 \left(6 + \frac{\mu^2}{I_4} \right) + X_4 \left(24 + \frac{12\mu^2}{I_4} + \frac{\mu^4}{I_4^2} \right) \right). \quad (3.85)$$

It is helpful to use (3.85) to express one of the coefficients, F_4 , E_4 , X_4 , in terms of the other coefficients and the multipole moment, M_3^{-2} . This is to incorporate the fact that the multipole moment is fixed. We choose to express F_4 in terms of the other coefficients and the multipole moment,

$$F_4 = \frac{2|I_4|^{\frac{9}{2}}}{\sqrt{\pi}\mu^4 i} e^{-\frac{\mu^2}{2I_4}} M_3^{-2} - E_4 \left(6 + \frac{\mu^2}{I_4} \right) - X_4 \left(24 + \frac{12\mu^2}{I_4} + \frac{\mu^4}{I_4^2} \right). \quad (3.86)$$

There is a trade-off between the number of terms in the expansion of $\rho_3(\mathbf{x})$ in (3.84) and the accuracy of our fit. We start by considering the minimal set of parameters with $X_4 = E_4 = 0$ and find the value of I_4 (recalling that F_4 is determined by I_4 and the multiple moment) which gives the least absolute error for $M_3^{-2}(r)$ as shown in Figure 3.11.

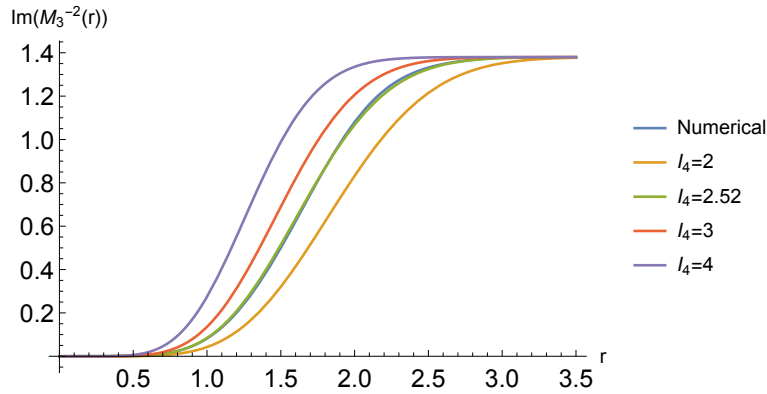


Fig. 3.11 The moment functions, $M_3^{-2}(r)$, with varying values of I_4 ($E_4 = 0$, $X_4 = 0$).

We find that the optimal value of I_4 is 2.52 and that there is quite a close fit as shown in Figure 3.11 where the green and blue curves almost lie on top of each other. However, we would like to see how much better a fit we can achieve by allowing E_4 to be non-zero and then by allowing E_4 and X_4 to both be non-zero.

We see in Figure 3.12 that we can achieve a significant decrease in the absolute error by allowing E_4 to be non-zero but only a slight further improvement by allowing X_4 to be non-zero as well. Therefore we choose the parameter set $I_4 = 2.88$, $E_4 = -10.6$, $X_4 = 0.00$ for the ρ_3 field of the $B = 4$ Skyrmion, finding that this provides the best compromise between simplicity and accuracy of the fit.

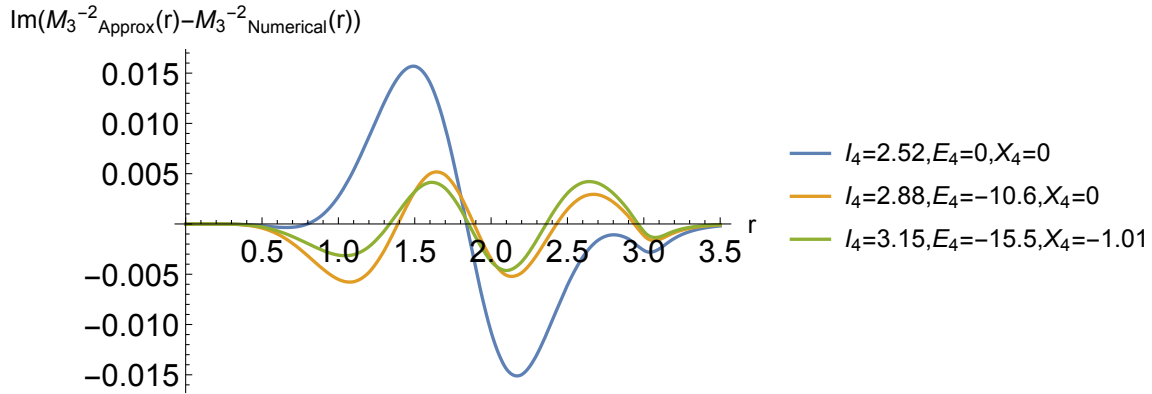


Fig. 3.12 The difference between the numerical and approximate moment functions for different sets of parameters.

3.5 The interaction energy between Skyrmions

Having found accurate approximations for the pion fields of the first four Skyrmions we can now use the calculated coefficients, $a_{l,m,n}$, to determine the interaction energy between them for a range of different separations and orientations. In this section, we go into the details of some important interactions and show how our approximation can be applied to vibrational quantization and $B = 4N$ cluster nuclei.

3.5.1 Two $B = 1$ Skyrmions

The simplest interaction that we can consider is between two $B = 1$ Skyrmions; this interaction depends on the separation vector, \mathbf{X} , between the two Skyrmions and also their relative orientations. Their relative orientations can be captured via the Euler rotation matrix, $\mathcal{R}(\alpha, \beta, \gamma)$, that relates them. The combinations of the positional and rotational degrees of freedom gives us a six dimensional configuration space in total. In [40] it is shown that the interaction potential must be of the form,

$$V(\mathbf{X}, \mathcal{R}) = V_0(|\mathbf{X}|) + V_1(|\mathbf{X}|)\text{Tr}(\mathcal{R}) + V_2(|\mathbf{X}|)\frac{\mathbf{X}^T \mathcal{R} \mathbf{X}}{|\mathbf{X}|^2}. \quad (3.87)$$

This means that once we have calculated V_0, V_1 and V_2 in our approximation we can express any interaction in terms of them. Following the method outlined in [40], we find that, in our approximation, the potentials are,

$$V_0(r) = 0 \quad (3.88)$$

Fig. 3.13 The attractive channel for two $B = 1$ Skyrmions.

$$V_1(r) = \frac{A_1^2}{8G_1^{7/2}\pi^{3/2}} \left(\frac{1}{r} \frac{\partial}{\partial r} \right) f \left(\frac{G_1}{2}; r \right) \quad (3.89)$$

$$V_2(r) = \frac{A_1^2}{8G_1^{7/2}\pi^{3/2}} r^2 \left(\frac{1}{r} \frac{\partial}{\partial r} \right)^2 f \left(\frac{G_1}{2}; r \right). \quad (3.90)$$

where f is defined in equation (3.17).

We now apply equation (3.87) to find the potential for two $B = 1$ Skyrmions in the attractive channel: this is the interaction between two $B = 1$ Skyrmions where the Skyrmions' orientations differ by a rotation of π about an axis orthogonal to their separation vector, \mathbf{X} . In other words the points of least separation for each Skyrmion have the same colour as seen in Figure 3.13. Note that one can rotate the $B = 1$ Skyrmions about the axis of separation and the interaction energy will not change. Two $B = 1$ Skyrmions in the attractive channel have the least interaction energy for a given separation and will form a $B = 2$ torus when they get sufficiently close. In our approximation the interaction energy of the attractive channel, as a function of separation, r , is,

$$V_{att}(r) = -\frac{A_1^2}{8G_1^{7/2}\pi^{3/2}} \left(\frac{1}{r} \frac{\partial}{\partial r} + r^2 \left(\frac{1}{r} \frac{\partial}{\partial r} \right)^2 \right) f \left(\frac{G_1}{2}; r \right). \quad (3.91)$$

In Figure 3.14 we plot the interaction energy between two $B = 1$ Skyrmions in the attractive channel as a function of separation. We also plot the interaction energy obtained via numerical simulation and the interaction energy given by the point multipole model (found by taking the limit $G_1 \rightarrow \infty$ in our model). The numerical simulations in this chapter, which are for the interactions between two Skyrmions, are all performed by taking an initial configuration with two well-separated Skyrmions with small initial velocities towards each other and evolving via second order time

evolution as in [41]. We remove the kinetic energy from the system if the system has increased its total energy after a step.

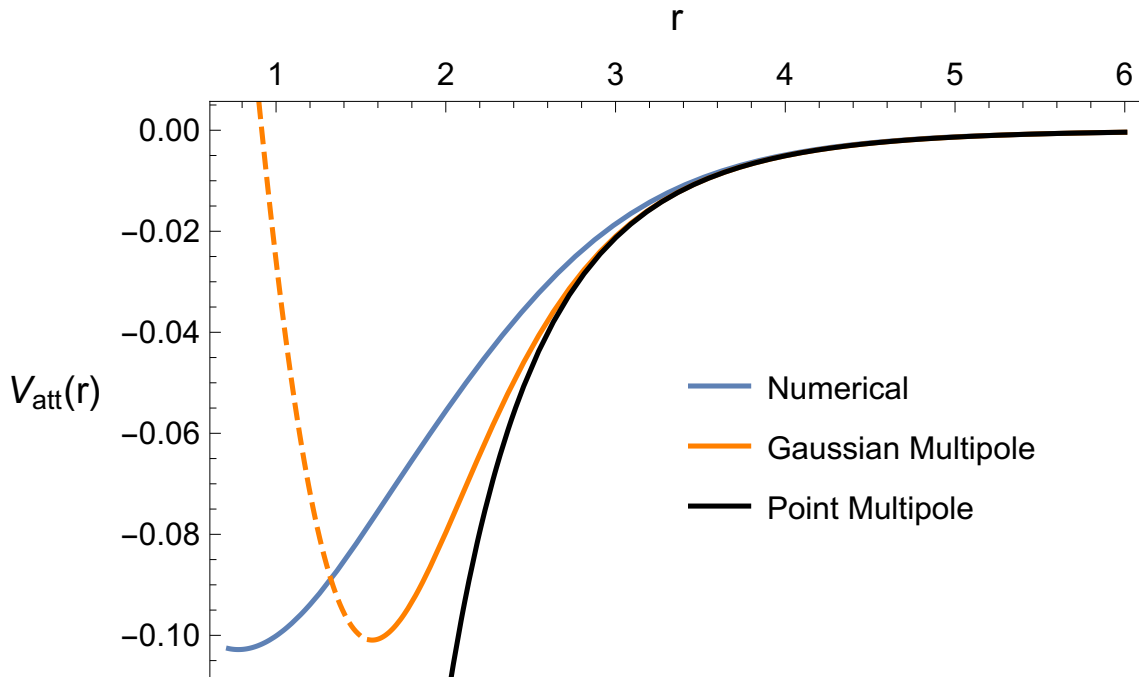


Fig. 3.14 The interaction energy for two $B = 1$ Skyrmions in the attractive channel.

At this point it is worth pointing out one of the benefits of using our approximation rather than a numerical simulation. In our approximation, each source has an origin and we can use this origin to define the position of the Skyrmion; this means that we have a concrete definition of the separation between two Skyrmions. The numerical solution for a single Skyrmion also has a good definition for the position of the Skyrmion; there is usually a central point where the lines of symmetry of the Skyrmion all cross and this can be considered the position of the Skyrmion. For the $B = 1$ Skyrmion the sigma field, σ , takes value -1 at this centre which is a convenient way of finding this central point numerically.

However, once we consider two Skyrmions interacting with each other the positions of the individual Skyrmions become less well defined. The individual Skyrmions begin to deform as they approach each other, which breaks some of the symmetries of the Skyrmions and so we no longer have central points and thus positions of the Skyrmions. Eventually the Skyrmions may coalesce entirely as with the $B = 2$ torus which is the end point of two $B = 1$ Skyrmions interacting in the attractive channel; by this point there is no notion of individual Skyrmions at all and hence no notion of their positions or the separation between them.

In order to plot the interaction energy we require some notion of separation; to this end we consider the points at which $\sigma = -1$ to correspond to the centres and thus positions of the individual Skyrmions. This definition of position is more coherent for greater separations, because there is less deformation of the individual Skyrmions, and therefore it is important for the asymptotics of our approximated interaction energy to match those of the interaction energy obtained via numerical simulation; however, for shorter separations this definition breaks down and we focus on matching the minimum value of the interaction energy rather than the separation at which it occurs.

For the interaction of two $B = 1$ Skyrmions in the attractive channel we find that both the Gaussian and point multipole approximations capture the asymptotics well, and the Gaussian approximation provides a very close approximation to the minimal interaction energy. Note that the point multipole approximation does not exhibit a minimum on the graph in Figure 3.14 and indeed there is not a minimum at any separation.

This highlights a key advantage of the Gaussian multipole approximation over the point multipole approximation: the Gaussian multipole approximation will produce a stationary point for any interaction because all of the derivatives of $f(G; r)$ have a stationary point whereas the interaction between individual point multipole pairs never has a stationary point. The total interaction energy itself may have stationary points because it is a sum of many pairwise point multipole interactions some of which may be attractive and others repulsive.

The existence of a minimum for an attractive interaction is important because this means that the Skyrmions settle at some fixed separation from each other forming a composite Skyrmion. For the case of the $B = 1$ Skyrmions in the attractive channel we get a preferred separation of $r_0 = 1.57$ Skyrme units. This can be thought of as the bond length between these two Skyrmions and the radius of the $B = 2$ Skyrmion.

As seen in Figure 3.14 the Gaussian multipole approximation provides an interaction energy for separations shorter than r_0 , but we would not expect this to be accurate because at lengths shorter than r_0 we can no longer say that the interaction is asymptotic. As the Skyrmions become closer short-range interactions come into effect, which act repulsively, and thus we expect the interaction energy to increase rapidly after it reaches its minimum value.

3.5.2 Two $B = 4$ Skyrmions

In order to investigate which arrangements of alpha particles have the lowest energy for $B = 4N$ cluster Skyrmions, we must first investigate the accuracy of our approxi-

mation of the interaction energy between two $B = 4$ Skyrmions. The lowest energy arrangements of two $B = 4$ Skyrmions are those shown in Figure 3.15, where the separation vector passes through the faces of the individual $B = 4$ Skyrmions and these faces have the same colour. As the two $B = 4$ Skyrmions approach each other

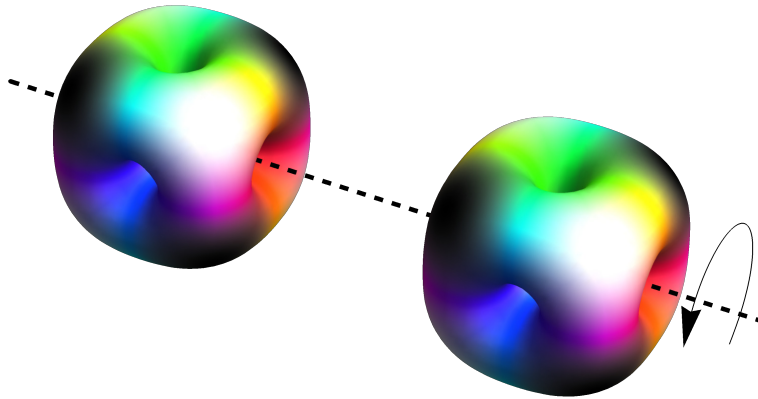


Fig. 3.15 The lowest energy arrangements of two $B = 4$ Skyrmions.

they combine to form a $B = 8$ Skyrmion of which there are two particularly important configurations. As seen in Figure 3.16, the unwisted $B = 8$ Skyrmion has the constituent $B = 4$ Skyrmions with the same orientation and the twisted $B = 8$ Skyrmion has the constituent $B = 4$ Skyrmions differing by a $\frac{\pi}{2}$ rotation about the separation vector. Using our approximation we can consider the whole range of different relative

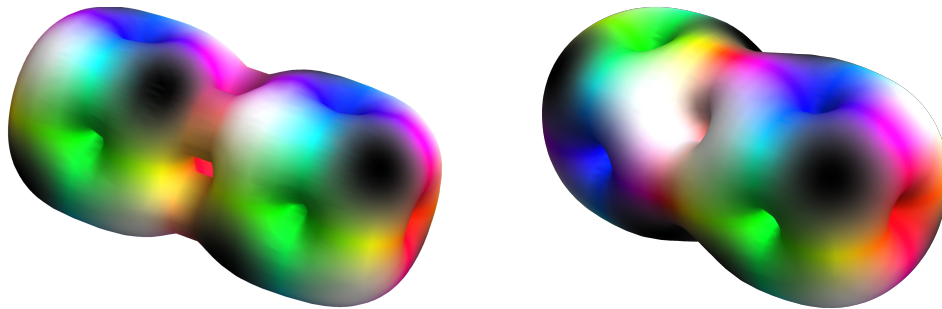


Fig. 3.16 The unwisted and twisted $B = 8$ configurations.

orientations and separations. In Figure 3.17, we see the effect that rotating one of the $B = 4$ Skyrmions has on the interaction energy for a separation of 3 and 4 units. This shows us that for large separations the unwisted configuration is favourable, but as the $B = 4$ Skyrmions approach each other the twisted configuration becomes the energy minimizer.

We now focus upon the unwisted and twisted channels and plot the interaction energy as a function of separation (figures 3.18 and 3.19); we find that in both cases

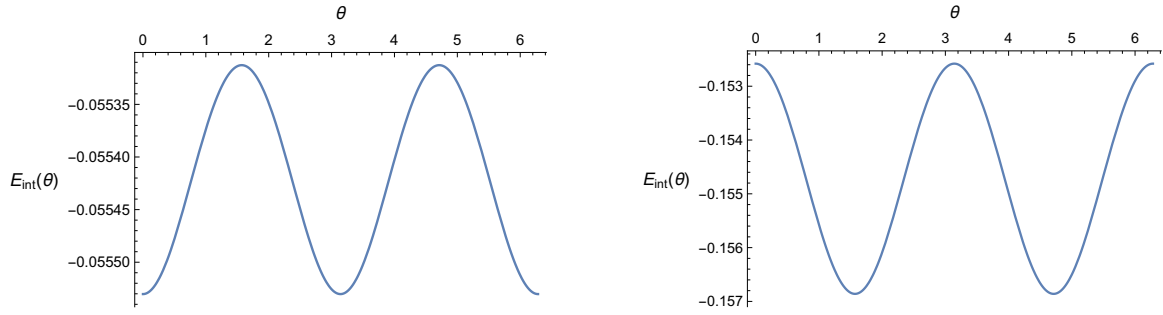


Fig. 3.17 The interaction energy as a function of angle of rotation θ for a separation of 4 and 3 Skyrme units.

our approximation predicts a minimum at a much lower interaction energy than is found via the numerical simulations. We also find that the difference between the energies of the untwisted and twisted configurations is less in our approximation than in the numerical simulations. In order to explain these discrepancies we need to break down the interaction energy into the individual interactions between multipoles.

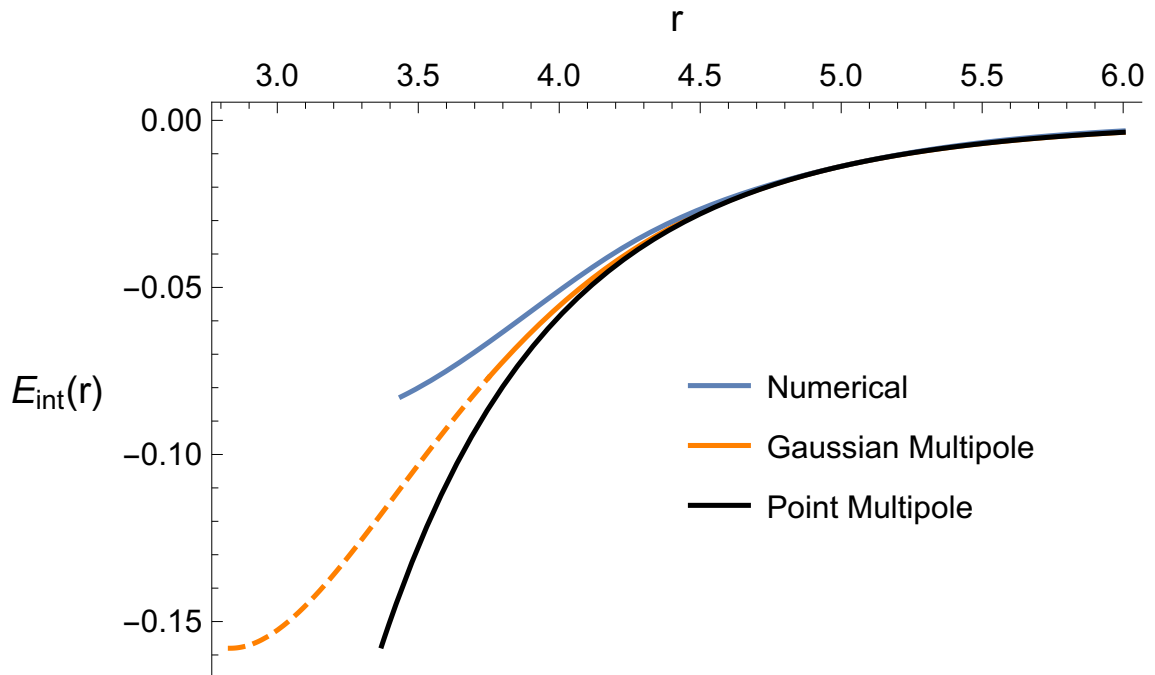


Fig. 3.18 The interaction energy as a function of separation for the untwisted channel.

Each Skyrmion has three pion fields and each pion field for one Skyrmion only interacts with the same pion field for the second Skyrmion. Within these pion fields interactions there are interactions between the different multipole moments. Let $E_{i;a,b}$ denote the interaction energy between the order 2^a and order 2^b multipoles of the i th

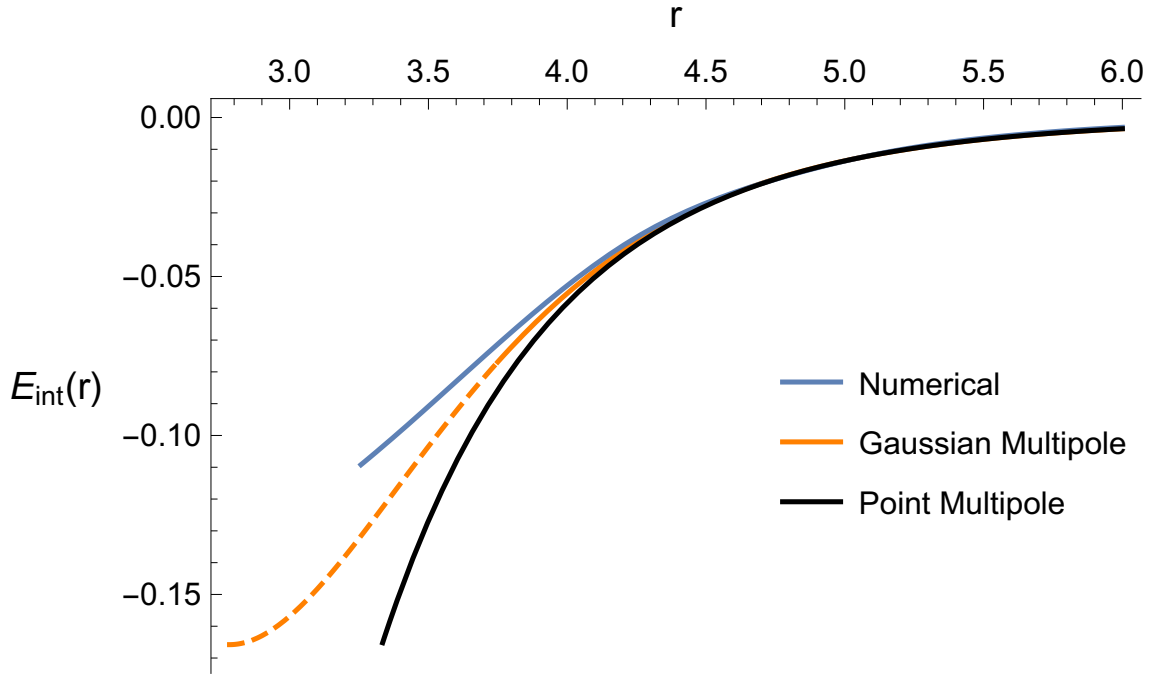


Fig. 3.19 The interaction energy as a function of separation for the twisted channel.

pion fields. Given that π_1 and π_2 have quadrupole and hexadecapole moments and π_3 has an octupole moments the total interaction energy can be expressed as,

$$E_{int} = E_{1;2,2} + E_{1;2,4} + E_{1;4,2} + E_{1;4,4} + E_{2;2,2} + E_{2;2,4} + E_{2;4,2} + E_{2;4,4} + E_{3;3,3}, \quad (3.92)$$

the sum of nine different multipole-multipole interactions.

Now as for the $B = 1$ Skyrmions in the attractive channel, none of these multipole-multipole interactions are trustworthy beyond their first stationary point. We find that, for both the untwisted and twisted channels, the interaction with the greatest separation at their first stationary point is $E_{1,4,4}$ with $r_0 = 3.75$, beyond this separation we would expect short-range forces to be repulsive and significant and so the interaction energy would increase sharply. When we introduce this cut-off to the total interaction energy (as shown by the ending of the solid line in figures 3.18 and 3.19) we find that the approximated interaction energy for the untwisted channel is close to the value found numerically. The energy for the twisted channel is not as accurate and we believe that this is because there is significant deformation of the individual $B = 4$ Skyrmions as they approach each other in the twisted channel, which can not be captured by our approximation.

We conclude that our approximation of the interactions between two $B = 4$ Skyrmions is trustworthy for large separations and always provides a closer fit to the interaction

energy found numerically than the point multipole approximation. As the Skyrmions get closer to each other we have to introduce a cut-off for the interaction energy which retains accuracy for the untwisted channel but the twisted channel is still difficult to model in our approximation. With this in mind we give particular attention to $B = 4N$ cluster nuclei where all of the shortest bonds are untwisted such as the $B = 32$ Skyrmion and the Skyrme crystal.

3.5.3 The $B = 32$ Skyrmion

The lowest known energy $B = 32$ Skyrmion is that of eight $B = 4$ cubes with the same orientation in a cubic arrangement as shown in Figure 3.20. If there were no

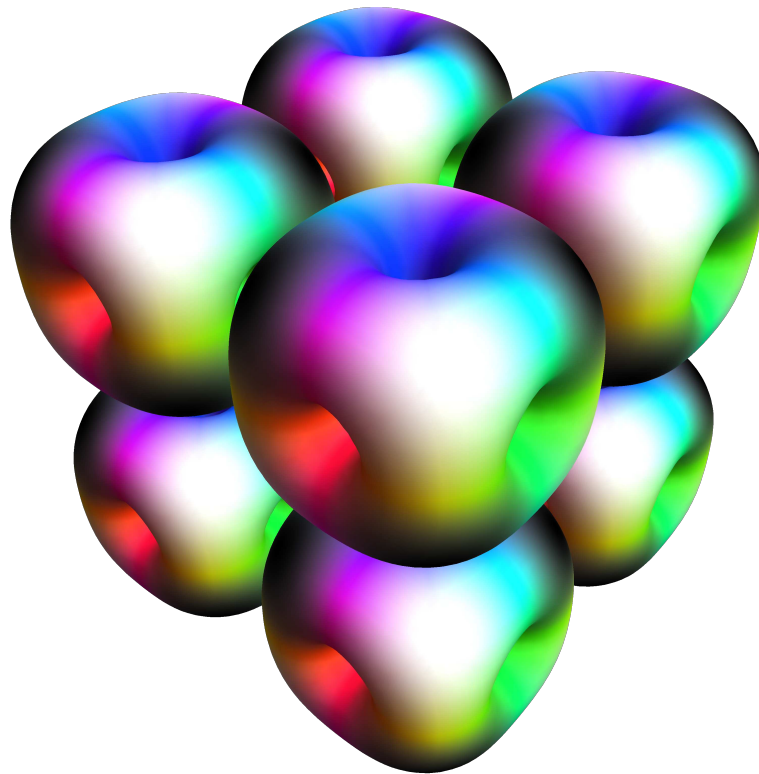


Fig. 3.20 The arrangement of eight $B = 4$ cubes in a $B = 32$ Skyrmions.

interactions between the constituent $B = 4$ Skyrmions then the $B = 32$ Skyrmion would have a configuration energy of 41.44 which is eight times the configuration energy of a $B = 4$ Skyrmion [5]. However, we must calculate the energy due to interactions between $B = 4$ Skyrmions and add this to 41.44.

The shortest bonds are between nearest neighbour $B = 4$ Skyrmions sharing an edge of the $B = 32$ cube which are untwisted; there are 12 of them in the $B = 32$ cube and

we suppose they have length r_0 . The next shortest bonds are between $B = 4$ Skyrmions separated by a face diagonal of the $B = 32$ cube, there are also 12 of them and they have length $\sqrt{2}r_0$. The longest bonds are between $B = 4$ Skyrmions separated by a body diagonal of the $B = 32$, there are only 4 of these and they have length $\sqrt{3}r_0$.

We see that the lengths of all the bonds only depend on the length of the shortest bond, which must be no shorter than 3.75. We then minimize the total interaction energy with this constraint and find that $r_0 = 3.75$ is the preferred length of the shortest bond. The total interaction energy is -1.04 with -0.92 of this coming from the shortest bonds alone, therefore it is not surprising that these bonds are at the optimal length for an untwisted bond. Whilst the other bonds are not untwisted they are sufficiently long that our approximation is trustworthy without worrying about cutoffs. This interaction energy means that, in our approximation, the $B = 32$ Skyrmion has a configuration energy of 40.40, which is comparable with the value of 40.51 found in [5].

3.5.4 The Skyrme crystal

The Skyrme crystal can be viewed as an infinite cubic lattice of $B = 4$ Skyrmions, which are in the same orientation [42], and we can apply our approximation method to calculate the energy per baryon of this lattice.

We again break this down into the number of bonds of each type. Using the same terminology as subsection 3.5.3 we find that each $B = 4$ cube has 6 bonds of the first type, 12 of the second type and 8 of the third type (bonds longer than the third type have a negligible contribution to the interaction energy); we then halve these numbers to account for the fact that each bond is between two $B = 4$ cubes and add up the interaction energies. We find that each $B = 4$ Skyrmion has an interaction energy of -0.243 , which means that, in our approximation, the Skyrme crystal has an energy per baryon of 1.234, which is comparable with the value of 1.238 found in [38].

3.5.5 The $B = 12$ Skyrmion

Whilst our approximation does not accurately model the twisted channel for two interacting $B = 4$ Skyrmions it does still provide a potential for all possible interactions of $B = 4$ Skyrmions and can provide some insight into arrangements of $B = 4$ Skyrmions. The $B = 12$ Skyrmion consists of three $B = 4$ Skyrmions and there are three distinct arrangements with low energy: the linear chain; the bent chain; and the triangle as shown in Figure 3.21. We use a bent chain with a 90° angle because we

believe that there may be a local minimum in the configuration energy close to this angle because the two shortest bonds are optimal here.

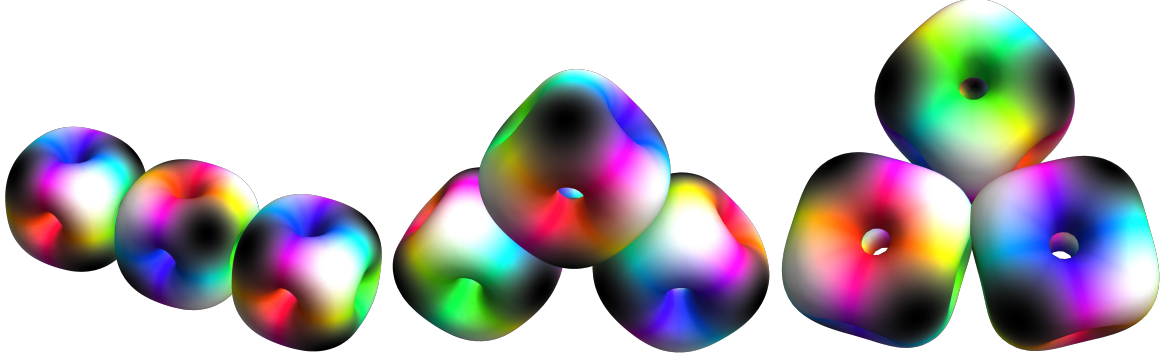


Fig. 3.21 The linear chain, bent chain and triangle configurations of the $B = 12$ Skyrmion

In these configurations the orientations are fixed and all bond lengths can be expressed in terms of the shortest bond present; as a result we can set up each arrangement and find the length of the shortest bond which gives the least interaction energy. We can then add this to the individual energies of the three constituent $B = 4$ Skyrmions to calculate the total energy of each of the three configurations.

In our approximation scheme the triangle has the lowest configuration energy at 15.02, the bent chain is next at 15.16 with the linear chain having the highest energy at 15.20. The ordering of the triangular configuration and the linear chain agrees with the ordering found in [17] and [19], which is required to explain the ground-state and Hoyle-state bands in the energy spectrum.

We also have reason to believe that the bent chain should have lower energy than the linear chain; both arrangements have two twisted bonds of roughly the same length r_0 . The remaining bond has length $\sqrt{2}r_0$ for the bent chain and $2r_0$ for the linear chain, both of these are sufficiently long that we can trust our approximation again. Since both bonds are in an attractive channel the bent chain has lower configuration energy because its longest bond is much shorter than the longest bond for the linear chain.

3.5.6 The E vibration of the $B = 16$ Skyrmion

We can go even further for the $B = 16$ Skyrmion because in [20] the Skyrme model is used to find dynamics along a line on the vibrational manifold as shown in Figure 3.22. This provides details about the positions and the orientations of the individual $B = 4$ Skyrmions which helps us to generate a potential along this line.



Fig. 3.22 The scattering line from $\theta = 0$ to $\theta = \pi$

Along this line the four $B = 4$ Skyrmions have positions $\left(-\frac{r}{\sqrt{2}} \sin \theta, -\frac{r}{\sqrt{2}} \sin \theta, r \cos \theta\right)$, $\left(-\frac{r}{\sqrt{2}} \sin \theta, \frac{r}{\sqrt{2}} \sin \theta, -r \cos \theta\right)$, $\left(\frac{r}{\sqrt{2}} \sin \theta, -\frac{r}{\sqrt{2}} \sin \theta, -r \cos \theta\right)$ and $\left(\frac{r}{\sqrt{2}} \sin \theta, \frac{r}{\sqrt{2}} \sin \theta, r \cos \theta\right)$ with Euler angles $\left(\frac{\pi}{4}, \beta, \frac{\pi}{4}\right)$, $\left(-\frac{\pi}{4}, -\beta, -\frac{\pi}{4}\right)$, $\left(-\frac{\pi}{4}, \beta, -\frac{\pi}{4}\right)$ and $\left(\frac{\pi}{4}, -\beta, \frac{\pi}{4}\right)$ respectively. As we go along the line we vary θ and then calculate the values of r and β which minimize the interaction energy. In Figure 3.23 we show how the interaction energy, E_{int} , scale factor, r , and orientations, β , of the Skyrmions vary with θ . Note that since r tends to infinity as θ tends to 0 or π so we cut off this graph at $r = 4$.

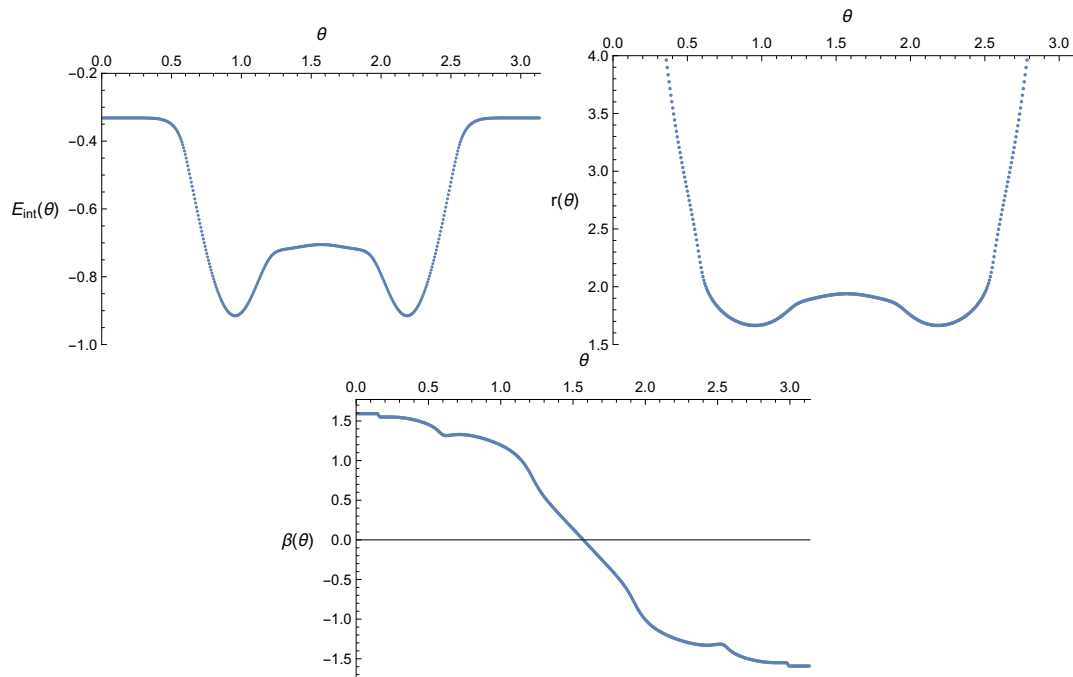


Fig. 3.23 The energy, scale factor and orientations of the $B = 16$ Skyrmion as a function of θ .

In the limit of $\theta \rightarrow 0$, we see that $E_{int} \rightarrow -0.332$, $r \rightarrow \infty$ and $\beta \rightarrow \frac{\pi}{2}$, this corresponds to two well separated twisted $B = 8$ Skyrmions as seen in the left image of Figure 3.24. We require $r \rightarrow \infty$ because the bond in the $B = 8$ Skyrmions has length

$2r \sin \theta$ and this must tend to $r_0 = 2.78$ as $\theta \rightarrow 0$ because this is the optimal length of a twisted bond.

As θ increases, the $B = 8$ Skyrmions approach each other and the interaction energy decreases because the $B = 8$ Skyrmions are attracting each other. Within each $B = 8$ Skyrmion the individual $B = 4$ Skyrmions pull away from each other and eventually at $\theta = \arccos \frac{1}{\sqrt{3}}$ we have a tetrahedral arrangement of $B = 4$ Skyrmions as seen in the central image of Figure 3.24. This is the minimal energy arrangement of four $B = 4$ Skyrmions with an interaction energy of -0.915 and also gives the smallest scale factor of any configuration at 1.66 which means that all bonds between $B = 4$ Skyrmions have length 2.72; note that each bond has interaction energy of -0.153 , so each bond is close in energy and length to the optimal twisted bond between two $B = 4$ Skyrmions, which has length 2.78 and energy -0.165 .

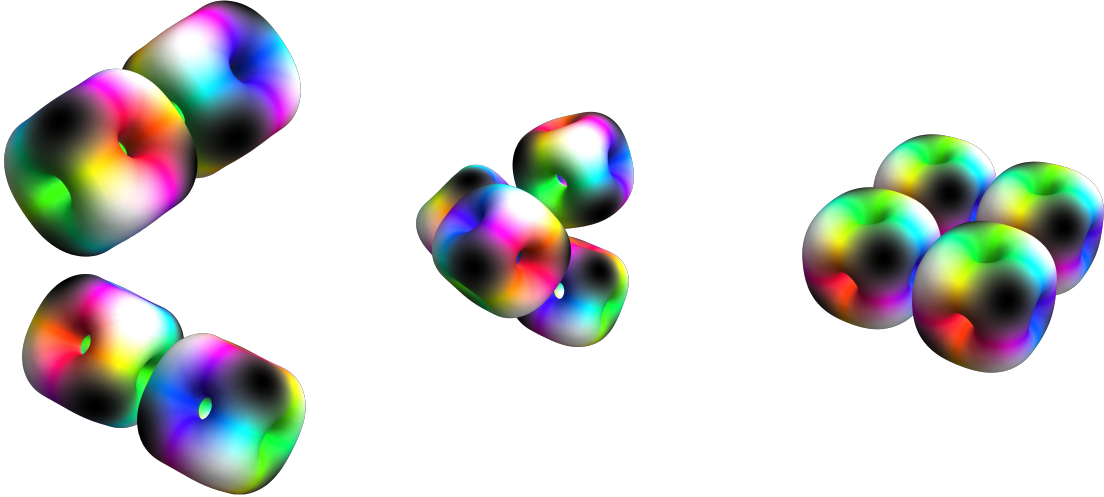


Fig. 3.24 The $\theta = 0$, $\theta = \arccos \frac{1}{\sqrt{3}}$ (tetrahedral) and $\theta = \frac{\pi}{2}$ (flat square) arrangements of $B = 4$ Skyrmions.

As θ increases further, the interaction energy decreases and the scale factor increases up until $\theta = \frac{\pi}{2}$ where we get the flat square arrangement as seen in the right image of Figure 3.24. This has an interaction energy of -0.705 and a scale factor of 1.94, both of which are local maxima, this means that the four shortest bonds have length 2.74 and the two longer diagonal bonds have length 3.88. This explains why the flat square has a higher configuration energy than the tetrahedron; they both have very similar short bonds but the tetrahedron has more of these bonds and therefore has lower energy.

As θ increases beyond $\frac{\pi}{2}$, we get the same arrangements as before but they are reflected meaning that E_{int} and r are unaltered but β changes sign. Across the whole

range of θ between 0 and π we can replicate the dynamics found in the Skyrme model as shown in Figure 3.22. This not only serves to provide us with a parameterization of this line in terms of θ but also gives us a potential, $E_{int}(\theta)$, along this line. We find that we agree with the general shape of the potential that was used as an approximation in chapter 2; along this line the tetrahedral arrangement is a global energy minimum, the flat square arrangement is a local energy maximum and the energy of the arrangements increases asymptotically to the arrangement of two well separated and twisted $B = 8$ Skyrmions.

3.5.7 The E vibration of the $B = 4$ Skyrmion

The energy minimizer in the $B = 4$ sector is the $B = 4$ Skyrmion with cubic symmetry, but this symmetry poses a problem when it comes to finding the energy spectrum via rigid body quantization. The large symmetry group means that spin states are heavily restricted, resulting in a calculated energy spectrum [40] which has many less states than the spectrum found experimentally for Helium-4. If instead we quantize over a wider range of low energy configurations, we can decrease the amount of symmetry and allow more quantum states. The $B = 4$ Skyrmion admits many different vibrational spaces, which are categorised by their symmetries, and the rational map approximation can be used to get a general idea for the configurations which feature in each space [43]. However, in order to quantize these spaces we will require a potential and the rational map approximation only provides a very crude approximation for the energies of configurations, especially far away from the cubic $B = 4$ Skyrmion.

We will use our approximation scheme to generate the potential for the E vibration of the $B = 4$ Skyrmion. The E vibration is part of the space of configurations which have D_2 symmetry and includes the minimal energy cubic $B = 4$ Skyrmion. The D_2 symmetry helps us determine the degrees of freedom and here it is useful to consider $B = 4$ configurations as arrangements of four $B = 1$ Skyrmions as in Figure 3.25.

Suppose that one of the $B = 1$ Skyrmions is at (x, y, z) with orientation (α, β, γ) (where α, β and γ are the Euler angles required to get to the orientation from the standard $B = 1$ Skyrmion orientation in Figure 3.1). Then the D_2 symmetry forces the other Skyrmions to be at $(-x, -y, z)$, $(-x, y, -z)$ and $(x, -y, -z)$ with orientations $(\pi + \alpha, \beta, \gamma)$, $(\pi - \alpha, \pi - \beta, \pi + \gamma)$ and $(2\pi - \alpha, \pi - \beta, \pi + \gamma)$ respectively. This gives us a 6-dimensional vibrational manifold which is still rather large; however, when we look at the individual interactions between pairs of $B = 1$ Skyrmions we find that all interactions are in the attractive channel for any values of (α, β, γ) and so the

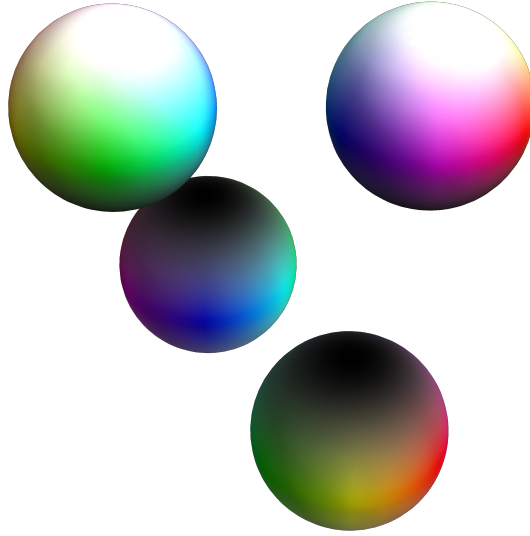


Fig. 3.25 The arrangement for four $B = 1$ Skyrmions at $\theta = \frac{\pi}{4}, \phi = \frac{\pi}{6}, \alpha = \beta = \gamma = 0$.

interaction energy does not depend on (α, β, γ) . Changing (α, β, γ) just has the effect of performing a global isorotation which can be quantised via rigid body quantization.

We currently have a 3-dimensional vibrational manifold, but this can be further split into a 1-dimensional vibration and a 2-dimensional vibrational manifold which are orthogonal. The 1-dimensional space is called the breather mode and corresponds to changing the overall size of the configurations by changing the scale factor, r . The remaining 2-dimensional space is called the E vibration and can be parametrized by (θ, ϕ) , where (r, θ, ϕ) denotes the position of one of the $B = 1$ Skyrmions in spherical polars. We must then find the value of r which minimizes the interaction energy for each configuration, which will define a surface. The four $B = 1$ Skyrmions reside on this surface and are constrained by D_2 symmetry. When it comes to quantization we would deal with this constraint by focusing on one $B = 1$ Skyrmion residing on a quarter of the surface with periodic boundary conditions.

There are six directions in which the $B = 1$ Skyrmions can escape to infinity; this occurs via the Skyrmions pairing off (and thus forming $B = 2$ tori) and then these $B = 2$ Skyrmions separating from each other. If we consider a $B = 4$ cubic Skyrmion (corresponding to the centre of the red regions in Figure 3.26) then this separation can be imagined as pulling opposing faces away from each other. This is analogous to the quantization of the $B = 16$ Skyrmion's E vibration by treating it as four $B = 4$ Skyrmions and as such we would expect the vibrational manifold to resemble a 6-punctured sphere as in Figure 3.26; however, whilst the vibrational manifold and the techniques used to quantize it may be similar to the $B = 16$ case, the potential that

we place on this manifold will be very different because we have the interactions of $B = 1$ Skyrmions rather than $B = 4$ Skyrmions.

The energy of a $B = 4$ configuration can be expressed as the energy of the four constituent $B = 1$ Skyrmions plus the interaction energy between them. This means that we have to consider the interactions between the six pairs of $B = 1$ Skyrmions. As stated previously all interactions are in the attractive channel and so have energy,

$$E_{1+1}(r) = V_{att}(r) = -\frac{A_1^2}{8G_1^{7/2}\pi^{3/2}} \left(\frac{1}{r} \frac{\partial}{\partial r} + r^2 \left(\frac{1}{r} \frac{\partial}{\partial r} \right)^2 \right) f \left(\frac{G_1}{2}, r \right). \quad (3.93)$$

as in (3.91). The configuration with a particle at (x, y, z) has three pairs of bonds with lengths $\sqrt{2x^2 + 2y^2}$, $\sqrt{2z^2 + 2x^2}$ and $\sqrt{2y^2 + 2z^2}$, so the total configuration energy is

$$E_{4B=1} = 4E_{B=1} + 2 \left(E_{1+1} \left(\sqrt{2x^2 + 2y^2} \right) + E_{1+1} \left(\sqrt{2z^2 + 2x^2} \right) + E_{1+1} \left(\sqrt{2y^2 + 2z^2} \right) \right). \quad (3.94)$$

Now that we have an expression for the interaction energy of a generic configuration with D_2 symmetry, we can use this to determine the vibrational manifold for the E vibration by finding the scale factor, r , which minimizes the interaction energy in (3.94). The potential on the manifold is just the value of the interaction energy at this minimum. However, for some configurations this method of determining the vibrational manifold and potential becomes problematic. There are four different regimes of configurations, corresponding to different relative lengths of bonds within the configuration, that we have to consider. Let us focus on the line $\phi = \frac{\pi}{4}$ between $\theta = 0$ and $\frac{\pi}{2}$ in our vibrational manifold, which corresponds to the black line in Figure 3.26, this means that one bond, denoted B_1 , has length $\sqrt{2}r \sin \theta$ and two bonds, denoted B_2 and B_3 , have lengths $r\sqrt{2 \cos^2 \theta + \sin^2 \theta}$.

Regime 1: $B_1 \ll B_2, B_3$

In regime 1 the shortest bond is much shorter than the other two bonds and in particular along our line we have $B_1 \ll B_2, B_3$. We plot the interaction energies of these bonds in Figure 3.27 for $\theta = \frac{\pi}{18}$. The curve corresponding to B_1 has a minimum at $r = 4.511$ and the curves corresponding to B_2 and B_3 have minima at $r = 0.789$, both with interaction energy -0.101 ; note that r does not correspond to the bond length but rather the scale factor of the entire configuration. All three bonds have a minimum at the same value of interaction energy because they all correspond to an interaction between two $B = 1$ Skyrmions in the attractive channel: the geometry of the configuration just means that the bonds have different lengths and therefore

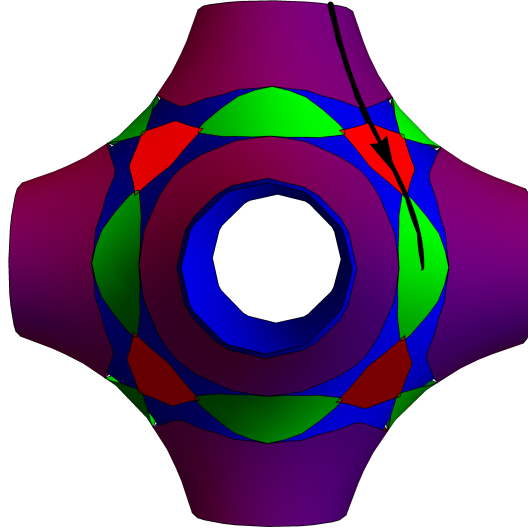


Fig. 3.26 Approximation of the vibrational manifold for four $B = 1$ Skyrmions. Regimes 1, 2, 3 and 4 are denoted by the purple, blue, red and green regions respectively. The line $\phi = \frac{\pi}{2}$ between $\theta = 0$ and $\frac{\pi}{2}$ is shown in black.

minima at different values of the scale factor, r . As seen with the blue curve of Figure 3.28, the global minimum of total interaction energy is at $r = 4.51$ with an interaction energy of -0.202 . We see that the minimum is dominated by the shortest bond, B_1 , which dictates its location and value, with B_2 and B_3 having very little effect.

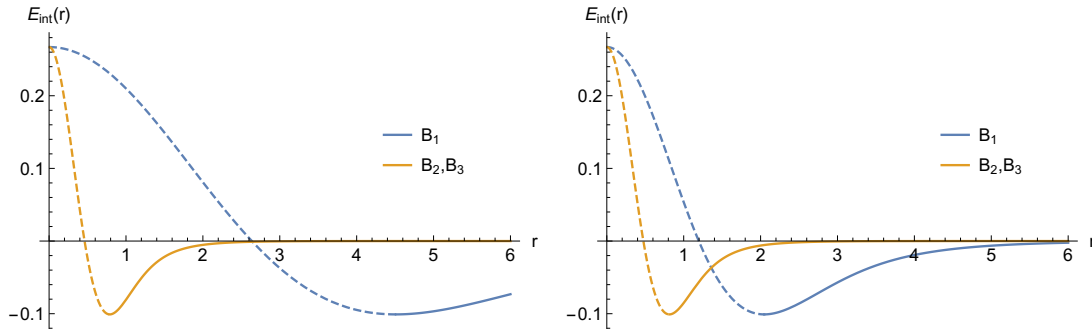


Fig. 3.27 The energies of the bonds B_1 , B_2 and B_3 at $\theta = \frac{\pi}{18}, \phi = 0$ (regime 1) and $\theta = \frac{\pi}{8}, \phi = 0$ (regime 2).

However, there is another local minimum at $r = 0.83$ with an interaction energy of 0.054 . This is due to the minima of the B_2 and B_3 bonds, but there is a large positive interaction energy coming from B_1 , because, at $r = 0.83$, B_1 is far shorter than its preferred length. However, the approximation for the interaction energy of B_1 is not trustworthy beyond its minimum value and therefore we can discount this second local minimum. Fortunately in regime 1, it is easy to separate the two minima due to the

substantial difference between the bond lengths of B_1 and B_2, B_3 . But as we increase θ , the bond lengths get closer to each other and we move into regime 2.

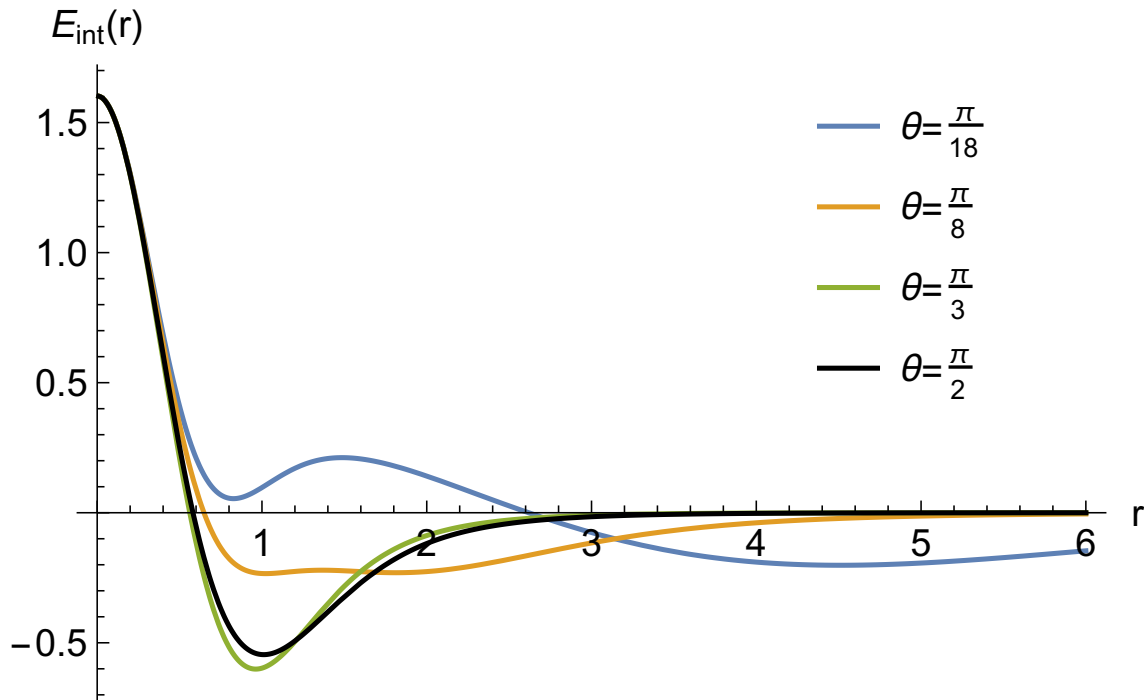


Fig. 3.28 The total interaction energy for $\theta = \frac{\pi}{18}$ (regime 1), $\theta = \frac{\pi}{8}$ (regime 2), $\theta = \frac{\pi}{3}$ (regime 3) and $\theta = \frac{\pi}{2}$ (regime 4).

Regime 2: $B_1 < B_2, B_3$

In regime 2, the length of the shortest bond is much closer to the lengths of the other two bonds and along our line we have $B_1 < B_2, B_3$. As seen in Figure 3.27, at $\theta = \frac{\pi}{8}$ the curve corresponding to B_1 has a minimum at $r = 2.05$ and the curve corresponding to B_2 and B_3 has a minimum at $r = 0.814$, but now the total interaction energy has two minima with very similar values. As shown by the orange curve of Figure 3.28, the first minimum is at $r = 1.813$ with an interaction energy of -0.231 and the second is at $r = 1.02$ with an interaction energy of -0.234 . The existence of two minima at similar values presents a problem in terms of how we choose the scale factor, r , and interaction energy for our vibrational manifold.

To see why there is a problem, consider moving along the line $\phi = \frac{\pi}{4}$. There is a value of θ ($\theta = 0.389$) where both of the minima present have the same height. Therefore for $\theta < 0.389$ the first minimum (the minimum at a larger value of r) has lower energy and for $\theta > 0.389$ the second minimum has lower energy. This bifurcation presents a problem because the preferred scale factor, the value of r at which the global minimum

lies, will be discontinuous at $\theta = 0.389$. This discontinuity will make it difficult to do quantum mechanics on our vibrational manifold.

One way to solve this problem, is to always take the scale factor and interaction energy that correspond to the first minimum of the total interaction energy, the minimum at the largest value of r . This takes into account the fact that if the shortest bond is shorter than the preferred length, $r_0 = 1.57$, as shown by the dotted parts of the curves in figures 3.27 and 3.29, then the interaction energy for this bond is not accurate and therefore neither is the total interaction energy. Therefore any minima beyond the first minimum would have a significant positive energy contribution from the shortest bond which would negate the negative interaction energies of the other longer bonds. However, this method of solving the problem is not sufficient because we see that the location of the first minimum of the total interaction energy is at a smaller value of r than the minimum of the shortest bonds interaction energy and therefore the energy is still not trustworthy at this first minimum.

Regime 3: $B_1 \simeq B_2, B_3$

As we increase θ further we enter regime 3 and the bonds lengths get closer to each other, becoming equal at $\theta = \arccos \frac{1}{\sqrt{3}}$. In this regime the location of the minimum is approximately equal for all three bonds, as seen in Figure 3.29 for $\theta = \frac{\pi}{3}$, and therefore the location of the minimum of the total interaction energy, as seen with the green curve in Figure 3.28, is very close to the location of the minimum of the interaction energy of the shortest bond. This means that both the preferred scale factor and potential can be determined accurately for configurations lying in regime 3.

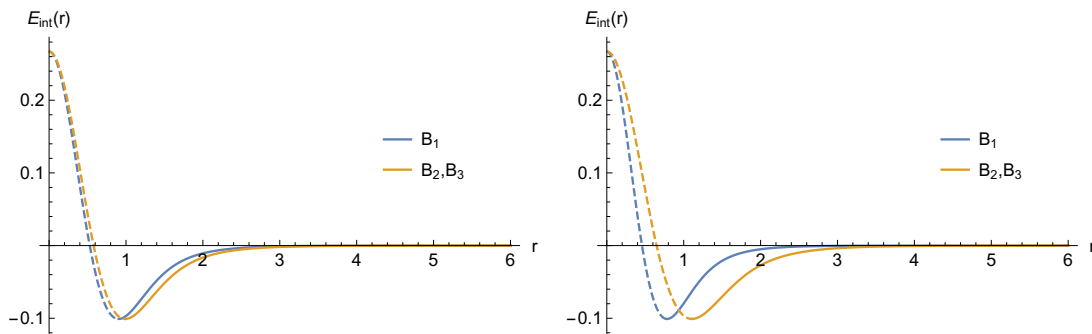


Fig. 3.29 The energies of the bonds B_1 , B_2 and B_3 at $\theta = \frac{\pi}{3}$ (regime 3) and $\theta = \frac{\pi}{2}$ (regime 4).

Regime 4: $B_2, B_3 < B_1$

In regime 4, there are two short bonds of similar length and one longer bond, which for our line corresponds to $\theta > \arccos \frac{1}{\sqrt{3}}$ where B_1 becomes the longest bond. As seen in Figure 3.29 for $\theta = \frac{\pi}{2}$, the curve corresponding to B_1 has a minimum at $r = 0.783$ and the curve corresponding to B_2 and B_3 has a minimum at $r = 1.108$. The total interaction energy only has one minimum, as seen in Figure 3.28, but it is at a location ($r = 1.011$) which means that B_2 and B_3 are shorter than their preferred length and therefore the interaction energies for these bonds are inaccurate. Therefore the value and location of this minimum is of dubious accuracy.

The problem that our approximation scheme has in regimes 2 and 4 mean that we need to change our method for finding the potential and scale factor on our vibrational manifold. The solution that we propose is that we always set the scale factor, r , of our configuration such that the shortest bond has length r_0 . This is equivalent to saying that a bond has infinite positive interaction energy for lengths less than r_0 . We then calculate the interaction energy for this value of r and take this to be the interaction energy of the configuration. In reality we would expect the scale factor of the configuration to be slightly less than the one from our method, because the longer bonds should have some effect on where the minimum lies. However, the true minimum should be very close to the minimum of the shortest bond because we expect the energy of this shorter bond to increase rapidly once it is shorter than r_0 thus increasing the interaction energy rapidly as well. This provides us with a scale factor and interaction energy which are continuous, but may have discontinuous derivatives in regimes 2 and 4; however, continuity is sufficient to quantize states on the vibrational manifold.

In Table 3.1 we show the effect that introducing this cut-off has on the location and value of the minima of the total interaction energy. We that in regime 1 the cut-off does not have an effect on the location or value of the minimum, but it does remove the second minimum. In regime 2 the cut-off still removes the second minimum, but there is also a significant adjustment to the location of the first minimum, this is because the longer bonds effect the location of the minimum of the total interaction energy but not the value. In regime 3 the cut-off only has a slight effect on the location and value of the minimum and in regime 4 the cut-off changes both the location and value of the minimum by a small amount.

We see that in the regimes where the total interaction energy is trustworthy at its minimum then the cut-off only has a small effect on this minimum; it is important that there is a good match between the cut-off and normal calculation for the location and value of the minimum for some configurations. The cut-off is able to alleviate the problem of multiple minima which means that it can be used to generate the potential

θ	No Cut-off		Cut-off	
	Location(s)	Value(s)	Location	Value
$\frac{\pi}{18}$	0.827, 4.510	0.054, -0.202	4.511	-0.202
$\frac{\pi}{8}$	1.022, 1.812	-0.234, -0.231	2.048	-0.224
$\frac{\pi}{3}$	0.962	-0.601	0.991	-0.599
$\frac{\pi}{2}$	1.011	-0.546	1.108	-0.530

Table 3.1 The locations and values of the minima of the total interaction energy with and without a cut-off.

and vibrational manifold for the E vibration of the $B = 4$ Skyrmion. We are able to calculate the scale factor and interaction energy for each value of θ and ϕ and thus generate the surface on which the four $B = 1$ Skyrmions must lie and this surface is shown in Figure 3.30.

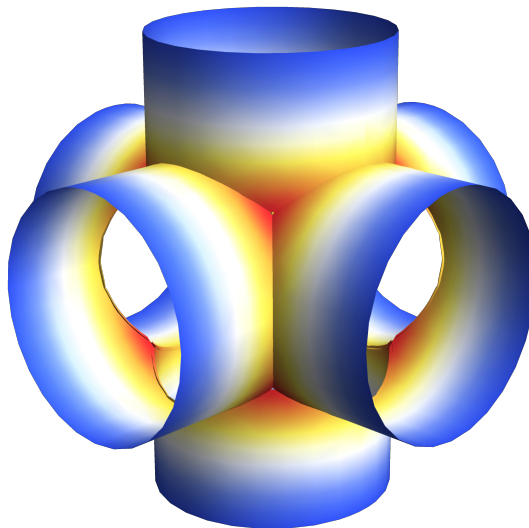


Fig. 3.30 The vibrational manifold and potential for four interacting $B = 1$ Skyrmions. Red corresponds to low interaction energy, blue corresponds to high interaction energy.

We see that this manifold still resembles the 6-punctured sphere from Figure 3.26; however the asymptotic directions now resemble cylinders rather than tapering towards a singularity. These asymptotic directions correspond to two $B = 2$ tori separating from each other and the diameters of these tori should tend to the value r_0 rather than tending to 0. This is what we see in Figure 3.30; the $B = 1$ Skyrmions do not get arbitrarily close to each other along these asymptotic directions. We see that the energy of the configurations increases in these asymptotic directions because the

separated $B = 2$ tori are in the attractive channel and prefer to be close to each other. We also see that the configuration with the lowest energy is the standard $B = 4$ cubic Skyrmion which agrees with our expectations of it being the energy minimizer. We have now defined the manifold and placed a potential on it. After choosing a metric on the manifold we could quantize this system numerically and investigate parts of the energy spectrum for Helium-4.

3.6 Conclusion

In this chapter we have tackled the problem of approximating the interaction energies between Skyrmions by expanding upon the ideas of [37] and [38] and using Gaussian multipole sources rather than point multipole sources to generate the pion fields of Skyrmions. We have found that our approximation is always an improvement upon the point multipole method and is able to accurately capture interactions between a range of Skyrmions. Crucially we are able to retain an analytic expression for the interaction energies between Skyrmions which makes our approximation well suited to tackling the problem of vibrational quantization.

We have also outlined a method for approximating the pion fields of Skyrmions and applied this to the first four Skyrmions, showing that our approximation scheme is versatile and can be applied to any Skyrmion. In particular we have found a very good analytic approximation for the radial profile function of the $B = 1$ Skyrmion. We have also applied our approximation to calculating the energies of $B = 4N$ cluster nuclei and found close agreement with results found numerically in the Skyrme model.

We have also found the potential along a scattering line of the E vibration of the $B = 16$ Skyrmion where the orientations of the Skyrmions is known. We have looked at the E vibration of the $B = 4$ Skyrmion and generated a potential for the entire vibrational manifold: a necessary piece to quantize the system. This was possible because the orientations of the individual $B = 1$ Skyrmions has no effect on the interaction energy.

We would also require the metric to quantize the E vibrations of both systems; however, in [44], it is shown that the metric for the case of two interacting $B = 1$ Skyrmions can be approximated by treating them as point dipoles. It would be interesting to see whether this can be extended to our Gaussian multipole approximation as well.

Given that our approximation is most accurate at large separations it could also be applied to the scattering of Skyrmions. The scattering of $B = 1$ Skyrmions is considered

in [45], where they use the point dipole approximation to approximate the interaction energy; this could be improved by use of the Gaussian multipole approximation meaning that scattering for a larger range of impact parameters could be approximated by our method

Chapter 4

Electron scattering intensities and Patterson functions of Skyrmions

This chapter is based on a joint paper with M. Karliner and N.S Manton [46].

4.1 Introduction

In this chapter we look at the problem of electrons scattering off Skyrmions. Experiments usually involve the electrons scattering from a sample of many identical, uncorrelated nuclei. We will model each of these nuclei as a quantised Skyrmion. An analogous approach to pion-nucleon scattering reproduces experimental phase shifts quite well [47–50]. The wavefunction of the Skyrmion provides the probabilities for each of the different orientations of the classical Skyrmion. If the spin is non-zero, then the wavefunction is not uniform with respect to body-fixed axes (and must satisfy Finkelstein–Rubinstein constraints). However, the projection of spin onto space-fixed axes is unconstrained if the nuclei are not polarised, so these projections occur with equal probability. The net effect is that all orientations of a Skyrmion occur with equal probability whatever the spin state.

In this chapter we will require each Skyrmion to have spin and isospin zero. These Skyrmions do not have an electric quadrupole or magnetic dipole moment; as a result their charge density is proportional to half their baryon density, $\rho(\mathbf{x}) = \frac{1}{2}B_0(\mathbf{x})$ [6, 51], which simplifies the calculation of scattering intensities. Note that only the $B = 1$ Skyrmion has a spherically symmetric baryon density.

An isospin zero nucleus must have equal numbers of protons and neutrons. Within the nucleus, nucleons have a strong tendency to pair with like nucleons such that their spins are anti-parallel; therefore in an even-even nucleus all protons and neutrons pair

in this manner, resulting in a spin and isospin zero nucleus. In an odd-odd nucleus we are left with a single proton and neutron after pairing; these have a stronger nuclear attraction between them if their spins are aligned, resulting in at least a spin one nucleus. Therefore spin and isospin zero nuclei must have baryon number $B = 4N$ where N is an integer.

The stationary Schrödinger equation for the electron involves the electrostatic potential, V . In turn V is related to the nucleus' charge density by Poisson's equation

$$\nabla^2 V = -\rho. \quad (4.1)$$

Phenomenological models of the nucleus describe the charge density as being spherically symmetric and approximated quite accurately by a Fermi distribution, $\rho(r) = \frac{\rho_0}{1 + \exp\left(\frac{r-a}{c}\right)}$. Variants with small oscillations and a central depression are also used, particularly for larger nuclei [52]. However, these variants require more parameters to fit the data closely and do not have a theoretical grounding which explains their values. We wish to see whether the Skyrme model can provide as good a fit with experimental scattering data, whilst being able to vary only one parameter, the length scale (we use the same pion mass throughout this chapter).

One method of calculating the electron scattering intensity off a Skyrmion is to consider the semiclassical, spin zero quantum state, and then calculate the form factor. The electron effectively scatters off the spherically averaged charge density of the Skyrmion. We call this the quantum averaging method; it has been considered previously [53, 54].

An alternative method of calculation is to consider the electrons as moving fast and scattering off the Skyrmion in a brief moment. In this scattering time the Skyrmion has no time to change orientation. Nuclear rotational motion, from a classical perspective, is slow, like molecular rotational motion. We can therefore model the nucleus by a Skyrmion with a fixed orientation at the time that the electron scatters off it. We then average over Skyrmion orientations, because the nuclei are not polarised and all orientations are equally likely. We call this the classical averaging method.

For both methods of calculation we use the Born approximation [55], used routinely in quantum mechanical and X-ray scattering calculations. The classical averaging method involves the Patterson function of the Skyrmion because the method is analogous to an X-ray powder diffraction calculation, where the crystal fragments have random orientations [56–58].

The electron is energetic and fast because we want to probe length scales comparable to the nuclear radius. In fact the electron can have energy of order 1 GeV and be relativistic; therefore we use QED to calculate the cross section, resulting in the Mott scattering formula. The Born approximation is then equivalent to the one-photon exchange approximation.

4.2 Form factors and intensities

4.2.1 Scattering from a fixed Skyrmion

The expression for the electromagnetic current of a Skyrmion is

$$\mathcal{J}_\mu = \frac{1}{2}B_\mu + I_\mu^3, \quad (4.2)$$

where B_μ is the baryon current and I_μ^3 is the third component of the isospin Noether current. A Skyrmion in an isospin zero state has I_0^3 equal to zero and so \mathcal{J}_0 is half the baryon density; thus we consider scattering off a charge density $\rho(\mathbf{x}) = \frac{1}{2}B_0(\mathbf{x})$.

In the Born approximation, the electron scattering amplitude off a Skyrmion with fixed orientation is a constant multiple of

$$\tilde{V}(\mathbf{q}) = \int V(\mathbf{x}) e^{-i\mathbf{q}\cdot\mathbf{x}} d^3\mathbf{x}. \quad (4.3)$$

Here $q^\mu = k^\mu - k'^\mu = (q^0, \mathbf{q})$ is the momentum of the photon, where $k^\mu = (E, 0, 0, E)$ is the momentum of the incoming electron, and $k'^\mu = (E', E' \sin \theta \cos \phi, E' \sin \theta \sin \phi, E' \cos \theta)$ is the momentum of an electron scattered in the direction (θ, ϕ) (Figure 4.1). We neglect the electron's mass because it is negligible compared to its kinetic energy. The invariant photon mass satisfies $q^2 = -4EE' \sin^2 \frac{\theta}{2} = -\frac{4E^2 \sin^2 \frac{\theta}{2}}{1 + \frac{2E}{M} \sin^2 \frac{\theta}{2}}$, where M is the mass of the nucleus being scattered off. $V(\mathbf{x})$ is the electrostatic potential of the Skyrmion and \tilde{V} is simply the Fourier transform of this. The differential cross section, $\frac{d\sigma}{d\Omega}$, is proportional to $|\tilde{V}(\mathbf{q})|^2$.

It is desirable to have an expression for the scattering amplitude in terms of the charge density, ρ , rather than the potential, V , as it is the charge density (half the baryon density) that is known for Skyrmions. V and ρ are related by (4.1), and fortunately, the Laplacian is simple in Fourier space. The Fourier transform of the charge density

$$F(\mathbf{q}) = \int \rho(\mathbf{x}) e^{-i\mathbf{q}\cdot\mathbf{x}} d^3\mathbf{x}, \quad (4.4)$$

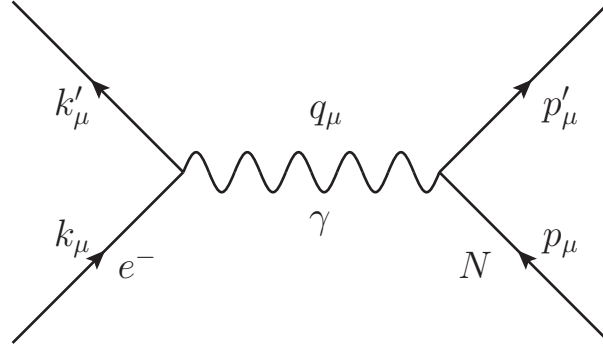


Fig. 4.1 Feynman diagram of the scattering process

is called the form factor. Equation (4.1) implies that $q^2 \tilde{V}(\mathbf{q}) = F(\mathbf{q})$, and the differential cross section [59] is

$$\frac{d\sigma}{d\Omega} = \frac{(B\alpha)^2}{16E^2 \sin^4 \frac{\theta}{2}} \frac{\cos^2 \frac{\theta}{2}}{1 + \frac{2E}{M} \sin^2 \frac{\theta}{2}} |F(\mathbf{q})|^2. \quad (4.5)$$

Here α is the fine-structure constant and B is the Baryon number. The prefactor is present for any charge density, so it is generally the modulus of the form factor $|F(\mathbf{q})|$ that is discussed. The scattering intensity is defined as $|F(\mathbf{q})|^2$.

The relationship between the form factor and the charge density in equation (4.4) only holds in the Breit frame (the frame where $q_0 = 0$ and $q^2 = -|\mathbf{q}|^2$), therefore one should take the Fourier transform of the Lorentz boosted charge density, not the static charge density. One of the effects of the Lorentz boost is to simply contract the nucleus when observed in the Breit frame; this has the effect of altering the argument of the Fourier transformed charge density. However, it is not trivial to determine how the boost operator acts upon a composite system and there are several different models [60, 61] which provide a relation between the form factor and the Fourier transform of a spherical charge density. They can be written in the form:

$$F(q^2) = \left(1 + \frac{q^2}{4M^2}\right)^{-n} \tilde{\rho} \left(\frac{q^2}{1 + \frac{q^2}{4M^2}}\right) \quad (4.6)$$

where $\tilde{\rho}$ is the Fourier transform of the charge density. The exponent n is model dependent, but typically a small positive integer.

In the Skyrme model we know that the charge density is proportional to the 0th component of the baryon current, B_μ , therefore we can simply apply a Lorentz transformation to this four vector to calculate the charge density in the boosted frame.

However, the largest value of q^2 that we consider in this chapter is 100 fm^{-2} , whereas the smallest nucleus considered is Helium-4 with mass $M \simeq 20 \text{ fm}^{-1}$, and so the largest value of $\frac{q^2}{4M^2}$ that we consider is around $1/16$. This is sufficiently small that we have decided to neglect the difference between the Breit frame and the lab frame in this chapter.

4.2.2 The quantum averaged intensity

We assume now that the electrons scatter off quantised Skyrmions in their spin zero ground state. The electrons therefore scatter off the spherically averaged charge density. This is obtained by integrating over a rotation matrix R , depending on three Euler angles, (α, β, γ) , with the standard normalised measure

$$dR = \frac{1}{8\pi^2} \sin \beta d\alpha d\beta d\gamma. \quad (4.7)$$

The spherically averaged charge density is

$$\rho(r) = \int \rho(R\mathbf{x}) dR \quad (4.8)$$

and is just a function of the radial coordinate, r . The form factor of the spherically averaged charge density is then

$$\mathcal{F}(q^2) = \int \rho(r) e^{-i\mathbf{q}\cdot\mathbf{x}} d^3\mathbf{x}, \quad (4.9)$$

and only depends on q^2 . (A calligraphic letter corresponds to a spherically averaged roman letter.)

To simplify this integral we may assume that $\mathbf{q} = (0, 0, q)$. Then using polar coordinates,

$$\begin{aligned} \mathcal{F}(q^2) &= \int \rho(r) e^{-iqr \cos \theta} r^2 \sin \theta dr d\theta d\phi \\ &= 2\pi \int \rho(r) e^{-iqr \cos \theta} r^2 \sin \theta dr d\theta \\ &= 2\pi \int \rho(r) \left[\frac{e^{-iqr \cos \theta}}{iqr} \right]_0^\pi r^2 dr \\ &= 4\pi \int_0^\infty \rho(r) \frac{\sin(qr)}{qr} r^2 dr \equiv 4\pi \int_0^\infty \rho(r) j_0(qr) r^2 dr, \end{aligned} \quad (4.10)$$

where $j_0(u) = \frac{\sin u}{u}$ is the zeroth spherical Bessel function.

As the Fourier transform is a linear operation, and the measure $d^3\mathbf{x}$ is rotationally invariant, the form factor of the spherically averaged charge density is the same as the spherically averaged form factor of the initial charge density. Therefore an alternative expression for $\mathcal{F}(q^2)$ is

$$\mathcal{F}(q^2) = \int F(R\mathbf{q}) dR, \quad (4.11)$$

where $F(\mathbf{q})$ is the form factor (4.4). Although this expression is less explicit than (4.10), we will have some use for it.

This form factor (or rather its modulus $|\mathcal{F}|$) is the function that is usually extracted from the experimental cross section data and gives one information about the spherically averaged charge density.

4.2.3 The angular velocity of a Skyrmion

It is important to know which electron energies allow us to treat the nucleus as having a fixed orientation, and therefore allow us to use the classical approximation.

Whilst the Skyrmion is originally spin 0 and therefore stationary, the electron scattering could cause the Skyrmion to rotate. It is difficult to know exactly what the resulting angular velocity would be, but we can consider the angular velocity of a spin 1 Skyrmion to get an estimate.

In order to calculate the angular velocity of the $B = 4$ Skyrmion, we need to choose values for F_π and e . The best way to do this is to calibrate to the mass and mean charge radius of an alpha particle, which requires $F_\pi = 87.3$ MeV and $e = 3.65$. This gives an energy unit of $\frac{F_\pi}{4e} = 5.98$ MeV and a length unit of $\frac{2}{eF_\pi} = 1.24$ fm. Thus the Skyrme unit of energy length becomes $\frac{F_\pi}{4e} \frac{2}{eF_\pi} = 7.39$ MeV fm, whilst $\hbar = 197$ MeV fm; therefore $\hbar = 26.7 = 2e^2$ in Skyrme units.

Consider the $B = 4$ Skyrmion rotating about the 3rd axis with angular momentum $L_3 = 1$; this means that the angular velocity $\omega = \frac{\hbar}{V_{33}}$, where $V_{33} = 663$ is the (3, 3) component of the spin inertia tensor in Skyrme units. Using this angular velocity and the mean charge radius (around 1.36 in Skyrme units), we calculate that the speed at the surface of the Skyrmion is around $\frac{1}{20}$ of the speed of light. This means that the time for the electron (travelling close to the speed of light) to cross the nucleus is around $\frac{1}{60}$ of the time for the nucleus to complete a full rotation.

For a roughly spherical object the moment of inertia is proportional to MR^2 , where M is the mass of the object and R is the radius, with the mass being proportional to R^3 . Thus, as we increase the baryon number of the Skyrmion (thereby increasing its mean charge radius), its angular velocity has a large suppression due to the increased

size. This means that the larger $B = 4N$ Skyrmions rotate more slowly than the $B = 4$ Skyrmion.

Therefore for all the Skyrmions considered, the time for the electron to scatter off the nucleus is much less than the period for a full rotation of the nucleus. Thus it is reasonable to treat the nucleus as having a fixed orientation during the scattering process for all electron energies of interest.

4.2.4 The classically averaged intensity

Here we assume that each electron scatters off a Skyrmion with fixed but random orientation, the Skyrmion having a non-spherically symmetric charge density. The contributions of the different orientations add incoherently, so the scattering intensities need to be spherically averaged over the orientations to find the total intensity.

For a Skyrmion with fixed orientation, the intensity is

$$I(\mathbf{q}) = |F(\mathbf{q})|^2 \quad (4.12)$$

$$= \int \rho(\mathbf{x}) \rho(\mathbf{x}') e^{i\mathbf{q}\cdot(\mathbf{x}-\mathbf{x}')} d^3\mathbf{x} d^3\mathbf{x}'. \quad (4.13)$$

If one writes $\mathbf{x}' = \mathbf{x} + \mathbf{w}$, and replaces the \mathbf{x}' integral by an integral over \mathbf{w} , then

$$I(\mathbf{q}) = \int \rho(\mathbf{x}) \rho(\mathbf{x} + \mathbf{w}) e^{-i\mathbf{q}\cdot\mathbf{w}} d^3\mathbf{x} d^3\mathbf{w}. \quad (4.14)$$

The \mathbf{x} integral here,

$$P(\mathbf{w}) = \int \rho(\mathbf{x}) \rho(\mathbf{x} + \mathbf{w}) d^3\mathbf{x}, \quad (4.15)$$

is called the Patterson function. Then

$$I(\mathbf{q}) = \int P(\mathbf{w}) e^{-i\mathbf{q}\cdot\mathbf{w}} d^3\mathbf{w}, \quad (4.16)$$

so the intensity is the Fourier transform of the Patterson function.

The Patterson function is employed in crystallography as a method of determining the interatomic distances in a crystal. It is not possible to calculate the charge density precisely as this would require knowledge of the phase and amplitude of the form factor, whereas the scattering intensity only provides the amplitude. A diffraction experiment has no way of finding out these phases, therefore the Patterson function is an important tool when trying to determine the structure of a crystal because it only requires knowledge of the scattering intensity.

Changing the orientation involves a rotation matrix R depending on Euler angles, (α, β, γ) , as before. We can define a rotationally averaged Patterson function

$$P(w) = \int P(R\mathbf{w}) dR, \quad (4.17)$$

which is just a function of $w = |\mathbf{w}|$. Then, by repeating the steps in subsection 2.2, we obtain the classically averaged intensity

$$\mathcal{I}(q^2) = 4\pi \int_0^\infty P(w) j_0(qw) w^2 dw. \quad (4.18)$$

Again there is an alternative expression, directly in terms of the charge density,

$$\mathcal{I}(q^2) = \int \rho(\mathbf{x}) \rho(\mathbf{x}') e^{iR\mathbf{q} \cdot (\mathbf{x} - \mathbf{x}')} d^3\mathbf{x} d^3\mathbf{x}' dR, \quad (4.19)$$

which simplifies to

$$\mathcal{I}(q^2) = \int \rho(\mathbf{x}) \rho(\mathbf{x}') j_0(q|\mathbf{x} - \mathbf{x}'|) d^3\mathbf{x} d^3\mathbf{x}', \quad (4.20)$$

a Debye-type scattering formula.

Note that we can also express this classically averaged intensity in terms of the form factor. From (4.19),

$$\mathcal{I}(q^2) = \int |F(R\mathbf{q})|^2 dR. \quad (4.21)$$

While it is straightforward to calculate $\mathcal{I}(q^2)$ from a given charge density, one cannot reconstruct the charge density from $\mathcal{I}(q^2)$. There are essential ambiguities in the reconstruction.

Properties of the Patterson function

The Patterson function has a couple of properties which hold for any charge distribution. It is invariant under $\mathbf{w} \rightarrow -\mathbf{w}$; this follows easily from the definition:

$$P(\mathbf{w}) = \int \rho(\mathbf{x}) \rho(\mathbf{x} + \mathbf{w}) d^3\mathbf{x} = \int \rho(\mathbf{x} - \mathbf{w}) \rho(\mathbf{x}) d^3\mathbf{x} = P(-\mathbf{w}), \quad (4.22)$$

where the second equality follows from a simple change of variables.

The second universal property is that $P(\mathbf{w})$ is maximal at $\mathbf{w} = \mathbf{0}$. We have, for any real a ,

$$\int (\rho(\mathbf{x}) + a\rho(\mathbf{x} + \mathbf{w}))^2 d^3\mathbf{x} \geq 0, \quad (4.23)$$

and after expanding the bracket,

$$\int \rho(\mathbf{x})^2 d^3\mathbf{x} + 2a \int \rho(\mathbf{x}) \rho(\mathbf{x} + \mathbf{w}) d^3\mathbf{x} + a^2 \int \rho(\mathbf{x} + \mathbf{w})^2 d^3\mathbf{x} \geq 0. \quad (4.24)$$

The first and third integrals are both equal to $P(\mathbf{0}) = \int \rho(\mathbf{x})^2 d^3\mathbf{x}$, because the domain of integration is all of space. The second integral is equal to $P(\mathbf{w})$, therefore

$$(1 + a^2)P(\mathbf{0}) + 2aP(\mathbf{w}) \geq 0 \quad (4.25)$$

for all a . This implies the discriminant condition

$$P(\mathbf{w})^2 \leq P(\mathbf{0})^2, \quad (4.26)$$

so the Patterson function is maximal at the origin.

4.2.5 Comparison of the scattering intensities

The classically averaged intensity, $\mathcal{I}(q^2)$, is the average of $|F(\mathbf{q})|^2$ over all directions \mathbf{q} ,

$$\mathcal{I}(q^2) = \int |F(R\mathbf{q})|^2 dR, \quad (4.27)$$

whereas the quantum averaged intensity, $|\mathcal{F}(q^2)|^2$, is the modulus squared of the average of $F(\mathbf{q})$ over all directions \mathbf{q} ,

$$|\mathcal{F}(q^2)|^2 = \left| \int F(R\mathbf{q}) dR \right|^2. \quad (4.28)$$

These are fundamentally different objects, and a Cauchy–Schwartz inequality informs us that $|\mathcal{F}(q^2)|^2 \leq \mathcal{I}(q^2)$.

We will present $|\mathcal{F}|$ and $\sqrt{\mathcal{I}}$ against q^2 for all the Skyrmions in this chapter, in order to illustrate the differences between the quantum and classically averaged intensities. Experimental electron scattering data is usually presented as the modulus of the form factor, $|\mathcal{F}|$, plotted against q^2 . It should be noted that extrema of \mathcal{F} appear as extrema of $|\mathcal{F}|$, but $|\mathcal{F}|$ has additional sharp minima at the zeros of \mathcal{F} . Thus it can be helpful to plot \mathcal{F} as well as $|\mathcal{F}|$, but this is only known in theoretical calculations, and not from the experimental data.

The formula (4.27) shows that $\mathcal{I}(q^2)$ is non-negative, and $\mathcal{I}(q^2)$ is zero for some value of q^2 only if $F(\mathbf{q}) = 0$ for all \mathbf{q} with $q^2 = |\mathbf{q}|^2$. For a non-spherically symmetric

charge distribution this is a shell of independent conditions, not generally all satisfied, so we would not expect $\mathcal{I}(q^2)$ to have any zeros.

For a spherically symmetric charge density, $F(\mathbf{q})$ is independent of the direction of \mathbf{q} , so this shell of conditions collapses to a single condition, and the intensity $\mathcal{I}(q^2)$ will generically have zeros. There are also extreme examples of non-spherically symmetric charge distributions for which $\mathcal{I}(q^2)$ has zeros.

This shows that there is an important difference between the electron scattering intensities of spherically and non-spherically symmetric models of nuclei; we expect some zeros in the former case and no zeros in the latter. This is also a difference between quantum and classically averaged intensities. Unfortunately, it is a difference that is difficult to probe by experiment. In an electron scattering experiment the differential cross section can only be found for a discrete set of momenta, \mathbf{q} . This means that there is effectively no chance of finding a value of q^2 that yields a zero in the intensity; thus, we are not able to distinguish between a sharp minimum and a zero.

4.3 Scattering intensities of $B = 4N$ Skyrmions

4.3.1 Calibration of Skyrme units

In order to compare our intensities with experimental scattering data, we need to perform some calibrations. We normalise the charge density ρ , so that it integrates to 1 over all space. This means that $\sqrt{\mathcal{I}}$ and $|\mathcal{F}|$ will be equal to 1 at $q^2 = 0$. In graphs of experimental scattering data the form factor is usually presented as $|\mathcal{F}(q^2)|/|\mathcal{F}(0)|$, so our choice of normalisation enables easier comparison with the data.

The Skyrmion's length scale is measured in Skyrme units, and the parameters F_π and e decide the conversion factor from Skyrme units to MeV and fermi. We must decide on a length scale of the nucleus to calibrate to, and there are a few choices. The most sensible choice [62] appears to be the (root mean square) charge radius, the square root of

$$\langle r^2 \rangle = \int \rho(\mathbf{x}) r^2 d^3\mathbf{x} = 4\pi \int_0^\infty \rho(r) r^4 dr. \quad (4.29)$$

This is a measure of the total size of a nucleus, and $\langle r^2 \rangle$ appears naturally in the spherically averaged form factor. For small q^2

$$\mathcal{F}(q^2) = 4\pi \int_0^\infty \rho(r) \frac{\sin qr}{qr} r^2 dr \approx 4\pi \int_0^\infty \rho(r) \left(1 - \frac{1}{3!} q^2 r^2\right) r^2 dr = 1 - \frac{q^2}{6} \langle r^2 \rangle. \quad (4.30)$$

We see that $\langle r^2 \rangle$ is -6 times the gradient of $\mathcal{F}(q^2)$ with respect to q^2 at the origin, so by calibrating to this we will have the correct charge radius.

An alternative calibration would be to fix the length scale such that the first minimum of the calculated and experimental scattering intensities are at the same value of q^2 . But this seems less fundamental, especially since the relation between characteristic length scales and locations of minima in momentum space is a complicated one.

The parameter set $F_\pi = 75.2$ MeV, $e = 3.26$ and $m_\pi = 138$ MeV provide reasonable accuracy for the masses and mean charge radii of several Skyrmions [62]. However, in this chapter we decided to recalibrate the parameter values such that the mean charge radius was correct for all the Skyrmions considered and the pion mass was fixed at 1. Therefore the parameters depend on baryon number.

Experimental values in Table 4.1 for $\langle r^2 \rangle^{\frac{1}{2}}$ are taken from [63]. The charge radius of Beryllium-8 is unknown due to its instability, so we will use the charge radius of Beryllium-9 instead (the instability also results in a lack of experimental scattering data to compare with, thus calibration is less important). $B = 108$ also poses a problem; an isotope with equal numbers of protons and neutrons at that baryon number would be highly unstable. In addition, charge radii calculations are usually model dependent in this region; we choose $^{107}_{47}\text{Ag}$ as a candidate, taking the value of $\langle r^2 \rangle$ from [64].

Baryon Number	$B = 4$	$B = 8$	$B = 12$	$B = 16$	$B = 32$	$B = 108$
$\langle r^2 \rangle^{\frac{1}{2}} \text{fm}$	1.68	2.52	2.47	2.70	3.26	4.50

Table 4.1 Table of charge radii for nuclei with zero isospin. The entries for $B = 8$ and $B = 108$ are estimates.

We ignore most of the Skyrmions after $B = 16$ because there is less confidence in their baryon densities. There is more confidence in $B = 32$ and $B = 108$ because of their cubic structure.

4.3.2 The $B = 4$ Skyrmion

The $B = 4$ Skyrmion is cubically symmetric (left image of Figure 4.2). The charge density (half the baryon density) is easily evaluated, and from this the spherically averaged form factor is calculated. Evaluating the Patterson function leads to the classically averaged intensity.

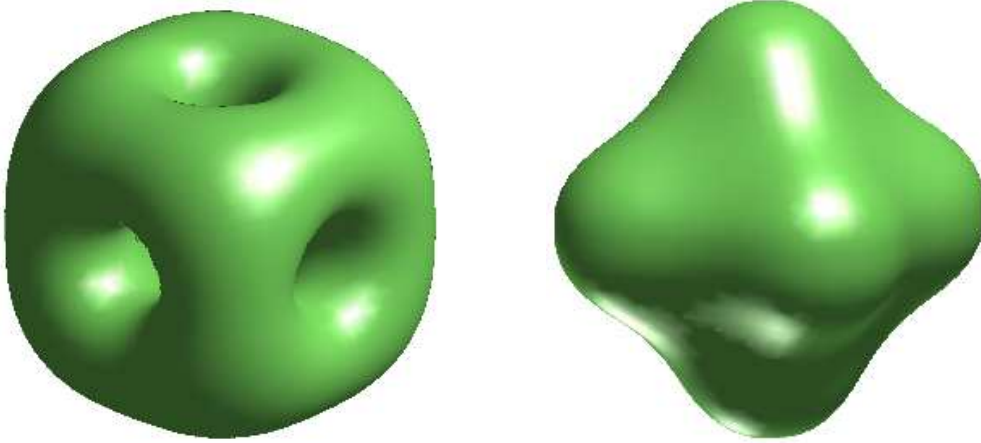


Fig. 4.2 Charge density and Patterson function isosurfaces for the $B = 4$ Skyrmion.

The Patterson function of the $B = 4$ Skyrmion

There are two main ways to see how the Patterson function, $P(\mathbf{w})$, varies with shift vector, \mathbf{w} . The first is to take an isosurface plot of $P(\mathbf{w})$, which shows surfaces of constant P . The second is to take a planar slice in \mathbf{w} -space and plot contours of constant P . All representations of the Patterson function will be in Skyrme units; these will then be converted into fermi (fm) to calculate intensities.

The Patterson function of the $B = 4$ Skyrmion is spherically symmetric for small w , where $w = |\mathbf{w}|$, and as w increases it takes on the shape of a concave octahedron (right image of Figure 4.2). The slowest descent occurs along shift vectors \mathbf{w} corresponding to the primary x, y, z axes of the $B = 4$ Skyrmion. We see from the left image of Figure 4.2 that the regions of highest charge density are the corners and edges of the $B = 4$ cube, so when we shift along the Cartesian axes by $w = a \approx 1.4$, the distance between opposite faces, there is strong overlap of high density regions. This is in contrast to shifting along the body diagonal direction; here one of the corners travels into the hollow centre of the cube, resulting in a weak overlap. As w increases further, the concave edges of the octahedron become convex. This is followed by the faces becoming convex, producing approximately cubic contours.

Figure 4.3 shows a contour plot of $P(\mathbf{w})$ in the $x - y$ plane. Red corresponds to the highest values of P and blue to the lowest; this colour scheme is retained for all contour plots in this chapter. Taking a slice in the $x - y$ plane allows us to see in which regions P varies the least. We observe that the contours are most widely spaced at the points $(0, a)$, $(a, 0)$ and (a, a) (ignoring $(0, 0)$, which is always a maximum). The Patterson function approximately levels off at shift vectors, \mathbf{w} , corresponding to the

three distinct types of separation vector between corners of the $B = 4$ Skyrmion (along an edge, diagonally across a face, and diagonally across the body).

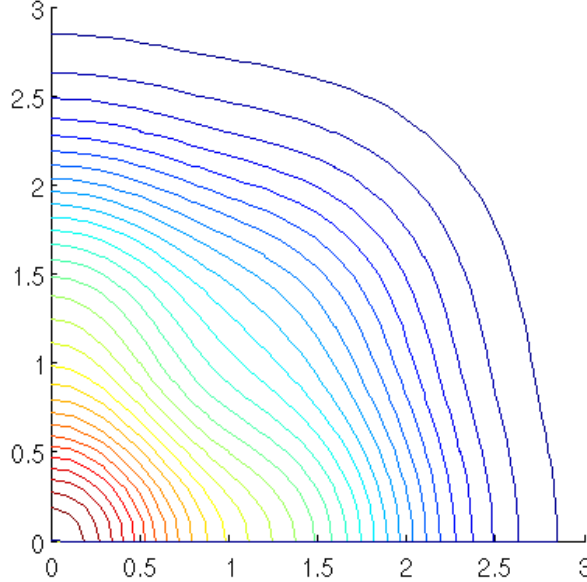


Fig. 4.3 Patterson function contours in the $x - y$ plane for the $B = 4$ Skyrmion.

The scattering intensity of the $B = 4$ Skyrmion

In Figure 4.4 the blue curve represents $\sqrt{\mathcal{I}}$ and the red curve represents $|\mathcal{F}|$ for the $B = 4$ Skyrmion, plotted on a logarithmic scale; this colour scheme and log scale are retained throughout the chapter. The Skyrmion has a characteristic length of around 1 fm, so our main interest is in q^2 greater than 1 fm^{-2} . We observe a minimum at $q^2 \approx 4.5 \text{ fm}^{-2}$ and close agreement between $\sqrt{\mathcal{I}}$ and $|\mathcal{F}|$ for $q^2 < 15 \text{ fm}^{-2}$.

The $B = 4$ Skyrmion is the best of the $B = 4N$ Skyrmions to compare with experimental data because electron scattering experiments on Helium-4 have been done up to $q^2 = 80 \text{ fm}^{-2}$. This is almost an order of magnitude greater than the highest energy data for other $B = 4N$ nuclei.

In Figure 4.4 the green circles represent experimental data for the form factor from electron scattering off a Helium-4 nucleus [65]. The shapes of the theoretical and experimental curves are quite similar for low values of q^2 , which is to be expected, because normalisation forces all three of them to have both $\mathcal{F}(0) = 1$ and the same gradient at $q^2 = 0$. There is a quite a difference in the q^2 value at the first minimum and an order of magnitude discrepancy in $|\mathcal{F}_{\max}|$, the value of $|\mathcal{F}|$ at the first maximum beyond the first minimum. The value of q^2 at the first minimum could be fixed by

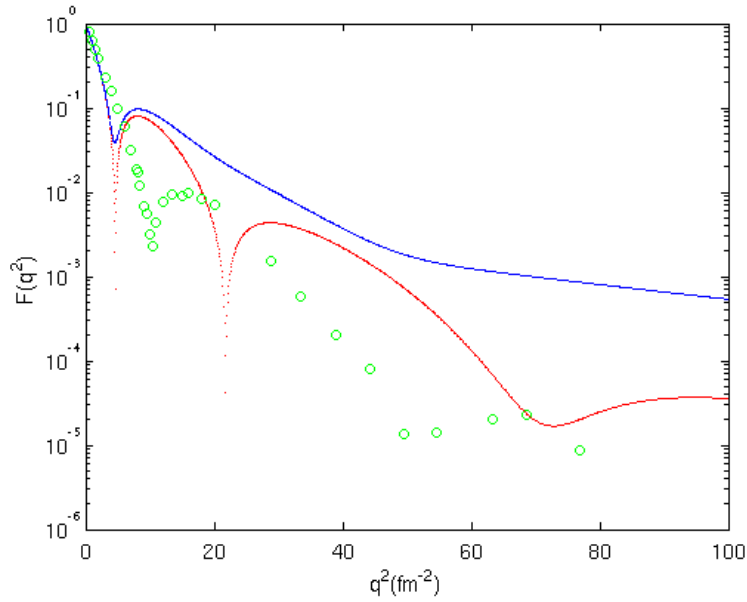


Fig. 4.4 Comparison of $\sqrt{\mathcal{I}}$ (blue) and $|\mathcal{F}|$ (red) for the $B = 4$ Skyrmion with the form factor from experimental scattering data (green) for the Helium-4 nucleus.

a different length calibration (although the derivatives at the origin would no longer match), but $|\mathcal{F}_{\max}|$ is much harder to rectify because it is independent of the calibration.

The experimental data curve has a second minimum at $q^2 \approx 52 \text{ fm}^{-2}$, whereas the classically averaged Skyrmion curve (blue) fails to predict a second diffraction minimum at any value of q^2 . The quantum averaged Skyrmion curve (red) fares better, although it has too many minima in the region that we are considering. However, if the Skyrme length unit is recalibrated such that the first minima of the quantum averaged curve and data curve are at the same value of q^2 , then the second minima of the curves are within a few fm^{-2} of each other, and the third minimum of the quantum averaged curve moves outside the region that has been probed by experiment. This does not fix all of the problems; the values of $|\mathcal{F}|$ at the second maxima of the curves would disagree by two orders of magnitude.

4.3.3 The $B = 8$ Skyrmion

The $B = 8$ Skyrmion is approximated by a pair of $B = 4$ cubes joined on a face. It comes in two different forms with very similar energies: linear and twisted [14]. There is only a small difference between the form factors and Patterson functions of these two Skyrmions; therefore we will only present the twisted variant (left image of Figure 4.5).

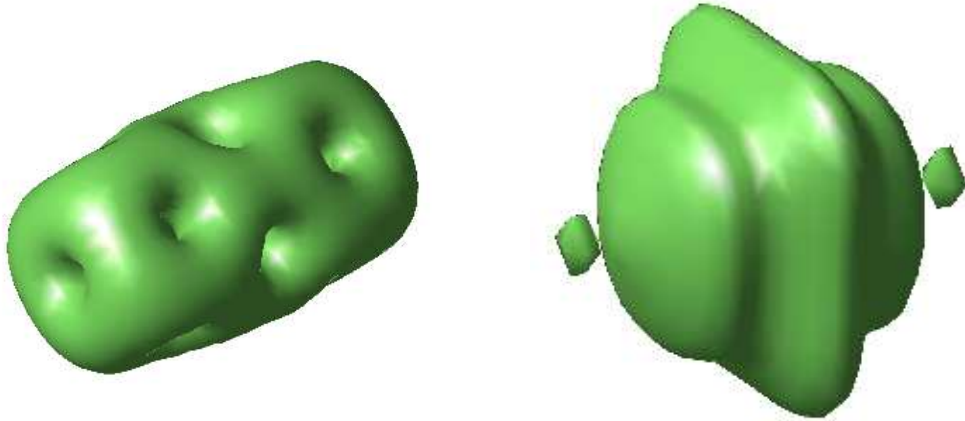


Fig. 4.5 Charge density and Patterson function isosurfaces for the twisted $B = 8$ Skyrmion.

The Patterson function of the $B = 8$ Skyrmion

The $B = 8$ Skyrmion has D_{4h} symmetry and this symmetry is inherited by the Patterson function (right image of Figure 4.5). In the $x - z$ plane (left image of Figure 4.6), with the y -axis corresponding the axis of C_4 symmetry, the Patterson function's contours display similar behavior to those of the $B = 4$ Skyrmion, which is not surprising, because shifting in this plane does not allow the two $B = 4$ cubes to overlap with each other. There is a slight reduction in concavity of the Patterson function for small w in comparison with the $B = 4$ Skyrmion, because the middle section of the $B = 8$ Skyrmion has different intrinsic axes to the cubes either side of it.

We see different behavior to the $B = 4$ case when shift vectors, \mathbf{w} , have a non-zero y component. The isosurface has an oscillatory nature, with level regions close to the various separation vectors between the 16 $B = 4$ cube corners of the $B = 8$ Skyrmion. There is a small range of values of P which exhibit disjoint isosurfaces; two balls occur when the shift vector is such that one cube coincides almost perfectly with the other cube. These balls indicate local maxima of the Patterson function, a feature not present for the Patterson function of the $B = 4$ Skyrmion.

A contour slice in the $x - y$ plane (right image of Figure 4.6) confirms these maxima. The slice also shows the locations of saddle points.

The scattering intensity of the $B = 8$ Skyrmion

The first minimum of $|\mathcal{F}|$ is not very close to a stationary point of $\sqrt{\mathcal{I}}$ as seen in Figure 4.7. The first minimum is related to the size of the Skyrmion, and we see

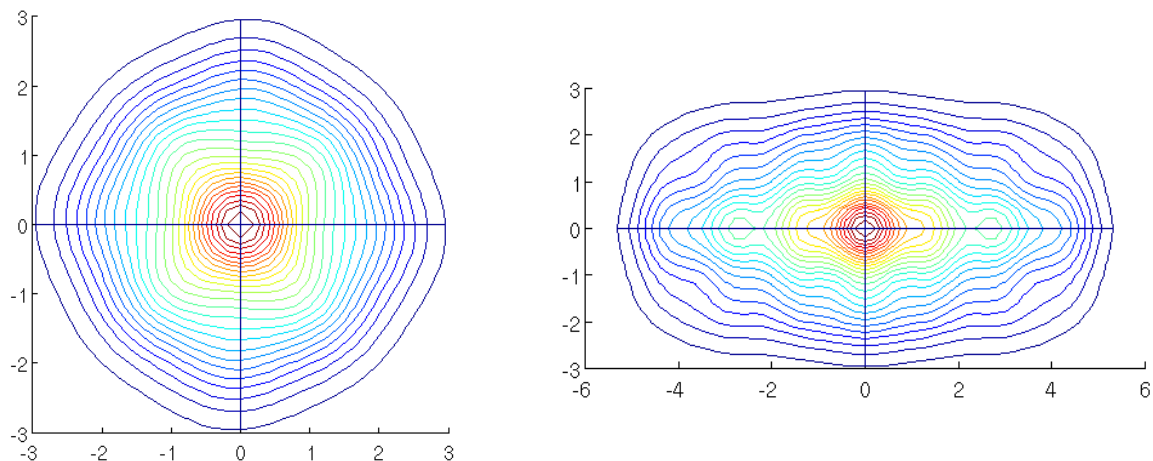


Fig. 4.6 Patterson function contours in the $x - z$ and $x - y$ planes for the twisted $B = 8$ Skyrmion.

that the intensity for the $B = 8$ Skyrmion has a first minimum at a lower value of q^2 ($\approx 3.4 \text{ fm}^{-2}$) than the $B = 4$ Skyrmion.

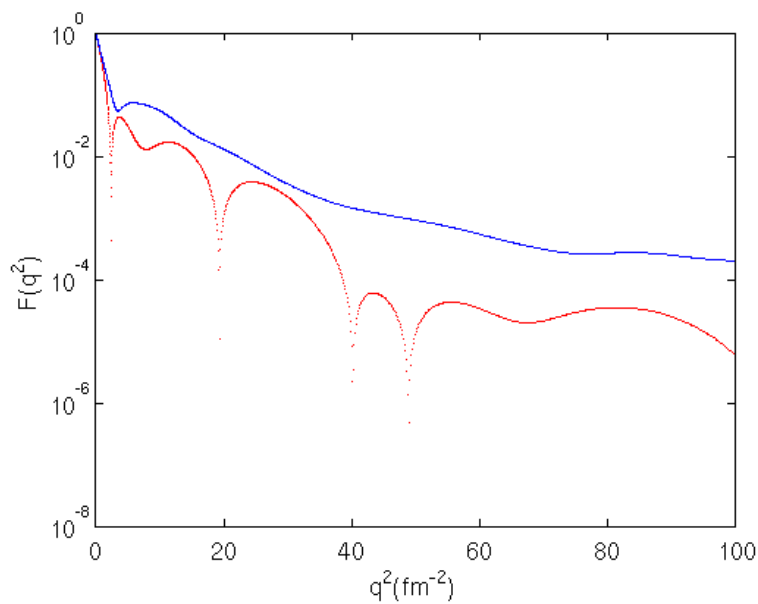


Fig. 4.7 \sqrt{I} and $|\mathcal{F}|$ for the twisted $B = 8$ Skyrmion

The spin zero $B = 8$ Skyrmion represents Beryllium-8, but this is very unstable, and there is no high-energy electron scattering data to compare with.

4.3.4 The $B = 12$ Skyrmion

We consider two different forms of the $B = 12$ Skyrmion: triangular and linear [14] as seen in the left and right images of Figure 4.8 respectively. The triangular Skyrmion, which has D_{3h} symmetry, corresponds to the ground state of ^{12}C modeled as a triangle of alpha particles. The linear Skyrmion, which has D_{4h} symmetry, corresponds to the Hoyle state modeled as a chain of alpha particles [17].

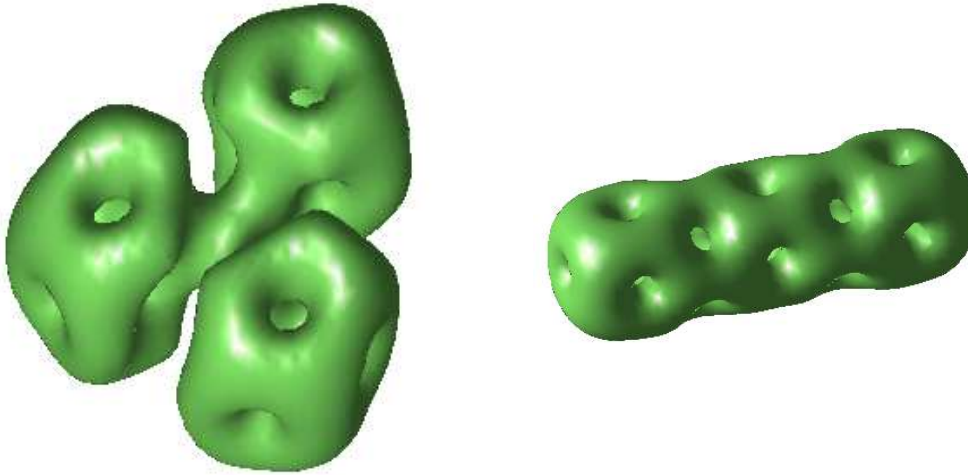


Fig. 4.8 Charge density isosurfaces for the triangular and linear $B = 12$ Skyrmions.

Patterson functions of the $B = 12$ Skyrmions

The triangular $B = 12$ Skyrmion:

The triangular $B = 12$ Skyrmion has C_3 symmetry about the z -axis, and this combines with the intrinsic $\mathbf{w} \rightarrow -\mathbf{w}$ symmetry of the Patterson function to give an overall D_{6h} symmetry of $P(\mathbf{w})$. The isosurface plots resemble a rounded hexagonal bipyramid (left image of Figure 4.9). The axes are chosen for this Skyrmion are defined such that the $x - z$ plane includes the origin and the centre of one of the three cubes. As seen in the left image of Figure 4.10 we see that the axis directions are distinguished for all but the largest shift vectors. This is because these directions correspond to one of the cubes shifting along an intrinsic axis, which results in a strong overlap of charge density. Rotating this plane by 30° about the z direction results in similar contours, but they are less oblong. When the cubes shift in the z direction, they have no overlap with themselves after moving more than a side length, so the Patterson function decreases rapidly.

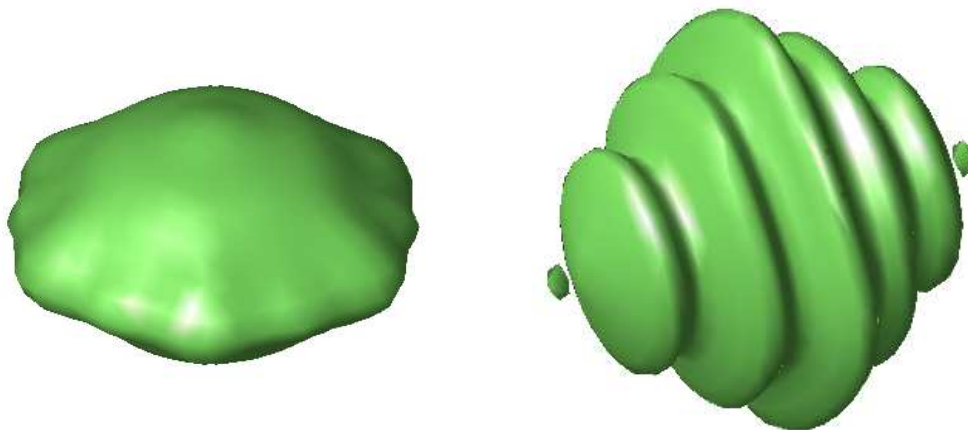


Fig. 4.9 Patterson function isosurfaces for the triangular and linear $B = 12$ Skyrmions.

The contours in the $x - y$ plane (right image of Figure 4.10) have a hexagonal structure, which reflects the symmetry of the Skyrmion.

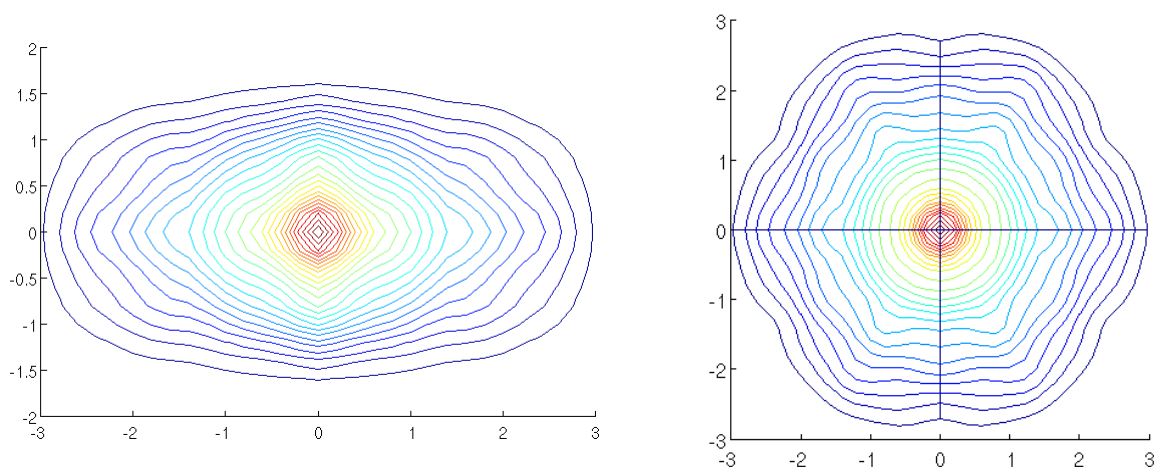


Fig. 4.10 Patterson function contours in the $x - z$ and $x - y$ planes for the triangular $B = 12$ Skyrmion.

The linear $B = 12$ Skyrmion:

The linear $B = 12$ Skyrmion is a chain of three $B = 4$ cubes with D_{4h} symmetry about the y -axis, and we expect similar characteristics to the $B = 8$ twisted Skyrmion. The Patterson function (right image pf Figure 4.9) also shares characteristics with that of the $B = 8$ Skyrmion.

In the $x - y$ plane (left image of Figure 4.11) there is a series of maxima and saddle points on the y -axis, with the oscillatory decreasing behaviour that we saw previously.

The presence of an extra cube increases the number of shift vectors between cube corners, which results in a greater number of local maxima and saddle points.

The Patterson function contours in the $x - z$ plane (right image of Figure 4.11) are almost the same as for the $B = 8$ Skyrmion; the presence of three $B = 4$ cubes rather than two making little difference.

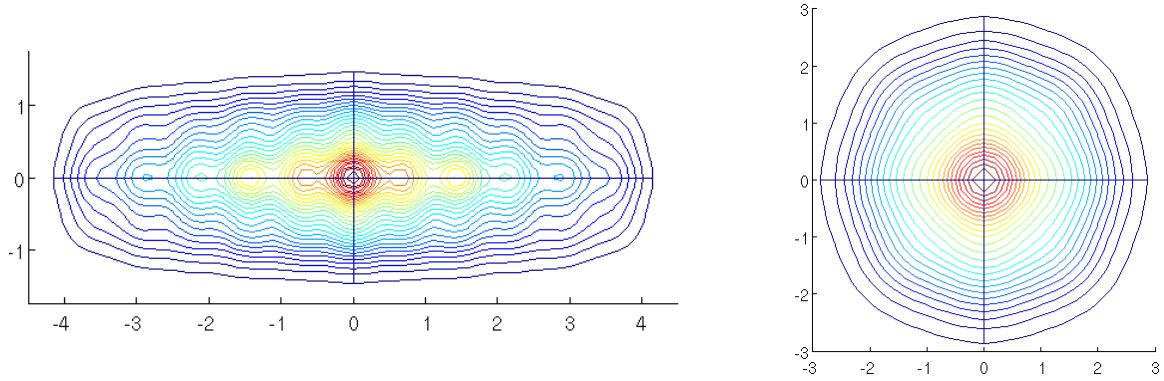


Fig. 4.11 Patterson function contours in the $x - y$ and $x - z$ planes for the linear $B = 12$ Skyrmion.

Scattering intensities of the $B = 12$ Skyrmions

The triangular $B = 12$ Skyrmion:

The first stationary point of $|\mathcal{F}|$ at $q^2 \approx 2.3 \text{ fm}^{-2}$ does not have a corresponding stationary point for $\sqrt{\mathcal{I}}$ (left image of Figure 4.12). The next two stationary points are in good agreement, but $\sqrt{\mathcal{I}}$ has a broad, flat maximum in between. This difference

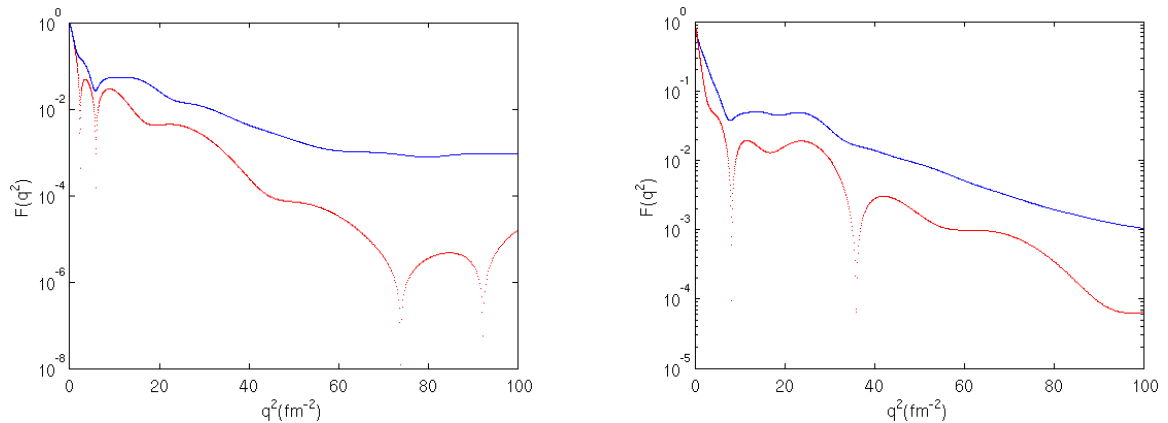


Fig. 4.12 $\sqrt{\mathcal{I}}$ and $|\mathcal{F}|$ for the triangular and linear $B = 12$ Skyrmions.

can be explained via looking at the profiles of $\rho(r)r^2$ and $P(w)w^2$, recalling that $\rho(r)$

and $P(w)$ refer to the spherically averaged charge density and Patterson function respectively.

The left image of Figure 4.13 displays the radial profile functions relevant to the triangular $B = 12$ Skyrmion. The green curve represents $\rho(r)r^2$, the blue curve represents $P(w)w^2$ and the red curve represents $j_0(qw) = \frac{\sin qw}{qw}$ for $q^2 \approx 12 \text{ fm}^{-2}$ which is the value at the midpoint of the broad maximum of $\sqrt{\mathcal{I}}$. As q^2 deviates slightly, away from 12 fm^{-2} , the third zero of $j_0(qw)$ moves across the maximum of $P(w)w^2$. However, this deviation does not produce a large change in $\sqrt{\mathcal{I}}$ because $P(w)w^2$ has a broad maximum. By contrast $\rho(r)r^2$ has quite a thin maximum, and this translates into a thinner maximum in $|\mathcal{F}|$.

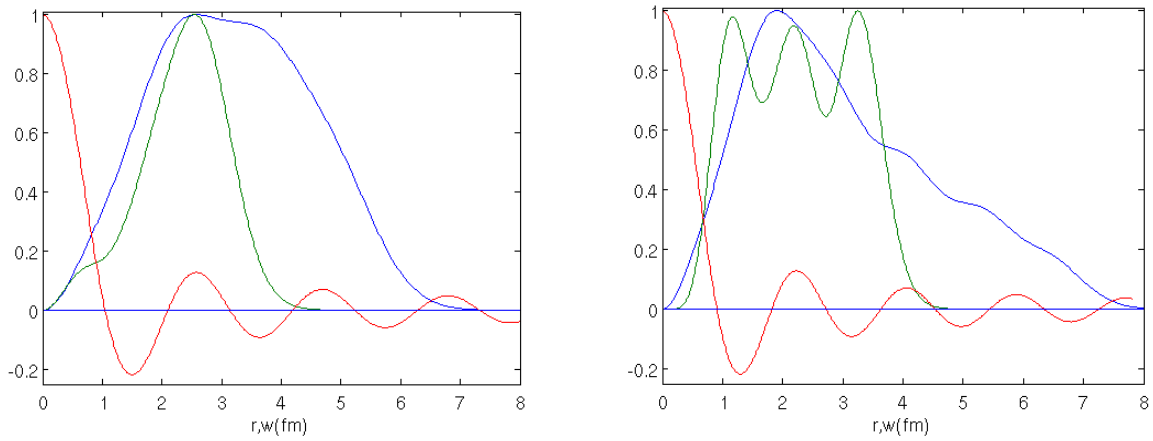


Fig. 4.13 Radial profile functions for the triangular and linear $B = 12$ Skyrmions: $\rho(r)r^2$ (green), $P(w)w^2$ (blue) and $j_0(qw)$ (red).

The linear $B = 12$ Skyrmion:

There is better agreement between the location of zeros and stationary points of $|\mathcal{F}|$ and $\sqrt{\mathcal{I}}$ (right image of Figure 4.12) for the $B = 12$ linear Skyrmion. The broad maximum of $\sqrt{\mathcal{I}}$ found for the triangular Skyrmion is no longer a feature because $P(w)w^2$ does not have a broad maximum. The second zero of $|\mathcal{F}|$ is at a considerably larger value of q^2 than the corresponding zero for the triangular Skyrmion. This is equivalent to saying that \mathcal{F} is negative for a larger range of q^2 . This increased range is caused by \mathcal{F} having a negative maximum between the two zeros (at around $q^2 = 17 \text{ fm}^{-2}$); this feature can be explained by looking at the radial profile, $\rho(r)r^2$. $\rho(r)r^2$ has three distinct peaks as seen in the right image of Figure 4.13, and the negative maximum of \mathcal{F} occurs when the first non-trivial maximum of $j_0(qr)$ coincides with the central maximum of $\rho(r)r^2$.

\mathcal{F} has a negative value because there is also coincidence of negative minima of $j_0(qr)$ with the two other positive maxima of $\rho(r)r^2$.

Comparison of the scattering intensity of the triangular $B = 12$ Skyrmion with experimental data

We only compare the triangular Skyrmion with experimental scattering data for Carbon-12 [66] because this is the Skyrmion that corresponds to the ground state. The comparison is shown in Figure 4.14.

The comparison of the scattering data with the classically averaged intensity $\sqrt{\mathcal{I}}$ suggests that the shoulder found in $\sqrt{\mathcal{I}}$ around $q^2 = 2.5 \text{ fm}^{-2}$ is not a desirable feature. The classical averaging method does, however, agree with the data about the number of minima in the range of q^2 considered.

$|\mathcal{F}|$ has quite a good agreement with the data up to the first minimum. But it predicts a second minimum shortly after the first, and this is not found in the experimental data.

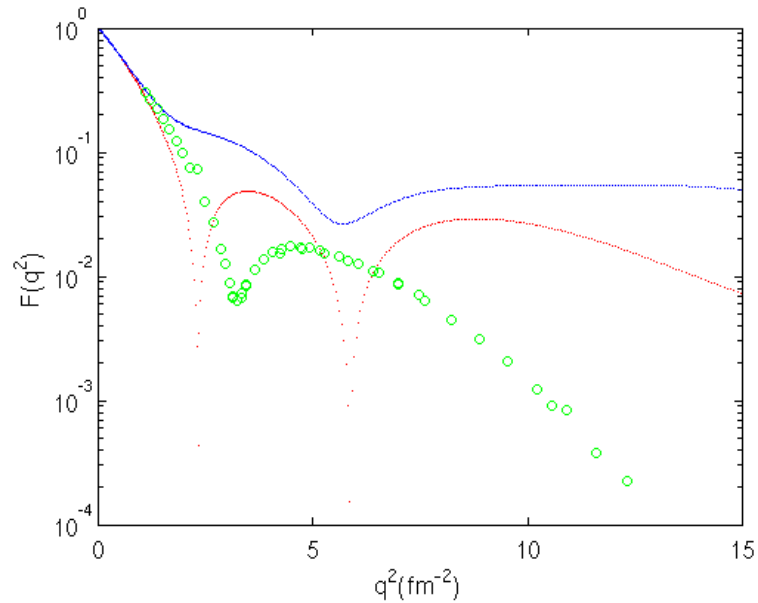


Fig. 4.14 Comparison of $\sqrt{\mathcal{I}}$ and $|\mathcal{F}|$ for the triangular $B = 12$ Skyrmion with the form factor from experimental scattering data for the Carbon-12 nucleus.

4.3.5 The $B = 16$ Skyrmion

The $B = 16$ Skyrmion (left image of Figure 4.15) is a bent square of four $B = 4$ cubes lying in the $x - z$ plane. It is midway between a flat square and a tetrahedral arrangement of $B = 4$ cubes as seen in chapter 2.

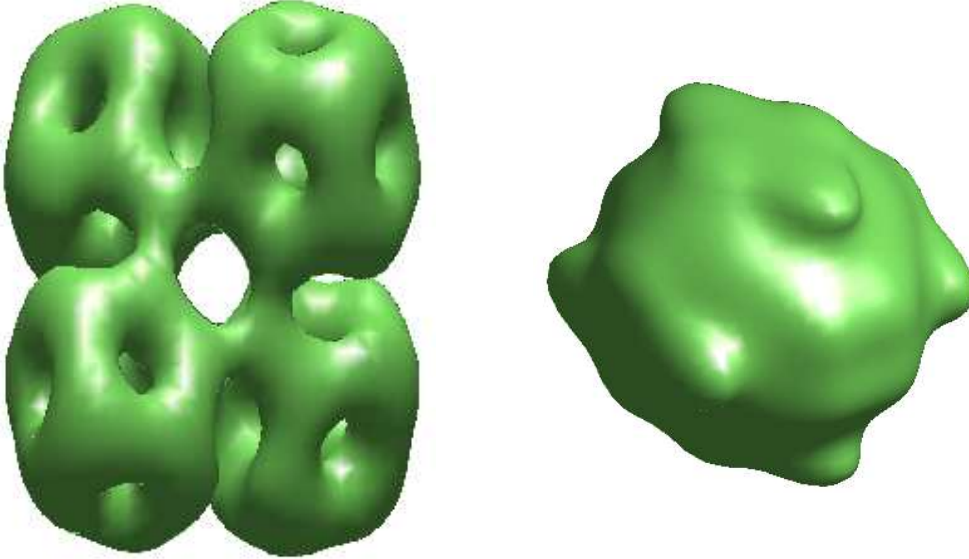


Fig. 4.15 Charge density and Patterson function isosurfaces for the $B = 16$ Skyrmion.

The Patterson function of the $B = 16$ Skyrmion

If one superimposes a second copy of the bent square that has undergone an inversion, $\mathbf{w} \rightarrow -\mathbf{w}$, on top of the original bent square, then this combination would have D_{4h} symmetry about the y -axis. The Patterson function has an intrinsic inversion symmetry, so it has this D_{4h} symmetry. Thus we have another example of the Patterson function having more symmetry than the Skyrmion that it is derived from. The Patterson function isosurface (right image of Figure 4.15) and contour plots (Figure 4.16) display this additional symmetry.

The scattering intensity of the $B = 16$ Skyrmion

$\sqrt{\mathcal{I}}$ has a shoulder whereas $|\mathcal{F}|$ has a zero at around $q^2 = 1.8 \text{ fm}^{-2}$ (Figure 4.17). This shoulder occurs when the first minimum of $j_0(qw)$ coincides with the maximum of $P(w)w^2$. $P(w)w^2$ has a broad maximum, which leads to a broad region of almost constant $\sqrt{\mathcal{I}}$. After this initial difference there is good agreement between the locations of stationary points and zeros of $\sqrt{\mathcal{I}}$ and $|\mathcal{F}|$.

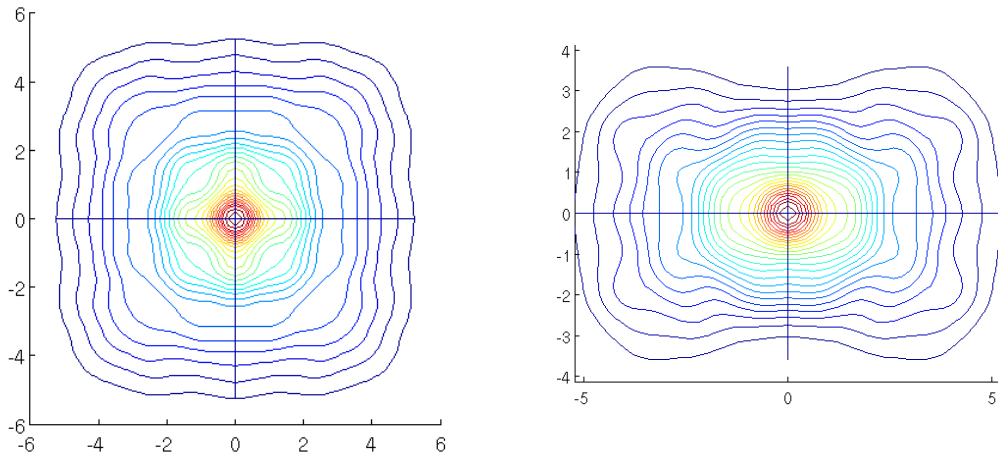


Fig. 4.16 Patterson function contours in the $x - z$ and $x - y$ planes for the $B = 16$ Skyrmion.

The calculated intensities for the $B = 16$ Skyrmion are compared with experimental electron scattering data off a Oxygen–16 nucleus [66] in Figure 4.17. The colour scheme is the same as in Figures 4.4 and 4.14.

We have further reinforcement that the shoulders observed in the classically averaged intensities of Skyrmions are not a desirable feature; they are again not present in the experimental data. The classically averaged intensity, $\sqrt{\mathcal{I}}$, bears little resemblance to the data curve.

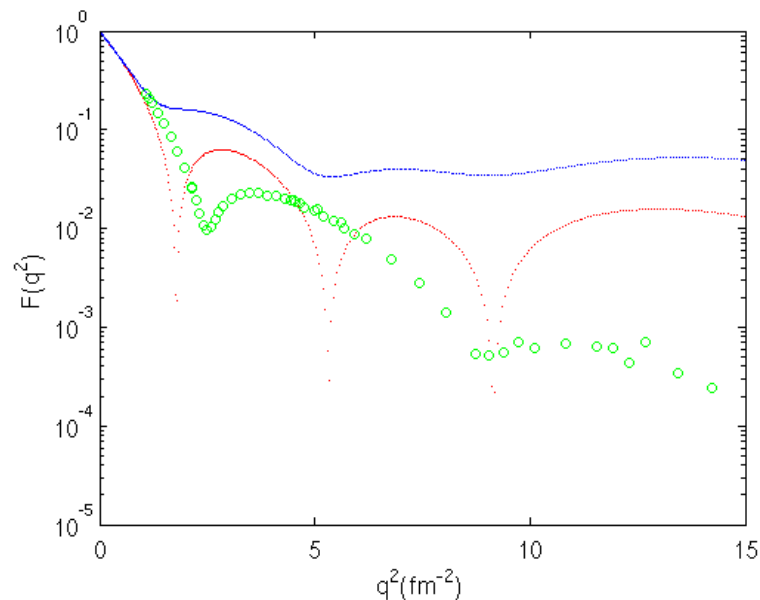


Fig. 4.17 Comparison of $\sqrt{\mathcal{I}}$ and $|\mathcal{F}|$ of the $B = 16$ Skyrmion with the form factor from experimental scattering data for the Oxygen–16 nucleus.

The form factor $|\mathcal{F}|$ again produces a closer fit to the data with quite good agreement up to the first minimum of the data curve. However, it still predicts too many minima in the data range that we are considering.

4.3.6 The $B = 32$ Skyrmion

The $B = 32$ Skyrmion has cubic symmetry as seen in the left image of Figure 4.18; it combines the internal symmetry of each $B = 4$ cube with the cubic arrangement of these cubes.

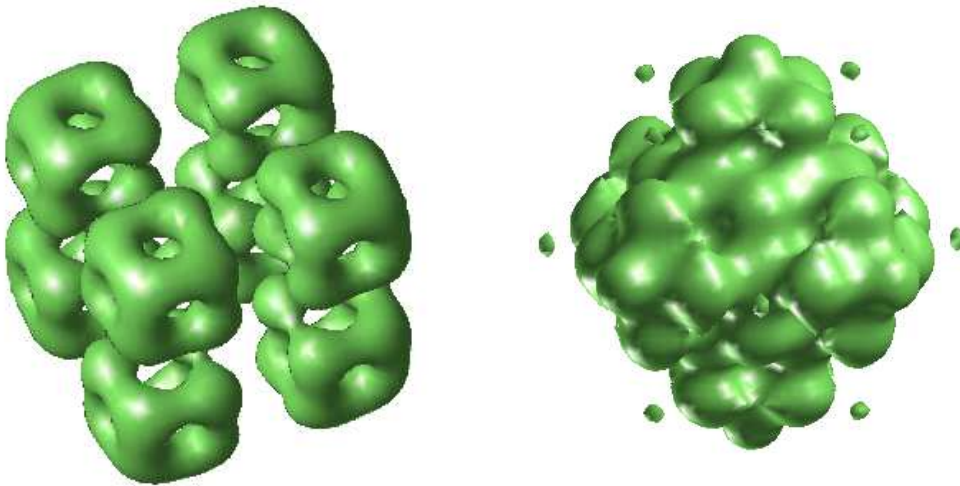


Fig. 4.18 Charge density and Patterson function isosurfaces for the $B = 32$ Skyrmion.

The Patterson function of the $B = 32$ Skyrmion

The cubic symmetry of the $B = 32$ translates to the Patterson function as seen in the right image of Figure 4.18. For small shift vectors, \mathbf{w} , the structure of the Patterson function is similar to that of a single $B = 4$ Skyrmion because the cubes are not yet overlapping. As we increase the shift vector, the Patterson function has local maxima occurring at shift vectors going between the centres of cubes; these manifest themselves as disjoint balls in the isosurface plots. Interestingly there are now some local minima, which appear as disjoint balls lying within the volume enclosed by the main isosurface. These minima occur at shift vectors going between the corner of a cube and the central cavity of a different cube.

The contour plot in Figure 4.19 give further information; $P(\mathbf{w})$ is small along vertical or horizontal lines with an axis intercept of 2.6 Skyrme units. $P(\mathbf{w})$ is large for axis

intercepts of 3.2 Skyrme units. This shows that alignment of the cubes in just one axis direction leads to a large value for P .

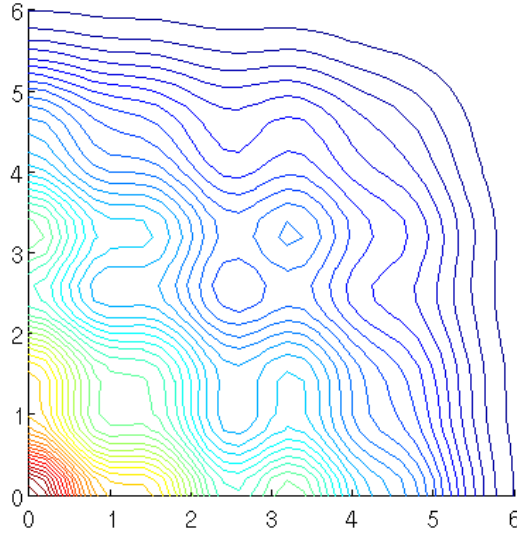


Fig. 4.19 Patterson function contours in the $x - y$ plane for the $B = 32$ Skyrmion.

The scattering intensity of the $B = 32$ Skyrmion

$\sqrt{\mathcal{I}}$ and $|\mathcal{F}|$ are in good agreement up to the first maximum at $q^2 \approx 2.2 \text{ fm}^{-2}$ (Figure 4.20). As q^2 increases, the agreement gets worse because $\sqrt{\mathcal{I}}$ has a shoulder whereas $|\mathcal{F}|$ has a minimum/maximum pair, but both curves have a minimum around $q^2 = 7.7 \text{ fm}^{-2}$.

4.3.7 The $B = 108$ Skyrmion

The $B = 108$ Skyrmion is essentially a larger version of the $B = 32$ Skyrmion [5]. It is a cubic arrangement of 27 $B = 4$ cubes as seen in the left image of Figure 4.21.

The Patterson function of the $B = 108$ Skyrmion

The Patterson function of the $B = 108$ Skyrmion (right image of Figure 4.21) is similar to that of the $B = 32$ Skyrmion, only more detailed. Another layer of cubes in the Skyrmion increases the number of shift vectors going between $B = 4$ cube corners, which causes more stationary points of $P(\mathbf{w})$, as seen in Figure 4.22.

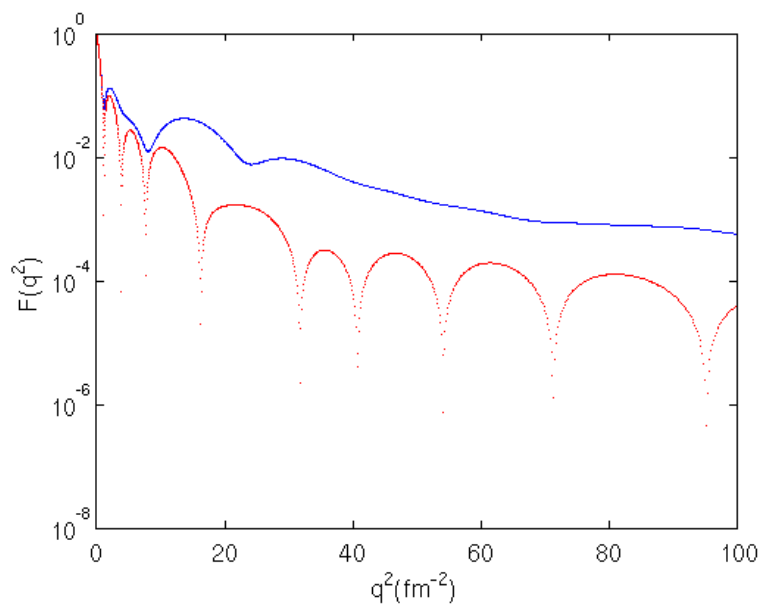


Fig. 4.20 $\sqrt{\mathcal{I}}$ and $|\mathcal{F}|$ for the $B = 32$ Skyrmion.

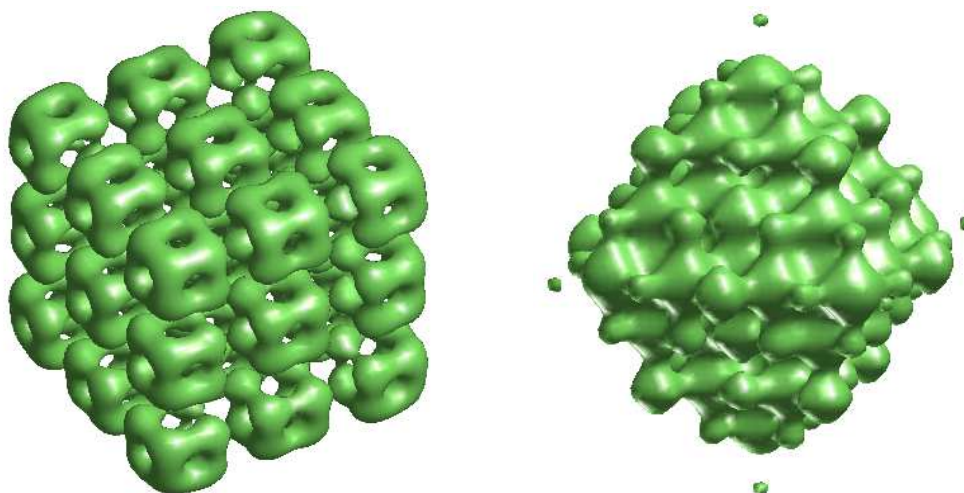


Fig. 4.21 Charge density and Patterson function isosurfaces for the $B = 108$ Skyrmion.

The scattering intensity of the $B = 108$ Skyrmion

The intensities (Figure 4.23) are also rather similar to those of the $B = 32$ Skyrmion; there are now more stationary points due to an increased number of relevant shift vectors.

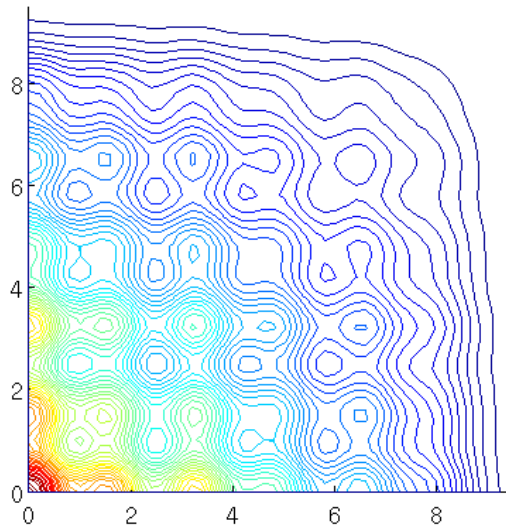


Fig. 4.22 Patterson function contours in the $x - y$ plane for the $B1082$ Skyrmion.

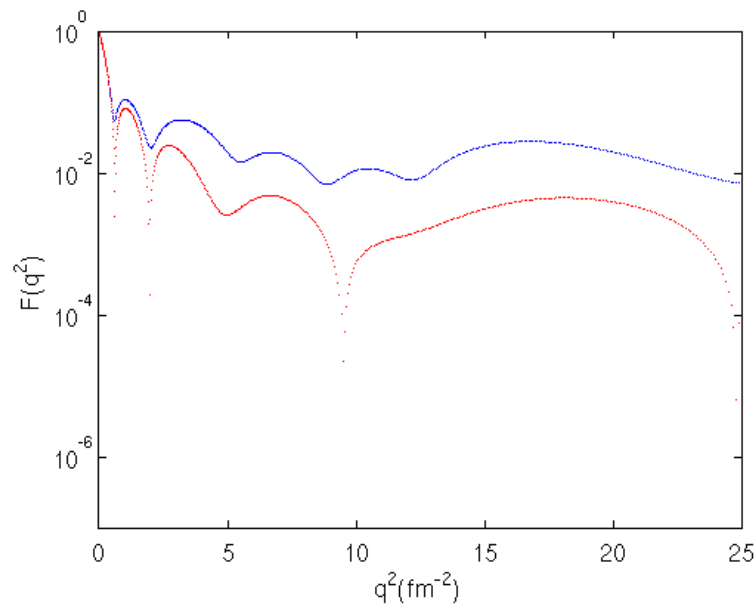


Fig. 4.23 $\sqrt{\mathcal{I}}$ and $|\mathcal{F}|$ for the $B = 128$ Skyrmion.

4.3.8 The Skyrme crystal

The Skyrme crystal can be viewed as an infinite cubic lattice of $B = 4$ Skyrmions with enhanced symmetries [67]. Its Patterson function can be well approximated by taking the central cube from a $B = 108$ Skyrmion, creating a $3 \times 3 \times 3$ grid of these, and calculating the Patterson function for the centre cube of this grid shifting towards its neighbours. The result is then extended periodically to give the Patterson function seen in Figure 4.24.

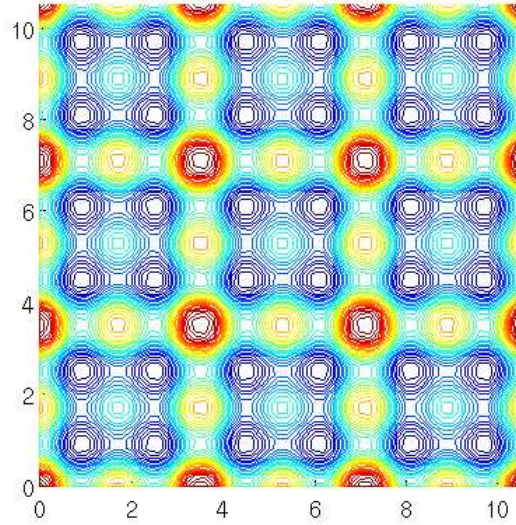


Fig. 4.24 Patterson function contours in the $x - y$ plane for the Skyrme crystal.

4.4 Approximating the zeros and stationary points of the form factor

It is important to know the locations of the zeros and stationary points of the form factor, \mathcal{F} . These locations are related to intrinsic features of the charge density, and it is useful to have an approximate method for finding them.

4.4.1 Zeros of the form factor

Consider the expression for the form factor, \mathcal{F} , in terms of the spherically averaged charge density, $\rho(r)$,

$$\mathcal{F}(q^2) = \int \rho(r) e^{-i\mathbf{q}\cdot\mathbf{x}} d^3\mathbf{x} = 4\pi \int_0^\infty \rho(r) r^2 \left(\frac{\sin qr}{qr} \right) dr. \quad (4.31)$$

Looking at this expression, it is not immediately obvious where the zeros of \mathcal{F} are. However, $\rho(r) r^2$ is quite localised and approximately symmetric about its maximum, so a truncated Taylor expansion of $\frac{\sin qr}{qr}$ about its first zero at $qr = \pi$ should lead to a good approximation to a value of q^2 where \mathcal{F} is zero.

For qr close to π ,

$$\frac{\sin qr}{qr} \simeq -\frac{1}{\pi}(qr - \pi) + \frac{1}{\pi^2}(qr - \pi)^2, \quad (4.32)$$

which gives an estimate for a zero of \mathcal{F} ,

$$\mathcal{F}(q^2) \simeq -4\pi \int_0^\infty \rho(r) r^2 \left(\frac{1}{\pi}(qr - \pi) - \frac{1}{\pi^2}(qr - \pi)^2 \right) dr = 0. \quad (4.33)$$

This implies that

$$\langle r^2 \rangle \left(\frac{q}{\pi} \right)^2 - 3\langle r \rangle \left(\frac{q}{\pi} \right) + 2 = 0, \quad (4.34)$$

where

$$\langle r^n \rangle = \int \rho(\mathbf{x}) r^n d^3\mathbf{x} = 4\pi \int_0^\infty \rho(r) r^{n+2} dr. \quad (4.35)$$

The solutions are

$$q = \frac{3\langle r \rangle \pm \sqrt{9\langle r \rangle^2 - 8\langle r^2 \rangle}}{2\langle r^2 \rangle} \pi, \quad (4.36)$$

and we choose the lower sign (smaller q) because the upper sign corresponds to the second zero of $\frac{\sin qr}{qr}$, and the approximation is poor to the right of this zero. We also only want to include one zero in the region of non-zero charge density. In conclusion, one can make a prediction for the location of the first zero of \mathcal{F} using only the first few radial moments of the charge density.

4.4.2 Stationary points of the form factor

The expression for $\frac{d\mathcal{F}}{dq^2}$ in terms of the charge density is

$$\frac{d\mathcal{F}}{dq^2} = \frac{2\pi}{q^2} \int \rho(r) r^2 \left(\cos qr - \frac{\sin qr}{qr} \right) dr. \quad (4.37)$$

Using a truncated Taylor series of $\left(\cos qr - \frac{\sin qr}{qr} \right)$ about its first positive zero leads to good approximation of the location of zeros of $\frac{d\mathcal{F}}{dq^2}$. The location of the first zero of $\left(\cos qr - \frac{\sin qr}{qr} \right)$ will be labeled by $qr = b$. The quadratic term of the Taylor series helpfully vanishes, so we are left with a linear equation to solve for q

$$\frac{d\mathcal{F}}{dq^2} \simeq -\frac{1}{2q^2} \int \rho(r) \sin b(qr - b) dr = 0, \quad (4.38)$$

which implies that

$$q = \frac{b}{\langle r \rangle}. \quad (4.39)$$

The stationary point lies at a value of q^2 such that $q\langle r \rangle$ (q times the mean of $\rho(r)r^2$) is equal to b .

The broad maxima found in the spherical averaged Patterson function, $P(w)$, means that the techniques above can not be used to approximate the stationary points of $\sqrt{\mathcal{I}}$. Many Skyrmions have good agreement between the locations of stationary points of $\sqrt{\mathcal{I}}$ and those of \mathcal{F} , but there does not seem to be a strong analytical link showing why. Some stationary points are only present in either $\sqrt{\mathcal{I}}$ or \mathcal{F} , so this good agreement cannot be used to approximate the locations of the stationary points of $\sqrt{\mathcal{I}}$ based on the approximations for \mathcal{F} .

4.4.3 Accuracy of approximations

Table 4.2 presents our estimated values of q^2 at the first zero and first minimum of \mathcal{F} compared to the actual values.

Skyrmion	Location of first zero (fm^{-2})		Location of first minimum (fm^{-2})	
	Approximation	Actual	Approximation	Actual
$B = 4$	4.57	4.57	7.47	8.01
$B = 8$ twisted	2.37	2.37	3.53	3.65
$B = 12$ triangular	2.38	2.31	3.66	3.50
$B = 12$ linear	n/a	8.18	3.89	11.63
$B = 16$	1.80	1.78	2.93	2.82
$B = 32$	1.15	1.15	2.04	1.96
$B = 108$	0.61	0.62	1.07	1.02

Table 4.2 Approximate and actual locations of first zero and first minimum of $\mathcal{F}(q^2)$.

The table shows that the approximations of the first zero and minimum of \mathcal{F} are generally very good. The exception is the linear $B = 12$ Skyrmion; the quadratic equation obtained from (4.34) for the zero of \mathcal{F} has no roots, and the prediction using (4.39) for the minimum is very far away from the actual location. This can be explained by noting the presence of the shoulder near $q^2 = 4 \text{ fm}^{-2}$ of \mathcal{F} (Figure 4.12) for the linear $B = 12$ Skyrmion. The location of the shoulder is close to our predicted location for the first stationary point of \mathcal{F} . The approximation finds the shoulder rather than the first true minimum of \mathcal{F} . The fact that \mathcal{F} does not have a zero before the shoulder explains why the quadratic equation (4.34) has no roots in this case.

4.5 Vibrational effects

In the quantum approach the electrons scatter off a spherically averaged charge density of the Skyrmion and in the classical approach the intensities obtained from scattering

off a fixed Skyrmion are found for each orientation and then it is these which are spherically averaged. In both cases the analysis involves scattering off of a rigid body, whereas we know that Skyrmions have vibrational degrees of freedom and that the ground state of a nucleus should be understood via a vibrational wavefunction over a space of distinct configurations [11, 36, 19, 20].

In chapter 2 we explicitly found these wavefunctions for the case of the E vibration of Oxygen–16. In this section we use these vibrational wavefunctions, along with an approximation for the charge densities of the configurations involved, to recalculate the form factor for Oxygen–16 in both the quantum and classical approaches. We show how this differs from the rigid body approach from section 4.3.5 and the experimental data in [66].

4.5.1 Approximation for the charge densities of Oxygen–16

In section 2.4.6 of chapter 2 we calculated the inertia tensors of configurations of Oxygen–16 in the red region of \mathcal{M}_H by treating configurations as a collection of four alpha particles with one particle at $\tilde{\mathbf{x}} = (\tilde{x}, \tilde{y}, \tilde{z}) = \left(\frac{\hat{x}(\zeta)}{\sqrt{1-\hat{z}(\zeta)^2}}, \frac{\hat{y}(\zeta)}{\sqrt{1-\hat{z}(\zeta)^2}}, \frac{\hat{z}(\zeta)}{\sqrt{1-\hat{z}(\zeta)^2}} \right)$, where $\hat{\mathbf{x}}(\zeta) = (\hat{x}, \hat{y}, \hat{z})$ is the point on the Riemann sphere corresponding to the point ζ on \mathcal{M}_H , and the other alpha particles at positions related by D_2 symmetry. Using these positions we create a crude approximation for the charge density of the corresponding configurations,

$$\rho(\mathbf{x}) = \frac{1}{4} \sum_{i=1}^4 \delta^{(3)}(\mathbf{x} - \tilde{\mathbf{x}}_i) \quad (4.40)$$

where $\tilde{\mathbf{x}}_1 = \tilde{\mathbf{x}} = (\tilde{x}, \tilde{y}, \tilde{z})$, $\tilde{\mathbf{x}}_2 = (\tilde{x}, -\tilde{y}, -\tilde{z})$, $\tilde{\mathbf{x}}_3 = (-\tilde{x}, \tilde{y}, -\tilde{z})$ and $\tilde{\mathbf{x}}_4 = (-\tilde{x}, -\tilde{y}, \tilde{z})$. The factor of $\frac{1}{4}$ is because we want a normalized charge density. Improvements of this approximation would treat the constituent alpha particles as extended objects with orientations depending on the coordinate ζ on \mathcal{M}_H . The approximation in (4.40) has the benefits of providing analytic expressions for many of the quantities that we wish to calculate.

4.5.2 The scattering intensity of a single configuration of Oxygen–16

To calculate the quantum averaged intensity it is helpful to first calculate the spherically averaged charge density, as in (4.8), and this calculation is simplified by the fact that $|\tilde{\mathbf{x}}_i|$ is the same for all i . Therefore the spherically averaged charge density must be a radial delta function,

$$\rho(r) = \frac{\delta(r - |\tilde{\mathbf{x}}|)}{4\pi r^2}, \quad (4.41)$$

where again the factors are determined by the normalisation. We now use the formula in (4.10) to calculate the spherically averaged form factor,

$$\mathcal{F}_0(q^2) = \frac{\sin q|\tilde{\mathbf{x}}|}{q|\tilde{\mathbf{x}}|}. \quad (4.42)$$

To calculate the classically averaged intensity it is helpful to consider the spherically averaged Patterson function, as defined in (4.17), and for the charge density in (4.40) this gives,

$$P(w) = \frac{1}{16\pi^2 w^2} \left(\delta(w) + \delta\left(w - 2\sqrt{\tilde{x}^2 + \tilde{y}^2}\right) + \delta\left(w - 2\sqrt{\tilde{z}^2 + \tilde{x}^2}\right) + \delta\left(w - 2\sqrt{\tilde{y}^2 + \tilde{z}^2}\right) \right). \quad (4.43)$$

We then use the Patterson function to evaluate the classical averaged intensity as defined in (4.19) to give,

$$\mathcal{I}_0(q^2) = \frac{1}{4} \left(1 + \frac{\sin\left(2q\sqrt{\tilde{x}^2 + \tilde{y}^2}\right)}{2q\sqrt{\tilde{x}^2 + \tilde{y}^2}} + \frac{\sin\left(2q\sqrt{\tilde{z}^2 + \tilde{x}^2}\right)}{2q\sqrt{\tilde{z}^2 + \tilde{x}^2}} + \frac{\sin\left(2q\sqrt{\tilde{y}^2 + \tilde{z}^2}\right)}{2q\sqrt{\tilde{y}^2 + \tilde{z}^2}} \right). \quad (4.44)$$

4.5.3 The scattering intensity of the ground state of Oxygen–16

Now that we have expressions for the quantum and classically averaged intensities of a single configuration we need to use the vibrational wavefunction for the ground state, $\psi_{T,0}^+$, to take an average over the vibrational manifold \mathcal{M} . This is achieved by performing the integrals,

$$\mathcal{F}(q^2) = \int |\psi_{T,0}^+(\zeta)|^2 \mathcal{F}_0(q^2) d\zeta \quad \text{and} \quad \mathcal{I}(q^2) = \int |\psi_{T,0}^+(\zeta)|^2 \mathcal{I}_0(q^2) d\zeta, \quad (4.45)$$

where the integrals are taken over the domain \mathcal{M}_H . $|\mathcal{F}|$ and $\sqrt{\mathcal{I}}$ are then the quantum and classical form factors of the ground state of Oxygen–16 in the Skyrme model. We could also take this vibrational average over a different wavefunction such as $\psi_{T,1}^+$ which corresponds to the first excited 0^+ state of Oxygen–16.

To see the effect of considering the vibrational degrees of freedom we should compare $|\mathcal{F}|$ and $\sqrt{\mathcal{I}}$ to $|\mathcal{F}_0|$ and $\sqrt{\mathcal{I}_0}$ calculated at the tetrahedral configuration; then the only difference is whether vibrational degrees of freedom are considered because the approximation for the charge densities is the same. We plot the quantum and classically averaged form factors for the ground state and first excited state of Oxygen–16 in Figure 4.25.

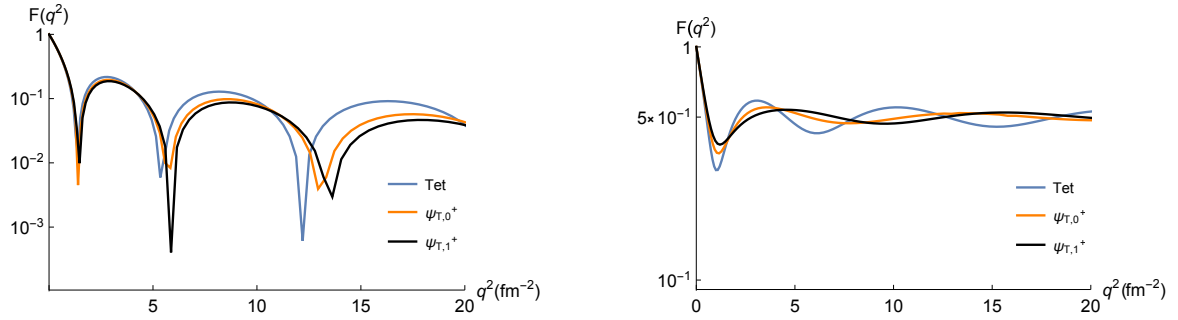


Fig. 4.25 The quantum (left) and classically (right) averaged form factors for the tetrahedral configuration and the vibrational wavefunctions, $\psi_{T,0}^+$ and $\psi_{T,1}^+$.

We see in Figure 4.25 that, for our crude approximation of the charge densities, there is not a significant difference between taking an average of the form factors over many different configurations via vibrational wavefunctions or just finding the form factor for the tetrahedral configuration. The quantum averaged form factor, $|\mathcal{F}|$, is not too different from the bent square calculation found in section 4.3.5 but there is a significant difference for the classical averaged form factor, $\sqrt{\mathcal{I}}$. The classically averaged form factor for the point particle approximation of charge density falls away much slower than the form factor from the more accurate bent square calculation. The point particle form factor also lacks the shoulder found in the graph of the bent square form factor in Figure 4.17.

4.6 Conclusions

We have calculated the charge densities and Patterson functions of several Skyrmions with baryon number a multiple of four. From these we have calculated the quantum averaged electron scattering intensity, $|\mathcal{F}(q^2)|^2$, and the classically averaged electron scattering intensity, $\mathcal{I}(q^2)$, for the Skyrmion's states with spin and isospin zero and found that there is a sizeable difference between them. This shows that it is important to make the distinction between the methods when considering non-spherically symmetric charge densities. However, we have found that neither method gives results in good agreement with experimental electron scattering data.

Of the two methods, the quantum averaged form factor gives the better fit to the experimental data; however, there are still some problems. For all of the Skyrmions that we have considered, the calculated intensity has too many minima when compared to the scattering data and the entire curve $|\mathcal{F}(q^2)|$ generally lies above the data points (a

problem exacerbated for the classically averaged intensity because of a Cauchy–Schwartz inequality).

There is also the problem that the calculated first minimum of the intensity is frequently at too low a momentum and that the intensity at the second maximum has a higher value than the experimental data. We have investigated the effect of introducing a central depression for a few well known charge densities and found that a large depression causes the various problems stated above. This would indicate that the region of near-zero baryon density found at the centre of many of the Skyrmions is a feature which does not agree with experimental electron scattering data.

Our hope was that vibrational averaging using the wavefunctions from chapter 2 of this thesis would result in a charge density with significantly less structure because the central region of near-zero baryon density would be partially washed-out. Unfortunately such vibrational averaging seems to have negligible effect on the form factors from either the quantum or classical methods.

We have found that it is possible to predict the locations of the first zero and stationary point of $|\mathcal{F}|$ using moments of the charge density. Disappointingly, we have also found that it is difficult to predict the locations of stationary points of $\sqrt{\mathcal{I}}$ using moments of the Patterson function. However, given their similarities, there is probably a link between the stationary points of $\sqrt{\mathcal{I}}$ and $|\mathcal{F}|$.

Chapter 5

Conclusions and outlook

In this thesis we have investigated a variety of different problems involving $B = 4N$ nuclei in the Skyrme model and as a result we have created novel techniques which can be applied to all Skyrmions. One of the key problems remaining is the energy spectrum of the $B = 4$ Skyrmion which should be tackled using vibrational quantisation. We already know the structure of its vibrational spaces and that a local approach is not sufficient but we hope that a global approach, as used in Chapter 2, will lead to an improvement of the current situation.

In Chapter 2 we studied the Oxygen-16 nucleus by approximating it as a collection of four $B = 4$ Skyrmions. The Skyrme model provided us with scattering lines which we then used to construct a vibrational manifold which the low energy $B = 16$ configurations. This approach provided an excellent fit with experimental data and a novel interpretation of some of the states in the energy spectrum. However, we only looked at the E vibration of the tetrahedron with our global approach. Our hope is that we can use the techniques that we have developed to improve our understanding of the A and F vibrations as well. Within the E vibration there is also some room for improvement; we would like to calculate the rotational energy in a non-perturbative way. We would also like to generate the potential on the vibrational manifold in a less ad hoc way perhaps by using the method for approximating the interaction energy between Skyrmions outlined in Chapter 3.

In Chapter 3 we developed a new way of approximating the interactions between Skyrmions in the hope that this could be used in vibrational quantisation and $B = 4N$ cluster nuclei. We built on the idea of using point multipoles by using Gaussian sources to generate the pion fields of Skyrmions. This gave us analytic approximation for the pion fields of and interaction energies between Skyrmions. We found accurate approximations for the first four Skyrmions, in particular the $B = 1$ Skyrmion, using

a method which could be easily extrapolated to larger Skyrmions such as the $B = 7$ Skyrmion. We compared our approximations for the interaction energy of Skyrmions with those obtained through numerical simulation and found a good fit for a few different situations, in particular we always improve upon the approximation found using point multipole sources. We then showed how our approximation could be applied to vibrational quantization and $B = 4N$ cluster nuclei.

In Chapter 4 we considered a novel way of interpreting electron scattering off slowly rotating nuclei and applied this to Skyrmions. We compared the quantum and classical methods of calculating scattering intensities and found the Patterson functions for several $B = 4N$ nuclei. Unfortunately we found that the scattering intensities for both methods did not agree with experimental data. We considered whether introducing vibrational degrees of freedom would alleviate this problem but found that it made little difference. However, we were able to find accurate approximations for the first zero and minimum of the form factor which could also be applied to different models for the baryon density of nuclei.

References

- [1] T.H.R. Skyrme, *A nonlinear field theory*, *Proc. R. Soc. Lond. A* **260** (1961) 127.
- [2] T.H.R. Skyrme, *Particle states of a quantized meson field*, *Proc. R. Soc. Lond. A* **262** (1961) 237.
- [3] G.H. Derrick, *Comments on nonlinear wave equations as models for elementary particles*, *J. Math. Phys.* **5** (1964) 1252.
- [4] C.J. Houghton, N.S. Manton and P.M. Sutcliffe, *Rational maps, monopoles and Skyrmions*, *Nucl. Phys. B* **510** (1998) 2.
- [5] D.T.J. Feist, P.H.C. Lau and N.S. Manton, *Skyrmions up to baryon number 108*, *Phys. Rev. D* **87** (2013) 085034.
- [6] G.S. Adkins, C.R. Nappi and E. Witten, *Static properties of nucleons in the Skyrme model*, *Nucl. Phys. B* **228** (1983) 552.
- [7] O.V. Manko, N.S. Manton and S.W. Wood, *Light nuclei as quantized Skyrmions*, *Phys. Rev. C* **76** (2007) 055203.
- [8] D. Finkelstein and J. Rubinstein, *Connection between spin, statistics and kinks*, *J. Math. Phys.* **9** (1968) 1762.
- [9] S. Krusch, *Finkelstein-Rubinstein constraints for the Skyrme model with pion masses*, *Proc. Roy. Soc. Lond. A* **462** (2006) 2001.
- [10] D. Giulini, *On the possibility of spinorial quantization of the Skyrme model*, *Mod. Phys. Lett. A* **8** (1993) 1917.
- [11] C. Barnes, W.K. Baskerville and N. Turok, *Normal modes of the $B = 4$ Skyrme soliton*, *Phys. Rev. Lett.* **79** (1997) 367.
- [12] W.T. Lin and B. Piette, *Skyrmion vibration modes within the rational map ansatz*, *Phys. Rev. D* **77** (2008) 125028.
- [13] P. Irwin, *Zero mode quantization of multi-Skyrmions*, *Phys. Rev.* **D61** (2000) 114024.
- [14] R. Battye, N.S. Manton and P. Sutcliffe, *Skyrmions and the alpha-particle model of nuclei*, *Proc. Roy. Soc. Lond. A* **463** (2007) 261.
- [15] J.M. Blatt and V.F. Weisskopf, *Theoretical Nuclear Physics*. Wiley, 1952.

- [16] D.M. Brink, H. Friedrich, A. Weiguny and C.W. Wong, *Investigation of the alpha-particle model for light nuclei*, *Phys. Lett. B* **33** (1970) 143.
- [17] P.H.C. Lau and N.S. Manton, *States of Carbon-12 in the Skyrme model*, *Phys. Rev. Lett.* **113** (2014) 232503.
- [18] M. Haberichter, P.H.C. Lau and N.S. Manton, *Electromagnetic transition strengths for light nuclei in the Skyrme model*, *Phys. Rev.* **C93** (2016) 034304.
- [19] J.I. Rawlinson, *An alpha particle model for Carbon-12*, *Nucl. Phys. A* **975** (2018) 122.
- [20] C.J. Halcrow, C. King and N.S. Manton, *A dynamical α -cluster model of ^{16}O* , *Phys. Rev. C* **95** (2017) 031303.
- [21] J. A. Wheeler, *Molecular viewpoints in nuclear structure*, *Phys. Rev.* **52** (1937) 1083.
- [22] D.M. Dennison, *Energy levels of the ^{16}O nucleus*, *Phys. Rev.* **96** (1954) 378.
- [23] R. Bijker and F. Iachello, *Evidence for tetrahedral symmetry in ^{16}O* , *Phys. Rev. Lett.* **112** (2014) 152501.
- [24] R. Bijker and F. Iachello, *The algebraic cluster model: structure of ^{16}O* , *Nucl. Phys.* **A957** (2017) 154.
- [25] W. Bauhoff, H. Schultheis and H. Schultheis, *Alpha cluster model and the spectrum of ^{16}O* , *Phys. Rev.* **C29** (1984) 1046.
- [26] E. Epelbaum, H. Krebs, T.A. Lähde, D. Lee, U.G. Meißner and G. Rupak, *Ab initio calculation of the spectrum and structure of ^{16}O* , *Phys. Rev. Lett.* **112** (2014) 102501.
- [27] J.K. Perring and T.H.R. Skyrme, *The alpha-particle and shell models of the nucleus*, *Proc. Phys. Soc. Lond.* **A69** (1956) 600.
- [28] W.H. Bassichis and G. Ripka, *A Hartree-Fock calculation of excited states of ^{16}O* , *Phys. Lett.* **15** (1965) 320.
- [29] J.M. Irvine, C.D. Latorre and V.F.E. Pucknell, *The structure of ^{16}O ; a review of the theory*, *Adv. in Phys.* **20:88** (1971) 661.
- [30] H.M. Farkas and I. Kra, *Theta constants, Riemann surfaces and the modular group*. American Mathematical Society: Providence RI, 2001.
- [31] J.H. Kelley, D.R. Tilley, H.R. Weller and C.M. Cheves, *Energy levels of light nuclei $A = 16 - 17$* , *Nucl. Phys.* **A564** (1993) 1.
- [32] C.J. Halcrow, *Skymions – beyond rigid body quantisation*, Ph.D. thesis, University of Cambridge, 2017.

- [33] C. Yuan, T. Suzuki, T. Otsuka, F. Xu and N. Tsunoda, *Shell-model study of Boron, Carbon, Nitrogen, and Oxygen isotopes with a monopole-based universal interaction*, *Phys. Rev.* **C85** (2012) 064324.
- [34] R.A. Battye, M. Haberichter and S. Krusch, *Classically isospinning skyrmion solutions*, *Phys. Rev.* **D90** (2014) 125035.
- [35] C. Barnes, W.K. Baskerville and N. Turok, *Normal mode spectrum of the deuteron in the Skyrme model*, *Phys. Lett. B* **411** (1997) 180.
- [36] C.J. Halcrow, *Vibrational quantisation of the $B = 7$ Skyrmion*, *Nucl. Phys. B* **904** (2016) 106.
- [37] N.S. Manton, B.J. Schroers and M.A. Singer, *The interaction energy of well separated Skyrme solitons*, *Commn. Math. Phys* **245** (2004) 123.
- [38] D.T.J. Feist, *Interactions of $B = 4$ Skyrmions*, *JHEP* **1202** (2012) 100.
- [39] M. Abramowitz and I.A. Stegun, *Handbook of mathematical functions*. U.S. Department of Commerce, 1968.
- [40] M. Gillard, D. Harland, E. Kirk, B. Maybee and M. Speight, *A point particle model of lightly bound Skyrmions*, *Nucl. Phys. B* **917** (2017) 286.
- [41] R.A. Battye and P.M. Sutcliffe, *Skyrmions, fullerenes and rational maps*, *Rev. Math. Phys.* **14** (2002) 29.
- [42] J. Silva Lobo, *Deformed Skyrme crystals*, *JHEP* **1010** (2010) 029.
- [43] W.T. Lin and B. Piette, *Skyrmion vibration modes within the rational map ansatz*, *Phys. Rev. D* **77** (2008) 125028.
- [44] B.J. Schroers, *Dynamics of moving and spinning Skyrmions*, *Z. Phys.* **61** (1994) 479.
- [45] D. Foster and S. Krusch, *Scattering of Skyrmions*, *Nucl. Phys. B* **897** (2015) 697.
- [46] M. Karliner, C. King and N.S. Manton, *Electron scattering intensities and Patterson functions of Skyrmions*, *J. Phys. G* **43** (2016) 055104.
- [47] M. Karliner and r. Mattis, *The baryon spectrum of the Skyrme model*, *Phys. Rev. D* **31** (1985) 2833.
- [48] M.E. Peskin, *Pion - Skyrmion scattering: Collective coordinates at work*, in *Recent Developments in Quantum Field Theory: Proc. N. Bohr Centennial Conf. Copenhagen 1985* (J. A. et al., ed.), p. 129, Amsterdam, North-Holland, 1985.
- [49] M. Karliner and M.P. Mattis, *πN , KN and $\bar{K}N$ scattering: Skyrme model versus experiment*, *Phys. Rev. D* **34** (1986) 1991.
- [50] M. Karliner, *How chiral solitons relate $\bar{K}N$ and πN scattering*, *Phys. Rev. Lett.* **57** (1986) 523.

- [51] C.G. Callan Jr. and E. Witten, *Monopole catalysis of Skyrmion decay*, *Nucl. Phys. B* **239** (1984) 161.
- [52] P.E. Hodgson, *Nuclear Reactions and Nuclear Structure* §2.3. Clarendon Press, 1971.
- [53] E. Braaten and L. Carson, *The deuteron as a toroidal Skyrmion: Electromagnetic form-factors*, *Phys. Rev. D* **39** (1989) 838.
- [54] N.S. Manton and S.W. Wood, *Light nuclei as quantized Skyrmions: Energy spectra and form factors*, in *Proceedings of Quarks*, 2008.
- [55] L.D. Landau and E.M. Lifshitz, *Quantum Mechanics*. Pergamon, 3rd ed., 1977.
- [56] A.L. Patterson, *A fourier series method for the determination of the components of interatomic distances in crystals*, *Phys. Rev.* **46** (1934) 372.
- [57] A. Guinier, *X-Ray Diffraction in Crystals, Imperfect Crystals, and Amorphous Bodies*. Freeman, 1963.
- [58] C.H. Schwalbe, *Arthur Lindo Patterson, his function and element preferences in early crystal structures*, *Crystallography Rev.* **20** (2014) 295.
- [59] S.D. Drell and J.D. Walecka, *Electrodynamic processes with nuclear targets*, *Ann. Phys.* **28** (1964) 18.
- [60] X. Ji, *Order alpha-s corrections to heavy meson semileptonic decay form-factors*, *Phys. Lett. B* **254** (1991) 456.
- [61] A.N. Mitra and I. Kumari, *Relativistic form-factors for clusters with nonrelativistic wave functions*, *Phys. Rev. D* **15** (1977) 261.
- [62] N.S. Manton and S.W. Wood, *Reparametrising the Skyrme model using the Lithium-6 nucleus*, *Phys. Rev. D* **74** (2006) 125017.
- [63] I. Angeli and K.P. Marinova, *Table of experimental nuclear ground state charge radii: An update*, *Atomic Data and Nuclear Data Tables* **99** (2013) 69.
- [64] H. Schopper, *Nuclear Charge Radii (Landolt-Börnstein - Group 1 Elementary Particles, Nuclei and Atoms)*, vol. 20. Springer, 2004.
- [65] A. Camsonne, A.T. Katramatou, M. Olson and N. Sparveris, *JLab measurement of the ^4He charge form factor at large momentum transfers*, *Phys. Rev. Lett.* **112** (2014) 132503.
- [66] I. Sick and J.S. McCarthy, *Elastic electron scattering from C-12 and O-16*, *Nucl. Phys. A* **150** (1970) 631.
- [67] N. Manton and P. Sutcliffe, *Topological Solitons*. Cambridge University Press, 2004.

Appendix A

Spin states for each representation

Below are tables which show how states split into representations for low spin and isospin. Tables A.1 and A.2 are for isospin 0 and Tables A.3 and A.4 are for isospin 1. For the higher dimensional representations we only list on the states; the other states can be found by applying the transformations in (2.44) for the standard representation and (2.66) for the F representation which are found in chapter 2.

J	Trivial/Sign $ \Theta\rangle, T/S, P$	Standard $ W\rangle$
0	(1), $T, +$	None
1	None	None
2	None	(0, 0, 1, 0, 0)
3	(0, 1, 0, 0, 0, -1, 0), $S, -$	None
4	$(\sqrt{5}, 0, 0, 0, \sqrt{14}, 0, 0, 0, \sqrt{5}), T, +$	(0, 0, 1, 0, 0, 0, 1, 0, 0)

Table A.1 The isospin 0 states in the trivial, sign and standard representations up to spin 4. The i th component of the vector in the spin J row corresponds to the coefficient of the spin state, $|J, J + 1 - i\rangle$. The letter T or S next to the state denotes whether the state is in the trivial or sign representations and the sign next to the state denotes the intrinsic parity. States in the standard representation allow either parity.

J	F $ A\rangle, P$
0	None
1	$(e^{\frac{3i\pi}{4}}, 1, e^{\frac{i\pi}{4}}), -$
2	$(-1, \sqrt{2}e^{\frac{i\pi}{4}}, 0, \sqrt{2}e^{-\frac{i\pi}{4}}, 1), +$
3	$(\sqrt{5}e^{-\frac{3i\pi}{4}}, 0, \sqrt{3}e^{-\frac{i\pi}{4}}, 2\sqrt{2}, \sqrt{3}e^{-\frac{3i\pi}{4}}, 0, \sqrt{5}e^{\frac{i\pi}{4}}), -$ $(\sqrt{3}e^{\frac{3i\pi}{4}}, -2i, \sqrt{5}e^{-\frac{i\pi}{4}}, 0, \sqrt{5}e^{-\frac{i\pi}{4}}, -2i, \sqrt{3}e^{-\frac{i\pi}{4}}), +$
4	$(2, e^{\frac{i\pi}{4}}, 0, \sqrt{7}e^{-\frac{i\pi}{4}}, 0, \sqrt{7}e^{\frac{i\pi}{4}}, 0, e^{-\frac{i\pi}{4}}, -2), -$ $(0, \sqrt{7}e^{-\frac{i\pi}{4}}, -2, e^{-\frac{3i\pi}{4}}, 0, e^{\frac{3i\pi}{4}}, 2, \sqrt{7}e^{\frac{i\pi}{4}}, 0), +$

Table A.2 The isospin 0 states in the F representation up to spin 4. The i th component of the vector in the spin J row corresponds to the coefficient of the spin state, $|J, J + 1 - i\rangle$. The sign next to the vector denotes the intrinsic parity.

J	Trivial/Sign $ \Theta\rangle, T/S, P$	Standard $ W\rangle$
0	$\begin{pmatrix} 0 \\ 1 \\ 0 \end{pmatrix}, +$	$\begin{pmatrix} e^{\frac{i\pi}{6}} \\ 0 \\ e^{-\frac{i\pi}{6}} \end{pmatrix}$
1	None	None
2	$\begin{pmatrix} e^{-\frac{5i\pi}{6}} & 0 & \sqrt{2}e^{\frac{2i\pi}{3}} & 0 & e^{-\frac{5i\pi}{6}} \\ 0 & 0 & 0 & 0 & 0 \\ e^{\frac{5i\pi}{6}} & 0 & \sqrt{2}e^{-\frac{2i\pi}{3}} & 0 & e^{\frac{5i\pi}{6}} \end{pmatrix}, S, -$ $\begin{pmatrix} e^{-\frac{i\pi}{3}} & 0 & \sqrt{2}e^{-\frac{5i\pi}{6}} & 0 & e^{-\frac{i\pi}{3}} \\ 0 & 0 & 0 & 0 & 0 \\ e^{\frac{i\pi}{3}} & 0 & \sqrt{2}e^{\frac{5i\pi}{6}} & 0 & e^{\frac{i\pi}{3}} \end{pmatrix}, T, -$	$\begin{pmatrix} e^{\frac{2i\pi}{3}} & 0 & \sqrt{2}e^{-\frac{5i\pi}{6}} & 0 & e^{\frac{2i\pi}{3}} \\ 0 & 0 & 0 & 0 & 0 \\ e^{-\frac{2i\pi}{3}} & 0 & \sqrt{2}e^{\frac{5i\pi}{6}} & 0 & e^{-\frac{2i\pi}{3}} \end{pmatrix}$ $\begin{pmatrix} 0 & 0 & 0 & 0 & 0 \\ 1 & 0 & 0 & 0 & 1 \\ 0 & 0 & 0 & 0 & 0 \end{pmatrix}$

Table A.3 The isospin 1 states in the trivial, sign and standard representations up to spin 2. The (i, j) th entry of the matrix in the spin J row corresponds to the coefficient of the spin and isospin state, $|J, J + 1 - i\rangle |1, 2 - j\rangle$. The letter T or S next to matrix denotes whether the state is in the trivial or sign representations and the sign next to the matrix denotes the intrinsic parity. States in the standard representation allow either parity.

J	F $ A\rangle, P$
0	None
1	$\begin{pmatrix} 0 & e^{\frac{3i\pi}{4}} & 0 \\ 0 & 0 & 0 \\ 0 & e^{\frac{i\pi}{4}} & 0 \end{pmatrix}, +$ $\begin{pmatrix} (2 + \sqrt{3})e^{-\frac{5i\pi}{12}} & (1 + \sqrt{3})e^{-\frac{i\pi}{6}} & e^{-\frac{i\pi}{12}} \\ 0 & 0 & 0 \\ e^{-\frac{i\pi}{12}} & (1 + \sqrt{3})e^{-\frac{5i\pi}{6}} & (2 + \sqrt{3})e^{\frac{5i\pi}{12}} \end{pmatrix}, -$ $\begin{pmatrix} (2 + \sqrt{3})e^{\frac{i\pi}{12}} & (1 + \sqrt{3})e^{\frac{i\pi}{3}} & e^{\frac{7i\pi}{12}} \\ 0 & 0 & 0 \\ e^{-\frac{7i\pi}{12}} & (1 + \sqrt{3})e^{\frac{2i\pi}{3}} & (2 + \sqrt{3})e^{-\frac{i\pi}{12}} \end{pmatrix}, +$
2	$\begin{pmatrix} 0 & 0 & 0 & 0 & 0 \\ 1 & e^{-\frac{3i\pi}{4}} & 0 & e^{\frac{3i\pi}{4}} & -1 \\ 0 & 0 & 0 & 0 & 0 \end{pmatrix}, -$ $\begin{pmatrix} \sqrt{2}e^{\frac{i5\pi}{6}} & (\sqrt{3} - 1)e^{\frac{i\pi}{12}} & 0 & (1 + \sqrt{3})e^{\frac{7i\pi}{12}} & \sqrt{2}e^{-\frac{i\pi}{6}} \\ 0 & 0 & 0 & 0 & 0 \\ \sqrt{2}e^{\frac{i\pi}{6}} & (1 + \sqrt{3})e^{\frac{5i\pi}{12}} & 0 & (\sqrt{3} - 1)e^{\frac{11i\pi}{12}} & \sqrt{2}e^{-\frac{5i\pi}{6}} \end{pmatrix}, +$ $\begin{pmatrix} \sqrt{2}e^{\frac{i\pi}{3}} & (\sqrt{3} - 1)e^{-\frac{5i\pi}{12}} & 0 & (1 + \sqrt{3})e^{\frac{i\pi}{12}} & \sqrt{2}e^{-\frac{2i\pi}{3}} \\ 0 & 0 & 0 & 0 & 0 \\ \sqrt{2}e^{\frac{2i\pi}{3}} & (1 + \sqrt{3})e^{\frac{11i\pi}{12}} & 0 & (\sqrt{3} - 1)e^{-\frac{7i\pi}{12}} & \sqrt{2}e^{-\frac{i\pi}{3}} \end{pmatrix}, -$

Table A.4 The isospin 1 states in the F representation up to spin 2. The (i, j) th entry of the matrix in the spin J row corresponds to the coefficient of the spin and isospin state, $|J, J + 1 - i\rangle |1, 2 - j\rangle$. The sign next to the matrix denotes the intrinsic parity.

Appendix B

Combining vibrations

In chapter 2 we states how the different representation combine with each other. In this appendix we show how these combinations work explicitly for some states.

First we look at combining two states in the E representation via the example of multiplication of the two spin 2 states:

$$|\Psi_1\rangle = (u - v) (|2, 2\rangle + |2, -2\rangle) - \sqrt{6}(u + v) |2, 0\rangle \quad (\text{B.1})$$

and

$$|\Psi_2\rangle = (U - V) (|2, 2\rangle + |2, -2\rangle) - \sqrt{6}(U + V) |2, 0\rangle. \quad (\text{B.2})$$

We just take the direct product of these states, using Clebsch-Gordan coefficients to calculate the new rovibrational state. This produces states for a variety of different spins.

For spin 0, we have the state proportional to

$$(2uU + 2vV + uV + vU) |0, 0\rangle. \quad (\text{B.3})$$

In order to find which representation this lies in we must check how the combination $2uU + 2vV + uV + vU$, transforms under the elements (12) and (123) of S_3 . We find that it is invariant under both of these and therefore lies in the trivial rep.

The product of $|\Psi_1\rangle$ and $|\Psi_2\rangle$ does not produce any states for spin 1 because these would have to lie in the F representation which is not permitted.

For spin 2, we have the state proportional to

$$(u' - v') (|2, 2\rangle + |2, -2\rangle) - \sqrt{6}(u' + v') |2, 0\rangle, \quad (\text{B.4})$$

where $u' = uU - uV - vU - 2vV$ and $v' = vV - vU - uV - 2uU$. This states transforms according to the standard representation of S_3 .

For spin 3, we have the state proportional to

$$(uV - vU) (|3, 2\rangle - |3, -2\rangle) \quad (\text{B.5})$$

which transforms under the sign representation.

For spin 4, we have the state proportional to

$$2(u' - v') (|4, 2\rangle + |4, -2\rangle) - (u' + v') (\sqrt{7}|4, 4\rangle - \sqrt{10}|4, 0\rangle + \sqrt{7}|4, -4\rangle), \quad (\text{B.6})$$

with u' and v' defined as above, which is in the standard representation, and another state proportional to

$$(2uU + 2vV + uV + vU) (\sqrt{5}|4, 4\rangle + \sqrt{14}|4, 0\rangle + \sqrt{5}|4, -4\rangle), \quad (\text{B.7})$$

which is in the trivial representation.

To show how a state in the E representation combines with a state in the F representation we consider the product of the states,

$$|\Psi_1\rangle = (u - v) (|2, 2\rangle + |2, -2\rangle) - \sqrt{6}(u + v) |2, 0\rangle, \quad (\text{B.8})$$

in the E representation, with the state,

$$|\Psi_2\rangle = -(X - iY) |1, 1\rangle + \sqrt{2}Z |1, 0\rangle + (X + iY) |1, -1\rangle, \quad (\text{B.9})$$

in the F representation.

For spin 1, we have the state proportional to

$$-(X' - iY') |1, 1\rangle + \sqrt{2}Z' |1, 0\rangle + (X' + iY') |1, -1\rangle, \quad (\text{B.10})$$

where $X' = uX$, $Y' = vY$ and $Z' = -(u + v)Z$, which lies in the F representation.

For spin 2, we have the state proportional to

$$Z' (|2, 2\rangle - |2, -2\rangle) - (X' + iY') |2, 1\rangle - (X' - iY') |2, -1\rangle \quad (\text{B.11})$$

where $X' = (u + 2v)X$, $Y' = -(v + 2u)Y$ and $Z' = (u - v)Z$, which lies in the F representation.

For spin 3, we produce a positive parity state proportional to

$$\sqrt{3}(X' - iY') |3, 3\rangle + \sqrt{8}Z' |3, 2\rangle + \sqrt{5}(X' + iY') |3, 1\rangle \quad (\text{B.12})$$

$$-\sqrt{5}(X' - iY') |3, -1\rangle + \sqrt{8}Z' |3, -2\rangle - \sqrt{3}(X' + iY') |3, -3\rangle \quad (\text{B.13})$$

where $X' = (u + 2v)X$, $Y' = -(v + 2u)Y$ and $Z' = (u - v)Z$, which lies in the F representation. We also produce a negative parity state proportional to

$$-\sqrt{5}(X' + iY') |3, 3\rangle + \sqrt{3}(X' - iY') |3, 1\rangle + \sqrt{16}Z' |3, 0\rangle \quad (\text{B.14})$$

$$-\sqrt{3}(X' + iY') |3, -1\rangle + \sqrt{5}(X' - iY') |3, -3\rangle \quad (\text{B.15})$$

where $X' = uX$, $Y' = vY$ and $Z' = -(u + v)Z$, which also lies in the F representation.

To show how two states in F representation combine we consider the product of the states,

$$|\Psi_1\rangle = -(X - iY) |1, 1\rangle + \sqrt{2}Z |1, 0\rangle + (X + iY) |1, -1\rangle, \quad (\text{B.16})$$

and

$$|\Psi_2\rangle = -(x - iy) |1, 1\rangle + \sqrt{2}z |1, 0\rangle + (x + iy) |1, -1\rangle, \quad (\text{B.17})$$

which are both in the F representation.

For spin 0, we produce a state proportional to,

$$(xX + yY + zZ) |0, 0\rangle \quad (\text{B.18})$$

which is in the trivial representation.

For spin 1, we have the state proportional to

$$-(X' - iY') |1, 1\rangle + \sqrt{2}Z' |1, 0\rangle + (X' + iY') |1, -1\rangle \quad (\text{B.19})$$

where $X' = yZ - zY$, $Y' = zX - xZ$ and $Z' = xY - yX$, which is in the F representation.

For spin 2, we have the state proportional to

$$Z' |2, 2\rangle - (X' + iY') |2, 1\rangle - (X' - iY') |2, -1\rangle - Z' |2, -2\rangle \quad (\text{B.20})$$

where $X' = yZ + zY$, $Y' = zX + xZ$ and $Z' = xY + yX$, which is in the F representation, and another state proportional to

$$(u' - v') (|2, 2\rangle + |2, -2\rangle) - \sqrt{6}(u' + v') |2, 0\rangle, \quad (\text{B.21})$$

where $u' = 2xX - yY - zZ$ and $v' = 2yY - zZ - xX$, which transform according to the standard representation of S_3 .

Now that we know how states from different vibrations combine we can find the spectrum of these combined vibrations as shown in Table 2.4.